METHODS AND APPLICATIONS IN STRIATED MUSCLE PHYSIOLOGY

EDITED BY: Joseph J. Bass, Ma Qiang, Norio Fukuda, Peter T. Wright and
Stefano Biressi

PUBLISHED IN: Frontiers in Physiology

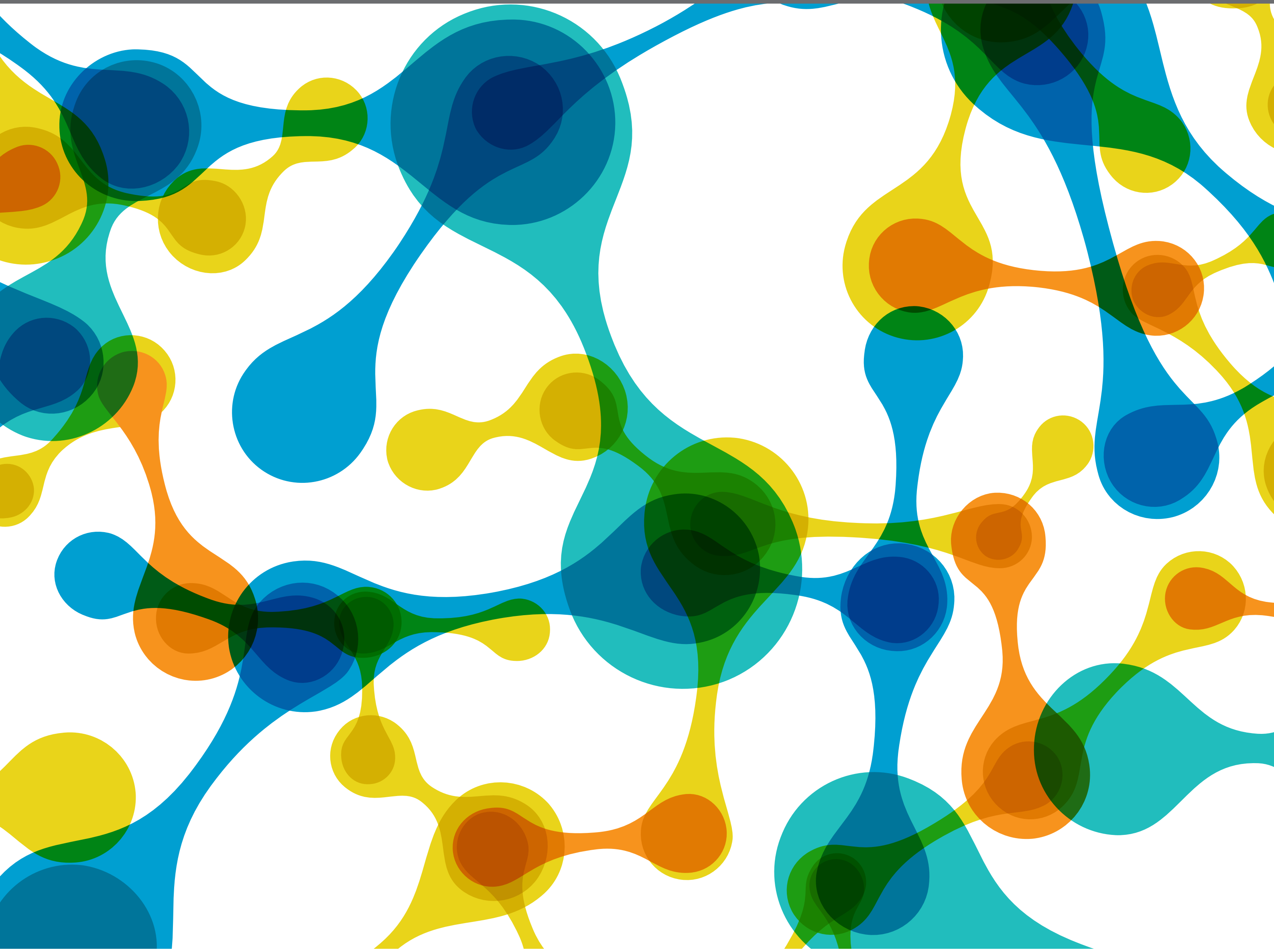

frontiers Research Topics

ISSN 1664-8714
ISBN 978-2-83250-067-5
DOI 10.3389/978-2-83250-067-5

About Frontiers

Frontiers is more than just an open-access publisher of scholarly articles: it is a pioneering approach to the world of academia, radically improving the way scholarly research is managed. The grand vision of Frontiers is a world where all people have an equal opportunity to seek, share and generate knowledge. Frontiers provides immediate and permanent online open access to all its publications, but this alone is not enough to realize our grand goals.

Frontiers Journal Series

The Frontiers Journal Series is a multi-tier and interdisciplinary set of open-access, online journals, promising a paradigm shift from the current review, selection and dissemination processes in academic publishing. All Frontiers journals are driven by researchers for researchers; therefore, they constitute a service to the scholarly community. At the same time, the Frontiers Journal Series operates on a revolutionary invention, the tiered publishing system, initially addressing specific communities of scholars, and gradually climbing up to broader public understanding, thus serving the interests of the lay society, too.

Dedication to Quality

Each Frontiers article is a landmark of the highest quality, thanks to genuinely collaborative interactions between authors and review editors, who include some of the world's best academicians. Research must be certified by peers before entering a stream of knowledge that may eventually reach the public - and shape society; therefore, Frontiers only applies the most rigorous and unbiased reviews.
Frontiers revolutionizes research publishing by freely delivering the most outstanding research, evaluated with no bias from both the academic and social point of view.
By applying the most advanced information technologies, Frontiers is catapulting scholarly publishing into a new generation.

What are Frontiers Research Topics?

Frontiers Research Topics are very popular trademarks of the Frontiers Journals Series: they are collections of at least ten articles, all centered on a particular subject. With their unique mix of varied contributions from Original Research to Review Articles, Frontiers Research Topics unify the most influential researchers, the latest key findings and historical advances in a hot research area! Find out more on how to host your own Frontiers Research Topic or contribute to one as an author by contacting the Frontiers Editorial Office: frontiersin.org/about/contact

METHODS AND APPLICATIONS IN STRIATED MUSCLE PHYSIOLOGY

Topic Editors:
Joseph J. Bass, University of Nottingham, United Kingdom
Ma Qiang, Southern Medical University, China
Norio Fukuda, Jikei University School of Medicine, Japan
Peter T. Wright, University of Roehampton London, United Kingdom
Stefano Biressi, University of Trento, Italy

Citation: Bass, J. J., Qiang, M., Fukuda, N., Wright, P. T., Biressi, S., eds. (2022). Methods and Applications in Striated Muscle Physiology.
Lausanne: Frontiers Media SA. doi: 10.3389/978-2-83250-067-5

Table of Contents

frontiers | Frontiers in Physiology

TYPE Editorial
PUBLISHED 11 August 2022
DOI 10.3389/fphys.2022.979237

OPEN ACCESS

EDITED AND REVIEWED BY
Paul M. L. Janssen,
The Ohio State University, United States

*CORRESPONDENCE
Stefano Biressi,
stefano.biressi@unitn.it

SPECIALTY SECTION
This article was submitted to Striated Muscle Physiology,
a section of the journal
Frontiers in Physiology

RECEIVED 27 June 2022
ACCEPTED 15 July 2022
PUBLISHED 11 August 2022

CITATION
Biressi S, Ma Q, Fukuda N, Bass JJ and Wright PT (2022), Editorial: Methods and applications in striated muscle physiology.
Front. Physiol. 13:979237.
doi: 10.3389/fphys.2022.979237

Editorial: Methods and applications in striated muscle physiology

Stefano Biressi[1]*, Qiang Ma[2], Norio Fukuda[3], Joseph J. Bass[4] and Peter T. Wright[5]

[1]Department of Cellular, Computational and Integrative Biology (CIBIO), University of Trento, Trento, Italy, [2]Department of Biopharmaceutics, School of Laboratory Medicine and Biotechnology, Southern Medical University, Guangzhou, Guangdong, China, [3]Department of Cell Physiology, The Jikei University School of Medicine, Tokyo, Japan, [4]MRC-Versus Arthritis Centre for Musculoskeletal Ageing Research, NIHR Nottingham Biomedical Research Centre, Centre of Metabolism, Ageing, and Physiology, School of Medicine, University of Nottingham, Derby, United Kingdom, [5]School of Life and Health Sciences, University of Roehampton, London, United Kingdom

KEYWORDS

tecniques, innovation, skeletal, cardiac, muscle

Editorial on the Research Topic
Methods and applications in striated muscle physiology

Striated muscle exists in two types, skeletal and cardiac. They share numerous operational and structural characteristics, including sarcomere organization, with repeating functional units that confer the typical striated appearance observed in microscopic images of this tissue. Striated muscle is a highly adaptive and critically important metabolic tissue with intrinsic roles in health and disease. Striated muscle contraction supports various crucial physiological processes, including respiration, locomotion, posture (skeletal muscle), and pumping blood throughout the vascular system (cardiac muscle). Striated muscles are affected by many acquired and genetic pathophysiological conditions, which represent significant health and economic burden for modern society. Cardiac disorders, including ischemia and arrhythmias, are among the leading cause of death worldwide. Loss of skeletal muscle mass and strength is an indicator of neuromuscular genetic pathologies, aging, cancer, and a variety of chronic or acute conditions that are systemic or primarily affecting different tissues.

This Research Topic aims to describe new technical approaches and critically discuss existing methods and protocols applicable to the study of striated muscle physiology. The goal is to provide investigators with novel reliable tools: 1) to understand the fundamental mechanisms controlling striated muscle biology, 2) to characterize and diagnose striated muscle degenerative conditions, and 3) to identify innovative therapeutic strategies to preserve skeletal and cardiac muscle homeostasis and function.

One of the major limitations of the study of striated muscle characteristics for both basic research and diagnostic purposes is obtaining and preparing tissue for subsequent *ex vivo* molecular analysis or cellular and histological characterization. This is particularly critical if the donors of the biopsies are in a particularly fragile category, such as old people or individuals presenting coagulation defects, such as patients with chronic liver diseases. The Bergström biopsy is the gold-standard technique for sampling skeletal muscle and is used worldwide. This approach relies on collecting 25–125 mg of tissue with a 3–5 mm needle. Quinlan et al. report the results obtained with cohorts of patients affected by end-stage liver disease and non-cirrhotic non-alcoholic fatty liver disease undergoing percutaneous *vastus lateralis* biopsies with a Bergström needle. They report 90% of successful biopsies in over 71 attempts and only one adverse event (hematoma). This study also identifies the presence of subcutaneous adipose tissue as a critical aspect hindering productive sampling, indicating that appropriate patient selection and good technique mitigate against potential risks. An alternative to Bergström biopsy is microbiopsy, obtained with a needle of smaller diameter (typically 2–2. 3 mm) and therefore characterized by decreased invasiveness. The size of tissue biopsy is generally smaller, ranging from 14 to 22 mg. Hester et al. show that percutaneous microbiopsy can be successfully performed in old individuals, and sufficient material is obtained for histological characterization of fiber types. This observation supports the idea that microbiopsies may be a valuable muscle sampling alternative to the Bergström technique, particularly for categories of fragile patients.

The obtainment and preparation of tissues for *ex vivo* investigation are also challenging for cardiac muscle. Cultivation of ventricular slices is increasingly used in basic and translational studies investigating mechanisms of ventricular dysfunction that lead to heart failure. Palmer and Bell describe, in the rat model, methods for removing and preparing cardiac papillary muscles and provide instruction for preparing cardiac slices for functional analyses. Klumm et al. describe a methodology that allows for long-term (up to 3 weeks) cultivation and functional analysis of beating human atrial myocardium. The possibility of establishing multicellular models of atrial myocardium expands the possibility of study beyond ventricular pathophysiology to discern atrial biology and atrial dysfunction.

The power of *in vitro* investigation in cardiac biology is disclosed by the methodological study reported by Krstic et al. They performed a visual characterization of beat-to-beat mitochondrial calcium fluxes in rat cardiomyocytes. For this purpose, they modify the fluorescent membrane-permeable Ca^{2+} indicator Rhod-2 by reducing it to di-hydroRhod-2, which is non-fluorescent unless it reaches the oxidative environment of mitochondria. This study highlights the need for optimized protocols to comprehend the complex mechanism underlying the contraction of striated muscle cells.

Calcium dynamics drive ATP production in the mitochondrial matrix, and play a critical role in the cytosol where Ca^{2+} governs striated muscle contraction and relaxation at the myofilament level via conformational modulations of the troponin complex. Rasmussen and Jin developed an approach using site-specific monoclonal antibodies as probes to monitor conformational changes of proteins. They applied this technique to study the Ca^{2+}-binding subunit and the tropomyosin-binding/thin filament-anchoring subunits of troponin. Measurements at the sub-cellular level are instrumental in investigating striated skeletal and cardiac muscle contractility. In his manuscript, Marston reviews the current methods for measuring force production at the subcellular level, including single myofibril and single myofilament techniques. Herzog further critically discusses this area of expertise, particularly focusing on the isolation and testing of single sarcomeres. Also focused on sarcomeres is the publication by Adkins et al. that reports a quantification of the variability of *in vivo* sarcomere length measures obtained in human upper limb skeletal muscle with second harmonic generation microendoscopy. This state-of-the-art technique allows minimally invasive measures of sarcomere length. The assessment of the natural variability associated with this approach guides the development of robust experimental design and the interpretation of *in vivo* analyses of sarcomere length.

Skeletal muscle is not only composed of contractile syncytial muscle fibers but also other mononucleated cellular types, such as muscle stem cells, immune cells, interstitial and stromal progenitors, all reportedly playing a crucial role during muscle regeneration. Florio et al. disclose the potential use of electro-enhanced DNA transfer to murine skeletal muscle to investigate the characteristics of these mononucleated cells. Importantly, this approach can be applied not only to the study of healthy muscle but also to the investigation of alterations of the phenotypic properties that have been associated with defective repair and fibrosis in aging and dystrophic tissues.

The overarching theme of this Research Topic is to better understand striated tissue biology and uncover new diagnostic and therapeutic approaches to treat striated muscle disease. In this light, the discussion put forward by Sarvazyan in a review centered on valveless pumping based on the Liebau mechanism is particularly intriguing. Here, the author describes the biological occurrence of Liebau pumps, highlights the differences between Liebau pumping and the peristaltic flow, and discusses the potential uses and body sites that can benefit from implantable Liebau-type pumps.

In conclusion, this Research Topic on *Methods and applications in striated muscle physiology* incorporates novel original techniques and reviews of methodological approaches that can be used by investigators operating in the field of skeletal or cardiac muscle biology.

Author contributions

All authors listed have made a substantial, direct, and intellectual contribution to the work and approved it for publication.

Funding

This work in the authors' laboratories is supported in part by JSPS KAKENHI—Grant Nos. 20H03421 (to NF) and 21K19929 (to NF), by AFM/Téléthon—Grant No. 23758 (to SB), and by the Muscular Dystrophy Association—Innovation Grant No. 874294 (to SB).

Acknowledgments

We would like to thank all the authors who have submitted manuscripts to this Research Topic.

Conflict of interest

The authors declare that the research was conducted in the absence of any commercial or financial relationships that could be construed as a potential conflict of interest.

Publisher's note

frontiers
in Physiology

ORIGINAL RESEARCH
published: 10 January 2022
doi: 10.3389/fphys.2021.756626

Microbiopsy Sampling for Examining Age-Related Differences in Skeletal Muscle Fiber Morphology and Composition

Garrett M. Hester[1]*, Trisha A. VanDusseldorp[1], Phuong L. Ha[1], Kaveh Kiani[2], Alex A. Olmos[1], Melody Jabbari[2], Shania Kalladanthyil[2], SooBin An[2], Alyssa R. Bailly[1], Benjamin E. Dalton[1] and Anton L. Bryantsev[2]*

[1] *Department of Exercise Science and Sport Management, Kennesaw State University, Kennesaw, GA, United States,*
[2] *Department of Molecular and Cellular Biology, Kennesaw State University, Kennesaw, GA, United States*

Edited by:
Joseph J. Bass,
University of Nottingham,
United Kingdom

Reviewed by:
Jonathan Quinlan,
University of Birmingham,
United Kingdom
Nima Gharahdaghi,
University of Nottingham,
United Kingdom

***Correspondence:**
Garrett M. Hester
ghester4@kennesaw.edu
Anton L. Bryantsev
abryants@kennesaw.edu

Specialty section:
This article was submitted to Striated Muscle Physiology, a section of the journal Frontiers in Physiology

Received: 10 August 2021
Accepted: 06 December 2021
Published: 10 January 2022

Citation:
Hester GM, VanDusseldorp TA, Ha PL, Kiani K, Olmos AA, Jabbari M, Kalladanthyil S, An S, Bailly AR, Dalton BE and Bryantsev AL (2022) Microbiopsy Sampling for Examining Age-Related Differences in Skeletal Muscle Fiber Morphology and Composition. Front. Physiol. 12:756626. doi: 10.3389/fphys.2021.756626

Introduction: The increasingly popular microbiopsy is an appealing alternative to the more invasive Bergström biopsy given the challenges associated with harvesting skeletal muscle in older populations. Parameters of muscle fiber morphology and composition derived from the microbiopsy have not been compared between young and older adults.

Purpose: The purpose of this study was to examine muscle fiber morphology and composition in young (YM) and older (OM) males using the microbiopsy sampling technique. A secondary aim was to determine if specific strength is associated with serum levels of C-terminal agrin fragment [CAF; an indicator of neuromuscular junction (NMJ) degradation].

Methods: Thirty healthy, YM ($n = 15$, age $= 20.7 \pm 2.2$ years) and OM ($n = 15$, age $= 71.6 \pm 3.9$ years) underwent ultrasound imaging to determine whole-muscle cross-sectional area (CSA) of the vastus lateralis and rectus femoris as well as isometric and isokinetic ($60°\cdot s^{-1}$ and $180°\cdot s^{-1}$) peak torque testing of the knee extensors. Microbiopsy samples of the vastus lateralis were collected from 13 YM and 11 OM, and immunofluorescence was used to calculate CSA and proportion of type I and type II fibers.

Results: Peak torque was lower in OM at all velocities ($p \leq 0.001$; $d = 1.39$–1.86) but only lower at $180°\cdot s^{-1}$ ($p = 0.003$; $d = 1.23$) when normalized to whole-muscle CSA. Whole-muscle CSA was smaller in OM ($p = 0.001$; $d = 1.34$), but atrophy was not present at the single fiber level ($p > 0.05$). Per individual, ~900 fibers were analyzed, and type I fiber CSA was larger ($p = 0.05$; $d = 0.94$) in OM which resulted in a smaller type II/I fiber CSA ratio ($p = 0.015$; $d = 0.95$). CAF levels were not sensitive to age ($p = 0.159$; $d = 0.53$) nor associated with specific strength or whole-muscle CSA in OM.

Conclusion: The microbiopsy appears to be a viable alternative to the Bergström biopsy for histological analyses of skeletal muscle in older adults. NMJ integrity was not influential for age-related differences in specific strength in our healthy, non-sarcopenic older sample.

Keywords: atrophy, muscle quality, microbiopsy, aging, myofiber, C-terminal agrin fragment (CAF), vastus lateralis, immunofluorescence

INTRODUCTION

The proportion of older Americans is expected to continue increasing, but the number of very old adults is projected to dramatically increase. For example, the number of adults 65 years and over is expected to nearly double from 49 million in 2018 to 95 million in 2060, whereas the number of adults 85 years and over is expected to double by 2035 and nearly triple by 2060 (Vespa et al., 2020). Sarcopenia, the aging-related loss in muscle mass and function, affects up to 40% of older adults making the study of skeletal muscle health an increasingly important area of research (Mayhew et al., 2019). Innovative methodological approaches that increase the feasibility of studying skeletal muscle in older adults, particularly the very old, are critical in creating additional opportunities to address the etiology of sarcopenia and effectiveness of interventions.

Introduced in the 1960s, the Bergström biopsy (Bergstrom, 1962) is the gold standard technique for sampling skeletal muscle and has been widely used for decades in biochemical and histological studies in young and older adults. The Bergström biopsy relies on a 3–5 mm hollow needle that retrieves 25–125 mg of muscle tissue depending on whether the suction-modified approach is utilized (Bergstrom, 1975; Tarnopolsky et al., 2011). The microbiopsy (or tiny percutaneous needle biopsy) has only recently gained attention as an alternative to the Bergström for histological analysis of skeletal muscle (Pietrangelo et al., 2011; Townsend et al., 2016), despite reports of the technique going back to the late 1990s (Vescovo et al., 1996). The microbiopsy typically involves a 13- or 14-gauge (2.3 or 2 mm) needle that retrieves skeletal muscle samples via a spring-loaded instrument without the need for the 4–5 mm incision that precedes the Bergström biopsy (Pietrangelo et al., 2011; Hughes et al., 2015; Townsend et al., 2016). The microbiopsy is an appealing alternative to the Bergström given its smaller needle diameter and decreased level of invasiveness. Indeed, subjects report less pain and a preference for the microbiopsy technique compared to the Bergström (Hayot et al., 2005; Bonafiglia et al., 2020). Despite its increasing popularity, there is a paucity of work using the microbiopsy for histological analyses, which is at least partially owed to hesitation regarding the smaller tissue sample reported to range from 14 to 22 mg (Hayot et al., 2005; Hughes et al., 2015; Townsend et al., 2016). Demonstrating the efficacy of microbiopsy sampling for examining muscle fiber type morphology and composition is critical for determining the utility of this technique in the field of skeletal muscle research. Further, age-related differences in muscle fiber properties derived from microbiopsy sampling are unclear as, to the best of our knowledge, there are no reports comparing young and older adults. Age-related comparisons will indicate whether the effectiveness of the microbiopsy technique is dependent upon the population and will offer preliminary, indirect comparisons with findings derived from the Bergström biopsy.

It is expected the microbiopsy will be effective for examining aging-related changes in single fiber properties, which is useful for understanding how these alterations affect muscle health (e.g., atrophy). However, there are other important considerations when aiming to investigate the influence of age on muscle function. Older adults demonstrate reduced specific strength (muscle strength relative to muscle size), particularly at higher contraction velocities (Frontera et al., 1991; Overend et al., 1992; Jubrias et al., 1997), indicating that physiological factors other than muscle size contribute to aging-related weakness (i.e., dynapenia). The various qualitative skeletal muscle and nervous system factors and their potential role in dynapenia have received increasingly more attention over the past decade (see review, Clark and Manini, 2010) particularly due to the divergent reductions in muscle size and strength with increasing age (Goodpaster et al., 2006; Delmonico et al., 2009). Based on rodent models, impaired action potential generation via neuromuscular junction (NMJ) degradation has been suggested to have a role in aging related weakness (Padilla et al., 2021) and is believed to precede muscle fiber atrophy (Deschenes et al., 2010). However, limited evidence exists on the NMJ in humans due to inherent methodological challenges with morphological analyses. Recently, the soluble 22 kDa C-terminal agrin fragment (CAF) has been identified as an indicator of NMJ deterioration (Bolliger et al., 2010) and shows promise as a blood biomarker for sarcopenia (Hettwer et al., 2013; Pratt et al., 2021). Despite building evidence toward the association between CAF levels and muscle mass, surprisingly little work has examined its association with muscle function. In the case that NMJ deterioration augments action potential transmission to muscle fibers, muscle function may be compromised prior to substantial muscle fiber atrophy. Examining the association between NMJ degradation (as indicated by circulating CAF levels) and specific strength is critical for determining its role, if any, in maintaining muscle quality.

The microbiopsy has the potential to increase skeletal muscle research opportunities in older or fragile populations due to its reduced degree of invasiveness. It is important to determine its efficacy for analysis of muscle fiber properties in young and, in particular, older adults. The purpose of this study was to examine muscle fiber morphology and composition in young and older males using the microbiopsy sampling technique, and a secondary aim was to determine if specific strength is associated serum CAF levels in older males. In line with previous research,

TABLE 1 | Characteristics and CAF levels for young and older males.

Variable	Young	Older	*d*
Age (years)	20.73 ± 2.22	71.60 ± 3.94	–
Height (cm)	175.50 ± 8.55	171.08 ± 9.91	0.47
Body mass (kg)	71.03 ± 8.98	86.65 ± 16.27*	1.18
BMI (kg·m^{-2})	23.05 ± 2.43	29.56 ± 4.99*	1.66
Body fat %	24.65 ± 6.24	33.83 ± 6.89*	1.39
ALM (kg/BMI)	1.06 ± 0.15	0.83 ± 0.15*	1.48
Whole-muscle CSA (cm^2)	36.21 ± 5.78	29.07 ± 4.79*	1.34
CAF (pg/ml)	369.72 ± 86.25	448.83 ± 186.61	0.53
HG strength (kg)	47.23 ± 11.56	42.45 ± 10.85	0.02

BMI, body mass index; ALM, appendicular lean mass; CSA, cross-sectional area; CAF, C-terminal agrin fragment; HG, handgrip.
**Indicates significant ($p < 0.05$) difference between groups.*

we hypothesize that muscle fiber composition will be similar, but type II muscle fiber size will be smaller in older males. In addition, we believe CAF levels will not be associated with specific strength in older males based on previous work indicating predominant sensitivity of CAF levels to muscle atrophy (Drey et al., 2013; Pratt et al., 2021).

MATERIALS AND METHODS

Subjects

Thirty healthy, young (YM; $n = 15$; range = 18–26 years) and older (OM; $n = 15$; range = 66–78 years) males completed this study. Characteristics for each group are displayed in **Table 1**. As specified below, due to limited funds, microbiopsy samples were obtained in a subset of each group. All subjects reported not having performed structured endurance or resistance training exercise in the past 5 years and were screened for the following exclusion criteria: presence of unstable cardiovascular, metabolic or renal disease, diagnosed myocardial infarction within the last 2-years, terminal illness, a history of cerebrovascular disease, any condition affecting neuromuscular function, an artificial lower-body joint, rheumatoid arthritis, a fracture within the past year, reliance upon an assistive walking device, and Mini-mental State Exam (Folstein et al., 1975) score less than 23. Subjects were recruited from senior centers and the surrounding community through word of mouth, email, and flyer advertisements. This study was approved by the University's Institutional Review Board prior to data collection. All subjects provided oral and written consent prior to beginning the study.

Experimental Design

Subjects visited the laboratory on two occasions separated by at least 3 days but not more than 7. Body composition assessment and familiarization with knee extensor (KE) testing was completed during the first visit. The second visit began with ultrasonography followed by KE testing and, after ∼30 min of rest (lying supine), a skeletal muscle microbiopsy. Leg dominance was determined via inquiry of preferred kicking leg (van Melick et al., 2017) and all testing was completed on the dominant leg. Subjects were instructed to avoid alcohol and vigorous physical activity for 24 and 48 h, respectively, before each visit.

Torque and velocity were recorded for the KEs using a calibrated Biodex 4 isokinetic dynamometer (Biodex Medical Systems, Inc. Shirley, NY, United States). Electromyography (EMG) of the vastus lateralis (VL) and rectus femoris (RF) was recorded using a parallel bar, bipolar surface electrode (Delsys Trigno, Delsys, Inc., Natick, MA, United States). The skin over the muscle was shaved, abraded, and cleaned with alcohol, and subsequently the electrode was placed over the muscle belly in accordance with the recommendations of the SENIAM project (Hermens et al., 1999). All signals were sampled at 2 kHz using EMGworks software (Delsys, Inc., Natick, MA, United States). Subjects were seated with hands across their chest, restraining straps over their trunk, pelvis, and thigh, and the input axis of the dynamometer aligned with the axis of rotation of the knee. Knee joint position was set at 110° (180° = full extension) for maximal voluntary isometric contractions (MVICs), while isokinetic testing involved an 80° range of motion (90°–170°).

Blood Analysis

Venous blood was collected via venipuncture of an antecubital vein during the morning of the first visit after a 12 h fast. Serum concentrations of CAF were determined according to manufacturer guidelines in duplicate via enzyme-linked immunosorbent assay (Glory Science Co., Ltd., Shanghai, China) and microplate reader (FilterMax F5 Multi-Mode Microplate Reader, LLC, Molecular Devices, San Jose, CA, United States) at a wavelength of 450 nm. The coefficient of variation (CV%) was 5.5%. Due to the CAF value being out of the kit range for one subject, a sample size for the YM group of 14 was used for analysis.

Body Composition

Height (cm) and weight (kg) were measured using an electronic scale (Tanita WB 3000, Arlington Heights, IL, United States). Body fat % was obtained via dual-energy x-ray absorptiometry in total body mode using a GE Lunar iDXA (GE Healthcare, Madison, WI, United States). Subsequently, appendicular lean mass (ALM) relative to body mass index was calculated using the region of interest function as suggested by Heymsfield et al. (1990). We have previously shown excellent reliability for the calculation of ALM ($ICC_{2,1}$, SEM and CV% were 0.999, 0.042 kg·m^2, and 1.2%, respectively) (Olmos et al., 2019).

Panoramic images of the VL and RF were obtained using a B-mode ultrasound (LOGIQ S7, General Electric Company, Milwaukee, WI, United States). Subjects rested in the supine position for 10 min prior to the images being captured. Images were acquired with a multifrequency linear-array probe (ML6-15 L; 5–13 MHz; 50mm field of view; General Electric Company, Milwaukee, WI, United States) using the LogiqVIEW function and following settings to ensure optimal image quality: gain = 50 dB, depth = 5.0 cm, and frequency = 12 MHz (Stratton et al., 2020). Three images of the VL and RF were captured at 50% the distance from the greater trochanter to lateral femoral epicondyle and 50% the distance from the anterior superior iliac spine to the superior border of the patella, respectively. The same investigator obtained all images while subjects were in a supine position with the knee fully extended. The investigator slowly moved the probe in the transverse plane while applying minimal and consistent pressure. Thick, double-sided tape was placed over each muscle in the transverse plane to ensure the probe was moved perpendicular to the skin. Images were scaled from pixels to centimeters prior to analysis. Cross-sectional area (CSA) of each muscle was determined using the polygon function in ImageJ software[1] (version 1.46r, National Institutes of Health, Bethesda, MD, United States) to select as much of the muscle as possible without including the surrounding fascia. For statistical analysis, whole-muscle CSA was calculated as the sum of the VL and RF. A subset of young subjects ($n = 11$) returned for a third visit to assess test-retest reliability. Excellent reliability was shown for whole-muscle CSA ($ICC_{2,1} = 0.957$, SEM = 1.35 cm^2, CV = 3.7%).

Maximal Isometric and Isokinetic Testing

Prior to KE testing, for the purpose of characterizing sarcopenia status, handgrip strength was obtained using a dynamometer (Jamar Plus Hand Dynamometer, Patterson Medical, Cedarburg, WI, United States) while subjects were seated with the elbow joint at ∼90° and wrist in a neutral position. Subjects completed 3 trials with each hand and the highest value was used for subsequent analysis. Subjects began KE testing by performing 2 submaximal isometric contractions at 50 and 75% of perceived maximal effort. Subjects then performed 3-4 s MVICs separated by 2 min of rest. Subsequently, maximal isokinetic testing at $60°\cdot s^{-1}$ and $180°\cdot s^{-1}$, separated by 1–2 min of rest, was performed in a randomized order. Subjects were instructed to "kick out as *hard and fast* as possible" prior to each trial. Subjects were instructed to avoid pretension or a countermovement prior to each trial. Further, the baseline signals were visually examined after each trial to ensure adherence to instructions, and additional trials were performed as needed. Strong verbal encouragement and visual biofeedback was provided during testing.

The scaled, gravity corrected torque and velocity signals were digitally filtered with a zero lag, low-pass (40 Hz) Butterworth filter using custom written software (LabVIEW, National Instruments, Austin, TX, United States). EMG signals were processed using a 4th order Butterworth filter with a low- and high-frequency cutoff of 10 and 500 Hz, respectively, which was applied to the scaled zero means EMG signal. Peak torque (PT) was considered the highest 500 ms during MVICs, whereas it was defined as the highest 25 ms during isokinetic contractions. Specific PT was calculated via dividing the MVIC, $60°\cdot s^{-1}$, and $180°\cdot s^{-1}$ PT by whole-muscle CSA. EMG amplitude (RMS) for the VL and RF was obtained during the corresponding 500 ms epoch as isometric peak torque during MVICs, and throughout the entire load range for isokinetic trials at $60°\cdot s^{-1}$ and $180°\cdot s^{-1}$. RMS from isokinetic trials was normalized to EMG amplitude from the MVIC to serve as an indicator of muscle activation (Jenkins et al., 2015). The trial with the highest PT for all contraction types was used for subsequent analysis.

Skeletal Muscle Microbiopsy

Microbiopsy samples were obtained from 13 YM and 11 OM. No systematic process was used for choosing the subsets that underwent a microbiopsy. Skeletal muscle samples were obtained from the lateral aspect of the VL at 50% the distance from the greater trochanter to the lateral femoral epicondyle (Hughes et al., 2015; Townsend et al., 2016). The area over the predetermined site was cleaned and disinfected with a topical antiseptic (Betadine, Stamford, CT, United States). Approximately, 2–3 ml of lidocaine (2%, without epinephrine) was injected around the area. After the area was numb, an initial incision was made to a depth of ∼2 cm via a 14-gauge pilot needle and subsequently a muscle sample was collected at a depth of ∼3 cm with a 14-gauge biopsy needle (Argon Medical, Athens, TX, United States) using an automatic biopsy instrument (Pro-Mag^{TM} Ultra, Argon Medical, Athens, TX, United States). The biopsy needle was inserted at a 90° angle (perpendicular to the longitudinal axis of the VL) and length markers present on the needle were used to improve consistency of sampling depth. Muscle samples were obtained by the activation of a trigger button on the biopsy instrument, which unloaded the spring and engaged the needle to collect a tissue sample. Up to 4 samples (punches) were collected from the same location and stored on ice for ∼30 min. After weighing, the samples were rinsed with phosphate buffer saline (PBS) and cleaned of skin and fat tissue under a dissecting microscope, embedded in Tissue-Tek OCT compound (Sakura Finetek), flash-frozen in liquid nitrogen, and stored at –80°C. There were no complications associated with the microbiopsy for YM or OM.

Immunofluorescence Staining

Serial 10-um transverse sections were produced with a cryostat (CryoStar NX50, Thermo Fisher Scientific) and then attached to a microscope slide (SuperFrost^{TM} Plus, Fisher). For some subjects, 2–3 punches (separate clumps of muscle tissue) needed to be sectioned and stained to optimize fiber yield. Sections were air-dried, fixed with 3.7% formaldehyde for 10 min at room temperature (RT), permeabilized for 30 min in phosphate-buffered saline (PBS) containing 1% Triton X-100, blocked with 1% bovine serum albumin (BSA), and stained according to the multiplex staining scheme in **Table 2**. We used a mixture of two antibodies to invariably detect all subtypes of type II fibers, including hybrids. Fab immunoglobulin fragments were used as secondary antibodies to eliminate any possibility of non-specific cross-reactivity. Separate staining trials with each primary antibody alone were performed to confirm the specificity of the multiplex staining. All incubations were done at RT in a humidified chamber with a coverslip placed on top of staining solutions; a brief rinse in PBTx (PBS, 0.1% Triton X-100) was used between incubations. Stained slides were permanently mounted with Mowiol medium, according to previously published procedures (i.e., Rodig, 2019) and stored at 4°C.

Laser Confocal Microscopy

Stained tissue sections were imaged using Zeiss LSM 900 system (Carl Zeiss Microscopy, LLC, White Plains, NY, United States), equipped with a 10X Plan-Neofluar objective and Zen Black software. Tiling with digital stitching was enabled to seamlessly image the entire area of each section. Stacks of optical

---

[1] https://imagej.nih.gov

TABLE 2 | Immunofluorescence staining protocol.

Staining stages (incubation parameters)	Staining mix, (source), [titer]
Step 1 (overnight at RT)	Mouse anti-slow myosin type I IgG [clone BA-F8, Developmental Studies Hybridoma Bank (DSHB), University of Iowa, IA 52242], [1:100]
Step 2 (1 h at RT)	Goat anti-mouse IgG, Fab fragments, Alexa 488-labeled (115-547-003, Jackson ImmunoResearch), [1:400]
Step 3 (overnight at RT)	Mouse anti-fast myosin type IIA IgG (clone SC-71, DSHB) [1:100] Rabbit anti-fast myosin type II (ab91506, Abcam), [1:200]
Step 4 (1 h at RT)	Goat anti-Mouse, Cy3-labeled (115-167-003, Jackson ImmunoResearch) [1:400] Goat anti-Rabbit, Fab fragments, Alexa 647-labeled (111-607-003, Jackson ImmunoResearch) [1:400] DAPI, (D9542, Sigma) [1 ug/ml]

RT, room temperature.

sections spanning the entire depth of the section were flattened with the maximum intensity projections algorithm to produce the final image.

Fiber Composition and Morphology Analysis

Boundaries of individual fibers from confocal images were manually traced using Zen software using the spline contour tool. Further analysis was conducted using ImageJ software[1]. Data for each muscle fiber was catalogued in a spreadsheet file with identification number, CSA, and the assigned fiber type. Fiber typing was conducted by a team of 3–5 operators not aware of the subject's age and only considering the intensity of each fiber for fiber-specific myosin. Fiber type composition was calculated as the ratio of counts obtained for each fiber type to the total number of analyzed fibers from each subject. Mean CSA and CSA heterogeneity (coefficient of variation, CV) was calculated for each fiber type. Finally, as an indicator of aging-related muscle fiber remodeling (Sonjak et al., 2019), the ratio between type II and type I muscle fiber CSA for each subject was determined.

Statistical Analyses

Normality of data was assessed via the Kolmogorov-Smirnov test. Independent samples *t*-tests were used for age-related comparisons of normally distributed variables, whereas Mann-Whitney tests were conducted for non-normally distributed variables. Levene's test was used to test equality of variance. Associations between CAF levels, specific strength, whole-muscle CSA, and ALM were examined using Pearson product-moment correlation coefficients. Associations were only assessed in the OM group since CAF is suggested to be a biomarker of muscle health in this population. Relationships were categorized as weak, moderate, or strong relationships for correlation coefficient values of 0.35 or less, 0.36 to 0.67, and 0.68 or more (Taylor, 1990). Statistical analyses were performed using PASW software version 27.0 (SPSS Inc, Chicago, IL, United States) and an alpha level of $p \leq 0.05$ was used to determine statistical significance. Effect size was reported using Cohen's d and 0.30, 0.50, and 0.80 were used to indicate small, medium, and large effects (Cohen, 1988). All data in text and table are reported as mean ± SD, and as described below for box plots. Box plots were generated with an online resource at http://shiny.chemgrid.org/boxplotr (Spitzer et al., 2014).

RESULTS

Group Characteristics and C-Terminal Agrin Fragment Levels

Characteristics and CAF levels for both groups are displayed in **Table 1**. OM were heavier ($p = 0.004$) and had a higher body mass index (BMI) ($p < 0.001$) as well as body fat % ($p = 0.001$). ALM ($p < 0.001$) and whole-muscle CSA ($p = 0.001$) were lower in OM, whereas CAF levels ($p = 0.159$) and handgrip strength ($p = 0.253$) were similar between groups. When VL and RF CSA were analyzed separately, VL (YM: 24.09 ± 3.52 cm^2, OM: 18.40 ± 3.68 cm^2; $p < 0.001$; $d = 1.57$) but not RF (YM: 12.11 ± 2.68 cm^2, OM: 10.67 ± 2.23 cm^2; $p = 0.121$; $d = 0.58$) CSA was lower in OM.

Absolute and Specific Peak Torque

Absolute and specific PT data is displayed in **Figure 1**. Absolute PT (**Figure 1A**) was lower for $0°{\cdot}\text{s}^{-1}$ (isometric) ($p < 0.001$; $d = 1.68$), $60°{\cdot}\text{s}^{-1}$ ($p = 0.001$; $d = 1.39$) and $180°{\cdot}\text{s}^{-1}$ ($p < 0.001$; $d = 1.86$) in OM, whereas specific PT (**Figure 1B**) was lower at $180°{\cdot}\text{s}^{-1}$ ($p = 0.003$; $d = 1.23$) but not $0°{\cdot}\text{s}^{-1}$ ($p = 0.066$; $d = 0.69$) or $60°{\cdot}\text{s}^{-1}$ ($p = 0.170$; $d = 0.51$). Findings were similar when specific PT was calculated using only VL CSA. VL activation was similar between groups at $60°{\cdot}\text{s}^{-1}$ (YM: 0.82 ± 0.20 % MVIC, OM: 0.95 ± 0.10 % MVIC; $p = 0.060$; $d = 0.79$) and $180°{\cdot}\text{s}^{-1}$ (YM: 0.91 ± 0.23 % MVIC, OM: 0.99 ± 0.26 % MVIC; $p = 0.400$; $d = 0.32$) and the same was found for RF activation at $60°{\cdot}\text{s}^{-1}$ (YM: 0.98 ± 0.16 % MVIC, OM: 0.90 ± 0.11 % MVIC; $p = 0.130$; $d = 0.59$) and $180°{\cdot}\text{s}^{-1}$ (YM: 0.93 ± 0.15 % MVIC, OM: 0.90 ± 0.22 % MVIC; $p = 0.670$; $d = 0.16$).

Composition and Morphology of Muscle Fibers

Average wet weight per microbiopsy punch was 14.39 ± 3.84 mg and 15.84 ± 4.12 mg for YM and OM ($p > 0.05$), respectively (**Figure 2A**). The number of fibers per cross-section was similar between YM (587.75 ± 216.58 fibers) and OM (543.27 ± 273.47 fibers) and overall, utilizing a quarter to half of the biopsied tissue, we analyzed 904.23 ± 436.31 fibers per sample and 889.15 ± 319.91 fibers per sample for YM and OM, respectively (**Figure 2B**). More detailed analysis of fiber type composition was performed via immunofluorescence (**Figure 3A**). Composition was similar for type I ($p = 0.331$; $d = 0.39$) and type II ($p = 0.332$; $d = 0.39$) fibers between YM and OM (**Figure 3B**). Hybrids between type I and type

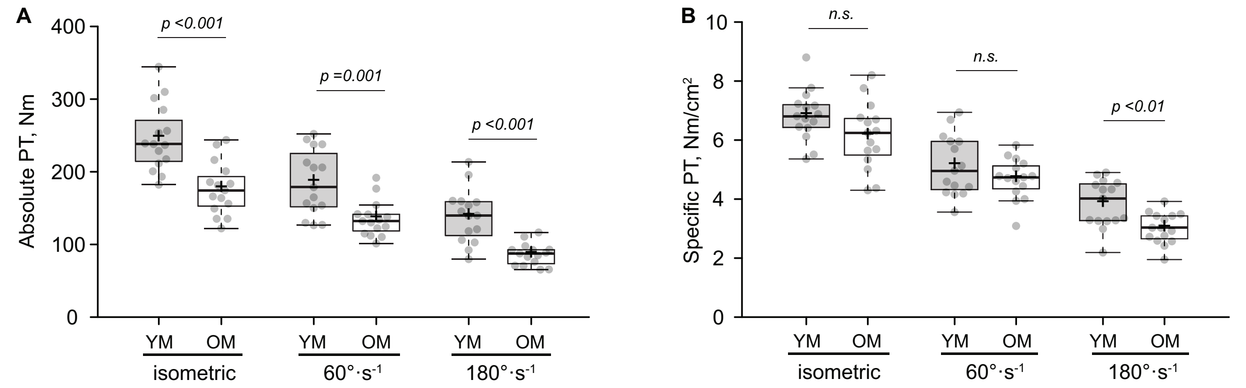

FIGURE 1 | Isometric and isokinetic muscle function of the knee extensors. Absolute **(A)** and specific **(B)** peak torque (PT) in young (YM) and older (OM) males. Means and medians are represented by "+" and midlines in boxes, respectively; whiskers calculated by Tukey test. n.s., non-significant.

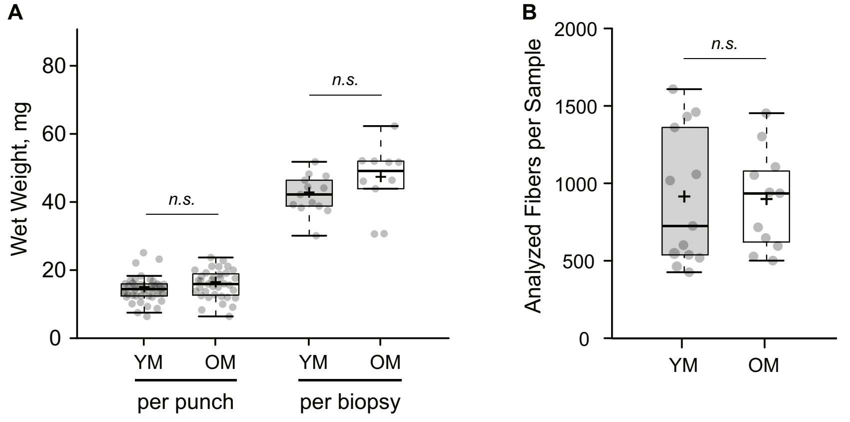

FIGURE 2 | Gross parameters of muscle tissue obtained with the microbiopsy technique. **(A)** Total wet weight of tissue obtained with each individual microbiopsy sample (punch) and total per biopsy protocol (sum of punches). **(B)** Numbers of accessible muscle fibers analyzed per subject on cross sections. YM, young males; OM, older males; Means and medians are represented by "+" and midlines in boxes, respectively; whiskers calculated by Tukey test. n.s., non-significant.

II fibers were extremely rare and could not be analyzed statistically. CSA was similar for type II fibers ($p = 0.467$; $d = 0.18$) between groups, however, type I fibers were larger in OM ($p = 0.05$; $d = 0.094$) (**Figure 3C**). OM demonstrated a smaller type II to I fiber CSA ratio (YM: 1.22 ± 0.21, OM: 0.97 ± 0.31; $p = 0.015$; $d = 0.95$). Finally, CSA was more heterogenous in OM for type II fibers ($p < 0.001$; $d = 1.84$) fibers, but not type I fibers ($p = 0.343$; $d = 0.38$) (**Figure 3D**).

Associations

C-terminal agrin fragment levels were not correlated with ALM (**Figure 4A**), whole-muscle CSA (**Figure 4B**), isometric specific PT (**Figure 4C**), specific PT at $180°\cdot s^{-1}$ (**Figure 4D**), or specific PT at $60°\cdot s^{-1}$ in OM. These findings remained the same when specific PT was calculated using only VL CSA. Similarly, CAF levels were not associated with absolute PT at any testing velocity ($r = 0.213$–0.379; $p = 0.163$–0.446), nor any single fiber variables ($p > 0.05$).

DISCUSSION

The purpose of this study was to examine muscle fiber morphology and composition in young and older males using the microbiopsy sampling technique, and a secondary aim was to determine if specific strength is associated with serum CAF levels in older males. To the best of our knowledge, this is the first study to (1) investigate the effect of age on muscle fiber properties using the microbiopsy technique and (2) assess associations between muscle quality (i.e., specific strength) and CAF levels. We demonstrated the ability to analyze hundreds of muscle fibers per subject, on par with the gold standard Bergström technique, with a relatively high proportion of type II fibers compared to previous reports using the Bergström. Our findings indicated whole-muscle atrophy in older males, but no decrements at the single fiber level. Rather, evidence of age-related remodeling was found via enlarged type I fibers and a decreased type II to I muscle fiber CSA ratio in older males. Finally, correlational evidence indicated no association between NMJ deterioration and specific strength, which was at least partially due to there being no

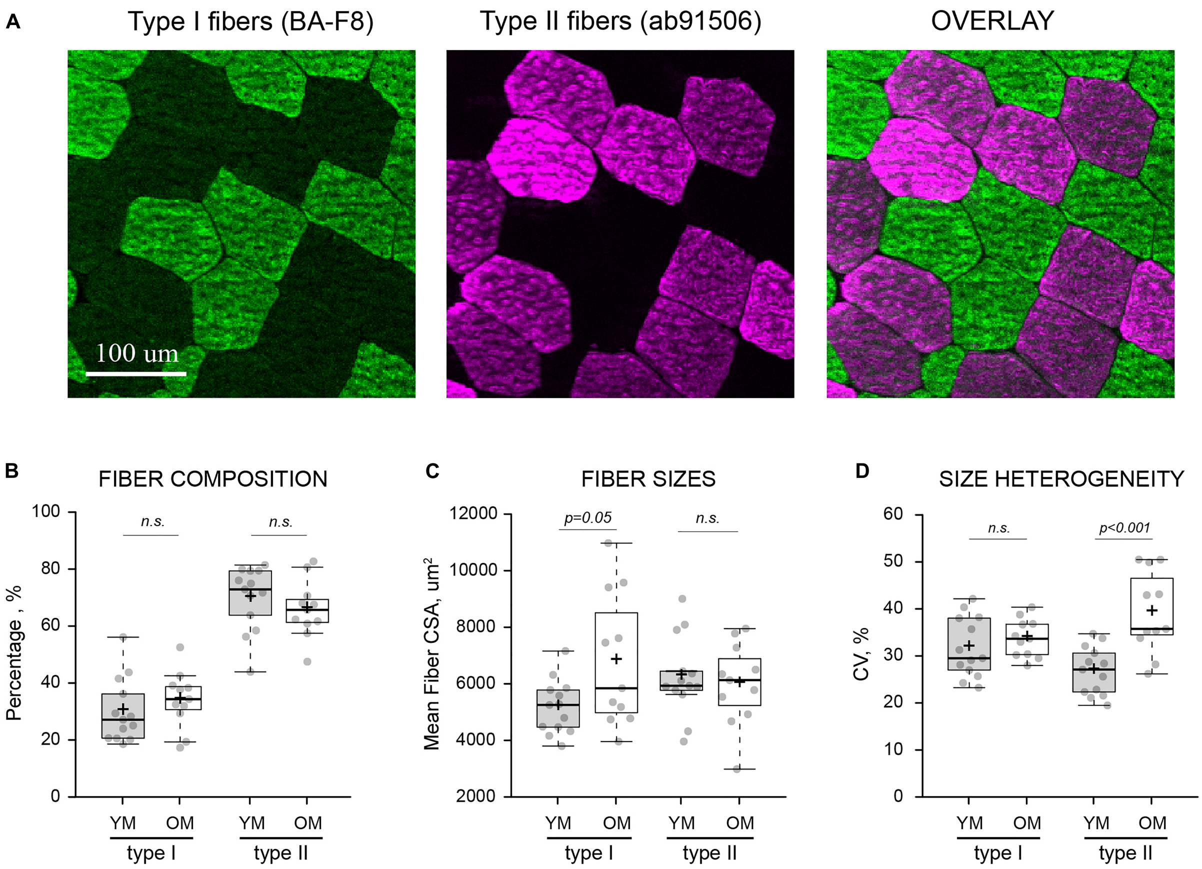

FIGURE 3 | Fiber type-specific composition and morphology. **(A)** Visualization of type I and type II muscle fibers from the same area of a transversely sectioned biopsied material via multi-colored immunofluorescence and type-specific antibodies (indicated in parentheses). **(B)** Fiber type composition, expressed as the percentage of each fiber type relative to the total number of analyzed fibers. **(C)** Average cross-sectional area (CSA) of individual muscle fibers in each sample. **(D)** Heterogeneity of fiber sizes expressed as coefficient of variance (CV) for all fibers of the same type measured within each sample. YM, young males; OM, old males; Means and medians are represented by "+" and midlines in boxes, respectively; whiskers calculated by Tukey test. n.s., non-significant.

age-related difference in CAF levels suggesting maintenance of neuromuscular integrity in our older cohort.

The capability of the microbiopsy to yield a high number of fibers, comparable to the Bergström biopsy, for histological analyses is significant. The average number of fibers analyzed across studies varies widely from 10 to 20 (Tesch et al., 1984) to a thousand (Roberts et al., 2018) per sample using the Bergström biopsy. It has been suggested that as few as 50 fibers (McCall et al., 1998) is necessary to accurately characterize the sample collected, but depending on the specific fiber type, the need to harvest up to 200 fibers has been reported (McGuigan et al., 2002). Townsend et al. (2016) analyzed ~150 fibers on average in young males using the microbiopsy in a pilot study, but fiber yield is unclear for other studies using this technique (Hughes et al., 2015; Bonafiglia et al., 2020). We were able to analyze a few hundred fibers (>500) per microbiopsy sample in a young and older cohort, and a yield of several hundred fibers was possible by combining data from multiple cross-sections of tissue. Though combining multiple-cross sections of tissue was useful for optimizing the number of analyzed fibers, it is worth noting that a single cross-section afforded a high number of fibers (range: 188–1,059 fibers). This was despite the relatively small tissue yield compared to the Bergström, which has been the primary reason for hesitation toward microbiopsy technique. The finding that a sufficient number of fibers can be harvested for myosin heavy chain composition and histological analysis via microbiopsy presents a unique opportunity for skeletal muscle researchers. The microbiopsy has the potential to advance the study of skeletal muscle, particularly in older or fragile (e.g., sarcopenic and diseased) populations in which the increased discomfort and tissue sample size (Hughes et al., 2015; Bonafiglia et al., 2020) associated with the Bergström biopsy are a limiting factor. Future work that examines the validity of the microbiopsy technique in these population is a worthwhile endeavor. Tissue yield may even be sufficient via microbiopsy for researchers conducting multiple cellular and molecular analyses, but this is dependent on the analyses of interest and microbiopsy procedures. For example, we extracted ~45 mg of tissue from three microbiopsy punches, whereas Hughes et al. (2015) retrieved ~80 mg (and up to 120 mg) after 5 punches. Further, due to the well documented heterogeneity of muscle fiber types (Lexell and Taylor, 1989a,b; Horwath et al., 2021), it is recommended that more than one

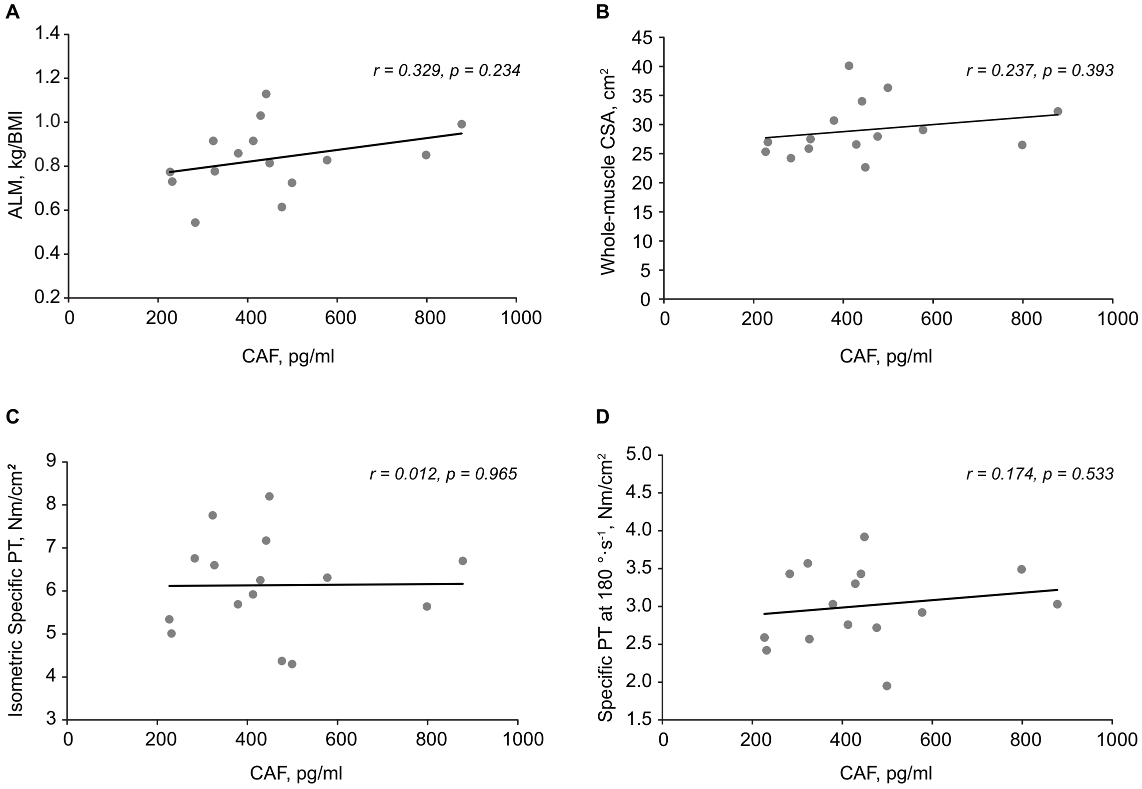

FIGURE 4 | Associations between C-terminal agrin fragment (CAF) levels, body composition, and muscle function. Scatterplots demonstrating no relationship between CAF levels and appendicular lean mass (ALM) **(A)**, whole-muscle cross-sectional area (CSA) **(B)**, isometric specific peak torque (PT) **(C)**, and Specific PT at 180°·s^{-1} **(D).**

biopsy be conducted per visit (Lexell and Taylor, 1989b; Horwath et al., 2021) which is more feasible with the microbiopsy given it is minimally invasive.

Muscle fiber CSA values were similar to several Bergström studies (Verdijk et al., 2007; Nilwik et al., 2013; Horwath et al., 2021). The present study found no evidence of age-related muscle fiber atrophy, and while similar findings have been reported for type II muscle fibers in males (Trappe et al., 2003; Roberts et al., 2018), this is in disagreement with consistent reports of preferential type II muscle fiber atrophy (Lexell et al., 1988; Walker et al., 2012; Nilwik et al., 2013). This finding is at least partially due to our older sample being healthy and non-sarcopenic as indicated by ALM (kg/m^2) and handgrip strength values (Cruz-Jentoft et al., 2019). More specifically, only two older males had an ALM less than 7.0 kg/m^2 while none were below the threshold for handgrip strength (27 kg), thus sarcopenia was not present in our older sample. The increased type II to I muscle fiber CSA ratio was driven by enlarged type I muscle fibers, and not atrophied type II fibers, in older males. These findings likely characterize compensatory changes at the cellular level (Aniansson et al., 1992; Frontera et al., 2008) that contribute to the healthy, non-sarcopenic status of the older males. As suggested by Roberts et al. (2018), the greater heterogeneity in CSA for type II fibers may indicate both, hypertrophic and atrophic responses in individuals from the older male group. Whole-muscle atrophy, of the VL in particular, was present in older males, which given the lack of muscle fiber atrophy, suggests that the loss of muscle fibers was influential for this finding (Lexell et al., 1988; Frontera et al., 2000). Composition of muscle fiber type was similar between age groups, which is in line with previous studies (Lexell et al., 1988; Snijders et al., 2014; Sonjak et al., 2019). Generally, most studies using the Bergström biopsy report proportions of 40–50% for type I and type II fibers, but we found type II fiber composition to be 69% and 65% in young and older males, respectively. Our type II fiber composition data is similar to two other studies using the microbiopsy (Hayot et al., 2005; Hughes et al., 2015). Hughes et al. (2015) directly compared the microbiopsy and Bergström technique and found a higher proportion of type IIx fibers with the microbiopsy. The relatively large proportion of type II fibers is noteworthy and may be attributed to more superficial sampling using the microbiopsy (Lexell et al., 1983). Indeed, in consideration of the smaller tissue sample yield from the microbiopsy, the use of ultrasonography for needle guidance (Jandova et al., 2020) should be considered for future work to ensure consistent depth of muscle sampling in young and older subjects as age-related changes in subcutaneous fat are expected. Importantly, the novel data in the present work provides a descriptive age-related comparison using the microbiopsy, but more work is needed to further elucidate if age-related differences in fiber type composition and histology are dependent up sampling technique. Follow-up work directly comparing muscle fiber properties using the Bergström and microbiopsy (with special attention to sampling depth) in young and older adults is required to verify the level of agreement between the techniques.

Similar to previous research, we showed that specific strength was only decreased at a higher contraction velocity (180° s^{-1}) (Frontera et al., 1991; Overend et al., 1992; Jubrias et al., 1997) in older males. This suggest that qualitative factors are influential for the age-related loss of strength, particularly during a higher contraction velocity. Atrophy or preferential loss of type II fibers were not responsible as neither were present in our older sample. Decreased tendon stiffness in older males (Quinlan et al., 2017) cannot be ruled out and could be expected to diminish force transmission at higher contraction velocities (Hauraix et al., 2013). We conducted an inquiry on the association between NMJ degradation (as indicated by CAF levels) and specific strength. CAF levels were not associated with specific strength at any velocity, nor whole-muscle CSA or ALM in older males. It is unclear what contributed to the age-related decrease in specific strength at 180° s^{-1} but changes at the molecular level such as slowed cross-bridge kinetics could be responsible (Höök et al., 2001; Miller et al., 2013). These findings are in contrast with recent studies demonstrating a negative relationship between CAF levels and lean mass (Drey et al., 2013; Pratt et al., 2021). The size and composition of our sample were likely influential for these findings as previous studies were conducted in larger, more heterogenous populations (e.g., greater age range). Indeed, given the non-sarcopenic phenotype of our older sample, the moderate effect size though non-significant result for CAF levels between age groups is not overly surprising. This is because CAF levels appear to be influenced by sarcopenia status and not aging *per se* (Hettwer et al., 2013; Olmos et al., 2019). Accordingly, the finding that CAF levels were not associated with specific strength supports the concept that this biomarker is particularly sensitive to muscle wasting (Pratt et al., 2021) and less so to other physiological factors influencing strength. Nevertheless, evidence on CAF levels as an indicator of NMJ degradation and the role this plays in distinguishing sarcopenia severity is still in its infancy, thus these findings contribute to the understanding of this biomarker as an emerging biomarker for sarcopenia.

There were a few limitations associated with the current study. Our findings only characterize males, which is an important consideration since there are sex differences associated with aging-related changes in whole-muscle and single fiber size (Reid et al., 2014; Roberts et al., 2018). Particularly for findings derived from the microbiopsy, our sample size was limited and may not have possessed the necessary statistical power for between groups analyses. Despite our muscle fiber CSA values being similar to previous data obtained from the Bergström biopsy (Verdijk et al., 2007; Nilwik et al., 2013; Horwath et al., 2021), it is possible the 30-min delay in freezing samples affected muscle fiber size. Given the post-biopsy procedures were identical for all subjects and sample wet weight was similar between young and older males, it is unlikely any influence of the 30-min delay was age dependent. While isopentane is often used as an intermediate coolant, a potential advantage of the microbiopsy method is its compatibility with a simple flash-freezing technique. Upon analyzing hundreds of cryosections, we did not detect systemic presence of freezing artifacts, which suggests that smaller-than-typical muscle tissue volume receives adequate cooling rates when plunged directly into liquid nitrogen (Lee et al., 2020). Finally, while it was not the purpose of this study to directly compare the microbiopsy and Bergström techniques, the lack of a comparison could be considered a limitation. Indirect comparisons based on previous studies using the Bergström technique were emphasized with the intention to provide a preliminary perspective and bring attention to the need for comparing the techniques for examining aging-related changes in muscle fiber properties.

The present study demonstrated, for the first time, the efficacy of the microbiopsy sampling technique to be used for analysis of muscle fiber morphology and composition in older adults. We showed that the microbiopsy can yield more than a sufficient number of fibers for histological analyses, which suggest the microbiopsy is a viable muscle sampling alternative to the Bergström for researchers wanting to minimize the challenges associated with the more invasive Bergström technique. Further, as human lifespan continues to increase and the study of skeletal muscle health in advanced age (i.e., ≥ 8th decade) becomes increasingly relevant, we posit that the microbiopsy technique will be critical in the advancement of therapies for improving quality of life. With regard to our age-related findings, no muscle fiber atrophy or changes in composition were found but enlarged type I fibers were present in older males. These findings were at least partially due to our high-functioning older sample and indicate healthy aging. No association was found between a relatively new biomarker of neuromuscular junction degradation (circulating C-terminal agrin fragment levels) and whole-muscle CSA, appendicular lean mass, or specific strength. These findings in conjunction with those from others suggest that aging-related deterioration of the neuromuscular junction may primarily contribute to muscle wasting and not necessarily muscle function.

DATA AVAILABILITY STATEMENT

The raw data supporting the conclusions of this article will be made available by the authors, without undue reservation.

ETHICS STATEMENT

The studies involving human participants were reviewed and approved by Kennesaw State University Institutional Review Board. The patients/participants provided their written informed consent to participate in this study.

AUTHOR CONTRIBUTIONS

GH and ALB contributed to study conceptualization and design, supervision, data processing, statistical analysis, data interpretation, and writing of the manuscript. TV contributed to the study conceptualization and design, supervision, data processing, and editing of the manuscript. PH, AO, BD, ARB, KK, MJ, SK, and SA contributed to data collection, data processing, and editing of the manuscript. All authors contributed to the article and approved the submitted version.

FUNDING

This work was supported by the Office for the Vice President of Research, Kennesaw State University. The microscope equipment used in this study was funded by NSF Major Research Instrument grant DBI-1229237.

ACKNOWLEDGMENTS

The authors would like to thank Jeremy Townsend for his technical assistance with the microbiopsy technique and Christina Talley for her assistance with image analysis. Microscopy and Histology core facilities, that were instrumental in this study, are maintained by the College of Science and Mathematics, KSU.

REFERENCES

Aniansson, A., Grimby, G., and Hedberg, M. (1992). Compensatory muscle fiber hypertrophy in elderly men. *J. Appl. Physiol (1985)* 73, 812–816. doi: 10.1152/jappl.1992.73.3.812

Bergstrom, J. (1962). Muscle electrolytes in man. *Scand. J. Clin. Lab. Invest.* 14, 511–513.

Bergstrom, J. (1975). Percutaneous needle biopsy of skeletal muscle in physiological and clinical research. *Scand. J. Clin. Lab. Invest.* 35, 609–616. doi: 10.3109/00365517509095787

Bolliger, M. F., Zurlinden, A., Luscher, D., Butikofer, L., Shakhova, O., Francolini, M., et al. (2010). Specific proteolytic cleavage of agrin regulates maturation of the neuromuscular junction. *J. Cell Sci.* 123(Pt 22), 3944–3955. doi: 10.1242/jcs.072090

Bonafiglia, J. T., Islam, H., Preobrazenski, N., Drouin, P., Ma, A., Gerhart, A., et al. (2020). A comparison of pain responses, hemodynamic reactivity and fibre type composition between Bergström and microbiopsy skeletal muscle biopsies. *Curr. Res. Physiol.* 3, 1–10. doi: 10.1016/j.crphys.2020.05.001

Clark, B. C., and Manini, T. M. (2010). Functional consequences of sarcopenia and dynapenia in the elderly. *Curr. Opin. Clin. Nutr. Metab. Care* 13:271. doi: 10.1097/MCO.0b013e328337819e

Cohen, J. (1988). *Statistical Power Analysis For The Social Sciences*. Hillsdale, NJ: L. Erlbaum Associates.

Cruz-Jentoft, A. J., Bahat, G., Bauer, J., Boirie, Y., Bruyere, O., Cederholm, T., et al. (2019). Sarcopenia: revised European consensus on definition and diagnosis. *Age Ageing* 48:601. doi: 10.1093/ageing/afz046

Delmonico, M. J., Harris, T. B., Visser, M., Park, S. W., Conroy, M. B., Velasquez-Mieyer, P., et al. (2009). Longitudinal study of muscle strength, quality, and adipose tissue infiltration. *Am. J. Clin. Nutr.* 90, 1579–1585. doi: 10.3945/ajcn.2009.28047

Deschenes, M. R., Roby, M. A., Eason, M. K., and Harris, M. B. (2010). Remodeling of the neuromuscular junction precedes sarcopenia related alterations in myofibers. *Exp .Gerontol.* 45, 389–393. doi: 10.1016/j.exger.2010.03.007

Drey, M., Sieber, C., Bauer, J., Uter, W., Dahinden, P., Fariello, R., et al. (2013). C-terminal agrin fragment as a potential marker for sarcopenia caused by degeneration of the neuromuscular junction. *Exp. Gerontol.* 48, 76–80. doi: 10.1016/j.exger.2012.05.021

Folstein, M. F., Folstein, S. E., and McHugh, P. R. (1975). "Mini-mental state". A practical method for grading the cognitive state of patients for the clinician. *J. Psychiatr. Res.* 12, 189–198. doi: 10.1016/0022-3956(75)90026-6

Frontera, W. R., Hughes, V. A., Fielding, R. A., Fiatarone, M. A., Evans, W. J., and Roubenoff, R. (2000). Aging of skeletal muscle: a 12-yr longitudinal study. *J. Appl. Physiol. (1985)* 88, 1321–1326. doi: 10.1152/jappl.2000.88.4.1321

Frontera, W. R., Hughes, V. A., Lutz, K. J., and Evans, W. J. (1991). A cross-sectional study of muscle strength and mass in 45- to 78-yr-old men and women. *J. Appl. Physiol. (1985)* 71, 644–650. doi: 10.1152/jappl.1991.71.2.644

Frontera, W. R., Reid, K. F., Phillips, E. M., Krivickas, L. S., Hughes, V. A., Roubenoff, R., et al. (2008). Muscle fiber size and function in elderly humans: a longitudinal study. *J. Appl. Physiol. (1985)* 105, 637–642. doi: 10.1152/japplphysiol.90332.2008

Goodpaster, B. H., Park, S. W., Harris, T. B., Kritchevsky, S. B., Nevitt, M., Schwartz, A. V., et al. (2006). The loss of skeletal muscle strength, mass, and quality in older adults: the health, aging and body composition study. *J. Gerontol. Ser. A* 61, 1059–1064. doi: 10.1093/gerona/61.10.1059

Hauraix, H., Nordez, A., and Dorel, S. (2013). Shortening behavior of the different components of muscle-tendon unit during isokinetic plantar flexions. *J. Appl. Physiol.* 115, 1015–1024. doi: 10.1152/japplphysiol.00247.2013

Hayot, M., Michaud, A., Koechlin, C., Caron, M. A., Leblanc, P., Prefaut, C., et al. (2005). Skeletal muscle microbiopsy: a validation study of a minimally invasive technique. *Eur. Respir. J.* 25, 431–440. doi: 10.1183/09031936.05.00053404

Hermens, H. J., Freriks, B., Merletti, R., Stegeman, D., Blok, J., Rau, G., et al. (1999). *European Recommendations For Surface Electromyography ISBN 90-75452-15-2*. Enschede, NL: Roessingh Research and Devlopment.

Hettwer, S., Dahinden, P., Kucsera, S., Farina, C., Ahmed, S., Fariello, R., et al. (2013). Elevated levels of a C-terminal agrin fragment identifies a new subset of sarcopenia patients. *Exp. Gerontol.* 48, 69–75. doi: 10.1016/j.exger.2012.03.002

Heymsfield, S. B., Smith, R., Aulet, M., Bensen, B., Lichtman, S., Wang, J., et al. (1990). Appendicular skeletal muscle mass: measurement by dual-photon absorptiometry. *Am. J. Clin. Nutr.* 52, 214–218. doi: 10.1093/ajcn/52.2.214

Höök, P., Sriramoju, V., and Larsson, L. (2001). Effects of aging on actin sliding speed on myosin from single skeletal muscle cells of mice, rats, and humans. *Am. J. Physiol. Cell Physiol.* 280, C782–C788. doi: 10.1152/ajpcell.2001.280.4.C782

Horwath, O., Envall, H., Roja, J., Emanuelsson, E. B., Sanz, G., Ekblom, B., et al. (2021). Variability in vastus lateralis fiber type distribution, fiber size, and myonuclear content along and between the legs. *J. Appl. Physiol. (1985)* 131, 158–173. doi: 10.1152/japplphysiol.00053.2021

Hughes, M. C., Ramos, S. V., Turnbull, P. C., Nejatbakhsh, A., Baechler, B. L., Tahmasebi, H., et al. (2015). Mitochondrial bioenergetics and fiber type assessments in microbiopsy vs. bergstrom percutaneous sampling of human skeletal muscle. *Front. Physiol.* 6:360. doi: 10.3389/fphys.2015.00360

Jandova, T., Bondi, D., Verratti, V., Narici, M., Steffl, M., and Pietrangelo, T. (2020). The importance of sonographic evaluation of muscle depth and thickness prior to the 'tiny percutaneous needle biopsy'. *Eur. J. Transl. Myol.* 30:8851. doi: 10.4081/ejtm.2019.8851

Jenkins, N. D., Housh, T. J., Palmer, T. B., Cochrane, K. C., Bergstrom, H. C., Johnson, G. O., et al. (2015). Relative differences in strength and power from slow to fast isokinetic velocities may reflect dynapenia. *Muscle Nerve* 52, 120–130. doi: 10.1002/mus.24505

Jubrias, S. A., Odderson, I. R., Esselman, P. C., and Conley, K. E. (1997). Decline in isokinetic force with age: muscle cross-sectional area and specific force. *Pflugers Arch.* 434, 246–253. doi: 10.1007/s004240050392

Lee, C. C., Hoang, A., Segovia, D., Herbst, A., Barthelemy, F., Gibbs, E., et al. (2020). Enhanced methods for needle biopsy and cryopreservation of skeletal muscle in older adults. *J. Cytol. Histol.* 11:7. doi: 10.37421/jch.2020.11.553

Lexell, J., and Taylor, C. C. (1989a). Variability in muscle fibre areas in whole human quadriceps muscle. How much and why? *Acta Physiol. Scand.* 136, 561–568. doi: 10.1111/j.1748-1716.1989.tb08702.x

Lexell, J., and Taylor, C. C. (1989b). Variability in muscle fibre areas in whole human quadriceps muscle: how to reduce sampling errors in biopsy techniques. *Clin. Physiol.* 9, 333–343. doi: 10.1111/j.1475-097x.1989.tb00987.x

Lexell, J., Henriksson-Larsen, K., Winblad, B., and Sjostrom, M. (1983). Distribution of different fiber types in human skeletal muscles: effects of aging studied in whole muscle cross sections. *Muscle Nerve* 6, 588–595. doi: 10.1002/mus.880060809

Lexell, J., Taylor, C. C., and Sjostrom, M. (1988). What is the cause of the ageing atrophy? Total number, size and proportion of different fiber types studied in whole vastus lateralis muscle from 15- to 83-year-old men. *J. Neurol. Sci.* 84, 275–294. doi: 10.1016/0022-510x(88)90132-3

Mayhew, A. J., Amog, K., Phillips, S., Parise, G., McNicholas, P. D., de Souza, R. J., et al. (2019). The prevalence of sarcopenia in community-dwelling older adults, an exploration of differences between studies and within definitions: a systematic review and meta-analyses. *Age Ageing* 48, 48–56. doi: 10.1093/ageing/afy106

McCall, G. E., Byrnes, W. C., Dickinson, A. L., and Fleck, S. J. (1998). Sample size required for the accurate determination of fiber area and capillarity of human skeletal muscle. *Can. J. Appl. Physiol.* 23, 594–599. doi: 10.1139/h98-034

McGuigan, M. R., Kraemer, W. J., Deschenes, M. R., Gordon, S. E., Kitaura, T., Scheett, T. P., et al. (2002). Statistical analysis of fiber area in human skeletal muscle. *Can. J. Appl. Physiol.* 27, 415–422. doi: 10.1139/h02-022

Miller, M. S., Bedrin, N. G., Callahan, D. M., Previs, M. J., Jennings, M. E., Ades, P. A., et al. (2013). Age-related slowing of myosin actin cross-bridge kinetics is sex specific and predicts decrements in whole skeletal muscle performance in humans. *J. Appl. Physiol.* 115, 1004–1014. doi: 10.1152/japplphysiol.00563.2013

Nilwik, R., Snijders, T., Leenders, M., Groen, B. B., van Kranenburg, J., Verdijk, L. B., et al. (2013). The decline in skeletal muscle mass with aging is mainly attributed to a reduction in type II muscle fiber size. *Exp. Gerontol.* 48, 492–498. doi: 10.1016/j.exger.2013.02.012

Olmos, A. A., Stratton, M. T., Ha, P. L., VanDusseldorp, T. A., Bailly, A. R., Feito, Y., et al. (2019). Neuromuscular function of the plantar flexors and predictors of peak power in middle-aged and older males. *Exp. Gerontol.* 125, 110677. doi: 10.1016/j.exger.2019.110677

Overend, T. J., Cunningham, D. A., Kramer, J. F., Lefcoe, M. S., and Paterson, D. H. (1992). Knee extensor and knee flexor strength: cross-sectional area ratios in young and elderly men. *J. Gerontol.* 47, M204–M210. doi: 10.1093/geronj/47.6.m204

Padilla, C. J., Harrigan, M. E., Harris, H., Schwab, J. M., Rutkove, S. B., Rich, M. M., et al. (2021). Profiling age-related muscle weakness and wasting: neuromuscular junction transmission as a driver of age-related physical decline. *Geroscience* 43, 1265–1281. doi: 10.1007/s11357-021-00369-3

Pietrangelo, T., D'Amelio, L., Doria, C., Mancinelli, R., Fulle, S., and Fano, G. (2011). Tiny percutaneous needle biopsy: an efficient method for studying cellular and molecular aspects of skeletal muscle in humans. *Int. J. Mol. Med.* 27, 361–367. doi: 10.3892/ijmm.2010.582

Pratt, J., De Vito, G., Narici, M., Segurado, R., Pessanha, L., Dolan, J., et al. (2021). Plasma C-Terminal agrin fragment as an early biomarker for sarcopenia: results from the genofit study. *J. Gerontol. A Biol. Sci. Med. Sci.* 76, 2090–2096. doi: 10.1093/gerona/glab139

Quinlan, J. I., Maganaris, C. N., Franchi, M. V., Smith, K., Atherton, P. J., Szewczyk, N. J., et al. (2017). Muscle and tendon contributions to reduced rate of torque development in healthy older males. *J. Gerontol.* 73, 539–545. doi: 10.1093/gerona/glx149

Reid, K. F., Pasha, E., Doros, G., Clark, D. J., Patten, C., Phillips, E. M., et al. (2014). Longitudinal decline of lower extremity muscle power in healthy and mobility-limited older adults: influence of muscle mass, strength, composition, neuromuscular activation and single fiber contractile properties. *Eur. J. Appl. Physiol.* 114, 29–39. doi: 10.1007/s00421-013-2728-2

Roberts, B. M., Lavin, K. M., Many, G. M., Thalacker-Mercer, A., Merritt, E. K., Bickel, C. S., et al. (2018). Human neuromuscular aging: sex differences revealed at the myocellular level. *Exp. Gerontol.* 106, 116–124. doi: 10.1016/j.exger.2018.02.023

Rodig, S. J. (2019). Counterstaining, mounting, and photographing stained cells. *Cold Spring Harb. Protoc.* 10, 302–305. doi: 10.1101/pdb.prot099770

Snijders, T., Verdijk, L. B., Smeets, J. S., McKay, B. R., Senden, J. M., Hartgens, F., et al. (2014). The skeletal muscle satellite cell response to a single bout of resistance-type exercise is delayed with aging in men. *Age (Dordr)* 36:9699. doi: 10.1007/s11357-014-9699-z

Sonjak, V., Jacob, K., Morais, J. A., Rivera-Zengotita, M., Spendiff, S., Spake, C., et al. (2019). Fidelity of muscle fibre reinnervation modulates ageing muscle impact in elderly women. *J. Physiol.* 597, 5009–5023. doi: 10.1113/JP278261

Spitzer, M., Wildenhain, J., Rappsilber, J., and Tyers, M. (2014). BoxPlotR: a web tool for generation of box plots. *Nat. Methods* 11, 121–122. doi: 10.1038/nmeth.2811

Stratton, M. T., Tinsley, G. M., Alesi, M. G., Hester, G. M., Olmos, A. A., Serafini, P. R., et al. (2020). Four weeks of time-restricted feeding combined with resistance training does not differentially influence measures of body composition, muscle performance, resting energy expenditure, and blood biomarkers. *Nutrients* 12:1126. doi: 10.3390/nu12041126

Tarnopolsky, M. A., Pearce, E., Smith, K., and Lach, B. (2011). Suction-modified Bergstrom muscle biopsy technique: experience with 13,500 procedures. *Muscle Nerve* 43, 717–725. doi: 10.1002/mus.21945

Taylor, R. (1990). Interpretation of the correlation coefficient: a basic review. *J. Diagn. Med. Sonogr.* 6, 35–39. doi: 10.1177/875647939000600106

Tesch, P., Thorsson, A., and Kaiser, P. (1984). Muscle capillary supply and fiber type characteristics in weight and power lifters. *J. Appl. Physiol.* 56, 35–38. doi: 10.1152/jappl.1984.56.1.35

Townsend, J. R., Hoffman, J. R., Fragala, M. S., Oliveira, L. P., Jajtner, A. R., Fukuda, D. H., et al. (2016). A microbiopsy method for immunohistological and morphological analysis: a pilot study. *Med. Sci. Sports Exerc.* 48, 331–335. doi: 10.1249/MSS.0000000000000772

Trappe, S., Gallagher, P., Harber, M., Carrithers, J., Fluckey, J., and Trappe, T. (2003). Single muscle fibre contractile properties in young and old men and women. *J. Physiol.* 552(Pt 1), 47–58. doi: 10.1113/jphysiol.2003.044966

van Melick, N., Meddeler, B. M., Hoogeboom, T. J., Nijhuis-van der Sanden, M. W., and van Cingel, R. E. (2017). How to determine leg dominance: the agreement between self-reported and observed performance in healthy adults. *PLoS One* 12:e0189876. doi: 10.1371/journal.pone.0189876

Verdijk, L. B., Koopman, R., Schaart, G., Meijer, K., Savelberg, H. H., and van Loon, L. J. (2007). Satellite cell content is specifically reduced in type II skeletal muscle fibers in the elderly. *Am. J. Physiol. Endocrinol. Metab.* 292, E151–E157. doi: 10.1152/ajpendo.00278.2006

Vescovo, G., Serafini, F., Facchin, L., Tenderini, P., Carraro, U., Dalla Libera, L., et al. (1996). Specific changes in skeletal muscle myosin heavy chain composition in cardiac failure: differences compared with disuse atrophy as assessed on microbiopsies by high resolution electrophoresis. *Heart* 76, 337–343. doi: 10.1136/hrt.76.4.337

Vespa, J., Armstrong, D. M., and Medina, L. (2020). *Demographic Turning Points for the United States: Population Projections for 2020 to 2060*. Washington, DC: US Census Bureau, 25–1144.

Walker, D. K., Fry, C. S., Drummond, M. J., Dickinson, J. M., Timmerman, K. L., Gundermann, D. M., et al. (2012). PAX7+ satellite cells in young and older adults following resistance exercise. *Muscle Nerve* 46, 51–59. doi: 10.1002/mus.23266

Conflict of Interest: The authors declare that the research was conducted in the absence of any commercial or financial relationships that could be construed as a potential conflict of interest.

METHODS
published: 24 January 2022
doi: 10.3389/fphys.2021.808798

Visualization of Dynamic Mitochondrial Calcium Fluxes in Isolated Cardiomyocytes

Anna Maria Krstic[1], **Amelia Sally Power**[1,2] **and Marie-Louise Ward**[1]*

[1] Department of Physiology, Faculty of Medical and Health Sciences, University of Auckland, Auckland, New Zealand,
[2] Department of Physiology, University of Otago, Dunedin, New Zealand

Background: Cardiomyocyte contraction requires a constant supply of ATP, which varies depending on work rate. Maintaining ATP supply is particularly important during excitation-contraction coupling, where cytosolic Ca^{2+} fluxes drive repeated cycles of contraction and relaxation. Ca^{2+} is one of the key regulators of ATP production, and its uptake into the mitochondrial matrix occurs *via* the mitochondrial calcium uniporter. Fluorescent indicators are commonly used for detecting cytosolic Ca^{2+} changes. However, visualizing mitochondrial Ca^{2+} fluxes using similar methods is more difficult, as the fluorophore must be permeable to both the sarcolemma and the inner mitochondrial membrane. Our aim was therefore to optimize a method using the fluorescent Ca^{2+} indicator Rhod-2 to visualize beat-to-beat mitochondrial calcium fluxes in rat cardiomyocytes.

Methods: Healthy, adult male Wistar rat hearts were isolated and enzymatically digested to yield rod-shaped, quiescent ventricular cardiomyocytes. The fluorescent Ca^{2+} indicator Rhod-2 was reduced to di-hydroRhod-2 and confocal microscopy was used to validate mitochondrial compartmentalization. Cardiomyocytes were subjected to various pharmacological interventions, including caffeine and β-adrenergic stimulation. Upon confirmation of mitochondrial Rhod-2 localization, loaded myocytes were then super-fused with 1.5 mM Ca^{2+} Tyrodes containing 1 μM isoproterenol and 150 μM spermine. Myocytes were externally stimulated at 0.1, 0.5 and 1 Hz and whole cell recordings of both cytosolic ($[Ca^{2+}]$cyto) and mitochondrial calcium ($[Ca^{2+}]_{mito}$) transients were made.

Results: Myocytes loaded with di-hydroRhod-2 revealed a distinct mitochondrial pattern when visualized by confocal microscopy. Application of 20 mM caffeine revealed no change in fluorescence, confirming no sarcoplasmic reticulum compartmentalization. Myocytes loaded with di-hydroRhod-2 also showed a large increase in fluorescence within the mitochondria in response to β-adrenergic stimulation ($P < 0.05$). Beat-to-beat mitochondrial Ca^{2+} transients were smaller in amplitude and had a slower time to peak and maximum rate of rise relative to cytosolic calcium transients at all stimulation frequencies ($P < 0.001$).

Edited by:
Norio Fukuda,
Jikei University School of Medicine,
Japan

Reviewed by:
Toshiko Yamazawa,
Jikei University School of Medicine,
Japan
Kotaro Oyama,
National Institutes for Quantum
and Radiological Science
and Technology, Japan

***Correspondence:**
Marie-Louise Ward
m.ward@auckland.ac.nz

Specialty section:
This article was submitted to
Striated Muscle Physiology,
a section of the journal
Frontiers in Physiology

Received: 04 November 2021
Accepted: 30 December 2021
Published: 24 January 2022

Citation:
Krstic AM, Power AS and
Ward M-L (2022) Visualization
of Dynamic Mitochondrial Calcium
Fluxes in Isolated Cardiomyocytes.
Front. Physiol. 12:808798.
doi: 10.3389/fphys.2021.808798

Conclusion: Myocytes loaded with di-hydroRhod-2 revealed mitochondrial specific compartmentalization. Mitochondrial Ca^{2+} transients recorded from di-hydroRhod-2 loaded myocytes were distinct in comparison to the large and rapid Rhod-2 cytosolic transients, indicating different kinetics between $[Ca^{2+}]_{cyto}$ and $[Ca^{2+}]_{mito}$ transients. Overall, our results showed that di-hydroRhod-2 loading is a quick and suitable method for measuring beat-to-beat $[Ca^{2+}]_{mito}$ transients in intact myocytes.

Keywords: calcium, cardiomyocytes, di-hydroRhod-2AM, excitation-contraction coupling, fluxes, mitochondria

INTRODUCTION

Cardiomyocytes are the working cells of the heart, and consequently are large consumers of ATP. In cardiac muscle, approximately 90–95% of ATP production occurs by mitochondrial oxidative phosphorylation (OXPHOS). Cardiomyocyte excitation-contraction (EC) coupling is driven by cytosolic Ca^{2+} fluxes, which lead to repeated cycles of contraction and relaxation (Bers, 2000). This process requires a constant supply of ATP to fuel key ATP-dependent transporters (i.e., the sarcoplasmic reticulum Ca^{2+} ATPase, sarcolemmal Na^{+}/K^{+} ATPases and for contractile protein force production, the myosin ATPase). Therefore, supply must be closely regulated to match the ATP demands of different work rates. When the heart is subjected to greater workloads, the rate of OXPHOS must increase to keep up with the high metabolic demands. There are two important processes that match ATP production to metabolic demand in cardiomyocytes: (i) mitochondrial ADP reuptake upon hydrolysis in the cytosol or (ii) an increase in cytosolic Ca^{2+} concentration (for review see: Maack and O'Rourke, 2007). It is unknown whether these mechanisms work independently or in parallel, however, it is well understood that both are involved in synchronizing energy supply to enable the heart to meet the body's ever changing metabolic demands.

Synchronized contraction of the whole heart is achieved through tightly regulated EC coupling, which is a process that occurs in every cardiomyocyte of the heart. The spread of electrical activity is initiated by depolarization of the cardiomyocytes from the cardiac pacemaker cells in the sinoatrial node (Keith and Flack, 1907), which is then conducted in a synchronized manner throughout the myocardium. Within each cardiomyocyte, depolarization leads to Ca^{2+} entry *via* voltage gated L-type Ca^{2+} channels. In turn, the L-type Ca^{2+} current rapidly induces release of Ca^{2+} from the sarcoplasmic reticulum (SR) during the "Ca^{2+} transient," whereby cytosolic Ca^{2+} concentration ($[Ca^{2+}]_{cyto}$) reaches levels of up to 1 μM (Bers, 2000). Ca^{2+} then diffuses to the contractile proteins initiating cross-bridge cycling and subsequent force development. In order for the heart to relax, cardiomyocyte $[Ca^{2+}]_{cyto}$ returns to resting levels by either: (i) reuptake back into the SR *via* the SR ATPase, (ii) extrusion through the sarcolemmal Na^{+}/Ca^{2+} exchanger, or (iii) reuptake into the mitochondria (Bers, 2001). Both the frequency of contraction (heart rate) and the size of the $[Ca^{2+}]_{cyto}$ transient can influence the amount of force developed, which consequently affects the energetic demands of the heart. The mitochondria play a key role in meeting these demands by maintaining ATP supply, which is regulated by mitochondrial Ca^{2+} reuptake.

Ca^{2+} ions are taken up into the mitochondria through the electrogenic mitochondrial Ca^{2+} uniporter (MCU), which is a low affinity transporter located on the inner mitochondrial membrane. The MCU complex is gated by Ca^{2+}, and is regulated by its two subunits MICU1 and MICU2 (Plovanich et al., 2013). The MCU drives Ca^{2+} ions from the cytosol down its large electrochemical gradient and into the mitochondrial matrix, where OXPHOS takes place. Mitochondrial Ca^{2+} uptake enhances ATP synthesis by activating Ca^{2+} sensitive Krebs cycle dehydrogenases, which ultimately increases [NADH] and the "push" of electrons through the electron transport chain (Brandes and Bers, 1997). This "push" of electrons enhances proton pumping across the inner mitochondrial membrane, which ultimately increases ATP phosphorylation at the final complex of the electron transport chain (F_1F_0ATPase), resulting in greater energy supply. Uptake of Ca^{2+} can occur either gradually or on a beat-to-beat basis, as cytosolic Ca^{2+} increases during EC coupling (Isenberg et al., 1993; Hajnóczky et al., 1995). Since the MCU has a low affinity for Ca^{2+}, this limits the amount of Ca^{2+} uptake during diastole and/or Ca^{2+} transients when at rest (Andrienko et al., 2009). It is estimated that about 1% of cytosolic Ca^{2+} released during the Ca^{2+} transient is taken up by the MCU (Bassani et al., 1992).

Mitochondria make up ∼30–40% of total cardiomyocyte volume (Else and Hulbert, 1985), and are in close association with the SR and the sarcomeres, which are areas of high energy consumption (**Figure 1**). Local Ca^{2+} microdomains are situated in close proximity to both the mitochondria and the SR, where $[Ca^{2+}]_{cyto}$ can reach up to 10 μM (Rizzuto et al., 1993). Ca^{2+} microdomains enable adjacent mitochondria to rapidly sense the amount of Ca^{2+} released and match ATP production accordingly. This is particularly important when energy demand is high during increased work rates, and ATP supply needs to be met. Furthermore, the release of mitochondrial Ca^{2+} is of equal importance to its uptake, in order to avoid Ca^{2+} overload and consequential opening of the mitochondrial permeability transition pore. Ca^{2+} ions are extruded from the mitochondrial matrix by either (i) the mitochondrial Na^{+}/Ca^{2+} exchanger ($3Na^{+}:1Ca^{2+}$), (ii) the mitochondrial H^{+}/Ca^{2+} exchanger (using the large pH gradient), or (iii) the mitochondrial permeability transition pore, which largely becomes active at

---

Abbreviations: $[Ca^{2+}]_{cyto}$, Cytosolic calcium concentration; DhRhod-2, Di-hydroRhod-2; K_d, Dissociation constant; EC coupling, Excitation-contraction coupling; ISO, Isoproterenol; $[Ca^{2+}]_{mito}$, Mitochondrial calcium concentration; MCU, Mitochondrial calcium uniporter; OXPHOS, Oxidative phosphorylation; SR, Sarcoplasmic reticulum.

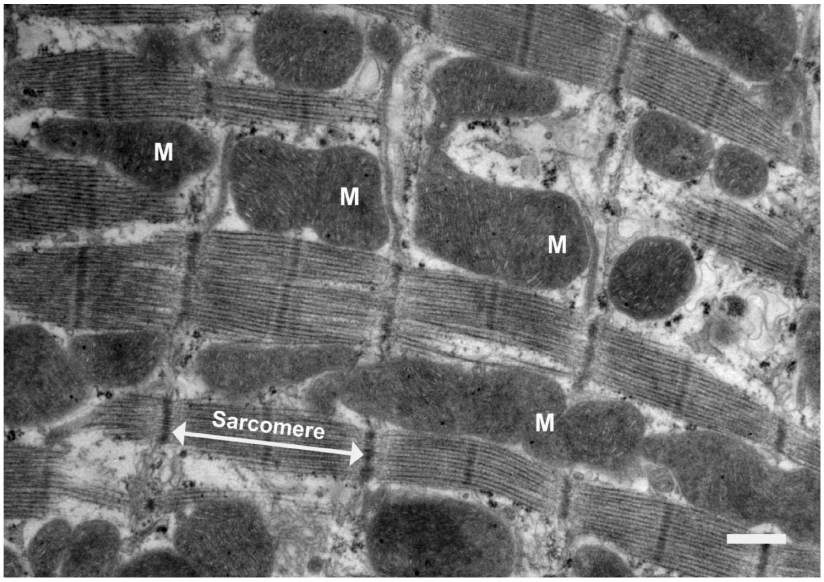

FIGURE 1 | Electron micrograph of a longitudinal section of rat ventricular tissue. Scale bar = 1 μm. Mitochondria are labeled "M" and a sarcomere is indicated by the white arrows. Sarcomeres are the key contractile units of the myocyte. This image depicts the way mitochondria are closely associated with the sarcomeres, which is where cross-bridge cycling takes place. Sarcomeres are sites of high energy consumption, therefore close localization with mitochondria is important for optimal cardiomyocyte function.

high mitochondrial Ca^{2+} concentration and/or in the presence of increased oxidative stress (Halestrap and Pasdois, 2009).

The importance of cytosolic Ca^{2+} in driving ATP synthesis is becoming more recognized in the Literature (Maack and O'Rourke, 2007), yet the kinetics of the mitochondrial Ca^{2+} fluxes, and how they are altered by disease are poorly understood. Failing hearts have been classified as an "engine out of fuel" (Neubauer, 2007), as there have been several associations between heart failure and impaired energy supply. Therefore, there is undeniable utility for a suitable method which allows us to study the links between mitochondrial Ca^{2+} fluxes and ATP production in health and disease. A significant number of findings related to myocardial OXPHOS were determined from studies using isolated mitochondria. Although this technique is commonly used, it can be problematic as damage to the mitochondria can occur during the isolation process, ultimately resulting in misleading interpretation of results (Wilson, 2017). Isolated mitochondria also remove the influence of sarcolemmal Ca^{2+} fluxes on MCU Ca^{2+} uptake. We therefore saw a need for a method that allowed investigation of mitochondrial Ca^{2+} fluxes that could be performed in intact cells. Previously, different methods have been implemented for studying real time changes in mitochondrial Ca^{2+} uptake in cardiomyocytes, but these have been accompanied by many technical challenges. These challenges were mainly associated with the need to obtain a measure of mitochondrial Ca^{2+} without contamination with cytosolic or SR Ca^{2+}, or in obtaining measurements that were of sufficient spatiotemporal resolution. One of the current methods for measuring mitochondrial Ca^{2+} uptake in cardiomyocytes includes injection of adenoviral probes (e.g., mitoCam) that target the inner mitochondria in cultured myocytes (Wüst et al., 2017; Hamilton et al., 2018; Miranda-Silva et al., 2020). MitoCam measurements have shown promising results for beat-to-beat changes in $[Ca^{2+}]_{mito}$ in intact myocytes, particularly because of its loading specificity. Although the use of adenoviral probes is beneficial for this reason, myocytes must be cultured for transfection of the probes. This process can change cardiomyocyte physiology and sub-cellular structural architecture, which is important for mitochondrial Ca^{2+} uptake (Bell et al., 2006; Hamilton et al., 2021). In addition, these methods are not well-suited to all lab groups, as it requires specialized equipment and skills for construction of adenoviral probes and introduction into cultured cardiomyocytes. Another method for measuring mitochondrial $[Ca^{2+}]$ includes loading either intact (Trollinger et al., 1997; Bowser et al., 1998; Maack et al., 2006; Fazal et al., 2017) or permeabilized myocytes (Andrienko et al., 2009; Oropeza-Almazán and Blatter, 2020) with Ca^{2+} specific fluorescent indicators. Some of these studies used ratiometric Ca^{2+} indicators (i.e., Indo-1AM) with quenchers such as Mn^{2+} to minimize cytosolic contamination, based on the idea that Mn^{2+} would remain in the cytosol and not enter the mitochondria (Miyata et al., 1991; Zhou et al., 1998). Other studies used a low affinity Ca^{2+} indicator such as Rhod-2 (Trollinger et al., 1997; Bowser et al., 1998; Maack et al., 2006). Rhod-2 has an *in vitro* dissociation constant (K_d) of 570 nM, which is probably higher once loaded into a cell. The positively charged Rhod-2 makes it suitable for mitochondrial compartmentalization, as the mitochondrial membrane is highly polarized. Using confocal microscopy, studies by Trollinger et al. (1997) and Bowser et al. (1998) showed selective mitochondrial loading of Rhod-2, but were unable to detect $[Ca^{2+}]_{mito}$ transient kinetics due to temporal limitations during acquisition. Therefore, limitations in both aspects (i.e., mitochondrial compartmentalization and modes of acquisition) have led to the uncertainty of how the $[Ca^{2+}]_{mito}$ fluxes might differ from the $[Ca^{2+}]_{cyto}$ kinetics.

Our group has employed a method that takes advantage of the low affinity/cationic nature of the fluorescent Ca^{2+} indicator Rhod-2. We then enhanced mitochondrial specific loading of Rhod-2 by combining the indicator with a reducing agent (i.e., Na^+ borohydride) dissolved in a small amount of methanol (Bowser et al., 1998). The combination of Rhod-2 with Na^+ borohydride reduced the indicator to non-fluorescent di-hydroRhod-2 (dhRhod-2), which was not only permeable to the sarcolemma, but also the mitochondrial membrane. Within the mitochondria, dhRhod-2 is oxidized back to Rhod-2, due to the presence of mitochondrial reactive oxidative species. This improves detection of mitochondrial Ca^{2+} signals. Any remaining dhRhod-2 in the cytosol is not oxidized and therefore would not respond to changes in $[Ca^{2+}]$. Hajnóczky et al. (1995) were the first to describe the method of reducing Rhod-2 to dhRhod-2 in isolated hepatocytes. Their study investigated the control of Ca^{2+} sensitive mitochondrial dehydrogenases by monitoring $[Ca^{2+}]_{mito}$ and $[Ca^{2+}]_{cyto}$ over a long time scale (i.e., 0–1,000 s). The purpose of our study was to measure mitochondrial Ca^{2+} changes in cardiomyocytes on a millisecond time scale to show beat-to-beat changes. This was done by loading cardiomyocytes with 5 μM dhRhod-2 for 1 h at 37°C. Loaded cells were excited at 542 nm and emission was collected at 581 nm. This allowed us to make dynamic measurements of mitochondrial Ca^{2+} fluxes in live, field stimulated cardiomyocytes. The aims of our study were therefore: (i) to confirm dhRhod-2 is giving a mitochondrial signal that is uncontaminated with cytosolic Ca^{2+}, (ii) to test mitochondrial Ca^{2+} signals in isolated cardiomyocytes by exposing them to pharmacological interventions known to modulate energy demand and/or mitochondrial Ca^{2+} levels and (iii) to develop a technique that can be used for fluorometric mitochondrial Ca^{2+} measurements.

MATERIALS AND EQUIPMENT

For Cell Isolation

Ca^{2+} Free Tyrodes buffer[1]
Type 2 Collagenase (275 U/mL, Worthington Biochemical)
Protease (1.8 U/mL, Sigma Aldrich)
Trypsin inhibitor (0.05%, Worthington Biochemical)
Bovine Serum Albumin (0.1%, Thermo Fisher Scientific; IgG free)
Constant pressure Langendorff Perfusion System
1 M $CaCl_2$ stock solution

For Di-HydroRhod-2 Loading

50 μg vial Rhod-2 (Invitrogen, Thermo Fisher Scientific, Life Technologies NZ, cat. no. R-1244)[2]
DMSO anhydrous (Invitrogen, Thermo Fisher Scientific, Life Technologies NZ, cat. no. D12345)[2]
20% Pluronic (Invitrogen, Thermo Fisher Scientific, Life Technologies NZ, cat. no. P6867)[2]
Na^+ Borohydride (Sigma Aldrich, cat no. 452882)[2]
50 μg vial Mitotracker Deep Red (Invitrogen, Thermo Fisher Scientific, Life Technologies NZ, cat. no. M22426)
1.5 mM Ca^{2+} Tyrodes

[1] Ca^{2+} Free Tyrodes solution contains (in mM): 140 NaCl, 4 KCl, 10 Hepes, 1 $MgCl_2.6H_2O$, 10 Glucose. Adjusted to pH 7.4 with 5 M NaOH.

[2] To make 1 mM di-hydroRhod-2 solution: Dissolve 1 μg vial of Rhod-2 with 22.25 μL DMSO. Add 22.25 μL of 20% Pluronic in DMSO. Once dissolved, add 10 μL of Na^+ borohydride dissolved in 20 μL methanol. Wait until solution becomes colorless, add 5 μL to 1 mL of cell suspension for 5 μM working concentration.

[3] 100 nM mitotracker deep red: Dissolve 50 μg vial of mitotracker with 90 μL DMSO (brings stock concentration to 1 mM). Dilute further to 0.1 mM using DMSO then load 1 mL cells with 1 μL for 100 nM working concentration.

METHODS

Harvesting of Tissue

Healthy, Wistar rats (male, 300–350 g) were anesthetized using 2% isoflurane in 100% O_2 as a carrier gas. Once unconscious, the rat was euthanized by decapitation, hearts excised at the aorta and placed in ice cold Ca^{2+} free Tyrode's buffer (refer to section "For Cell Isolation"). Approval for this research was provided by the University of Auckland Animal Ethics Committee (AEC: 001929), in accordance with the Code of Ethical Conduct of The University of Auckland, and the New Zealand Animal Welfare Act 1999.

Cell Isolation

Within 30 s after dissection, hearts were cannulated by the aorta, secured with suture, and Langendorff-perfused with oxygenated Ca^{2+} free Tyrode's buffer for 5 min at 37°C using a gravity fed system. During this time blood should be cleared from the coronary circulation and effluent should run clear demonstrating adequate perfusion of the coronary circulation. Perfusion was then switched to 0.2 mM Ca^{2+} Tyrode's containing enzymes: 275 U/mL Type 2 Collagenase (Worthington Biochemical Corp, United States) and 1.8 U/mL Protease (Sigma Aldrich, United States). After 9–12 min of enzymatic digestion, ventricles were cut off and immersed in 0.15 mM Ca^{2+} Tyrode's containing 0.1% BSA (Sigma Aldrich, United States) and 0.05% Trypsin inhibitor (Worthington Biochemical, United States). The ventricles were minced to yield isolated, quiescent myocytes and extracellular Ca^{2+} was gradually increased to 1.5 mM.

Loading of Rhod-2 and Di-HydroRhod-2

As previously mentioned, Rhod-2 is a positively charged fluorescent Ca^{2+} indicator which results in electrical potential-driven uptake into the mitochondria (Hajnóczky et al., 1995). The acetoxymethyl (AM) form of Ca^{2+} indicators can readily cross the sarcolemma and enter the cytosol, where it becomes de-esterified. However, we used a method that exploited the activity of the mitochondrial reactive oxidative species, in order to enhance mitochondrial Ca^{2+} signal specificity. This was done by reducing Rhod-2 to di-hydroRhod-2 (dhRhod-2) prior to introducing it into the cardiomyocytes (Bowser et al., 1998). The reduction of Rhod-2 to dhRhod-2 improves the selectivity for mitochondrial loading as the reduced dye does not display Ca^{2+} dependent fluorescence (Hajnóczky et al., 1995). DhRhod-2 then re-oxidizes to Rhod-2 in the mitochondria, resulting in mitochondrial-specific Ca^{2+} signals (refer to **Supplementary Figure 1**). To make a 1 mM stock of Rhod-2, one 50 μg vial of Rhod-2 indicator (Invitrogen, Thermo Fisher Scientific, Life Technologies NZ, catalog no. R-1244) was dissolved in 22.25 μL dimethyl sulphoxide anhydrous (DMSO) and 22.25 μL 20% Pluronic in DMSO (Invitrogen, Thermo Fisher Scientific, Life Technologies NZ, cat no. D12345 and P6867). The smallest possible amount of Na^{+} borohydride was dissolved in 20 μL methanol, then 10 μL was added as the reducing agent to the Rhod-2 vial. The indicator then transitioned from a pink color to a clear, colorless solution after 5–10 min. Cardiomyocytes were then loaded with 5 μM dhRhod-2 solution for 1 h, carried out at 37°C to further increase compartmentalization of the indicator into the mitochondria. To allow for de-esterification, cardiomyocytes were washed in 1.5 mM Ca^{2+} Tyrode's for at least 30 min prior to imaging. Loading of Rhod-2 for cytosolic measurements was completed using the steps above but excluding the addition of Na^{+} borohydride in methanol. A group of myocytes were also loaded with a ratiometric cytosolic Ca^{2+} indicator Fura-2AM, to compare its kinetics to Rhod-2 cytosolic transients. A single 50 μg vial of Fura-2AM (Invitrogen, Thermo Fisher Scientific, Life Technologies NZ, catalog no. F1221) was diluted to a 1 mM stock solution with DMSO and 20% Pluronic. For a working concentration of 10 μM, 10 μL of 1 mM Fura-2AM solution was added to 1 mL of cells. Cells were subsequently loaded for 20 min at room temperature then washed with 1.5 mM Ca^{2+} Tyrode's for 10 min to allow de-esterification.

Live Cell Confocal Imaging

In order to validate Rhod-2 localization in the mitochondria, cardiomyocytes were simultaneously loaded with 100 nM mitotracker deep red (refer to section "For Di-HydroRhod-2 Loading" subscript 3) and 5 μM Rhod-2 or dhRhod-2 (Thermo Fisher Scientific, Life Technologies NZ). A perspex cell bath was fixed to the stage of an inverted laser scanning confocal microscope (LSM 710, Zeiss, Oberkochen, Germany). Using a Zeiss 63x oil-immersion objective lens (NA 1.40), images with a 0.1 μm pixel resolution were captured using two lasers sequentially: 561 nm (Rhod-2) and 633 nm (Mitotracker) at 2% laser power. Images obtained for the validation experiments were a single-framed snapshot of the whole myocyte with 2 channels (dhRhod-2/Rhod-2 and Mitotracker), which were subsequently merged for analysis (see section "Data Analysis"). Furthermore, cardiomyocytes loaded with dhRhod-2 (and Rhod-2) were electrically stimulated (D100, Digitimer, Welwyn, United Kingdom) with 5 ms pulses at 1 Hz (room temperature) before (baseline) addition of 20 mM caffeine (Sigma Aldrich, cat. no C0750). The response to caffeine was also measured by delivering a 20 mM bolus to the cardiomyocyte in the absence of electrical stimulation. This technique was used to detect potential loading of dhRhod-2 into the SR. The response to caffeine was then compared between myocytes loaded with dhRhod-2 and those loaded with Rhod-2. Using a similar method, the response to 1 μM isoproterenol (Sigma Aldrich, cat. no I6379) was recorded by collecting the emitted fluorescence from the whole cell over 2–3 min (1 frame/s). Cardiomyocytes loaded with dhRhod-2 were electrically stimulated with 5 ms pulses at 1 Hz (room temperature) before (baseline) and during addition of isoproterenol. This method was employed to determine whether dhRhod-2 signals were enhanced during beta-adrenergic stimulation. The response to 1 μM isoproterenol was also tested in cells that were pre-treated with 50 μM MCU inhibitor Ru265 for 30–60 min. Further evidence against cytosolic contamination was obtained by imaging permeabilized cardiomyocytes loaded with dhRhod-2. For cell permeabilization, cardiomyocytes were loaded with dhRhod-2 (as stated in section "Loading of Rhod-2 and Di-HydroRhod-2"), then washed in intracellular buffer containing (in mM); 2 $CaCl_2$ (for 100 nM free $[Ca^{2+}]_i$), 5 NaCl, 140 KCl, 1 $MgCl.6H_2O$, 5 Glucose, 10 Hepes, 15 butanedione monoxime and 5 EGTA. Myocytes were imaged as above, at baseline and after bolus application of 0.05% saponin, which was used for cell permeabilization.

Fluorometric Measurements in Live Myocytes

Fluorometric measurements were made from cardiomyocytes loaded with di-hydroRhod-2 to determine beat-to-beat changes in mitochondrial Ca^{2+} fluxes. Loaded cardiomyocytes were transferred into a perspex cell bath, which was fixed to the stage of an inverted fluorescence microscope. Cells were then externally field stimulated between 0.1 and 1 Hz (room temperature) and continuously super-fused with 1.5 mM Ca^{2+} Tyrodes containing 1 μM isoproterenol and 150 μM spermine (Cayman Chemical United States, cat no. 136587-13-8). Spermine is an allosteric MCU agonist, which increases MCU affinity to Ca^{2+}, enhancing its uptake into the mitochondria (Nicchitta and Williamson, 1984). Therefore, its addition with isoproterenol is useful in enhancing the total dhRhod-2 signal. Myocytes were imaged using a 20x objective lens, 0.75 NA, and illuminated with a 542 ± 10 nm excitation wavelength using an Optoscan monochromator and spectrofluorometric, PMT based system (Cairn, Faversham, United Kingdom). Recordings were acquired at a rate of 400 Hz and sampled in 10 ms intervals using Acquisition Engine software (Cairn, Faversham, United Kingdom). Emitted fluorescence was collected at 581 nm (± 10 nm) from the whole cell (approx. 100–150 × 10–30 μm collection window). The total emitted fluorescence was used as a measure of mitochondrial Ca^{2+}. The mitochondrial Ca^{2+} fluxes were then compared with cytosolic Ca^{2+} transients recorded in Rhod-2-loaded myocytes. Cytosolic Ca^{2+} transients were also recorded in myocytes loaded with Fura-2. Using the same spectrofluorometric system, cardiomyocytes loaded with Fura-2 were illuminated with alternating 340 and 380 nm excitation wavelengths every 5 ms. Emitted 510 ± 15 nm fluorescence was acquired at 400 Hz using Acquisition Engine software (Cairn, Faversham, United Kingdom) from the whole cell.

Data Analysis

Confocal data was acquired using Zen Blue software (Zeiss, Germany) and analyzed using FIJI (ImageJ analysis). The relationship in fluorescence intensity was measured by calculating the correlation index from a specific region of each cardiomyocyte co-labeled with Rhod-2/mitotracker and dhRhod-2/mitotracker. The correlation index, also known as Pearson's coefficient, measures the overlap of pixels from two-channel images. The ImageJ Analysis Software Plugin "Just Another Co-localization Program" or "JACoP" (Bolte and Cordelieres, 2006), was used to determine the correlation index between Rhod-2/mitotracker and dhRhod-2/mitotracker. The mean correlation index between Rhod-2/mitotracker and dhRhod-2/mitotracker was then analyzed by unpaired, two-tailed *t*-tests to compare the overlap between the two indicators. The correlation index indicated the degree of mitochondrial localization, with a value of 1 representing mitochondrial compartmentalization and a value of 0 representing no compartmentalization (Bolte and Cordelieres, 2006). In addition, the intensity plots from myocytes exposed to pharmacological interventions were statistically analyzed by unpaired, two-tailed *t*-tests to compare the amplitudes at the peaks of dhRhod-2 fluorescence at baseline vs. during maximum drug response.

In separate experiments, fluorometric measurements of cytosolic and mitochondrial Rhod-2 fluorescence were carried out using an Optoscan monochromator (Cairn Research Ltd., Faversham, United Kingdom). Comparison of the following parameters were made from both the mitochondrial and cytosolic Ca^{2+} transients: ΔF/F0, where ΔF is the transient amplitude and F0 the baseline fluorescence, maximum rate of fluorescence rise, time to peak fluorescence following stimulation, and time constant of fluorescence decay. Ca^{2+} transients were acquired once steady state was obtained for all stimulation frequencies measured, and the parameters from an average of three sequential transients were analyzed. Mean data from fluorometric measurements of Rhod-2 cytosolic Ca^{2+} transients and dhRhod-2 mitochondrial Ca^{2+} transients were analyzed using two-way ANOVA for multiple comparisons between groups and stimulation frequencies. Statistical significance was indicated by a *P*-value of < 0.05 for all data sets. All mean data (including confocal) was statistically analyzed using Prism 9 Analysis software.

RESULTS

Validation of Mitochondrial Localization

Rhod-2 Localization

The localization of the non-reduced indicator Rhod-2 was first investigated in isolated cardiomyocytes. **Figure 2** shows a representative isolated ventricular myocyte co-loaded with Mitotracker (red) and Rhod-2 (green). **Figure 2A** displays the separate channels for each indicator alongside an overlay of both channels when "merged." The Mitotracker label (red) displays a distinct longitudinal mitochondrial pattern with visible striations, whereas Rhod-2 (green) is present globally across the myocyte, also revealing faint striations. When merged, there is minimal overlap between the two indicators. **Figure 2B** shows the intensity plot profile of Mitotracker and Rhod-2 fluorescence intensity, which was analyzed across the transverse section of the myocyte labeled with a white line in **Figure 2A**. The Mitotracker label displayed prominent peaks and troughs in intensity, which is indicative of the distribution of mitochondria across the myocyte, whereas the Rhod-2 intensity peaks did not match the mitotracker label distribution.

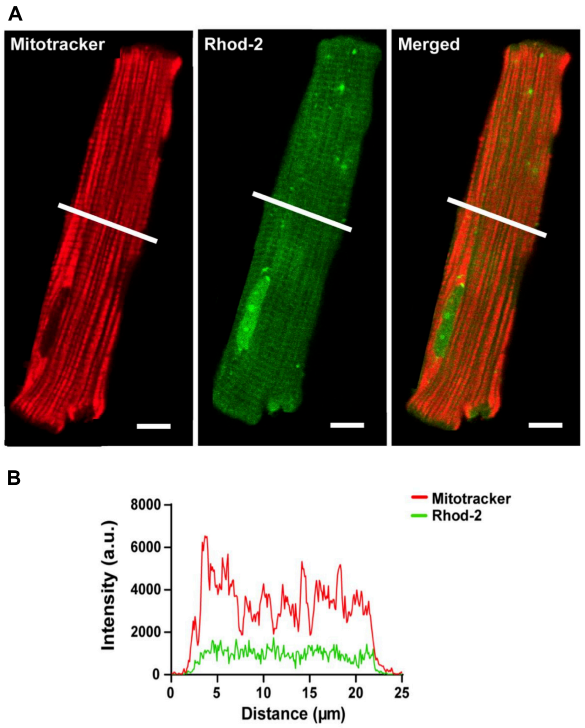

FIGURE 2 | Confocal analysis of a representative isolated rat ventricular myocyte loaded with Mitotracker Deep Red and non-reduced Rhod-2 (Scale bar = 10 μm). **(A)** Shows a representative myocyte loaded with Mitotracker (red) and Rhod-2 (non-reduced form, green). The third image in **(A)** shows both indicators when merged. **(B)** Shows the intensity plot profile of both Mitotracker (red) and Rhod-2 (green) fluorescence intensity, which was analyzed at the transverse section of the myocyte represented by the white lines in **(A)**.

Di-HydroRhod-2 Localization

The localization of the di-hydroRhod-2 (dhRhod-2) loaded cells was then investigated and compared to that of Rhod-2. Myocytes were co-loaded with dhRhod-2 (green) and Mitotracker (red) as shown in **Figure 3**. Both Mitotracker and dhRhod-2 showed a typical longitudinal pattern consistent with mitochondrial distribution between the myofibrils, along with visible striations. There was also a distinct overlap between the two indicators when merged and the mitochondria

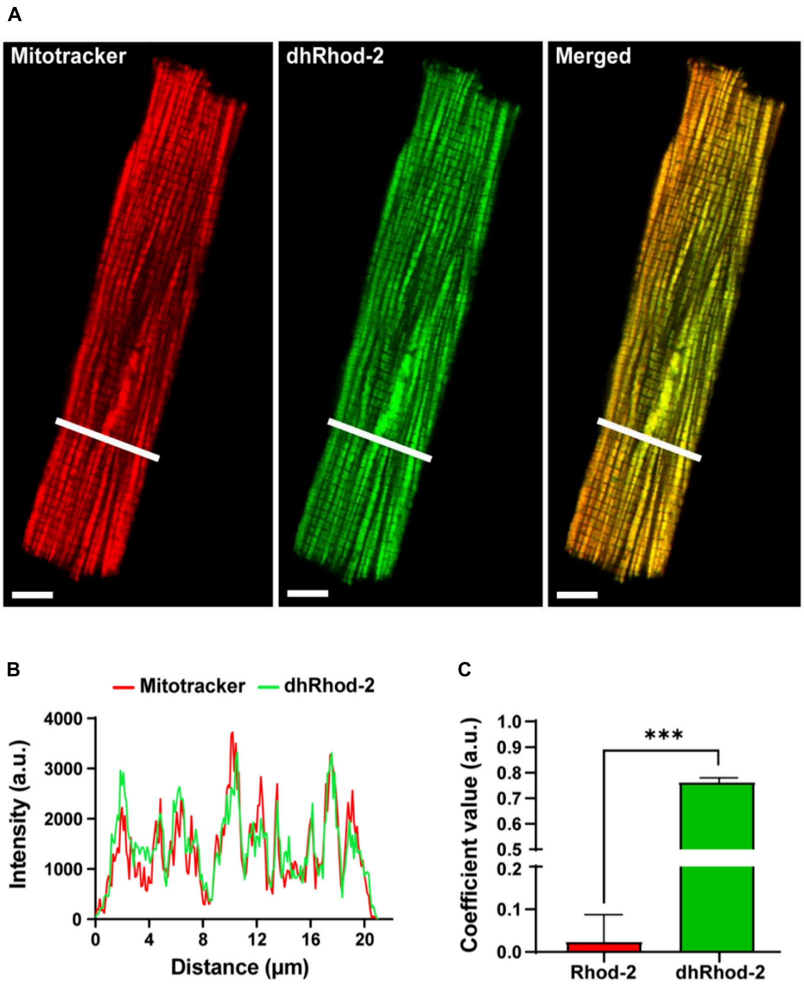

FIGURE 3 | Confocal analysis of a representative isolated rat ventricular myocyte loaded with Mitotracker Deep Red and di-hydroRhod-2 (Scale bar = 8 µm). **(A)** Shows a representative myocyte loaded with Mitotracker (red) and di-hydroRhod-2 (dhRhod-2, green). The third myocyte in **(A)** shows both indicators when merged. **(B)** Shows the plot profile of both Mitotracker (red) and dhRhod-2 (green) fluorescence intensity, which was analyzed across a transverse section of the myocyte represented by the white lines in **(A)**. **(C)** Displays the Pearson's coefficient value, which represents the correlation index between Rhod-2/mitotracker (*n* = 6 cardiomyocytes) and dhRhod-2/mitotracker (*n* = 7 cardiomyocytes). Results are presented as mean ± SEM, $^{***}P < 0.001$.

appear yellow. This was evident in the intensity plot profile in **Figure 3B**, which showed equal distribution of both indicators, where most peaks and troughs aligned at the same point across the transverse section of the myocyte. Furthermore, **Figure 3C** shows the correlation index between dhRhod-2/mitotracker labeling (mean ± SEM, 0.76 ± 0.02 a.u. $n = 7$ cells) was greater relative to the correlation index between Rhod-2/mitotracker labeling (0.02 ± 0.06 a.u. $n = 6$ cells, $P < 0.001$), further revealing dhRhod-2 mitochondrial localization.

Response of $[Ca^{2+}]_{mito}$ to Pharmacological Interventions

Response to High Dose of Caffeine

The first pharmacological intervention was used to determine potential loading of dhRhod-2 in the SR. **Figure 4** shows two representative isolated myocytes loaded with either Rhod-2 or dhRhod-2. Myocytes were bathed in 1 mM Ca^{2+} Tyrodes and were imaged across a time series in the absence of stimulation. **Figures 4A,B** captured the myocytes at the start of the time series while in baseline conditions (pre-caffeine), while **Figures 4C,D** show the myocytes during exposure to 20 mM caffeine to release compartmentalized Ca^{2+} into the cytosol from the SR (Bassani et al., 1992). In baseline conditions, myocytes showed distinct differences in the distribution of fluorescence with Rhod-2 (**Figure 4A**) relative to dhRhod-2 (**Figure 4B**). There was an overall global increase in Rhod-2 fluorescence throughout the myocyte during the peak response to caffeine (**Figure 4C**). The plot profile in **Figure 4E** shows increased caffeine-induced Rhod-2 fluorescence (green) relative to baseline (black), which was analyzed across the transverse portion of the myocyte as indicated by the white lines in **Figures 4A,C**. In contrast, myocytes loaded with the reduced form dhRhod-2, showed

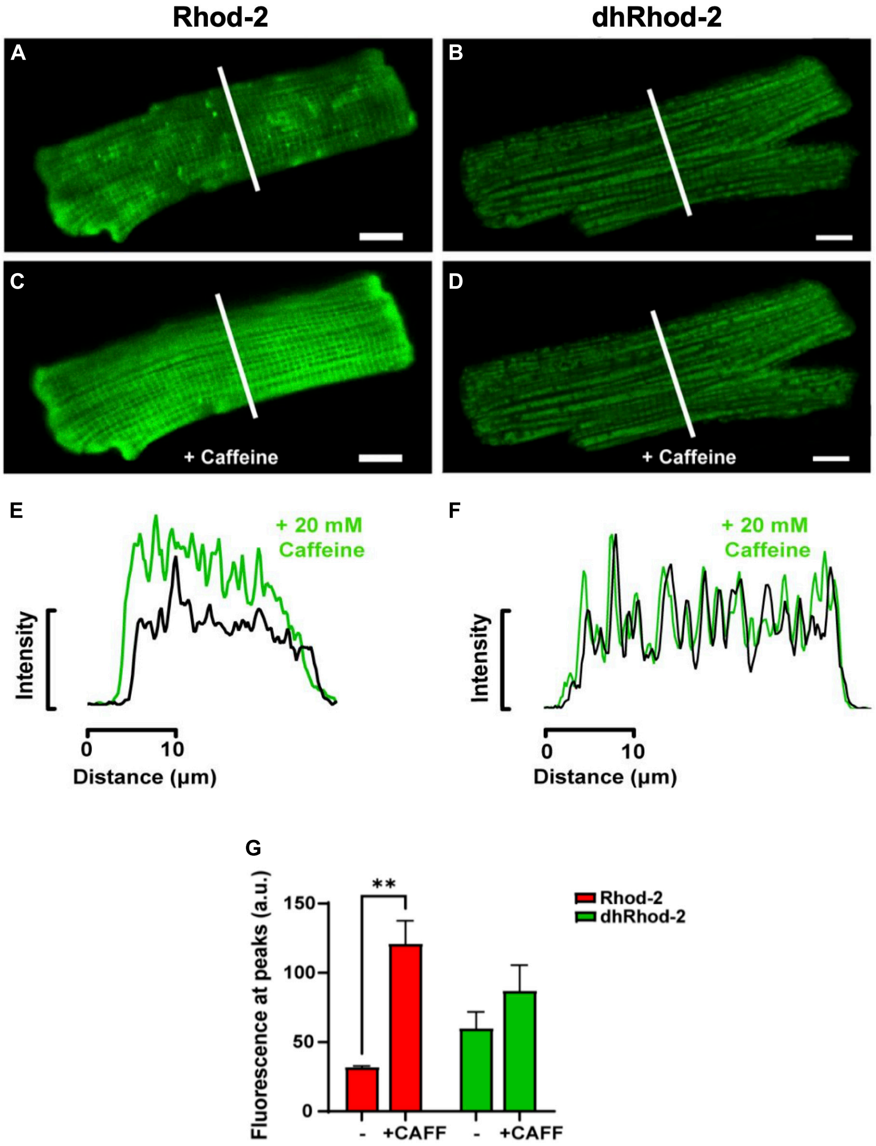

FIGURE 4 | Confocal analysis of representative isolated rat ventricular myocytes loaded with non-reduced Rhod-2 **(A,C,E)** and di-hydroRhod-2 **(B,D,F)** at baseline and during the response to a 20 mM caffeine bolus (scale bar = 10 μm). Myocytes in **(A,B)** were captured during baseline conditions prior to caffeine application, while myocytes in **(C,D)** were taken during the peak response to a 20 mM bolus of caffeine. The intensity plot profile of Rhod-2 fluorescence **(E)** and di-hydroRhod-2 (dhRhod-2) fluorescence **(F)** shows fluorescence intensity before and during the response to caffeine. The plot profiles were analyzed across the transverse portion of the myocyte indicated by the white lines in **(A–D)**. **(G)** Shows Rhod-2 and dhRhod-2 fluorescence at baseline vs. post caffeine application. Results are presented as mean ± SEM, *n* = 4 cardiomyocytes, $^{**}P < 0.01$.

little change in fluorescence intensity upon caffeine application relative to baseline (4B & 4D), and illustrated in the intensity plot profile (4F). **Figure 4F** shows similar magnitudes and distribution of peaks and troughs of dhRhod-2 fluorescence at baseline (black) and post caffeine application (green). **Figure 4G** shows Rhod-2 fluorescence increased from 31.9 ± 0.9 a.u. (mean ± SEM) at baseline to 121.0 ± 16.5 a.u. ($n = 4$ cells, $P = 0.01$) at maximum response to caffeine. However, dhRhod-2 fluorescence did not change in response to caffeine (baseline, 60.0 ± 11.8 a.u. vs. maximum caffeine response, 87.1 ± 18.5 a.u. $n = 4$ cells).

Response to β-Adrenergic Stimulation

In order to increase mitochondrial Ca^{2+} uptake, myocytes loaded with dhRhod-2 were also subjected to the non-selective β-adrenergic agonist, isoproterenol (ISO, 1 μM). Myocytes were continuously stimulated at 1 Hz and imaged across a time series as stated in section "Live Cell Confocal Imaging." Images were captured across three different time points during the response to ISO. **Figure 5A** shows the change in dhRhod-2 fluorescence at 0 s (baseline), 60 and 120 s, the latter considered as the maximum ISO effect. The myocyte shows distinctive dhRhod-2 distribution at baseline, which is retained throughout the response to ISO.

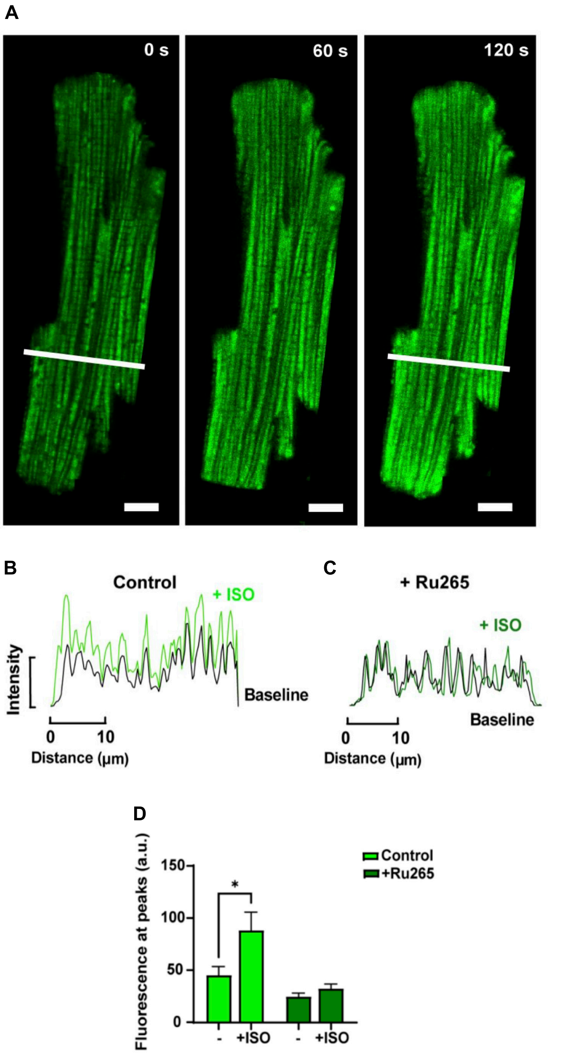

FIGURE 5 | Confocal analysis of a representative isolated rat ventricular myocyte loaded with di-hydroRhod-2 during the response to 1 μM isoproterenol (scale bar = 10 μm). **(A)** Shows a loaded myocyte at baseline (0 s), then 60 and 120 s post 1 μM isoproterenol (ISO) application. **(B,C)** Show intensity plot profiles of di-hydroRhod-2 (dhRhod-2) fluorescence at baseline and during maximum ISO response in control **(B)** and Ru-265 pre-treated cardiomyocytes **(C)**. Mean intensity values in **(B)** were analyzed across a transverse section of the myocyte represented by the white lines in **(A)**. **(D)** Shows dhRhod-2 fluorescence at baseline (0 s) and during maximum ISO response (120 s) with and without pre-treatment of 50 μM Ru265 in $n = 6$ cardiomyocytes. Results are presented as mean ± SEM, $^*P < 0.05$.

The intensity plot profile (**Figure 5B**) shows an increase in the magnitude of dhRhod-2 fluorescence during ISO relative to baseline, while the distribution of the peaks and troughs remain unchanged. Meanwhile, the intensity plot profile of the response to ISO in Ru-265 pre-treated cells (**Figure 5C**), shows no change in dhRhod-2 fluorescence from baseline to maximum ISO response. The mean fluorescence intensity values (**Figure 5D**) also showed an approximately twofold increase in dhRhod-2 intensity with ISO (mean ± SEM, 88.2 ± 17.6 a.u.) relative to baseline (45.0 ± 8.7 a.u. in $n = 6$ cells, $P < 0.05$). Pre-treatment of cells with MCU inhibitor Ru265, prevented the ISO-stimulated increase in dhRhod-2 fluorescence (baseline, 24.4 ± 3.6 a.u. vs. ISO, 32.2 ± 4.3 a.u. in $n = 7$ cells), however, there was no change in baseline fluorescence in the presence of Ru265 ($P = 0.08$).

Fluorometric Measurements of $[Ca^{2+}]_{mito}$ vs. $[Ca^{2+}]_{cyto}$

Fluorometric measurements were optimized and made following the protocols stated in section "Fluorometric Measurements in Live Myocytes" in order to: (i) determine the characteristics of the mitochondrial Ca^{2+} transient relative to the cytosolic Ca^{2+} transient and (ii) to record beat-to-beat mitochondrial Ca^{2+} fluxes at different stimulation frequencies. **Figure 6A** shows two single transients recorded from representative myocytes loaded with Rhod-2 (black) and dhRhod-2 (red). When comparing a Rhod-2 cytosolic Ca^{2+} transient superimposed with a dhRhod-2 mitochondrial Ca^{2+} transient, visually there are clear differences in both the transient amplitude and kinetics. **Figure 6B** shows the Rhod-2 transient resembles a cytosolic Ca^{2+} transient with similar characteristics to a transient recorded from a representative myocyte loaded with the commonly used cytosolic Ca^{2+} indicator, Fura-2 (green).

Mitochondrial Ca^{2+} Transients and Stimulation Frequency

Mitochondrial and cytosolic Ca^{2+} transients were recorded from cells subjected to stimulation frequencies of 0.1, 0.5, and 1 Hz. **Figure 7A** shows steady-state $[Ca^{2+}]_{cyto}$ transients (black) and $[Ca^{2+}]_{mito}$ transients (red) recorded from representative myocytes loaded with Rhod-2 and dhRhod-2, respectively. **Figure 7B** displays mean transient amplitude data (ΔF/F0, refer to section "Data Analysis") comparing cytosolic and mitochondrial Ca^{2+} transients at different stimulation frequencies. While there was no change in either group between frequencies, the Rhod-2 loaded myocytes had larger $[Ca^{2+}]_{cyto}$ transient amplitudes relative to $[Ca^{2+}]_{mito}$ transient amplitude at all stimulation frequencies ($P < 0.001$). **Figures 7C,D** shows a clear difference in Ca^{2+} transient kinetics, whereby Rhod-2 $[Ca^{2+}]_{cyto}$ transients had faster maximum rates of rise and time to peak fluorescence relative to dhRhod-2 $[Ca^{2+}]_{mito}$ transients at all stimulation frequencies ($P < 0.001$). The time constant of decay was not different between $[Ca^{2+}]_{cyto}$ and $[Ca^{2+}]_{mito}$ transients at any stimulation frequency (**Figure 7E**). Overall, there were no differences within groups in any of the measured transient parameters between frequencies.

DISCUSSION

Validation of Mitochondrial Localization

Loading myocytes with Rhod-2 resulted in widespread, non-localized fluorescence (**Figures 2A,B**). However, there was apparently some Rhod-2 mitochondrial compartmentalization, as several peaks visible in the intensity plot profile (**Figure 2B**) coincided with smaller amplitude peaks observed with the mitotracker label. This differed to the punctate mitochondrial

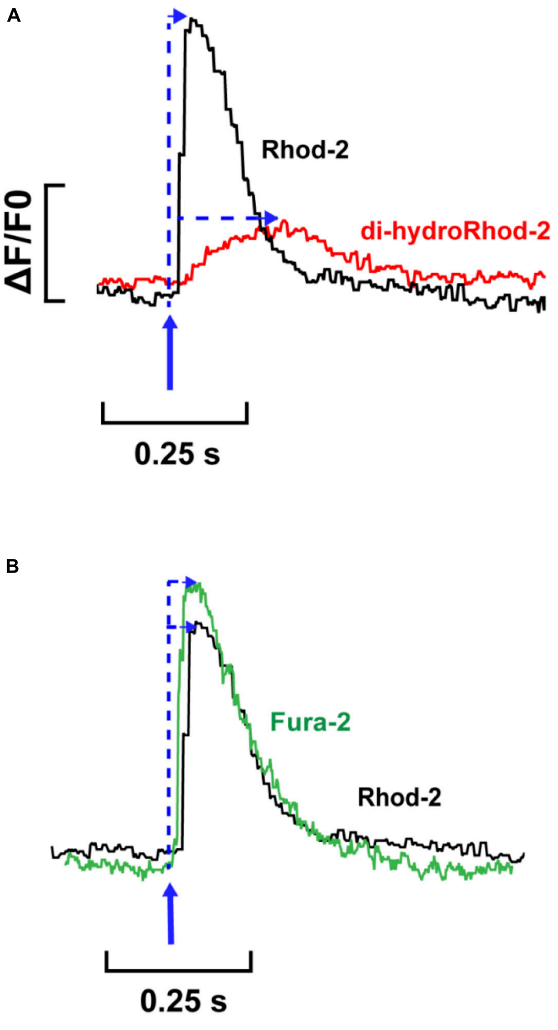

FIGURE 6 | Comparison between single Rhod-2, di-hydroRhod-2 and Fura-2 Ca^{2+} transients. **(A)** displays a single cytosolic Ca^{2+} transient (Rhod-2, black) superimposed with a single mitochondrial Ca^{2+} transient (di-hydroRhod-2, red). The transient amplitude is a represented as a ratio of the change in fluorescence/diastolic fluorescence (ΔF/F0). The blue arrows indicate the time to peak fluorescence after the stimulus. **(B)** Shows a comparison of the time courses of single cytosolic transients obtained in separate cells loaded with different Ca^{2+} indicators, Rhod-2 (black, as above) and ratiometric Ca^{2+} indicator Fura-2 (green).

pattern displayed in di-hydroRhod-2 (dhRhod-2) loaded myocytes (**Figure 3A**). DhRhod-2 substantially overlapped with the mitotracker indicator as shown in the intensity plot profile (**Figure 3B**). As mentioned in section "Data Analysis," the correlation index between Rhod-2/mitotracker and dhRhod-2/mitotracker indicated the degree of mitochondrial localization. DhRhod-2/mitotracker had a correlation index closer to 1 (**Figure 3C**), which confirmed mitochondrial specific loading of dhRhod-2. This was opposite to Rhod-2/mitotracker, which had a correlation index closer to 0, indicating only partial mitochondrial localization but mostly spread throughout the cytosol. As previously stated, Rhod-2 is a low affinity Ca^{2+} indicator, and increased mitochondrial specificity is achieved when reducing Rhod-2 to dhRhod-2. The reduced dhRhod-2 form of the indicator is reactive to mitochondrial reactive oxidative species (**Supplementary Figure 1**), which allows it to be re-oxidized to Rhod-2 specifically in the mitochondria (Bowser et al., 1998). This means that any un-oxidized dhRhod-2 in the cytosol, cannot respond to changes in $[Ca^{2+}]$, making it a useful indicator for specifically measuring mitochondrial Ca^{2+}. Trollinger et al. (1997) was the first group to show "cold loading" of Rhod-2 resulted in mitochondrial localization in adult rabbit cardiomyocytes. They also reported warm loading favors cytosolic dye retention, which can ultimately contaminate mitochondrial Ca^{2+} signals. This is contrary to the present study, where myocytes were loaded with dhRhod-2 at 37°C and imaged within 2 h. Our data showed strong mitochondrial localization whereby cytosolic contamination was negligible. This was also supported by our findings in permeabilized myocytes loaded with dhRhod-2 (**Supplementary Figure 2**), which still retain mitochondrial distribution in the absence of an intact cell membrane and subsequent removal of cytosolic contents.

Response of $[Ca^{2+}]_{mito}$ to Pharmacological Interventions

Response to High Dose of Caffeine

Upon validation of mitochondrial specific Ca^{2+} signals, myocytes were loaded with dhRhod-2 following the protocol in section "Loading of Rhod-2 and Di-HydroRhod-2." Myocytes were bathed in 1 mM Ca^{2+} Tyrode's, then imaged as stated in section "Live Cell Confocal Imaging." Images of myocytes were captured at baseline and during exposure to two pharmacological interventions. The response to caffeine was tested to further validate mitochondrial loading. Rhod-2 has a Ca^{2+} dissociation constant (K_d) of 570 nM as opposed to cytosolic Ca^{2+} indicators (i.e., Fura-2), which has a K_d of 140 nM, therefore, Rhod-2 has a lower the affinity for Ca^{2+}. This makes it useful for compartmentalization into areas with higher Ca^{2+} concentrations relative to the cytosol. The cytosol has a low diastolic $[Ca^{2+}]$ of 100 nM, which can increase up to 1 μM at the peak of the $[Ca^{2+}]_{cyto}$ transient (Bers, 2000). These values are similar to that of the mitochondrial matrix, where reported measurements of free $[Ca^{2+}]$ were in the range of 100–200 nM at lower stimulation frequencies, and around 500–800 nM with β-adrenergic stimulation (Finkel et al., 2015). However, intra-SR free $[Ca^{2+}]$ can reach up to concentrations of 1–1.5 mM at the end of diastole (Shannon et al., 2003). Therefore, to test whether Rhod-2 was compartmentalizing in areas of high $[Ca^{2+}]$, it was important to acknowledge potential loading of dhRhod-2 in SR. In order to test whether dhRhod-2 was loading in the SR, loaded myocytes were subjected to 20 mM caffeine (**Figure 4**). Caffeine increases the opening probability of the ryanodine (RyR2) receptors on the SR membrane, and at high concentrations it completely releases SR Ca^{2+} contents into the cytosol and in its continued presence, prevents further SR Ca^{2+} accumulation (Bassani et al., 1992). This was evident in **Figures 4A–G**, as Rhod-2 loading resulted in an approximately fourfold increase in fluorescence upon exposure to 20 mM caffeine. The Rhod-2

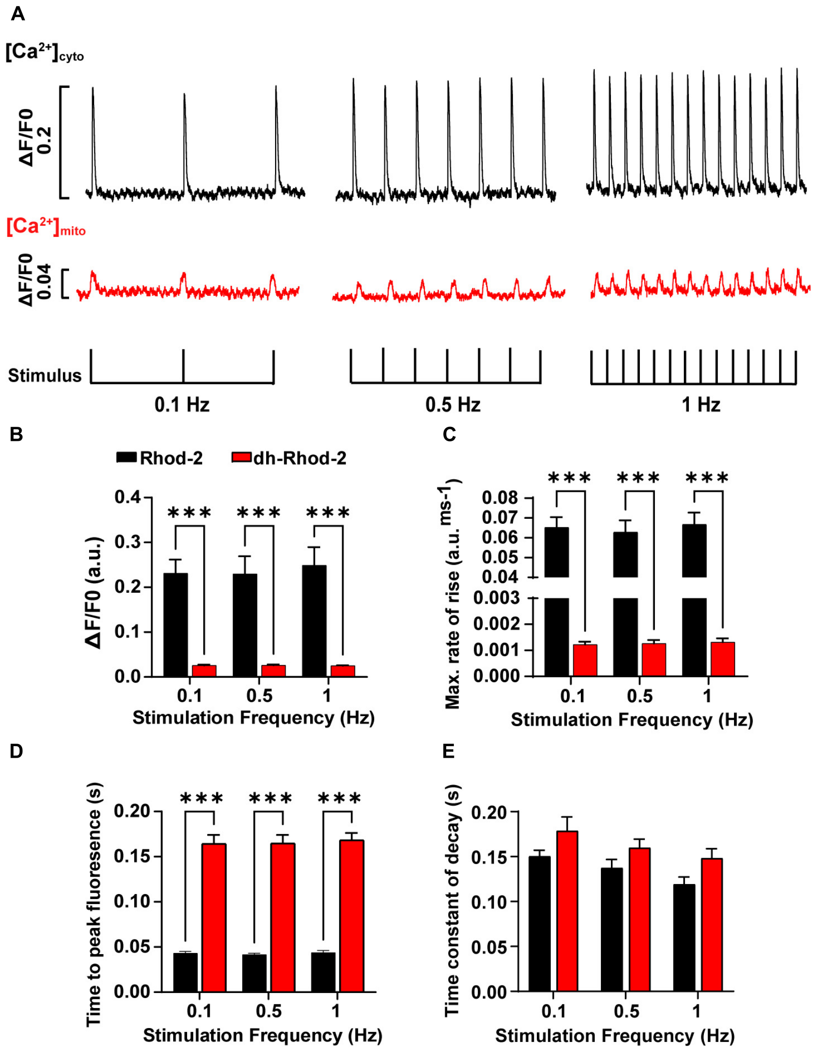

FIGURE 7 | Comparison of amplitudes and time courses between Rhod-2 and di-hydroRhod-2 calcium transients recorded at different stimulation frequencies. **(A)** Shows recordings from two representative myocytes loaded with Rhod-2 (black, $[Ca^{2+}]_{cyto}$ transients) and di-hydroRhod-2 (dhRhod-2, red, $[Ca^{2+}]_{mito}$ transients). Myocytes were super-perfused with 1.5 mM Ca^{2+} Tyrode's containing 150 μM spermine and 1 μM isoproterenol and externally stimulated at 0.1, 0.5, and 1 Hz. The transient amplitude is a represented as a ratio of the change in fluorescence/diastolic fluorescence (ΔF/F0). **(B)** Shows the mean Rhod-2 (black, $[Ca^{2+}]$cyto) and dhRhod-2 (red, $[Ca^{2+}]_{mito}$) transient amplitude expressed as ΔF/F0 at various stimulation frequencies. **(C,D)** Show the mean maximum rate of rise and time to peak fluorescence, respectively, while **(E)** displays the mean time constant of decay (tau) between groups and stimulation frequencies. Data from **(B–E)** were collected from *N* = 3 healthy rat hearts (*n* = 7 Rhod-2 and *n* = 11 dhRhod-2 loaded myocytes). Results are expressed as mean ± SEM, ****P* < 0.001.

loaded myocyte in **Figure 4A** also displayed Ca^{2+} sparks at baseline, which were not present in the dhRhod-2 loaded myocyte (**Figure 4B**). This is further evidence of Rhod-2 cytosolic loading, and absence of cytosolic dhRhod-2. Furthermore, the distinct peaks and troughs that are evident in the intensity plot profile of Rhod-2 in response to caffeine (**Figure 4E**) could also be a result of mitochondrial Ca^{2+} release superimposed with SR Ca^{2+} release. This confirms Rhod-2 was present in both the mitochondria and cytosol. Contrary to these findings, there was no change in dhRhod-2 fluorescence in response to caffeine (**Figures 4B–G**), which suggests that dhRhod-2 is not loading in the SR. Andrienko et al. (2009) also found SR depletion by caffeine terminated $[Ca^{2+}]_{mito}$ uptake. However, rapid emptying of the SR is still able to cause a small increase in mitochondrial Ca^{2+} reuptake as cytosolic Ca^{2+} reaches saturating concentrations, which activates the MCU and brings in Ca^{2+} in an attempt to reduce $[Ca^{2+}]_{cyto}$ (Sharma et al., 2000).

Response to β-Adrenergic Stimulation

The second intervention that was tested was the non-selective β-adrenergic agonist isoproterenol (ISO, 1 μM). The response to ISO was tested in order to determine whether MCU uptake was enhanced with β-adrenergic stimulation. **Figures 5A,B,D** shows application of ISO increased dhRhod-2 fluorescence intensity (mean ± SEM, 88.2 ± 17.6 a.u.) in comparison to baseline (45.0 ± 8.6 a.u.), confirming ISO augmented MCU Ca^{2+} uptake.

These findings are supported by Robert et al. (2001) who found that ISO increased $[Ca^{2+}]_{mito}$ transient amplitudes and frequencies in neonatal cultured myocytes, and (Finkel et al., 2015), who reported a fourfold increase in free matrix $[Ca^{2+}]$ in response to β-adrenergic stimulation *in situ*. Furthermore, the ISO-stimulated increase in dhRhod-2 fluorescence was abolished in Ru265 pre-treated cells (**Figures 5C,D**). Ru265 is a newly reported ruthenium based selective MCU inhibitor (Woods et al., 2019; Novorolsky et al., 2020), which is a structural analog of the commonly used MCU inhibitor Ru360 (Novorolsky et al., 2020). **Figure 5D** shows baseline fluorescence was unchanged in Ru265 pre-treated cardiomyocytes, which was expected as dhRhod-2 baseline signals were generally low, and cells were loaded with dhRhod-2 prior to pre-treatment with Ru265 (refer to section "Loading of Rhod-2 and Di-HydroRhod-2" and "Live Cell Confocal Imaging"). However, Ru265 inhibited MCU activity in the presence of ISO, as MCU activity normally becomes upregulated and $[Ca^{2+}]_{mito}$ uptake increases when $[Ca^{2+}]_{cyto}$ is high (i.e., with ISO exposure, as seen in **Figures 5A,B**). Similar findings were described in studies investigating cardiomyocytes subjected to the ruthenium based MCU blocker Ru360 (Maack et al., 2006; Liu and O'Rourke, 2008). However, Ru360 has reportedly been found to be impermeable to the cell membrane (Robert et al., 2001), therefore they are best suited when applied directly into the myocyte or exposed to isolated mitochondria and cells with permeabilized membranes. Ru265 is cell permeable and non-disruptive to cytosolic Ca^{2+} dynamics (Novorolsky et al., 2020), which makes it suitable for MCU inhibition upon incubation in intact cardiomyocytes. Overall, enhanced dhRhod-2 fluorescence during exposure to β-adrenergic highlights the importance of MCU Ca^{2+} uptake during increased workloads, which plays a key role in enhancing the rate of ATP production to fuel ATP transporters during faster rates of EC coupling.

Fluorometric Measurements of $[Ca^{2+}]_{mito}$ vs. $[Ca^{2+}]_{cyto}$

Using confocal microscopy, we were able to confirm localized dhRhod-2 loading (**Figure 3**). We were also able to confirm gradual enhancement of mitochondrial Ca^{2+} uptake with β-adrenergic stimulation (**Figure 5**). Next, we: (i) determined the characteristics of the mitochondrial Ca^{2+} transient relative to the cytosolic Ca^{2+} transient, and (ii) recorded beat-to-beat mitochondrial Ca^{2+} fluxes at different stimulation frequencies. Fluorometric measurements were made from cardiac myocytes loaded with dhRhod-2 to determine beat-to-beat changes in mitochondrial Ca^{2+} fluxes. This could not be achieved using confocal microscopy as these events occur at a timescale beyond the temporal acquisition rate. Faster changes in signal can be obtained in a smaller region of the myocyte using line scans. However, line scanning only captures a single region of the myocyte, which is insufficient when measuring a small change in mitochondrial Ca^{2+} flux. Imaging of the whole myocyte can be done (as discussed in section "Live Cell Confocal Imaging"), but only with a slower acquisition rate. Any changes that might occur < 300 ms apart cannot be detected due to limited temporal resolution. Therefore, we have developed a technique for fluorometric measurements of $[Ca^{2+}]_{mito}$ transients, which can capture changes that occur on a faster time scale (i.e., between 50 and 300 ms). Using a spectrofluorometric system, we acquired rapid changes in mitochondrial Ca^{2+} on a beat-to-beat basis (see section "Fluorometric Measurements in Live Myocytes"). A window was fitted around the perimeter of a single cell, which allowed for $[Ca^{2+}]_{mito}$ measurements across the whole cell (i.e., a "global" change).

Figure 6A shows a single $[Ca^{2+}]_{mito}$ transient superimposed with a single $[Ca^{2+}]_{cyto}$ transient. The $[Ca^{2+}]_{mito}$ transient had a smaller amplitude relative to the $[Ca^{2+}]_{cyto}$ transient. Interestingly, the $[Ca^{2+}]_{mito}$ also showed a slower time to peak fluorescence. When considering the kinetics of a $[Ca^{2+}]_{cyto}$ transient, the time to peak fluorescence occurs approximately 30–60 ms after the stimulus (Shannon et al., 2000; Dibb et al., 2007). This was evident in **Figure 6B**, which shows a single Fura-2 (ratiometric) $[Ca^{2+}]_{cyto}$ transient superimposed with a single Rhod-2 (non-ratiometric) $[Ca^{2+}]_{cyto}$ transient. The kinetics between Rhod-2 and Fura-2 transients were almost identical, which suggested that Rhod-2 was a suitable measure of cytosolic $[Ca^{2+}]$ for comparison to dhRhod-2 $[Ca^{2+}]_{mito}$ transients. **Figure 6A** shows MCU uptake begins to rise once the $[Ca^{2+}]_{cyto}$ transient has peaked, then it begins to decline at approximately 70–80% of the $[Ca^{2+}]_{cyto}$ transient decay. This is evidence that MCU uptake begins when intracellular $[Ca^{2+}]$ is highest (i.e., at the peak of the $[Ca^{2+}]_{cyto}$ transient) and then begins to decline as cytosolic Ca^{2+} approaches diastolic levels. This supports original findings from Isenberg et al. (1993), who showed peak $[Ca^{2+}]_{mito}$ occurred 40 ms after the start of systole and a subsequent decline in $[Ca^{2+}]_{mito}$ 95 ms after the start of systole. Studies using adenoviral probes targeted to the mitochondria also reported similar findings. For example, Robert et al. (2001) found beat-to-beat oscillations in cultured neonatal rat myocytes, whereby $[Ca^{2+}]_{cyto}$ peaked at 50–100 ms and $[Ca^{2+}]_{mito}$ peaked 100–150 ms after. Furthermore, in cultured rat adult myocytes, Bell et al. (2006) also observed $[Ca^{2+}]_{mito}$ transients at a cytosolic $[Ca^{2+}]$ of 0.9 μM, which is equivalent to the peak $[Ca^{2+}]_{cyto}$ transient at systole. These data are in contrast to a study by Maack et al. (2006) showing peak $[Ca^{2+}]_{mito}$ preceded peak $[Ca^{2+}]_{cyto}$ in isolated guinea pig myocytes. However, Maack et al. (2006) made measurements at 37°C as opposed to the present study where experiments were performed at 23°C, but it is not clear how a difference in temperature could account for the difference in transient kinetics. Unlike Maack et al. (2006), we could not record simultaneous Ca^{2+} transient events. However, we were able to compare the kinetics of Rhod-2 $[Ca^{2+}]_{mito}$ to $[Ca^{2+}]_{cyto}$ transients in separate myocytes as we used the same indicator, which allowed direct comparison without variability in the fluorophore binding kinetics. Collectively, our findings provide further evidence that mitochondrial Ca^{2+} fluxes occur during EC coupling, and are therefore able to regulate mitochondrial metabolism on a beat-to-beat basis.

Mitochondrial Ca^{2+} Transients and Stimulation Frequency

Once we were able to determine the characteristics of a single mitochondrial Ca^{2+} transient, the next aim was to record beat-to-beat mitochondrial Ca^{2+} fluxes at different stimulation frequencies. As mentioned above, we were able to do this using a spectrofluorometric system (see section "Fluorometric Measurements in Live Myocytes"). Cells were super-fused with 1.5 mM Ca^{2+} Tyrodes containing 1 μM ISO and 150 μM spermine (MCU agonist) and externally stimulated at frequencies of 0.1, 0.5, and 1 Hz until steady state was achieved. Fluorescence traces from representative myocytes in **Figure 7A** shows both $[Ca^{2+}]_{mito}$ and $[Ca^{2+}]_{cyto}$ transients occurred in response to each applied stimulus. Cytosolic Ca^{2+} transient amplitudes were larger, with faster maximum rates of rise and time to peak fluorescence (**Figures 7B–D**) relative to $[Ca^{2+}]_{mito}$ transients at all stimulation frequencies tested. Robert et al. (2001) showed similar trends in $[Ca^{2+}]_{mito}$ transient kinetics and amplitudes to the present study. However, they also found $[Ca^{2+}]_{mito}$ transient amplitudes increased with changes in $[Ca^{2+}]_{cyto}$ transient amplitudes and frequencies. Whereas Maack et al. (2006) reported no differences between $[Ca^{2+}]_{cyto}$ and $[Ca^{2+}]_{mito}$ transient amplitudes, and stated that an increased stimulation frequency would reduce $[Ca^{2+}]_{mito}$ transient amplitudes as a result of diastolic $[Ca^{2+}]_{mito}$ accumulation, which was subsequently confirmed in studies by Wüst et al. (2017) and Miranda-Silva et al. (2020). Each of these findings are contradictory to the results in the present study, as there were no evident changes in $[Ca^{2+}]_{mito}$ transient amplitude or kinetics with increasing stimulation frequency. This could be due to species differences, as Maack et al. (2006) measured $[Ca^{2+}]_{mito}$ and $[Ca^{2+}]_{cyto}$ transients in guinea pig isolated myocytes, or due to differences in $[Na^+]_i$, as they maintained $[Na^+]_i$ *via* an internal patch solution. None of the three studies had spermine present in their buffers, which could have also contributed to the differences in the response of $[Ca^{2+}]_{mito}$ to increasing stimulation frequencies. It is also important to acknowledge the effect of different experimental conditions, as increased stimulation frequencies are often associated with an increase in $[Ca^{2+}]_{cyto}$ transient amplitude at physiological temperatures (Dibb et al., 2007). In the present study, the experimental conditions limited the physiological response of $[Ca^{2+}]_{cyto}$ to increasing stimulation frequencies, as 0.1–1 Hz is considerably slow for rat myocytes. These conditions would also presumably affect the size and kinetics of the $[Ca^{2+}]_{mito}$ transient between frequencies, as we saw no differences in the time constant of decay between $[Ca^{2+}]_{cyto}$ and $[Ca^{2+}]_{mito}$ transients at all stimulation frequencies (**Figure 7E**). However, a study by Isenberg et al. (1993) revealed no changes in decay rate between $[Ca^{2+}]_{cyto}$ and $[Ca^{2+}]_{mito}$ transients, and stated that mitochondrial Ca^{2+} uptake contributes to the fast $[Ca^{2+}]_{cyto}$ transient decay. Therefore, the mitochondria act as a buffer and take up Ca^{2+} at peak $[Ca^{2+}]_{cyto}$, then release it once $[Ca^{2+}]_{cyto}$ reaches diastolic levels. This was also evident in our $[Ca^{2+}]_{mito}$ data presented in **Figure 6A**. Robert et al. (2001) reported slightly slower time constants of decay for $[Ca^{2+}]_{mito}$ transients (200–300 ms) compared to that of the present study. However, they acknowledge difficulties in measuring $[Ca^{2+}]_{mito}$ transient kinetics as aequorin systems cannot detect changes with high temporal resolution. Therefore, the use of spectrofluorometric systems has the advantage of detecting rapid changes in $[Ca^{2+}]_{mito}$ transient kinetics that might have been misinterpreted in past studies due to acquisition limitations.

In this study, fluorometric measurements of $[Ca^{2+}]_{mito}$ transients were enhanced by the presence of ISO and spermine, as baseline $[Ca^{2+}]_{mito}$ transients could not obtained. This could have suppressed the response of $[Ca^{2+}]_{mito}$ to increasing stimulation frequencies, as the SR may have already been at capacity. However, it is known that the MCU is mostly active at higher cytosolic $[Ca^{2+}]$ (i.e., during β-adrenergic stimulation) as it is a low affinity transporter, therefore basal MCU activity is limited at resting levels of cytosolic Ca^{2+} (Andrienko et al., 2009). An additional limitation to the present study is that Rhod-2 loading was compared to dhRhod-2 loading in the absence of cytosolic quenchers, which were previously used in studies reporting $[Ca^{2+}]_{mito}$ with cytosolic ratiometric indicator Indo-1AM (Miyata et al., 1991; Zhou et al., 1998). The addition of cytosolic quenchers would be required for Rhod-2 measurements of $[Ca^{2+}]_{mito}$. However, it would require further investigation to confirm that the specific quencher has no effect on mitochondrial Ca^{2+} signals. Therefore, the benefit of dhRhod-2 loading is that it does not require quenching of cytosolic dye, as it relies on mitochondrial oxidation to provide specific mitochondrial Ca^{2+} signals. Overall, despite these limitations, the methods presented in this study are suitable for analyzing relative changes in mitochondrial Ca^{2+} fluxes in live myocytes.

CONCLUSION

Myocytes loaded with di-hydroRhod-2 revealed mitochondrial localization of the Ca^{2+} fluorophore in the absence of cytosolic contamination such as that seen in Rhod-2 loaded cardiac myocytes. Di-hydroRhod-2 $[Ca^{2+}]_{mito}$ transients were distinct from the large and rapid Rhod-2 $[Ca^{2+}]_{cyto}$ transients, indicating that the kinetics between $[Ca^{2+}]_{cyto}$ and $[Ca^{2+}]_{mito}$ transients are considerably different. Overall, our results showed that di-hydroRhod-2 loading is a quick and suitable method for measuring beat-to-beat $[Ca^{2+}]_{mito}$ transients in intact myocytes. Furthermore, this method could also be used to measure changes in mitochondrial Ca^{2+} handling in intact diseased myocytes.

DATA AVAILABILITY STATEMENT

The raw data supporting the conclusions of this article will be made available by the authors, without undue reservation.

ETHICS STATEMENT

The animal study was reviewed and approved by the University of Auckland Animal Ethics Committee (AEC: 001929).

AUTHOR CONTRIBUTIONS

M-LW and AP conceived the study. AK performed the experiments and data analysis. AK and M-LW drafted the article. AK, AP, and M-LW performed the critical revision of the article for important intellectual content. All authors contributed to the article and approved the submitted version.

FUNDING

This research was funded by grants from the Auckland Medical Research Foundation (Project 1118006 to M-LW) and the Maurice and Phyllis Paykel Trust (Project 3721278 to M-LW). AK was the recipient of a University of Auckland Health Research Doctoral Scholarship and AP received a Kate Edgar Educational Charitable Trust Post-doctoral Research Award and a Heart Foundation Fellowship (Research Fellowship 1873).

SUPPLEMENTARY MATERIAL

The Supplementary Material for this article can be found online at: https://www.frontiersin.org/articles/10.3389/fphys.2021.808798/full#supplementary-material

REFERENCES

Andrienko, T. N., Picht, E., and Bers, D. M. (2009). Mitochondrial free calcium regulation during sarcoplasmic reticulum calcium release in rat cardiac myocytes. *J. Mol. Cell. Cardiol.* 46, 1027–1036. doi: 10.1016/j.yjmcc.2009.03.015

Bassani, R. A., Bassani, J. W., and Bers, D. M. (1992). Mitochondrial and sarcolemmal Ca2+ transport reduce [Ca2+]i during caffeine contractures in rabbit cardiac myocytes. *J. Physiol.* 453, 591–608. doi: 10.1113/jphysiol.1992.sp019246

Bell, C. J., Bright, N. A., Rutter, G. A., and Griffiths, E. J. (2006). ATP regulation in adult rat cardiomyocytes: time-resolved decoding of rapid mitochondrial calcium spiking imaged with targeted photoproteins. *J. Biol. Chem.* 281, 28058–28067. doi: 10.1074/jbc.M604540200

Bers, D. (2001). *Excitation-Contraction Coupling and Cardiac Contractile Force*, Vol. 237. Dordrecht: Springer.

Bers, D. M. (2000). Calcium fluxes involved in control of cardiac myocyte contraction. *Circ. Res.* 87, 275–281. doi: 10.1161/01.RES.87.4.275

Bolte, S., and Cordelieres, F. P. (2006). A guided tour into subcellular colocalisation analysis in light microscopy. *J. Microsc.* 224, 213–232. doi: 10.1111/j.1365-2818.2006.01706.x

Bowser, D. N., Minamikawa, T., Nagley, P., and Williams, D. A. (1998). Role of mitochondria in calcium regulation of spontaneously contracting cardiac muscle cells. *Biophys. J.* 75, 2004–2014. doi: 10.1016/S0006-3495(98)77642-8

Brandes, R., and Bers, D. M. (1997). Intracellular Ca2+ increases the mitochondrial NADH concentration during elevated work in intact cardiac muscle. *Circ. Res.* 80, 82–87. doi: 10.1161/01.RES.80.1.82

Dibb, K. M., Eisner, D. A., and Trafford, A. W. (2007). Regulation of systolic [Ca2+]i and cellular Ca2+ flux balance in rat ventricular myocytes by SR Ca2+, L-type Ca2+ current and diastolic [Ca2+]i. *J. Physiol.* 585(Pt 2), 579–592. doi: 10.1113/jphysiol.2007.141473

Else, P. L., and Hulbert, A. J. (1985). Mammals: an allometric study of metabolism at tissue and mitochondrial level. *Am. J. Physiol. Regul. Integr. Comp. Physiol.* 248, R415–R421. doi: 10.1152/ajpregu.1985.248.4.R415

Fazal, L., Laudette, M., Paula-Gomes, S., Pons, S., Conte, C., Tortosa, F., et al. (2017). Multifunctional mitochondrial Epac1 controls myocardial cell death. *Circ. Res.* 120, 645–657. doi: 10.1161/CIRCRESAHA.116.309859

Finkel, T., Menazza, S., Holmström, K. M., Parks, R. J., Liu, J., Sun, J., et al. (2015). The Ins and Outs of Mitochondrial Calcium. *Circ. Res.* 116, 1810–1819. doi: 10.1161/CIRCRESAHA.116.305484

Hajnóczky, G., Robb-Gaspers, L. D., Seitz, M. B., and Thomas, A. P. (1995). Decoding of cytosolic calcium oscillations in the mitochondria. *Cell* 82, 415–424. doi: 10.1016/0092-8674(95)90430-1

Halestrap, A. P., and Pasdois, P. (2009). The role of the mitochondrial permeability transition pore in heart disease. *Biochim. Biophys. Acta* 1787, 1402–1415. doi: 10.1016/j.bbabio.2008.12.017

Hamilton, S., Terentyeva, R., Kim, T. Y., Bronk, P., Clements, R. T., and Terentyev, D. (2018). Pharmacological Modulation of Mitochondrial Ca(2+) Content Regulates Sarcoplasmic Reticulum Ca(2+) Release *via* Oxidation of the Ryanodine Receptor by Mitochondria-Derived Reactive Oxygen Species. *Front. Physiol.* 9:1831. doi: 10.3389/fphys.2018.01831

Hamilton, S., Terentyeva, R., Perger, F., Hernández Orengo, B., Martin, B. Y., Gorr, M. W., et al. (2021). MCU overexpression evokes disparate dose-dependent effects on mito-ROS and spontaneous Ca2+ release in hypertrophic rat cardiomyocytes. *Am. J. Physiol. Heart Circ.* 321, H615–H632. doi: 10.1152/ajpheart.00126.2021

Isenberg, G., Han, S., Schiefer, A., and Wendt-Gallitelli, M.-F. (1993). Changes in mitochondrial calcium concentration during the cardiac contraction cycle. *Cardiovasc. Res.* 27, 1800–1809. doi: 10.1093/cvr/27.10.1800

Keith, A., and Flack, M. (1907). The form and nature of the muscular connections between the primary divisions of the vertebrate heart. *J. Anat. Physiol.* 41(Pt 3), 172.

Liu, T., and O'Rourke, B. (2008). Enhancing mitochondrial Ca^{2+} uptake in myocytes from failing hearts restores energy supply and demand matching. *Circ. Res.* 103, 279–288. doi: 10.1161/CIRCRESAHA.108.175919

Maack, C., Cortassa, S., Aon, M. A., Ganesan, A. N., Liu, T., and O'Rourke, B. (2006). Elevated Cytosolic Na+ Decreases Mitochondrial Ca2+ uptake during excitation-contraction coupling and impairs energetic adaptation in cardiac myocytes. *Circ. Res.* 99, 172–182. doi: 10.1161/01.RES.0000232546.92777.05

Maack, C., and O'Rourke, B. (2007). Excitation-contraction coupling and mitochondrial energetics. *Basic Res. Cardiol.* 102, 369–392. doi: 10.1007/s00395-007-0666-z

Miranda-Silva, D., Wüst, R. C. I., Conceição, G., Gonçalves-Rodrigues, P., Gonçalves, N., Gonçalves, A., et al. (2020). Disturbed cardiac mitochondrial and cytosolic calcium handling in a metabolic risk-related rat model of heart failure with preserved ejection fraction. *Acta Physiol.* 228:e13378. doi: 10.1111/apha.13378

Miyata, H., Silverman, H. S., Sollott, S. J., Lakatta, E. G., Stern, M. D., and Hansford, R. G. (1991). Measurement of mitochondrial free Ca2+ concentration in living single rat cardiac myocytes. *Am. J. Physiol. Heart Circ.* 261, H1123–H1134. doi: 10.1152/ajpheart.1991.261.4.H1123

Neubauer, S. (2007). The Failing Heart — An Engine Out of Fuel. *N. Engl. J. Med.* 356, 1140–1151. doi: 10.1056/NEJMra063052

Nicchitta, C. V., and Williamson, J. R. (1984). Spermine. A regulator of mitochondrial calcium cycling. *J. Biol. Chem.* 259, 12978–12983. doi: 10.1016/S0021-9258(18)90643-5

Novorolsky, R. J., Nichols, M., Kim, J. S., Pavlov, E. V., Wilson, J. J., and Robertson, G. S. (2020). The cell-permeable mitochondrial calcium uniporter inhibitor Ru265 preserves cortical neuron respiration after lethal oxygen glucose deprivation and reduces hypoxic/ischemic brain injury. *J. Cereb. Blood Flow Metab.* 40, 1172–1181. doi: 10.1177/0271678x20908523

Oropeza-Almazán, Y., and Blatter, L. A. (2020). Mitochondrial calcium uniporter complex activation protects against calcium alternans in atrial myocytes. *Am. J. Physiol. Heart Circ. Physiol.* 319, H873–H881. doi: 10.1152/ajpheart.00375.2020

Plovanich, M., Bogorad, R. L., Sancak, Y., Kamer, K. J., Strittmatter, L., Li, A. A., et al. (2013). MICU2, a Paralog of MICU1, resides within the mitochondrial uniporter complex to regulate calcium handling. *PLoS One* 8:e55785. doi: 10.1371/journal.pone.0055785

Rizzuto, R., Brini, M., Murgia, M., and Pozzan, T. (1993). Microdomains with high Ca2+ close to IP3-sensitive channels that are sensed by neighboring mitochondria. *Science* 262, 744–747. doi: 10.1126/science.8235595

Robert, V., Gurlini, P., Tosello, V., Nagai, T., Miyawaki, A., Di Lisa, F., et al. (2001). Beat-to-beat oscillations of mitochondrial [Ca2+] in cardiac cells. *EMBO J.* 20, 4998–5007. doi: 10.1093/emboj/20.17.4998

Shannon, T. R., Ginsburg, K. S., and Bers, D. M. (2000). Potentiation of fractional sarcoplasmic reticulum calcium release by total and free intra-sarcoplasmic reticulum calcium concentration. *Biophys. J.* 78, 334–343. doi: 10.1016/s0006-3495(00)76596-9

Shannon, T. R., Guo, T., and Bers, D. M. (2003). Ca2+ scraps: local depletions of free [Ca2+] in cardiac sarcoplasmic reticulum during contractions leave substantial Ca2+ reserve. *Circ. Res.* 93, 40–45. doi: 10.1161/01.RES.0000079967.11815.19

Sharma, V. K., Ramesh, V., Franzini-Armstrong, C., and Sheu, S. S. (2000). Transport of Ca2+ from sarcoplasmic reticulum to mitochondria in rat ventricular myocytes. *J. Bioenerg. Biomembr.* 32, 97–104. doi: 10.1023/A:1005520714221

Trollinger, D. R., Cascio, W. E., and Lemasters, J. J. (1997). Selective Loading of Rhod 2 into mitochondria shows mitochondrial Ca2+transients during the contractile cycle in adult rabbit cardiac Myocytes. *Biochem. Biophys. Res. Commun.* 236, 738–742. doi: 10.1006/bbrc.1997.7042

Wilson, D. F. (2017). Oxidative phosphorylation: regulation and role in cellular and tissue metabolism. *J. Physiol.* 595, 7023–7038. doi: 10.1113/JP273839

Woods, J., Nemani, N., Shanmughapriya, S., Kumar, A., Zhang, M., Nathan, S. R., et al. (2019). A Selective and Cell-Permeable Mitochondrial Calcium Uniporter (MCU) inhibitor preserves mitochondrial bioenergetics after hypoxia/reoxygenation injury. *ACS Cent. Sci.* 5, 153–166. doi: 10.1021/acscentsci.8b00773

Wüst, R. C., Helmes, M., Martin, J. L., van der Wardt, T. J., Musters, R. J., van der Velden, J., et al. (2017). Rapid frequency-dependent changes in free mitochondrial calcium concentration in rat cardiac myocytes. *J. Physiol.* 595, 2001–2019. doi: 10.1113/jp273589

Zhou, Z., Matlib, M. A., and Bers, D. M. (1998). Cytosolic and mitochondrial Ca2+ signals in patch clamped mammalian ventricular myocytes. *J. Physiol.* 507, 379–403. doi: 10.1111/j.1469-7793.1998.379bt.x

Conflict of Interest: The authors declare that the research was conducted in the absence of any commercial or financial relationships that could be construed as a potential conflict of interest.

frontiers
in Physiology

REVIEW
published: 27 January 2022
doi: 10.3389/fphys.2021.817036

Force Measurements From Myofibril to Filament

*Steven Marston**

NHLI, Imperial College London, London, United Kingdom

Contractility, the generation of force and movement by molecular motors, is the hallmark of all muscles, including striated muscle. Contractility can be studied at every level of organization from a whole animal to single molecules. Measurements at sub-cellular level are particularly useful since, in the absence of the excitation-contraction coupling system, the properties of the contractile proteins can be directly investigated; revealing mechanistic details not accessible in intact muscle. Moreover, the conditions can be manipulated with ease, for instance changes in activator Ca^{2+}, small molecule effector concentration or phosphorylation levels and introducing mutations. Subcellular methods can be successfully applied to frozen materials and generally require the smallest amount of tissue, thus greatly increasing the range of possible experiments compared with the study of intact muscle and cells. Whilst measurement of movement at the subcellular level is relatively simple, measurement of force is more challenging. This mini review will describe current methods for measuring force production at the subcellular level including single myofibril and single myofilament techniques.

Keywords: contractility, myofibril contractility, thick filament, thin filament, tension measurement

Edited by:
Peter T. Wright,
University of Roehampton,
United Kingdom

Reviewed by:
Chiara Tesi,
University of Florence, Italy
Douglas M. Swank,
Rensselaer Polytechnic Institute,
United States

****Correspondence:***
Steven Marston
s.marston@imperial.ac.uk

Specialty section:
This article was submitted to
Striated Muscle Physiology,
a section of the journal
Frontiers in Physiology

Received: *17 November 2021*
Accepted: *21 December 2021*
Published: *27 January 2022*

Citation:
Marston S (2022) Force
Measurements From Myofibril
to Filament.
Front. Physiol. 12:817036.
doi: 10.3389/fphys.2021.817036

INTRODUCTION

The production of force and movement by molecular motors is the essence of contractility. To understand the basic mechanisms of contraction and Ca^{2+} regulation we need to isolate the contractile elements from the physiological Excitation-Contraction (EC) system and from other, mainly parallel, mechanical elements that are present in whole muscle.

Contractility is usually measured in intact small muscle strips or single myocytes where contractility is dependent on the EC coupling system and neural and humoral stimulation that act on the Ca^{2+}-regulation of the contractile apparatus itself. Chemically skinned muscle offers a way to study Ca^{2+} regulation of contractility in isolation from EC coupling but retains confounding effects of parallel elasticity. Moreover, the usefulness of skinned fiber studies is limited by slow diffusion of solutes into the fiber that rules out dynamic measurements. We therefore need to study contractility at the subcellular level.

Contractility measurements at the sub cellular level in myofibrils and single filaments offer advantages that make their development worthwhile. Solution conditions are easy to manipulate and rapid (i.e., 10 ms) solution changing is possible since the solution diffuses rapidly into the myofibril so that the kinetics of the contractile response to rapid concentration jumps may be measured. There is no limitation on the source material that can be used and the quantities required are very small; myofibrils and myofilaments can be isolated from small samples (i.e., 20 mg) of muscle or cells. Fresh or frozen tissue are equally good sources and post-translational modifications can be changed or proteins substituted prior to measurement. Finally, since all measurements are made under the microscope it is possible to combine force measurements with additional video microscopy techniques such as observing sarcomeric structure dynamics and the turnover of fluorescent substrates.

To extend force measurements from muscle to single myofibrils or even single filaments requires a number of technological advances that were exceptional in the 1990s when these methods were first developed but have now become mainstream. Nevertheless, handling tiny samples is still challenging and is far from routine: whilst it is now easy to measure small forces, the problem of how to attach myofibrils and filaments to the measuring device is the greatest obstacle to high throughput experimentation.

In this review I will describe the current methodologies for single myofibril and single filament force measurements. At the time of writing none of the techniques described here can be bought as turnkey systems; to do such studies it is necessary to be able to build your own apparatus.

The principal of all force measurements is that the contractile element is attached to probes at both ends such that length changes can be imposed and force may be measured. The critical requirements for such measurements is that the contractile element is firmly attached to the probes and that the tension sensing probe be sufficiently compliant to enable probe movement to be translated into a signal yet sufficiently rigid that the contractile element is essentially isometric. The methods developed usually involve glass microneedles, AFM cantilevers or a stiff optical trap as the sensor. **Table 1** summarizes the various methods that have been published.

SINGLE MYOFIBRILS

Measurement of force in single myofibrils has become the main technique used to study contractility at the subcellular level. Iwazumi (1987) published the earliest studies on myofibril contraction based on an electromagnetic force transducer and this methodology was used by Friedman and Goldman (1996) with some success but low throughput. A more versatile technique for measuring force in single myofibrils, based on glass microneedles, was first described by Bartoo et al. (1993) and was developed by Colomo et al. (1997) for active force measurement and by Linke et al. (1997) for passive force measurement. The principle of using glass microneedles for force measurement was introduced by Kishino and Yanagida (1988). More recent accounts (Ayittey et al., 2009; Vikhorev et al., 2015) describe how to make and calibrate the bent microneedles capable of measuring force in the 0.1–0.3 μN range typical of single myofibrils. The prepared cantilever force probes have a compliance of 2–17 mm/mN when deflected by small forces pulling perpendicularly.

This methodology that has been adopted by a number of laboratories. An alternative measurement technique based on an AFM cantilever force detector produces broadly similar results (Stehle et al., 2002). The microneedle-based methodology was thoroughly documented by Vikhorev et al. (2015) see **Figure 1**. The heart of the instrument is the two microneedles. Myofibrils attach direct to glass and just touching the needle to the end of a myofibril results in firm adherence. In order to maximize the surface of myofibril attached to the probes they are manipulated to increase the myofibril wrapping around the microneedles. The tension transducer microneedle is crucial; the probe needs to be made in such a way that it is compliant enough to give sufficient bending under tension to be accurately measured in a position detector such as a split photodiode detector, yet stiff enough to keep the contracting muscle near isometric.

These force measurement methods are both sensitive and accurate, with high time resolution and low noise. They can be combined with rapid manipulation of length and uniquely can be used with fast solution changing and video microscopy of the sarcomere pattern, thus enabling a wide range of protocols that are not possible with large muscle preparations.

Rapid solution changing is the most important advantage of force measurements in myofibrils. Colomo et al. (1998) introduced the moving double-barreled pipette method that is almost universally used (**Figures 1E,F**). The time for solution switch to complete is less than 10 ms. Since the smallness of myofibrils means that there is no diffusional lag, the rates of crossbridge attachment on a Ca^{2+} jump can be measured and the time course of relaxation when Ca^{2+} is removed can be followed (**Figure 2**). The absence of diffusional lag can be demonstrated by measuring the rate of crossbridge attachment following a rapid release and re-stretch – K_{tr} (Tesi et al., 2002) which is found to equal the rate of tension increase on Ca^{2+} jump (**Figure 3A**). Rapid removal of Ca^{2+} in myofibrils has revealed a two phase relaxation process that could not be detected in skinned fibers even with caged EGTA (Johns et al., 1999). Multiple solution changes enable dose-response curves to be generated, for instance the Ca^{2+} activation curve (**Figure 3B**).

The basic measurement of myofibrillar contractility is the Ca^{2+} activation-relaxation cycle (**Figure 2**). Maximum isometric contraction is around 100 N/m^2. The contraction and relaxation transients represent fundamental processes of the contractile apparatus not measurable in larger preparations.

k_{ACT} represents the cross-bridge turnover rate which is determined by the dynamic equilibrium between the apparent rates with which cross bridges enter and leave the force generating states. It is dependent on the rate at which thin filaments are switched on by Ca^{2+} and is thus Ca^{2+} dependent (Vikhorev et al., 2014). Relaxation following a rapid drop in (Ca^{2+}) occurs in two phases. This pattern of results is only seen in myofibrils due to the rapid diffusion of Ca^{2+} away from the very small contractile element. Relaxation is initiated by Ca^{2+} dissociating from troponin C coupled to the release of the C-terminus of troponin I from troponin C and its attachment to actin, where it blocks cross-bridge binding cooperatively. The initial slow decrease in the force trace, defined by k_{LIN} and $t_{LIN,}$ has been ascribed to the time taken for the occupancy of cycling cross-bridges to drop below the threshold for cooperative activation of the thin filament, and the subsequent rapid-relaxation phase corresponds to the detachment of the remaining cross-bridges. t_{LIN} is shortened and k_{LIN} increased by high phosphate concentrations but lengthened by MgADP indicating

TABLE 1 | Techniques for single myofibril and single filament force measurements.

References	Attachment method	Force transducer
Myofibrils		
Bartoo et al., 1993	Silicone adhesive (Dow 3145 RTV)	Glass microneedle with split diode detector
Colomo et al., 1997	Myofibrils adhered directly to glass	Glass microneedle with split diode detector
Stehle et al., 2002	Silicon adhesive (Dow 3140 RTV)	Force modulation etched silicon probe-type atomic force cantilever (Nanosensors). Detected by the displacement of reflected beam
Pavlov et al., 2009	Glass microneedles inserted into myofibril	Microneedle movement detected by linear photodiode array (10,680 pixels)
Single filaments		
VanBuren et al., 1994a,b	Glass microneedle coated with HMM	Microneedle deflection detected by video microscopy
Holohan and Marston, 2005	Magnetic beads coated with gelsolin	Electromagnet and video microscopy
Kaya et al., 2017	Myosin/rod copolymer on glass surface, actin-biotin phalloidin TRITC attached to streptavidin coated bead	Optical trap detected by feedback needed to keep bead steady under load
Pertici et al., 2018	HMM on glass microfiber coated with nitrocellulose, actin attached to gelsolin coated bead	Optical trap detected by feedback needed to keep bead steady under load
Bing et al., 2000	a-actinin attached to cover glass	Indirect: quantity of a-actinin that stops actin filament movement
Cheng et al., 2020	Cantilever coated with a-actinin to specifically attach actin filament. Myosin adheres spontaneously	Microfabricated silicon nitride cantilever bending

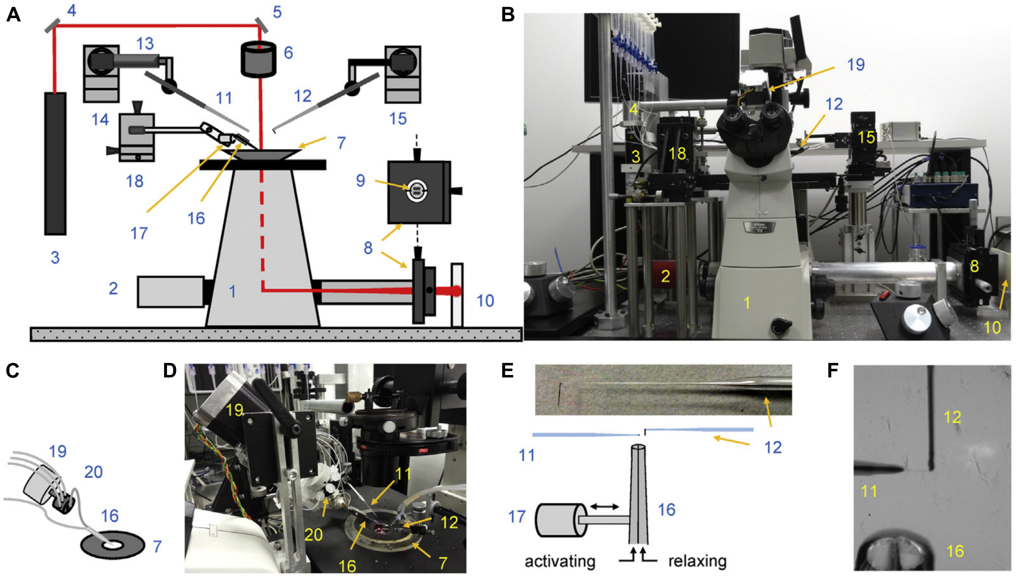

FIGURE 1 | Experimental setup. **(A,B)** Schematic overview **(A)** and photograph **(B)** show the key elements of the apparatus. **(C,D)** Schematics **(C)** and photograph **(D)** of multi-solution change system. **(E)** Schematics of cantilever and ultrafast solution change system. The left-sided microtool is relatively stiff and is mounted onto a piezo actuator for fast myofibril length change. The right-sided glass microtools is a high compliance L-shaped cantilever that acts as a force sensor. The inset shows a photograph showing the shape of the cantilever tip. **(F)** The photograph shows two microtools holding a small myofibril bundle. The relaxing and activating solutions are applied via the adjacent barrels of a double-barreled (Q) micropipette. The numbers on the figure indicate: 1, inverted microscope; 2, camera; 3, laser; 4 and 5, mirrors; 6, microscope condenser; 7, bath mounted onto a microscope stage; 8, XY positioning stage; 9, segmented photodiode; 10, projection plane for visual control of cantilever positioning; 11, left microtool; 12, right microtool (cantilever force sensor); 13, piezo actuator; 14 and 15, left and right micromanipulators for the positioning of left and right microtool, respectively; 16, double-barreled Q pipette; 17, stepper motor controlling the position of the double-barreled Q pipette; 18, XYZ positioning stage for the ultrafast two solutions switching system; 19, stepper motor controlling the valve opening of the eight-channel valve; 20, eight-channel valve. Reproduced from Vikhorev et al. (2015) with permission.

a close relationship of this process with the product release step of the crossbridge cycle (Tesi et al., 2002). The interpretation of the relaxation curve and its relationship to heterogeneous sarcomere lengthening was fully described by Stehle et al. (2009). Both k_{LIN}/t_{LIN} and k_{REL} are altered by physiological and pathological perturbations that affect thin filament relaxation rate such as cardiac TnI phosphorylation or HCM related mutations (Song et al., 2013; Vikhorev et al., 2014).

When fully implemented, the myofibril contractility method allows a wide range of measurement possibilities. Mechanical

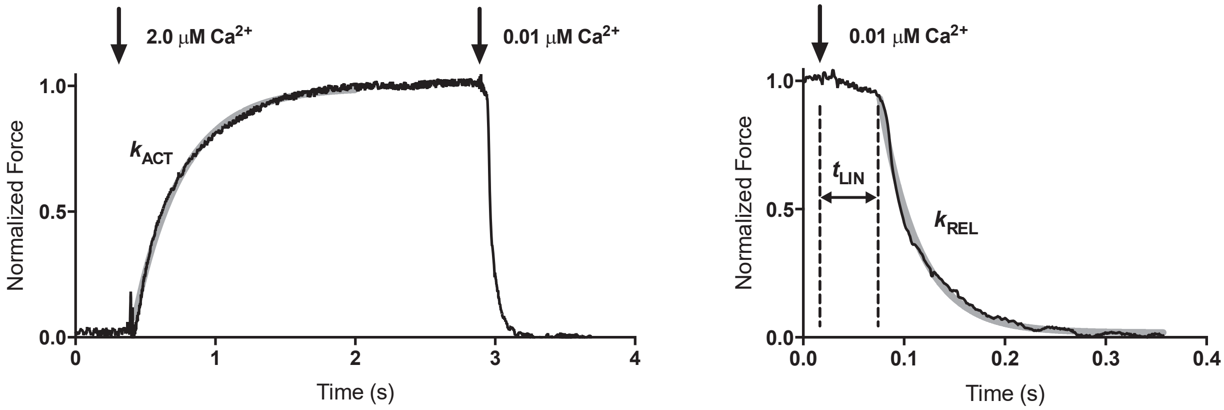

FIGURE 2 | Measurement of contractility in single mouse cardiac muscle myofibrils. Time course of contraction and relaxation. The arrows indicate the time when the solutions were switched. The kinetic parameters maximum force (F_{max}), rate of force development (k_{ACT}), duration (t_{LIN}) and slope (k_{LIN}) of the slow relaxation phase, and rate of the fast relaxation phase (k_{REL}) were determined from the traces. The slow-relaxation phase was counted from the initiation of micropipette movement. The beginning of the exponential phase of relaxation was considered as the end of slow-relaxation phase. The relaxation phase is shown over an expanded timescale to show the initial linear, nearly isometric force decay period tLIN, followed by an exponential relaxation with a rate constant kREL. The gray solid lines represent the best exponential fits to the data. The temperature was 17°C. Reproduced from Vikhorev et al. (2014) with permission.

kinetics similar to whole muscle fiber measurements are possible with myofibrils as demonstrated by the quick release/restretch protocol used to measure k_{tr} (**Figure 3A**). It is feasible to reproduce most of the mechanical perturbation protocols that have been used in chemically skinned fibers, but in practice these have not been extensively explored since they do not differ greatly whilst the opportunities for transient biochemical perturbation that is possible in myofibril studies yields exciting new insights. Passive stiffness can also be measured and provides results that are wholly due to sarcomeric elements, mainly titin (Linke et al., 1997; Makarenko et al., 2004; Opitz et al., 2004; **Figure 3C**). Solution changing can be adapted to measure response to a range of concentrations and generate dose-response curves (**Figure 3B**). A number of unique complex protocols are also accessible, for instance the simulation of the heart work cycle by combining carefully timed Ca^{2+} jumps up and down with length ramps simulating "systolic" shortening and "diastolic" lengthening between isometric phases (**Figure 3D**). The addition of video microscopy allows sarcomere length to be measured, enabling accurate sarcomere length adjustments, for instance when measuring length-dependent activation. During relaxation these observations have shown transient heterogeneous shortening of sarcomeres in a myofibril which has important implications for the structural changes behind the relaxation process (Stehle et al., 2002, 2009).

APPLICATIONS

Because the myofibril measurements can be made with any suitable source of muscle the methodology has been applied to many systems. The dynamics of Ca^{2+} activation of force, defined by F_{max}, k_{ACT}, t_{LIN}, k_{LIN}, and k_{REL} and Ca^{2+} activation curves have been measured in myofibrils from both skeletal and cardiac muscles. Studies include:

(1) Comparing wild type with mutant muscles from transgenic mice such as the ACTC mutations E99K (HCM) and E361G (DCM) (Song et al., 2013; Vikhorev et al., 2014) or in mutant human heart myofibrils such as MYH7 R403Q, TNNT2 K280N, and titin truncating mutations (Ferrantini et al., 2009; Piroddi et al., 2019; Vikhorev et al., 2020).

(2) Based on techniques developed in skinned fibers (Brenner et al., 1999), troponin or tropomyosin can be exchanged with recombinant troponin components such as the HCM mutations TNNI3 R145G and TNNT2 K280N (Kruger et al., 2005; Piroddi et al., 2019) or tropomyosin isoforms or mutations (Siththanandan et al., 2009; Janco et al., 2012; Nixon et al., 2013; Scellini et al., 2014). Such studies have clearly demonstrated the effects of mutations on Ca^{2+}-sensitivity and on the kinetic parameters.

(3) The same methodology can be applied to the effects of contractile protein phosphorylation, notably by PKA, on the Ca^{2+} sensitivity and relaxation kinetics (Vikhorev et al., 2014, 2020) and to determine the effects of myofilament targeting drugs such as Mavacamten and Omecamtiv Mecarbil (Scellini et al., 2020, 2021).

(4) The myofibril force assay is particularly useful when used with myofibrils from non-muscle sources. For instance in the study of embryonic heart, biopsies, cultured myocytes and particularly iPSC (Pioner et al., 2015, 2016; Racca et al., 2015; Iorga et al., 2018).

(5) A novel application is in measuring the effects of muscle stretch on passive elasticity and on active force generation. The former allows for assessment of titin mechanical properties (Linke et al., 1997; Makarenko et al., 2004;

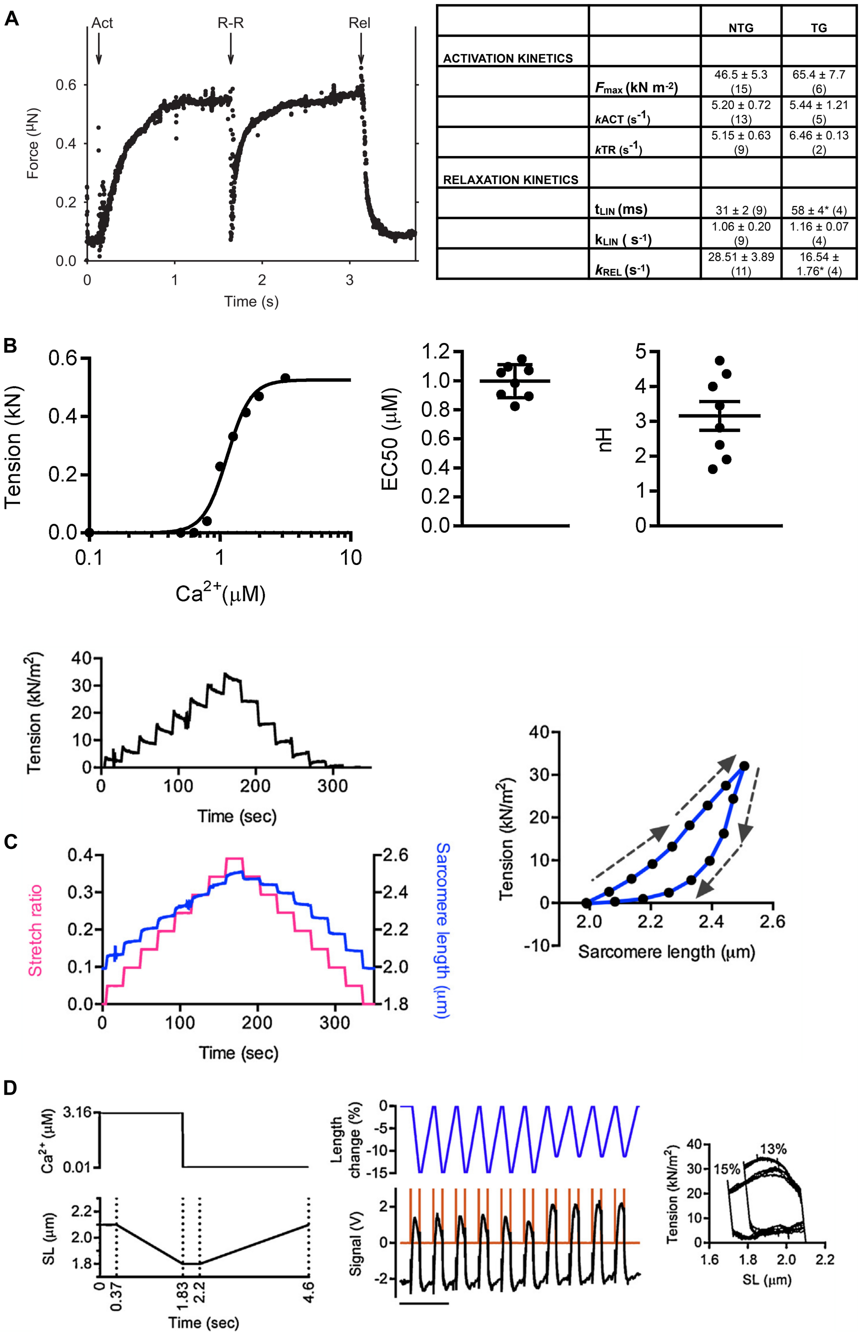

		NTG	TG
ACTIVATION KINETICS			
	F_{max} (kN m^{-2})	46.5 ± 5.3 (15)	65.4 ± 7.7 (6)
	kACT (s^{-1})	5.20 ± 0.72 (13)	5.44 ± 1.21 (5)
	kTR (s^{-1})	5.15 ± 0.63 (9)	6.46 ± 0.13 (2)
RELAXATION KINETICS			
	t_{LIN} (ms)	31 ± 2 (9)	58 ± 4* (4)
	k_{LIN} (s^{-1})	1.06 ± 0.20 (9)	1.16 ± 0.07 (4)
	k_{REL} (s^{-1})	28.51 ± 3.89 (11)	16.54 ± 1.76* (4)

FIGURE 3 | Examples of experiments with single myofibrils. **(A)** Determination of kinetic parameters in wild-type and transgenic (ACTC E99K) mouse myofibrils **(B)** Measurement of the Ca^{2+}-sensitivity of tension in mouse myofibrils. **(C)** Measurement of passive tension. **(D)** Simulated work lops. Arrows indicate stretch or release. Reproduced from Vikhorev et al. (2015) with permission.

Opitz et al., 2004; Vikhorev et al., 2017) whilst the latter allows measurement of length dependent activation. Such studies have confirmed that both PKA-dependent phosphorylation and titin mutations can modulate length dependent activation whist having little or no effect on baseline contractility (Vikhorev et al., 2020).

(6) The single myofibril force assay has been adapted to measure force from a single sarcomere or even half-sarcomeres. Contraction-relaxation cycles, a force-velocity relationship and even Length dependent activation was successfully measured in single sarcomeres (Pavlov et al., 2009; Minozzo et al., 2013; Lowey et al., 2018).

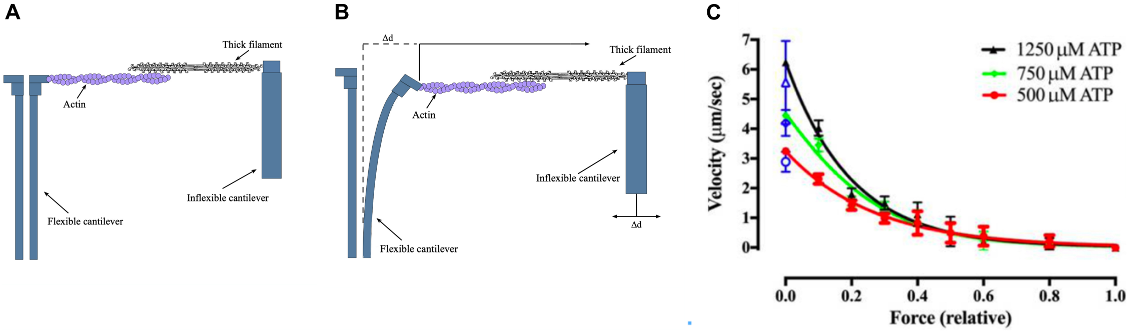

FIGURE 4 | The microfabricated cantilever single filament force assay. **(A,B)** Schematic view of the microfabricated cantilever experimental setup. Thick filament and actin filaments were attached to the cantilevers and brought into contact. The filaments y produce a force that causes the displacement of the flexible cantilever, which enabled force to be measured. **(C)** Example of a single filament force -velocity plot. Figures provided by Drs Y-S Sheng and DE Rassier.

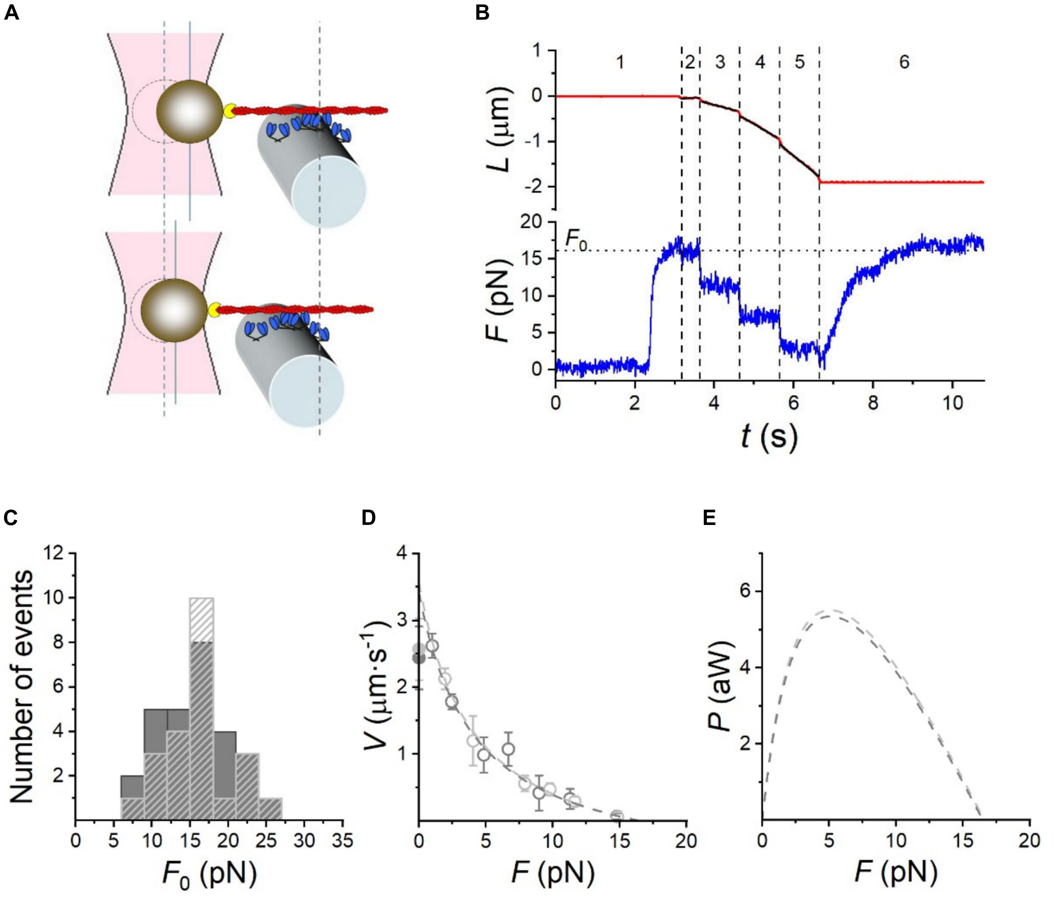

FIGURE 5 | Performance of the rabbit HMM-based nanomachine. **(A)** Schematic representation of two snapshots during the interaction between the actin filament and the motor ensemble. Upper panel: in position clamp at F0; lower panel: in force clamp at 0.4 F0. **(B)** Recording of the actin filament sliding (L, upper trace, red) and force (F, lower trace, blue) during an interaction. Numbers bounded by dashed lines identify the different time intervals (it) as detailed in the text. **(C)** Frequency distribution of F0. Data are plotted in classes of 3 pN; dark gray bars, measurements in 0.1 mM CaCl2 (=77 M free [Ca^{2+}]); light gray dashed bars, in the absence of Ca^{2+}. **(D)** F-V relation in 0.1 mM $CaCl_2$ (dark gray open circles) and in Ca^{2+}-free solution (light gray open circles). Points are mean ± SD from individual experiments, grouped in classes of force 0.15 F0 wide. Dark and light gray filled symbols on the ordinate are the Vf in the in vitro motility assay (IVMA) on rabbit HMM with and without Ca^{2+}, respectively. The dashed lines are Hill's hyperbolic equation fits to the data with the same color code as symbols. Data in c and d are from 28 experiments in 0.1 mM $CaCl_2$ and 23 experiments in Ca^{2+}-free solution. **(E)** Power (P) versus F, calculated from the corresponding F-V fits in **(D)**, with the same color code. Reproduced from Pertici et al. (2020) with permission.

SINGLE FILAMENT FORCE MEASUREMENTS

Measurement of contractility at the single filament level enables us to determine the characteristics of the actomyosin contractile machine in the absence of the effects of structure of the sarcomere. To go to singe filaments requires different, more sensitive techniques, generally derived from *in vitro* motility assay or optical trap methodology (see **Table 1**).

The *in vitro* motility assay was devised about 30 years ago (Kron et al., 1991) and has been immensely successful for assaying the unloaded contractility of muscle filaments, characterizing myosins and thin filament regulatory proteins and their post-translational modifications (Fraser and Marston, 1995; Gordon et al., 1997; Marston, 2003; Batters et al., 2014).

Adaptation of the IVMA to measure force requires a probe, usually attached to the thin filament, acting on immobilized myosin. In the first studies this was simply a bed of HMM molecules as used in normal IVMA but more sophisticated setups using whole thick filaments and introducing filament orientation have been devised.

The first studies used microneedles attached to thin filaments using NEM-HMM for attachment, developed by Kishino and Yanagida (1988) and Chaen et al. (1989). These were far more compliant than used for myofibrils since the forces obtained are in the region of 50 pN. Video microscopy is used to watch the needle bend until it stalls. The angle then represents the isometric force which is generally expressed as pN/μm length of the actin filament overlap; values in the region of 10 pN/μm actin are obtained. VanBuren successfully used this technique to determine the effects of light chain removal and of myosin and tropomyosin isoform switches on force generation (VanBuren et al., 1994a,b, 1999). Homsher et al. (2000) used this technique to demonstrate Ca^{2+} control of force in single regulated thin filaments.

A more recent version of this methodology uses microfabricated AFM cantilevers as the tension probe (**Figure 4**). The stiffness of the cantilever is 0.18 pN/nm. This study also used whole thick filaments in the correct orientation for optimum interaction with thin filaments. These measurements obtained values between 60 and 100 pN/μm which may more closely indicate the real maximum force generated by myosin motors. Since the inflexible cantilever can be moved to compensate for muscle shortening it is possible to make further measurements, such as a force-velocity plot, which closely resembles that of intact muscle (Cheng et al., 2020).

Another method used for imposing load on a single actin filament is by magnetic force. The actin filaments are attached to magnetic beads via gelsolin in a normal IVMA cell and an electromagnet applies a magnetic force. Bead-tailed filaments moving over a bed of HMM slowed down under an increasing magnetic load, eventually stalled and then slid backward under increasing load before detaching from the surface. Single-filament force–velocity curves were constructed and a stalling force of about 600 pN/μm of actin filament estimated. This method has not seen much use due to the very low yield of viable bead-tailed filaments (Bershitsky et al., 1996; Hamelink, 1999; Holohan and Marston, 2005).

A more widely used methodology for measuring force in single filaments is the indirect method, based on an internal load imposed on actin filaments by an anchored actin binding protein in a conventional *in vitro* motility assay. Warshaw et al. (1990) first demonstrated this principle using N-ethylmaleimide (NEM)-treated heavy meromyosin (HMM) and p-phenylenedimaleimide (pPDM)-treated HMM, while Janson et al. (1992) showed that a-actinin and filamin can also stop filament movement. The greater the myosin motor force on an actin filament, the higher the concentration of actin-binding protein needed to stop movement. Bing and Marston first demonstrated that the effect of a-actinin on the fraction of filaments moving is a consistent and sensitive method that can detect changes in isometric force of single actin filaments interacting with immobilized HMM (Bing et al., 2000). The initial studies investigated how tropomyosin and troponin may control force but only measured relative force, however, an analysis of how retardation works by Greenberg and Moore (2010) showed that it was possible to extract quantitative data from such measurements.

The optical trap has been used for many years to measure very small movements and has been mainly applied to single molecule studies of unloaded contractility. To measure force needs a much stiffer optical trap which can be limiting (Veigel et al., 1998, 2003). Recently the optical trap method has been used for force measurements of the interaction of actin with a small ensemble of myosin molecules. There is a trade-off here between the maximum amount of force the trap can handle and the minimum number of myosin-actin interactions needed for continuous movement. Skeletal muscle has a low "duty ratio" which means that if the steady-state number of interactions is too low the filaments can detach from the actin at physiological ATP concentrations. Kaya et al. (2017) used whole myosin filaments, but in order to reduce the interactions to not overload the optical trap the filaments were copolymers of myosin and myosin rod (1:200 ratio) and the estimated steady-state number of interactions was just 37 in a 600 nm myosin filament. Pertici et al. (2020) coated HMM onto a microfiber at an appropriate dilution that enabled a minimum of 32 steady state interaction (**Figure 5**). Pertici et al. suggest the geometry of their setup is superior to that of Kaya et al. (2017) since the actin and HMM can be adjusted to exert force in a linear rather than oblique direction and because the HMM, being concentrated on a small surface, has a constant area of actin-myosin overlap unlike the two-filament system where the length of overlap is a variable. On the other hand, the two-filament system using myosin filaments does have the correct orientation of myosin heads whereas in the "nanomachine" HMM is randomly orientated toward actin.

Both these methods found that myosin acts in a coordinated way when interacting with a single actin filament; maximum isometric force and a force-velocity curve were obtained (see **Figure 5**).

In general, single filament systems offer a potential tool for investigating muscle contractile and regulatory protein mechanisms and the effects of mutations and post-translational modifications on force production that could match the equivalent unloaded studies using the *in vitro* motility assay. So far such studies have been limited to the thick filament (Rassier and Leite, 2020; Pertici et al., 2021) with only one study using single filaments to study thin filament regulation (Ishii et al., 2019).

CONCLUSION

Over the last 20 years, techniques for measuring force in single myofibrils or myofilaments have increasingly been used for fundamental studies of striated muscle contractile mechanisms and their regulation by Ca^{2+}, post translational modifications and disease-related mutations. The techniques are exacting, and throughput is low but the results are accurate and provide detailed information of contractility at the subcellular level that cannot be obtained by any other method.

The key advantages of subcellular contractility measurement are twofold. Firstly, the contractile apparatus is directly studied and secondly, rapid solution changing permits the measurement of the kinetics of the force changes induced by Ca^{2+} concentration changes for the first time.

These methods have potential for investigating regulation, post translational modifications and mutations in a huge variety of systems. The versatility of these systems plus the ability to combine force measurements with optical measurements allows the possibility of new types of experiments not yet envisaged. For instance, single myofibril and myofilament data can be valuable to form the basis of multiscale modeling of muscle (Månsson, 2019, 2020).

AUTHOR CONTRIBUTIONS

The author confirms being the sole contributor of this work and has approved it for publication.

FUNDING

This work was supported by the BHF project Grant PG/17/5/32705 to Petr Vikhorev and SM.

REFERENCES

Ayittey, P. N., Walker, J. S., Rice, J. J., and de Tombe, P. P. (2009). Glass microneedles for force measurements: a finite-element analysis model. *Pflugers Arch.* 457, 1415–1422. doi: 10.1007/s00424-008-0605-3

Bartoo, M. L., Popov, V. I., Fearn, L. A., and Pollack, G. H. (1993). Active tension generation in isolated skeletal myofibrils. *J. Musc. Res. Cell Motily* 14, 498–510. doi: 10.1007/bf00297212

Batters, C., Veigel, C., Homsher, E., and Sellers, J. R. (2014). To understand muscle you must take it apart. *Front. Physiol.* 5:90. doi: 10.3389/fphys.2014.00090

Bershitsky, S., Tsaturyan, A. K., Bershitskaya, O. N., Blange, T., and Van Kaam, F. A. M. (1996). *Electromagnetic device for loading molecular motors. *J. Muscle Res. Cell Motil.* 17, 156.

Bing, W., Knott, A., and Marston, S. (2000). A simple method for measuring the relative force exerted by myosin on actin filaments in the *in vitro* motility assay: evidence that tropomyosin and troponin increase force in single filaments. *Biochem. J.* 350, 693–699. doi: 10.1042/0264-6021:3500693

Brenner, B., Kraft, T., Yu, L. C., and Chalovich, J. M. (1999). Thin filament activation probed by fluorescence of N-((2-(Iodoacetoxy)ethyl)-N-methyl)amino-7-nitrobenz-2-oxa-1, 3-diazole-labeled troponin I incorporated into skinned fibers of rabbit psoas muscle. *Biophys. J.* 77, 2677–2691. doi: 10.1016/s0006-3495(99)77102-x

Chaen, S., Oiwa, K., Shimmen, T., Iwarmoto, I., and Sugi, H. (1989). Simultaneous recordings of force and sliding movements between myosin coated glass microneedle and actin cables in vitro. *Proc. Natl. Acad. Sci. U.S.A.* 86, 1510–1514. doi: 10.1073/pnas.86.5.1510

Cheng, Y.-S., Leite, F. D. S., and Rassier, D. E. (2020). The load dependence and the force-velocity relation in intact myosin filaments from skeletal and smooth muscles. *Am. J. Physiol.* 318, C103–C110. doi: 10.1152/ajpcell.00339.2019

Colomo, F., Nencini, S., Piroddi, N., Poggesi, C., and Tesi, C. (1998). Mechanisms of work production and work absorption in muscle. *Adv. Exp. Med. Biol.* 453, 373–382. doi: 10.1007/978-1-4684-6039-1_42

Colomo, F., Piroddi, N., Poggesi, C., Kronnie, G. T., and Tesi, C. (1997). Active and passive forces of isolated myofibrils from cardiac and fast skeletal muscle of the frog. *J. Physiol.* 500, 535–548. doi: 10.1113/jphysiol.1997.sp022039

Ferrantini, C., Belus, A., Piroddi, N., Scellini, B., Tesi, C., and Poggesi, C. (2009). Mechanical and energetic consequences of HCM-causing mutations. *J. Cardiovasc. Trans. Res.* 2, 441–451. doi: 10.1007/s12265-009-9131-8

Fraser, I. D., and Marston, S. B. (1995). In vitro motility analysis of actin-tropomyosin regulation by troponin and calcium. The thin filament is switched as a single cooperative unit. *J. Biol. Chem.* 270, 7836–7841. doi: 10.1074/jbc.270.14.7836

Friedman, A. L., and Goldman, Y. E. (1996). Mechanical characterization of skeletal muscle myofibrils. *Biophys. J.* 71, 2774–2785. doi: 10.1016/s0006-3495(96)79470-5

Gordon, A. M., LaMadrid, M. A., Chen, Y., Luo, Z., and Chase, P. B. (1997). Calcium regulation of skeletal muscle thin filament motility in vitro. *Biophys. J.* 72, 1295–1307. doi: 10.1016/S0006-3495(97)78776-9

Greenberg, M. J., and Moore, J. R. (2010). The molecular basis of frictional loads in the in vitro motility assay with applications to the study of the loaded mechanochemistry of molecular motors. *Cytoskeleton (Hoboken, NJ)* 67, 273–285. doi: 10.1002/cm.20441

Hamelink, W. (1999). *Muscle Contraction At the Molecular Level: Actin Myosin Interaction Studied in An in Vitro Motility Assay*. Amsterdam: University of Amsterdam. .

Holohan, S.-J. P., and Marston, S. B. (2005). Force-velocity relationship of single actin filament interacting with immobilised myosin measured by electromagnetic technique. *IEE Proc. Nanobiotechnol.* 152, 113–120. doi: 10.1049/ip-nbt:20045003

Homsher, E., Lee, D. M., Morris, C., Pavlov, D., and Tobacman, L. S. (2000). Regulation of force and unloaded sliding speed in single thin filaments: effects of regulatory proteins and calcium. *J. Physiol. (Lond)* 524(Pt 1), 233–243. doi: 10.1111/j.1469-7793.2000.00233.x

Iorga, B., Schwanke, K., Weber, N., Wendland, M., Greten, S., Piep, B., et al. (2018). Differences in contractile function of myofibrils within human embryonic stem cell-derived cardiomyocytes vs. adult ventricular myofibrils are related to distinct sarcomeric protein isoforms. *Front. Physiol.* 8:1111. doi: 10.3389/fphys.2017.01111

Ishii, S., Suzuki, M., Ishiwata, S. I, and Kawai, M. (2019). Functional significance of HCM mutants of tropomyosin, V95A and D175N, studied with in vitro motility assays. *Biophys. Physicobiol.* 16, 28–40. doi: 10.2142/biophysico.16.0_28

Iwazumi, T. (1987). High-speed ultrasensitive instrumentation for myofibril mechanics measurements. *Am. J. Physiol.* 252(Pt 1), C253–C262. doi: 10.1152/ajpcell.1987.252.2.C253

Janco, M., Kalyva, A., Scellini, B., Piroddi, N., Tesi, C., Poggesi, C., et al. (2012). α-Tropomyosin with a D175N or E180G mutation in only one chain differs from tropomyosin with mutations in both chains. *Biochemistry* 51, 9880–9890. doi: 10.1021/bi301323n

Janson, L. W., Sellers, J. R., and Taylor, D. L. (1992). Actin-binding proteins regulate the work performed by myosin II motors on single actin filaments. *Cell Motil. Cytoskeleton* 22, 274–280. doi: 10.1002/cm.970220407

Johns, E. C., Ryder, K. O., Hodson, E. A., Hart, G., Mulligan, I. P., Lipscomb, S., et al. (1999). Investigating the relaxation rate, following diazo-2 photolysis, of a skinned trabecular preparation from guinea-pig hypertrophied left ventricle. *Pflugers Arch.* 438, 771–777. doi: 10.1007/s004249900131

Kaya, M., Tani, Y., Washio, T., Hisada, T., and Higuchi, H. (2017). Coordinated force generation of skeletal myosins in myofilaments through motor coupling. *Nat. Comm.* 8:16036. doi: 10.1038/ncomms16036

Kishino, A., and Yanagida, T. (1988). Force measurements by micromanipulation of a single actin filament by glass needles. *Nature* 334, 74–76. doi: 10.1038/334074a0

Kron, S. J., Toyoshima, Y. Y., Uyeda, T. Q., and Spudich, J. A. (1991). Assays for actin sliding movement over myosin-coated surfaces. *Methods Enzymol.* 196, 399–416. doi: 10.1016/0076-6879(91)96035-p

Kruger, M., Zittrich, S., Redwood, C., Blaudeck, N., James, J., Robbins, J., et al. (2005). Effects of the mutation R145G in human cardiac troponin I on the kinetics of the contraction-relaxation cycle in isolated cardiac myofibrils. *J. Physiol.* 564(Pt 2), 347–357. doi: 10.1113/jphysiol.2004.079095

Linke, W. A., Ivemeyer, M., Labeit, S., Hinssen, H., Rüegg, J. C., and Gautel, M. (1997). Actin-titin interaction in cardiac myofibrils: probing a physiological role. *Biophys. J.* 73, 905–919. doi: 10.1016/S0006-3495(97)78123-2

Lowey, S., Bretton, V., Joel, P. B., Trybus, K. M., Gulick, J., Robbins, J., et al. (2018). Hypertrophic cardiomyopathy R403Q mutation in rabbit β-myosin reduces contractile function at the molecular and myofibrillar levels. *Proc. Natl. Acad. Sci. U.S.A.* 115, 11238–11243. doi: 10.1073/pnas.1802967115

Makarenko, I., Opitz, C. A., Leake, M. C., Neagoe, C., Kulke, M., Gwathmey, J. K., et al. (2004). Passive stiffness changes caused by upregulation of compliant titin isoforms in human dilated cardiomyopathy hearts. *Circ. Res.* 95, 708–716. doi: 10.1161/01.RES.0000143901.37063.2f

Månsson, A. (2019). Comparing models with one versus multiple myosin-binding sites per actin target zone: the power of simplicity. *J. Gen. Physiol.* 151, 578–592. doi: 10.1085/jgp.201812301

Månsson, A. (2020). Hypothesis: single actomyosin properties account for ensemble behavior in active muscle shortening and isometric contraction. *Int. J. Mol. Sci.* 21:8399. doi: 10.3390/ijms21218399

Marston, S. (2003). Random walks with thin filaments: application of in vitro motility assay to the study of actomyosin regulation. *J. Musc. Res. Cell Motil.* 24, 149–156. doi: 10.1023/a:1026097313020

Minozzo, F. C., Baroni, B. M., Correa, J. A., Vaz, M. A., and Rassier, D. E. (2013). Force produced after stretch in sarcomeres and half-sarcomeres isolated from skeletal muscles. *Nat. Sci. Rep.* 3:2320. doi: 10.1038/srep02320

Nixon, B. R., Liu, B., Scellini, B., Tesi, C., Piroddi, N., Ogut, O., et al. (2013). Tropomyosin Ser-283 pseudo-phosphorylation slows myofibril relaxation. *Arch. Biochem. Biophys.* 535, 30–38. doi: 10.1016/j.abb.2012.11.010

Opitz, C. A., Leake, M. C., Makarenko, I., Benes, V., and Linke, W. A. (2004). Developmentally regulated switching of titin size alters myofibrillar stiffness in the perinatal heart. *Circ. Res.* 94, 967–975. doi: 10.1161/01.RES.0000124301.48193.E1

Pavlov, I., Novinger, R., and Rassier, D. E. (2009). The mechanical behavior of individual sarcomeres of myofibrils isolated from rabbit psoas muscle. *Am. J. Physiol.* 297, C1211–C1219. doi: 10.1152/ajpcell.00233.2009

Pertici, I., Bianchi, G., Bongini, L., Cojoc, D., Taft, M. H., Manstein, D. J., et al. (2021). Muscle myosin performance measured with a synthetic nanomachine reveals a class-specific Ca2+-sensitivity of the frog myosin II isoform. *J. Physiol.* 599, 1815–1831. doi: 10.1113/jp280976

Pertici, I., Bianchi, G., Bongini, L., Lombardi, V., and Bianco, P. (2020). A Myosin II-based nanomachine devised for the study of Ca2+-Dependent mechanisms of muscle regulation. *Int. J. Mol. Sci.* 21:7372. doi: 10.3390/ijms21197372

Pertici, I., Bongini, L., Melli, L., Bianchi, G., Salvi, L., Falorsi, G., et al. (2018). A myosin II nanomachine mimicking the striated muscle. *Nat. Comm.* 9:3532. doi: 10.1038/s41467-018-06073-9

Pioner, J. M., Pioner, J. M., Yang, K.-C., Pabon, L., Racca, A. W., Jeong, M. Y., et al. (2015). Cell and myofibril contractile properties of hiPSC-Derived cardiomyocytes from a patient with a MYH7 mutation associated with familial cardiomyopathy. *Biophys. J.* 108(Suppl. 1):201a. doi: 10.1016/j.bpj.2014.11.1110

Pioner, J. M., Racca, A. W., Klaiman, J. M., Yang, K.-C., Guan, X., Pabon, L., et al. (2016). Isolation and mechanical measurements of myofibrils from human induced pluripotent stem cell-derived cardiomyocytes. *Stem Cell Rep.* 6, 885–896. doi: 10.1016/j.stemcr.2016.04.006

Piroddi, N., Witjas-Paalberends, E. R., Ferrara, C., Ferrantini, C., Vitale, G., Scellini, B., et al. (2019). The homozygous K280N troponin T mutation alters cross-bridge kinetics and energetics in human HCM. *J. Gen. Physiol.* 151, 18–29. doi: 10.1085/jgp.201812160

Racca, A. W., Klaiman, J. M., Pioner, J. M., Cheng, Y., Beck, A. E., Moussavi-Harami, F., et al. (2015). Contractile properties of developing human fetal cardiac muscle. *J. Physiol.* 594, 437–452. doi: 10.1113/jp271290

Rassier, D. E., and Leite, F. D. S. (2020). Sarcomere length non-uniformity and force regulation in myofibrils and sarcomeres. *Biophys. J.* 119, 2372–2377. doi: 10.1016/j.bpj.2020.11.005

Scellini, B., Piroddi, N., Dente, M., Ferrantini, C., Coppini, R., Poggesi, C., et al. (2020). Impact of mavacamten on force generation in single myofibrils from rabbit psoas and human cardiac muscle. *Biophys. J.* 118:7a. doi: 10.1016/j.bpj.2019.11.231

Scellini, B., Piroddi, N., Dente, M., Vitale, G., Coppini, R., Ferrantini, C., et al. (2021). Omecamtiv mecarbil modulation of force generation in single myofibrils from human cardiac muscle. *Biophys. J.* 120:249a. doi: 10.1016/j.bpj.2020.11.1623

Scellini, B., Piroddi, N., Flint, G. V., Regnier, M., Poggesi, C., and Tesi, C. (2014). Impact of tropomyosin isoform composition on fast skeletal muscle thin filament regulation and force development. *J. Musc. Res. Cell Motil.* 36, 1–13. doi: 10.1007/s10974-014-9394-9

Siththanandan, V. B., Tobacman, L. S., Gorder, N. V., and Homsher, E. (2009). Mechanical and kinetic effects of shortened tropomyosin reconstituted into myofibrils. *Pflugers Arch. : Eur. J. physiol.* 458, 761–776. doi: 10.1007/s00424-009-0653-3

Song, W., Vikhorev, P. G., Kashyap, M. N., Rowlands, C., Ferenczi, M. A., Woledge, R. C., et al. (2013). Mechanical and energetic properties of papillary muscle from ACTC E99K transgenic mouse models of hypertrophic cardiomyopathy. *Am. J. Physiol. Heart Circ. Physiol.* 304, H1513–H1524. doi: 10.1152/ajpheart.00951.2012

Stehle, R., Kruger, M., and Pfitzer, G. (2002). Force kinetics and individual sarcomere dynamics in cardiac myofibrils after rapid ca(2+) changes. *Biophys. J.* 83, 2152–2161. doi: 10.1016/S0006-3495(02)73975-1

Stehle, R., Solzin, J., Iorga, B., and Poggesi, C. (2009). Insights into the kinetics of Ca2+-regulated contraction and relaxation from myofibril studies. *Pflugers Arch.* 458, 337–357. doi: 10.1007/s00424-008-0630-2

Tesi, C., Piroddi, N., Colomo, F., and Poggesi, C. (2002). Relaxation kinetics following sudden Ca(2+) reduction in single myofibrils from skeletal muscle. *Biophys. J.* 83, 2142–2151. doi: 10.1016/S0006-3495(02)73974-X

VanBuren, P., Palmiter, K. A., and Warshaw, D. M. (1999). Tropomyosin directly modulates actomyosin mechanical performance at the level of a single actin filament. *Proc. Natl. Acad. Sci. U.S.A.* 96, 12488–12493. doi: 10.1073/pnas.96.22.12488

VanBuren, P., Waller, G. S., Harris, D. E., Trybus, K. M., Warshaw, D. M., and Lowey, S. (1994a). The essential light chain is required for full force production by skeletal muscle myosin. *Proc. Natl. Acad. Sci. U.S.A.* 91, 12403–12407. doi: 10.1073/pnas.91.26.12403

VanBuren, P., Work, S. S., and Warshaw, D. M. (1994b). Enhanced force generation by smooth muscle myosin *in vitro*. *Proc. Natl. Acad. Sci. U.S.A.* 91, 202–205.

Veigel, C., Bartoo, M. L., White, D. C. S., Sparrow, J. C., and Molloy, J. E. (1998). The stiffness of rabbit skeletal actomyosin cross-bridges determined with an optical tweezers transducer. *Biophys. J.* 75, 1424–1438. doi: 10.1016/s0006-3495(98)74061-5

Veigel, C., Molloy, J. E., Schmitz, S., and Kendrick-Jones, J. (2003). Load-dependent kinetics of force production by smooth muscle myosin measured with optical tweezers. *Nat. Cell Biol.* 5, 980–986. doi: 10.1038/ncb1060

Vikhorev, P., Ferenczi, M. A., and Marston, S. (2015). Instrumentation to study myofibril mechanics from static to artificial simulations of cardiac cycle. *Methods X* 3, 156–170. doi: 10.1016/j.mex.2016.02.006

Vikhorev, P. G., Smoktunowicz, N., Munster, A. B., Copeland, O. X. N., Kostin, S., Montgiraud, C., et al. (2017). Abnormal contractility in human heart myofibrils from patients with dilated cardiomyopathy due to mutations in TTN and contractile protein genes. *Sci. Rep.* 7:14829. doi: 10.1038/s41598-017-13675-8

Vikhorev, P. G., Song, W., Wilkinson, R., Copeland, O., Messer, A. E., Ferenczi, M. A., et al. (2014). The dilated cardiomyopathy-causing mutation ACTC E361G in cardiac muscle myofibrils specifically abolishes modulation of Ca(2+) regulation by phosphorylation of troponin I. *Biophys. J.* 107, 2369–2380. doi: 10.1016/j.bpj.2014.10.024

Vikhorev, P. G., Vikhoreva, N. N., Yeung, W., Li, A., Lal, S., Remedios, C. G. D., et al. (2020). Titin-Truncating mutations associated with dilated cardiomyopathy alter length-dependent activation and its modulation via phosphorylation. *Cardiovasc. Res. [Online ahead of print]* cvaa316. doi: 10.1093/cvr/cvaa316

Warshaw, D. M., Desrosiers, J. M., Work, S. S., and Trybus, K. M. (1990). Smooth muscle myosin cross-bridge interactions modulate actin filament sliding velocity in vitro. *J. Cell Biol.* 111, 453–463. doi: 10.1083/jcb.111.2.453

Conflict of Interest: The author declares that the research was conducted in the absence of any commercial or financial relationships that could be construed as a potential conflict of interest.

frontiers
in Physiology

REVIEW
published: 31 January 2022
doi: 10.3389/fphys.2021.770906

Building Valveless Impedance Pumps From Biological Components: Progress and Challenges

*Narine Sarvazyan**

Department of Pharmacology and Physiology, School of Medicine and Health Science, The George Washington University, Washington, DC, United States

Valveless pumping based on Liebau mechanism entails asymmetrical positioning of the compression site relative to the attachment sites of the pump's elastic segment to the rest of the circuit. Liebau pumping is believed to play a key role during heart development and be involved in several other physiological processes. Until now studies of Liebau pump have been limited to numerical analyses, *in silico* modeling, experiments using non-biological elements, and a few indirect *in vivo* measurements. This review aims to stimulate experimental efforts to build Liebau pumps using biologically compatible materials in order to encourage further exploration of the fundamental mechanisms behind valveless pumping and its role in organ physiology. The covered topics include the biological occurrence of Liebau pumps, the main differences between them and the peristaltic flow, and the potential uses and body sites that can benefit from implantable valveless pumps based on Liebau principle. We then provide an overview of currently available tools to build such pumps and touch upon limitations imposed by the use of biological components. We also talk about the many variables that can impact Liebau pump performance, including the concept of resonant frequencies, the shape of the flowrate-frequency relationship, the flow velocity profiles, and the Womersley numbers. Lastly, the choices of materials to build valveless impedance pumps and possible modifications to increase their flow output are briefly discussed.

Keywords: valveless pumping, Liebau mechanism, tissue engineering, biofabrication, heart development

Edited by:
Peter T. Wright,
University of Roehampton London,
United Kingdom

Reviewed by:
Kenneth Ginsburg,
UC Davis, United States
Sara I. Abdelsalam,
National Autonomous University
of Mexico, Mexico

***Correspondence:**
Narine Sarvazyan
phynas@gwu.edu

Specialty section:
This article was submitted to
Striated Muscle Physiology,
a section of the journal
Frontiers in Physiology

Received: *06 September 2021*
Accepted: *08 December 2021*
Published: *31 January 2022*

Citation:
Sarvazyan N (2022) Building
Valveless Impedance Pumps From
Biological Components: Progress
and Challenges.
Front. Physiol. 12:770906.
doi: 10.3389/fphys.2021.770906

BRIEF HISTORY

About 70 years ago, German physician Gerhard Liebau came up with a new concept of valveless pumping (Liebau, 1954, 1955). It involves a periodic compression of a compliant tube connected to a stiffer tubing on both ends (**Figure 1**). Asymmetric positioning of the pincher is required to generate the flow, and the relationship between the pinching frequency and the flow is highly non-linear. This mechanism acquired the name of a "Liebau-pump" or a "Liebau-based" principle. Due to a common assumption that it is a mismatch in impedance at the junctions between compliant and stiff segments that generates net flow, the Liebau pump has also been referred to as a "valveless impedance pump."

Initially, the physiological significance of the Liebau pump was largely hypothetical; therefore, for the next 50 years, this concept remained of interest mainly to physicists (Thomann, 1978; Jung and Peskin, 2002; Borzì and Propst, 2003; Ottesen, 2003; Auerbach et al., 2004; Jung, 2007). However, in 2006, a landmark paper by Gharib's group provided the first direct experimental evidence that the Liebau-type mechanism might be involved in driving blood flow *in vivo*

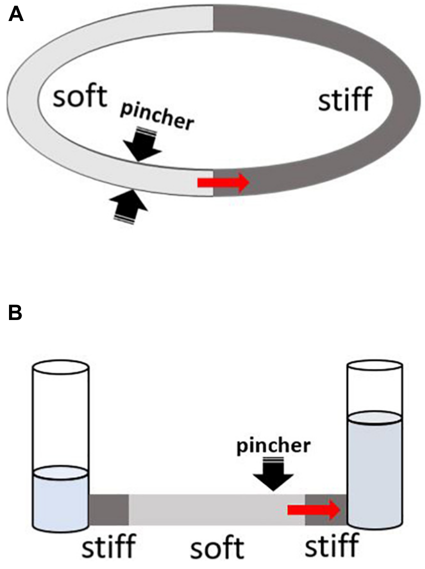

FIGURE 1 | Two main configurations for testing Liebau-based pumping. The red arrow depicts the direction of mean flow as originally reported by G. Liebau from pincher toward the nearest junction with stiff tubing. Depending on the compression frequency, the flow can also occur in an opposite direction. **(A)** Two tubes with different compliances are connected to form a close loop conduit. Pincher is typically a rectangular piston being pushed into soft tubing (light gray) by some form of linear actuator. When the asymmetrically positioned pincher is periodically compressed, it creates pulsative flow. **(B)** The compliant segment is depicted in light gray. On both ends, it connects to stiff tubes that are attached to open tanks filled with fluid. Pincher is an asymmetrically positioned piston that compresses the soft segment with a defined frequency.

(Forouhar et al., 2006). The authors' conclusions were based on tracking erythrocyte movement in the hearts of live zebrafish embryos. The data suggested that the observed flow pattern was more consistent with the Liebau pumping mechanism than that based on peristalsis. Modification of the Liebau pump that included an additional gelatinous layer was soon proposed to explain the physiological role of cardiac jelly in helping drive blood flow in embryonic hearts (Loumes et al., 2008). Additional modifications that mimic possible biological scenarios and further increase flow efficiency, have also been suggested. These included inclusion of bends (Hiermeier and Männer, 2017), insertion of cavities (Kozlovsky et al., 2015), use of tapered connectors (Lee et al., 2017), or asymmetric arrangement of resistances between the two sides of the compliant tube (Wen and Chang, 2009). Due to its complexity and dependence on many variables, the pumping mechanism proposed by Liebau remains the subject of interest across a wide range of disciplines, including physiology, engineering, physics, and biomedical research (Hickerson et al., 2005; Rinderknecht et al., 2005; Hickerson and Gharib, 2006; Manopoulos et al., 2006, 2020; Bringley et al., 2008; Timmermann and Ottesen, 2009; Rosenfeld and Avrahami, 2010; Meier, 2011; Lee et al., 2013; Kozlovsky et al., 2016; Zislin and Rosenfeld, 2018; Li et al., 2019; Davtyan and Sarvazyan, 2021).

BIOLOGICAL OCCURRENCE OF LIEBAU PUMPS

Today, the possibility of the physiological existence of Liebau-like pumps is rarely disputed, with ongoing discussions as to what degree embryonic heart tubes function as peristaltic vs. impedance-based pump (Männer et al., 2010). A number of papers have suggested that it is the combination of the two mechanisms that is involved (Santhanakrishnan et al., 2009; Santhanakrishnan and Miller, 2011; Kozlovsky et al., 2016). Indeed, at the end of the first month, the heart of the human embryo is still valveless, yet its beating yields unidirectional blood flow with a non-linear flow-frequency pattern (Forouhar et al., 2006). Behavior of an embryonic heart can be seen as a stage of early evolutionary development since the valveless circulatory system has been described for several classes of invertebrates and some lower vertebrates (Anderson, 1981). It was also suggested that circulation of cerebrospinal fluid (Longatti, 2018) as well as blood flow caused by compressions during cardiopulmonary resuscitation (Ottesen, 2003) can be explained, at least in part, by Liebau-type pumping. There is also an indirect evidence that the latter contributes to blood flow in other body locations, such as an aorta (Pahlevan and Gharib, 2013).

MAIN DIFFERENCES BETWEEN PERISTALTIC AND LIEBAU PUMPS

There are number of fundamental differences that distinguish the two types of valveless pumps found in Nature. Peristaltic pumps belong to the class of so-called positive displacement pumps. Contraction waves passing through the wall of the vessel lead to lumen compression, which squeezes the content of the vessel in the same direction as the contraction wave. As a result, continuous flow is generated with peak flow velocity equal to the speed of the propagating contraction wave. Peristaltic pumps exhibit a linear relationship between the compression frequency and the flowrate (Jaffrin and Shapiro, 1971).

The behavior of a Liebau pump exhibits a number of key differences. Only a small segment of the wall is actively compressed, with the rest of the pressure wave passively propagating through the vessel. Instant flow pattern is pulsatile with direction of flow changing back and forth within each compression event. The mean flowrate can be significant even in the absence of full lumen closure. When recorded over a wide range of compression frequencies, the relationship between the frequency and the mean flow rate is non-linear, including reversals in the direction of flow (Liebau, 1955).

POTENTIAL USES OF LIEBAU PUMPS MADE FROM BIOLOGICAL COMPONENTS

As of today (with two exceptions detailed below), studies of Liebau pumps have been limited to numerical analyses, *in silico* modeling, experiments using non-biological elements, and a few indirect *in vivo* measurements. Therefore, there is a need for experimental studies that recreate Liebau pumps from biological materials using tissue engineering methods, biofabrication tools or biomimetric approaches. Such efforts can yield multiple benefits. First, they will lead to a better understanding of physiological mechanisms responsible for blood flow generation during heart development, including cases of collapsed flow caused by cardiac malformations or genetic defects. Second, the creation of biofabricated Liebau pumps (abbreviated as BLP thereafter) will be of interest from a purely biological perspective. There is ample evidence that Liebau-type pumping is involved in the circulation of fluids in a wide variety of biological forms, including both vertebrates and invertebrates (Johansen et al., 1980) and it will be quite interesting to look into the evolutionary adaptation of these valveless pumps. Third, miniature self-beating BLPs can be used to circulate fluids in organ-on-a-chip or human-on-chip platforms (Zhang et al., 2018; Ma et al., 2021). Lastly, in the long term, one can envision the clinical use of biomimetic devices, such as those based on the Liebau principle, that will help drive the flow of fluids at various locations within the human body (Dai et al., 2006; Sarvazyan, 2014a,b; Swift et al., 2014). The next paragraph will consider the later possibilities in slightly more detail.

POSSIBLE BODY SITES THAT CAN BENEFIT FROM IMPLANTABLE BIOFABRICATED LIEBAU PUMPS

There are multiple types of fluids in the human body, including blood, lymph, saliva, gastric juice, semen, urine, tears, and many others. Some fluids are delivered by simple secretion into the target compartment or a duct, while others are delivered by active circulation. The most obvious instance of the latter is blood that circulates due to active pumping by the beating heart aided by contraction of skeletal muscle that surrounds valve-containing veins. Another example is a lymph flow, which is enabled by the presence of one-way valves and repetitive contractions of smooth muscle within walls of lymphatic vessels (Zawieja, 2009), again aided by compression by the surrounding skeletal muscle. An additional case is semen ejection, which is caused by contraction of smooth muscle within walls of vas deferens. One can also mention peristalsis of smooth muscle in the walls of the ureters that moves urine toward the urinary bladder. When, for a variety of reasons, these physiological pumping mechanisms become impaired, one can envision the use of BLP-based therapies to either aid or restore the flow. Importantly, the key components of BLPs can be added without disrupting the integrity of the vessel, and there are no requirements to create one-way valves. These key components can be positioned outside the vessel of interest and include a pair of low compliance cuffs and a band of periodically contracting muscles. The latter can be made from a patient's induced pluripotent stem cell (iPS) derived cardiomyocytes, or a stimulable ring of skeletal muscle cells. The most attractive aspect of such a design is that the integrity of the inner endothelial layer does not have to be disrupted, avoiding possible fibrosis, blockage, or, in case of blood flow, thrombi formation.

AVAILABLE BIOFABRICATION TOOLS

The last two decades have led to an explosion of biofabrication tools and approaches. It is now possible to build cell-free or cell-seeded vessels with different degrees of elasticity and compliance (Schuurman et al., 2011; Nguyen et al., 2016). Tissue engineered cardiac and skeletal muscle strips have been developed (Juhas et al., 2014). Initially, force generation by these engineered muscle constructs was quite low (Zimmermann et al., 2002), yet the use of electrical and mechanical stimulation (Radisic et al., 2004; Tandon et al., 2009; Khodabukus et al., 2019), enhanced perfusion (Carrier et al., 1999), and seeding cells into stretchable scaffolds (Zhang et al., 2013) or around suture templates (Nunes et al., 2013) led to a significant increase in the force of contraction that such engineered muscles can create. Tissue engineered muscle strips can now be developed from patient-specific iPSCs (Karabekian et al., 2015a; Breckwoldt et al., 2017) alleviating concerns of immunorejection when such constructs are implanted back into the patient (Karabekian et al., 2015a,b). Another set of useful tools comes from the optogenetic field. One can now repetitively stimulate muscle constructs made from cells that express light-sensitive channels using pulses of light (Burton et al., 2015; Raman et al., 2016; Entcheva and Kay, 2020). Optogenetics also offers the possibility of a programmable spatiotemporal coordination of excitability along the tissue engineered muscular construct (Entcheva, 2013). Ability to 3D-bioprint multicellular multilayered constructs (Cvetkovic et al., 2014; Kang et al., 2016; Zhang et al., 2017; Koti et al., 2019) is yet another tool that can be used to create BLPs. A particularly promising approach for this task is additive-lathe 3D printing, an approach that uses rotating cylindrical mandrel to bioprint tubular constructs (Reeser and Doiron, 2019).

PUBLISHED ATTEMPTS TO CREATE FUNCTIONAL BIOFABRICATED LIEBAU PUMPS

The design shown in **Figure 1A** is deceivingly simple. In fact, creating any sizable pressure or flow using Liebau pump built from biological elements has been a real challenge. To the best of our knowledge, as of today there is just one published peer-reviewed attempt to create a BLP (Li et al., 2019). Yet even this study created only a partial BLP, with its compression element made from biological material while the vessel parts were not. Specifically, Li et al. (2019) examined the ability of a ring formed by differentiated cells from mouse myoblast cell line C2C12 to create flow in a polyacrylamide-based compliant tube inserted into a more rigid PDMS mold. Repetitive compression of the tube by the tissue engineered muscle led to a 0.3–1% decrease in tube radius, yielding mean flowrates of $< 0.4\ \mu L/s$. Non-peer reviewed attempts to build BLPs can also be found in the PhD thesis of Hesham Azizgolshani from Gharib's lab (Azizgolshani, 2013).

These studies attempted to create BLPs using neonatal rat cardiac myocytes seeded onto vessels made from decellularized small intestinal submucosa. Cell contraction led to $< 2\%$ change in tube radius yielding < 20 nL/s mean flowrate.

The very low mean flow rates seen in these two studies (Azizgolshani, 2013; Li et al., 2019) are troublesome for two reasons. First, they offer little use for any real flow improvement in physiologically relevant settings. Second, they are in sharp contrast with much higher flow rate values obtained when using non-biological components of Liebau pumps. In the next section, we will consider factors that may limit the efficiency of BLPs, followed by the sections that consider ways to circumvent or minimize these limitations.

LIMITATIONS IMPOSED BY THE USE OF BIOLOGICAL COMPONENTS

There are several reasons behind the low flow rates reported by the above-mentioned attempts to build BLPs. The same reasons are likely to play a role in any future attempts to create Liebau pumps using biological components, particularly from mammalian cells and more specifically from their human counterparts.

The first reason is that, when compared to mechanical actuators, the pincher segment of a BLP can operate within a very limited range of compression frequencies. Cardiac myocytes isolated or derived from iPSC of animals with intrinsically high heart rates, such as mice, can be continually paced at frequencies up to 7–8 Hz (Bers, 2001). Their human counterparts are unlikely to go over 3 Hz. In most cases of skeletal muscle-based constructs, stimulation frequency can be increased to 10 Hz (Khodabukus et al., 2019), after which contractions become fused, leading to tetanus. Maximal frequency of smooth muscle contractions varies depending on muscle subtype and location, but in general, due to different molecular mechanisms underlying excitation-contraction coupling and relaxation cycles of smooth muscle, these cells are too slow to be viable candidates for repetitive fast contractions. To conclude, compression frequencies by a BLP pincher can hardly exceed 10 Hz, with 1–4 Hz being the most realistic range.

This leads us to the second reason: the limited degree of muscle shortening. By excluding smooth muscle as a main component of a BLP pincher, one is left with cross-striated muscle candidates, such as cardiac and skeletal muscle. Cross-striated muscle can shorten to only 15–20% of its resting length (Bers, 2001). Therefore, a pincher made from a muscular ring of cross-striated muscle has a limited ability to decrease the lumen. This limitation can be overcome by a non-conventional way of arranging muscle elements—some of which will be considered later. Notably, in previously mentioned studies by Azizgolshani (2013) and Li et al. (2019), decreases in lumen diameter were much smaller than the above-mentioned limit of 15–20%, leading us to the third reason.

The third reason involves the way in which the muscle layer is created. Both above-cited studies used a simple cell seeding approach to create a ring of tissue-engineered muscle (Zimmermann et al., 2002). It is now well recognized that such an approach yields a weakly contracting muscle due to underdeveloped connections between the cells and the lack of a well-organized sarcomere structure inside the cells. The use of preconditioned tissue-engineered muscle strips, strength of which has been increased by electrical and mechanical stimuli (Tandon et al., 2009; Nunes et al., 2013; Ronaldson-Bouchard et al., 2019) should significantly improve the outcome of BLPs. An additional consideration should be given to a spiral arrangement of multiple fibers within the pincher. The latter has been shown to greatly increase the efficiency of cardiac ejection (Torrent-Guasp et al., 2001) and is likely to do the same for the efficiency of the BLP pincher.

The fourth and the last reason why reported BLP yielded such low flow rates is that their design did not take into consideration insights from theoretical and experimental studies that used non-biological components. In the next sections, we will review available experimental reports and a few numerical studies with the goal of outlining strategies for more effective implementation of Liebau pumps using biofabrication tools. We will start by listing different parameters that can influence the performance of the Liebau pump.

VARIABLES THAT IMPACT LIEBAU PUMP PERFORMANCE

Despite its apparent simplicity, the physics behind flow and pressure generation by a Liebau pump is quite complex and, as such, remains the subject of intense interest by several generations of physicists and mathematicians (Takagi and Takahashi, 1985; Borzì and Propst, 2003; Manopoulos et al., 2006; Jung, 2007; Loumes et al., 2008; Kozlovsky et al., 2015). Because of its complexity, all modeling studies had to omit many involved variables. The list of such variables, each of which can potentially affect the mean flow rate created by a Liebau pump, can be seen in **Table 1**. They can be divided into four categories. The first category describes the overall pump design, including the tubing being closed or open, number of pinchers, presence of kinks or gelatinous inner layer, or difference in resistances by the two stiff ends. The second category includes the physical properties of compliant tube segments (notably, the impact of the physical properties of stiff tube segments remains to be explored). The third category includes properties of the pincher, such as its length, degree of vessel occlusion, its relative position with respect to the two ends of the compliant segment, compression frequency, duty cycle, and its dynamic waveform (i.e., square form vs. sinusoid). The fourth category includes properties of the fluid, including density, viscosity, and fluid volume, the latter having a direct impact on transmural pressure and therefore compliance of the elastic segment. For readers wanted to learn more, **Table 1** lists studies that considered, either numerically or experimentally, the impact of specific variables. Notably, the non-linear character of Liebau pumps precludes predicting, in a simple manner, the effect of many variables. Therefore,

TABLE 1 | Major variables that affect performance of Liebau pump.

Variable	*In vitro*	*In silico*	Combined
Group 1: Design			
Open vs. close	Rinderknecht et al., 2005		
Double wall	Hiermeier and Männer, 2017	Loumes et al., 2008	
Kinks	Hiermeier and Männer, 2017		
Tapering	Lee et al., 2017		
Branching		Rosenfeld and Avrahami, 2010; Zislin and Rosenfeld, 2018	
Buckle	Li et al., 2019		
Added cavities		Kozlovsky et al., 2015	
Group 2: Tube			
Length	Rinderknecht et al., 2005	Manopoulos et al., 2006; Zislin and Rosenfeld, 2018	Timmermann and Ottesen, 2009
Diameter	Hickerson et al., 2005; Rinderknecht et al., 2005	Zislin and Rosenfeld, 2018	
Wall thickness	Bringley et al., 2008	Jung, 2007	
Elastic modulus		Jung, 2007	
Loop resistance	Hickerson et al., 2005		
Shape	Wen and Chang, 2009		
Group 3: Pincher			
Width	Hickerson et al., 2005; Manopoulos et al., 2020	Manopoulos et al., 2006; Rosenfeld and Avrahami, 2010; Zislin and Rosenfeld, 2018	
Position	Hickerson et al., 2005; Bringley et al., 2008; Wen and Chang, 2009; Lee et al., 2013; Hiermeier and Männer, 2017; Manopoulos et al., 2020; Davtyan and Sarvazyan, 2021	Borzì and Propst, 2003; Rosenfeld and Avrahami, 2010; Zislin and Rosenfeld, 2018	Ottesen, 2003; Hickerson and Gharib, 2006; Timmermann and Ottesen, 2009
Force profile		Jung, 2007; Zislin and Rosenfeld, 2018	
% Occlusion	Hickerson et al., 2005; Wen and Chang, 2009; Manopoulos et al., 2020	Manopoulos et al., 2006; Jung, 2007; Rosenfeld and Avrahami, 2010; Kozlovsky et al., 2016	Ottesen, 2003
Duty cycle	Hickerson et al., 2005		
# Of pinchers	Lee et al., 2013		
Group 4: Fluid			
Fluid viscosity	Meier, 2011; Hiermeier and Männer, 2017; Davtyan and Sarvazyan, 2021		Timmermann and Ottesen, 2009
Fluid density	Hiermeier and Männer, 2017; Davtyan and Sarvazyan, 2021		Timmermann and Ottesen, 2009
Fluid volume	Hickerson et al., 2005		

changing the frequency of pinching from, for example, 10–20 Hz for the Liebau pump with one set of dimensions will increase the flow, while it will decrease it for the pump with different geometry. Such non-linearity and involvement of multiple variables explains a vast range of measured flow rate values created by experimental variations of the Liebau pump (**Table 2**).

RESONANT FREQUENCIES

Natural Frequency Concept

Based on the currently prevailing view, the main mechanism as to how the Liebau pump generates flow is depicted in **Figure 2**. Pressure waves generated by the periodic compression of the compliant segment reach the points of impedance mismatch. When the pincher is positioned asymmetrically, it leads to a dynamic pressure difference between the two ends of the compliant tube, which in turn generates the flow. It has been argued that for such a difference to be maximal, the system has to be near its resonant frequency (Hickerson et al., 2005; Hickerson and Gharib, 2006). Yet many experimental studies, including our own work (Davtyan and Sarvazyan, 2021), observed significant flow rates at frequencies that are far below the estimated natural frequency ($\mathbf{F_n}$) of the compliant segment. Let us consider the concept of $\mathbf{F_n}$ in more detail.

Frequencies at which the system resonates can be determined experimentally upon hitting the tube with a substantial force and applying a fast Fourier transform analysis to pressure signals (Manopoulos et al., 2020). There is also a simple formula to calculate the natural frequency of a tube:

$$\mathbf{F_n} = \mathbf{c}/\mathbf{2}\mathrm{L} \tag{1}$$

where **L** is the length of a tube and **c** is the velocity of the pressure or pulse wave. The latter can be measured experimentally by tracking the speed of wall deformation or via distally positioned pressure transducers. For thin-walled tubes, pulse wave velocity

TABLE 2 | Flow rate values created by experimental variations of the Liebau pump.

Year	First author	References #	Setup	Variables tested	Provided or estimated from the cited study								Calculated based on Eq. 1 and 3				
					L	*ID*	*h*	*E*	*F range*	*~Fmax*	*w*	*Qmax*	*h/D*	*c*	*c'*	*Fn*	*Qprst*
Non-biological					*cm*	*cm*	*cm*	*MPa*	*Hz*	*Hz*	*cm*	*ml/s*		*m/s*	*m/s*	*Hz*	*ml/s*
2003	Otteson	Ottesen, 2003	Closed	Frequency, pincher location, compression ratio	50	2.00	0.100	0.41	2.5–3.5	2.9	1.00	1.20	0.050	4.5	5.2	5	9.1
2005	Hickerson	Hickerson et al., 2005	Open	Frequency, elasticity, pincher size and location, system size, transmural pressure	15	1.91	0.079	1.19	1–8	4.7	2.54	40	0.042	7.0	8.1	23	34
			Closed		2	0.19	0.005	0.22	20–142	55	0.24	0.15	0.026	2.4	2.8	60	0.37
2005	Rinderknecht	Rinderknecht et al., 2005	Closed	Frequency, open vs. closed, open loop dimensions	1.96	0.20	0.005	0.40	1–180	55	0.24	0.18	0.025	3.2	3.6	81	0.41
			Open		1.20	0.025	0.005	2.00	82	82	0.04	0.0003	0.200	20.0	23	833	0.0016
2006	Hickerson	Hickerson and Gharib, 2006	Closed	Frequency, transmural pressure	15	2.00	0.080	1.19	0–8	5	2.50	20	0.040	6.9	7.9	23	37
2008	Bringley	Bringley et al., 2008	Closed	Frequency, pincher location, elastic tube rigidity	17	1.90	0.05	0.99	0.5–6.8	6.8	2.22	60	0.027	5.2	5.9	15	43
2009	Wen	Wen and Chang, 2009	open	Pincher location, symmetry, degree of compression, cross section shape	5	0.60	0.100	2.20	8–40	26	3.00	10	0.167	19.1	22	191	22
2011	Meier	Meier, 2011	Closed	Resistance, transmural pressure, wall thickness, pincher location, amplitude and offset of excitation	2	0.18	0.005	1.00	1–140	60	0.28	0.05	0.028	5.3	6.1	132	0.43
					2	0.15	0.025	13.50	1–140	140	0.28	0.14	0.167	47.4	54.5	1186	0.69
2013	Lee	Lee et al., 2013	Open	Frequency, pincher location	50	2.80	0.200	2.16	4–7	4.5	5.00	127	0.071	12.4	14.3	12	138
2017	Hiermeier	Hiermeier and Männer, 2017	Open	Frequency, viscosity, straight vs. kink, double walled	34.8	0.63	0.013		0.5–3	3	1.1	0.5	0.021				1.03
2020	Manoupolus	Manopoulos et al., 2020)	Closed	Frequency, cross-sectional area, pincher size & location	100	1.20	0.100	1.96	1–12	9.3	10.00	83	0.083	12.8	14.7	6	105
2021	Davtyan	(Davtyan and Sarvazyan, 2021	Closed	Frequency, pincher location, viscosity	3.8	0.50	0.10	0.05	0.5–2.5	2.5	0.35	0.04	0.200	3.1	3.5	40	0.17
Biological																	
2006	Forouhar	Forouhar et al., 2006	Closed	Frequency	0.02	0.006	0.002	0.002	1.6–3	2	0.00	1.0E–06	0.333	0.8	0.9	2041	1.3E-07
2013	Azizgolshani	Azizgolshani, 2013	Closed	Frequency, degree of cell seeding	5	0.40	0.010	0.40	1–4	2	0.75	0.00001	0.025	3.2	3.6	32	0.14
2019	Li	Li et al., 2019	Closed	Frequency, stimulation voltage, buckle vs. unbuckle	3	0.43	0.028	0.01	1–4	4	0.15	0.00020	0.064	0.8	0.9	13	0.09

Properties of elastic element provided/estimated from the cited study: L, length; ID, inner diameter; h, wall thickness; E, Young modulus; F_{range}, range of tested compression frequencies; F_{max}, estimated frequency at which the observed flowrate was maximal; w, width of pincher; Q_{max}, maximal flowrate observed in the study. Calculated based on Eq.1&3: h/D, ratio between the wall thickness and the inner diameter; c, estimated pulse wave velocity; c', with Poisson's ratio correction for wall thickness; F_n, estimated natural frequency based on c; Q_{prst}, estimated flowrate by a comparable peristaltic pump.

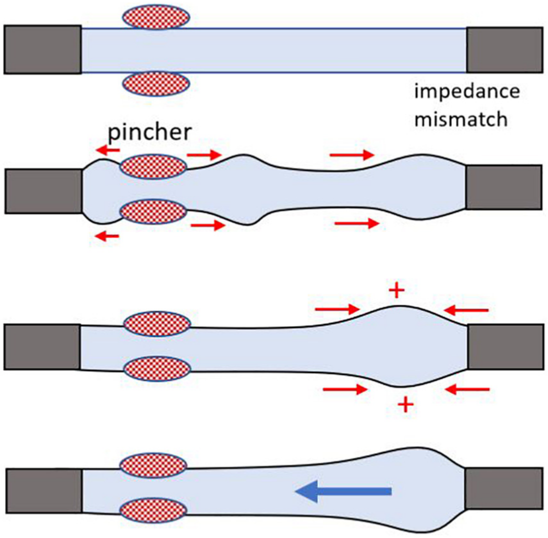

FIGURE 2 | Cartoon illustrating mismatch of impedance that creates a wave reflection site, leading to a one-way flow. A general cartoon of Liebau's principle for an open tube system. Rhythmic compressions of the flexible tube in the middle do not generate flow, while asymmetrically positioned pinch sites yield a one-way flow. The mismatch of impedance at the junction of the two tubes with different wall compliance creates a wave reflection site, a necessary condition to achieve pumping. Flow direction depends on the compression frequency, geometry, and physical properties of the tubes.

can be estimated using the Moens-Korteweg equation, where **E** is the Young modulus of the wall, **h** is wall thickness, **D** is the internal diameter, and **ρ** is fluid density:

$$\mathbf{c} = (\mathbf{Eh}/\boldsymbol{\rho}\mathbf{D})^{1/2} \tag{2}$$

For thick-walled vessels, the equation can be further modified using Poisson's ratio **υ**:

$$\mathbf{c}' = (\mathbf{Eh}/\boldsymbol{\rho}\mathbf{D}(1-\boldsymbol{\upsilon}^2))^{1/2} \tag{3}$$

Most biological materials can be considered incompressible with Poisson's ratio close to 0.5. Therefore, correcting for Poisson's ratio basically increases the estimated pulse velocity values by ∼15%.

Equation 1 implies that $\mathbf{F_n}$ is inversely proportional to the length of the compliant segment. Therefore, the smaller Liebau pump is, the higher $\mathbf{F_n}$ it is expected to have. Moreover, $\mathbf{F_n}$ is likely to increase as a result of increased values of **c**. This is because wall thickness **h** cannot decrease at the same rate as vessel diameter since this will render vessel too fragile to handle and/or to repetitively compress. Therefore, for very small Liebau pumps, one should expect **h/D** ratio in ***Equation 2*** to increase, leading to a further increase in **c** and consequently in $\mathbf{F_n}$ as per ***Equation 1***.

Calculated $\mathbf{F_n}$ value is affected by the energy losses in the system and is referred to as "damped natural frequency." These energy losses can be linked to the mass and viscosity of the moving fluid and expanding vessel walls (Babbs, 2010). They also include frictional losses from the interaction of flowing fluid with the walls of the vessel. More friction will occur in vessels with smaller diameters, with more $\mathbf{F_n}$ damping expected in narrow vessels. Additional changes to the calculated $\mathbf{F_n}$ of the complaint segment of the Liebau pump are imposed by the differences in compliance between the soft and stiff tube segments as well as the length of the latter. In the case of a closed flow loop, when the difference between the Young modules of compliant and stiff tubing decreases, the latter becomes part of the resonant system (Meier, 2011).

For the surveyed experimental studies of the Liebau pump listed in **Table 2**, we calculated pulse wave velocities **c** and undamped $\mathbf{F_n}$ values. This enabled us to compare $\mathbf{F_n}$ with the frequency at which the experimentally recorded flow rate was maximal ($\mathbf{F_{max}}$). Notably, here $\mathbf{F_{max}}$ is simply a frequency for which maximal mean flow rate was observed in *each specific study* and not what would have been observed if the *entire* range of frequencies had been examined. For calculations of $\mathbf{F_n}$ we used vessel dimensions and Young modulus provided by the authors, while filling any gaps by using information available elsewhere (indicated by asterisks). As **Table 2** shows, with few exceptions, most studies tested frequency ranges that lie *below* calculated undamped $\mathbf{F_n}$. In a few studies that examined frequency ranges that included the predicted $\mathbf{F_n}$, the $\mathbf{F_{max}}$ was actually very close to the calculated $\mathbf{F_n}$.

The overall conclusion from this section is the following: while the maximal flowrates created by Liebau pumps are predicted to occur near $\mathbf{F_n}$, published experimental studies suggest that sizable flowrates can be created using much lesser frequencies. What we mean by the word "sizable" is considered next.

COMPARISON WITH PERISTALTIC PUMPS OF SIMILAR DIMENSIONS

One way to evaluate the performance of Liebau pumps across different experimental studies is to compare them to peristaltic pumps of the same dimensions operating at the same frequency. To find a flow rate by a comparable peristaltic pump, $\mathbf{F_{max}}$ was multiplied by the volume of displaced fluid, the latter being a product of pincher width (**w**) and cross-sectional area of the tube (**A**):

$$\mathbf{Q_p} = \mathbf{F_{max}wA} \tag{4}$$

Note that to calculate the expected flow rate by peristaltic pumps, we assumed a complete closure of the lumen. The same cannot be expected for all Liebau pumps listed in **Table 2**, since the degree of lumen occlusion varied between the studies (the latter value is often omitted, with only ∼30% of surveyed studies mentioning it). Therefore, the reported maximal flow rates created by the Liebau pumps could have been higher if a complete lumen closure had been achieved. The outcome of the comparison is shown graphically in **Figure 3** using values listed in **Table 2**. The **Figure 3A** shows data from all surveyed experimental studies, while **Figure 3B** zooms in on pumps with the smallest dimensions. These plots suggest two things. First, there is a high degree of correlation between the maximal flow rates achievable by peristaltic vs. Liebau-based pumps of the same dimensions ($R^2 = 0.97$). Second, for larger

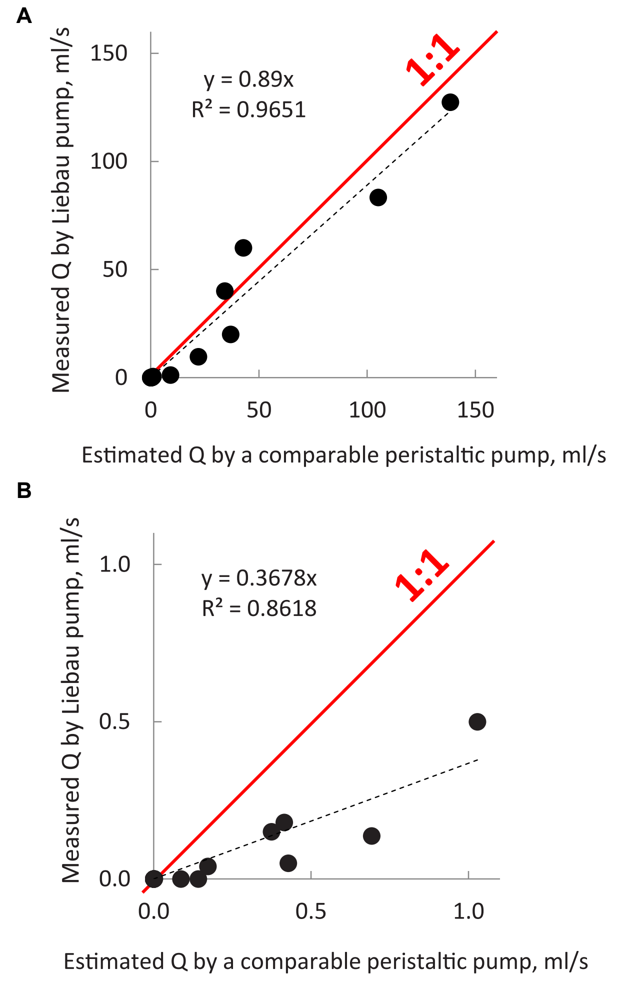

FIGURE 3 | Output of Liebau pumps in comparison to peristaltic pumps of the same dimensions. The graphs were compiled using MS Excel from published studies listed in **Table 2**. They illustrate the relative efficiency of Liebau pumps compared to peristaltic pumps of the same dimensions and compression frequencies. Dots above the red line indicate flow rates that were higher than the ones created by the peristaltic pumps; below the red line are lower. For macroscopic pumps, flow created by Liebau pumps was ∼90% from that of peristaltic flow, while for smaller pumps it was ∼40%. Data also point to a significant correlation between the two ways to pump fluid. To calculate the output of a comparable peristaltic pump, the cross-sectional area of the tube was multiplied by the width of the pincher element and the compression frequency at which the maximal flow was observed in each cited study of the Liebau pump. Red rectangle in **(A)** encompasses datapoints for micropumps. The latter has been shown in **(B)** using different scales.

pumps, this relationship is approaching 1:1, with two studies (Hickerson et al., 2005; Bringley et al., 2008) reporting flow rates exceeding the estimated peristaltic-based flow. The latter is rather remarkable since in the case of the peristaltic pump it is the entire length of the tube that needs to be engaged in active contraction, while in the Liebau pump it is only a small segment of the tube. In fact, when averaged across surveyed experimental studies, the width of the pincher was only about 12 ± 6% of the total length of the tube.

FLOW RATE-FREQUENCY RELATIONSHIP

Nearly all studies of Liebau pumps report pulsatile flow, the presence of flow reversals, and a non-linear flow rate-frequency relationship. Yet the exact shape of the latter curve, as well as the number of flow-frequency peaks, varies dramatically across studies. In addition, while some report maximal flowrate near $\mathbf{F_n}$ (Hickerson et al., 2005; Kozlovsky et al., 2015; Manopoulos et al., 2020), others report it being close to zero (Takagi and Takahashi, 1985; Borzì and Propst, 2003; Meier, 2011). In the latter cases, the performance of the valveless pump is maximum on either side of the resonant frequency, passing through zero flow rate at the resonant frequency. An interesting suggestion as to why such different patterns have been observed was made by Wen and Chang (2009). They have shown that the flow-frequency relationship shifts when the resistances between the two sides of stiff tubing to which the compliant tube is connected are different. Whether unintended small variations in resistances between the two sides can explain differently shaped frequency-flow rate curves near $\mathbf{F_n}$ values awaits further exploration.

FLOW VELOCITY PROFILES AND WOMERSLEY NUMBER

To scale and characterize the dynamics of flow in differently sized vessels, dimensionless Reynolds and Womersley numbers are commonly used. For cylindrical vessels under a steady pressure gradient, the Reynolds number<2,000 predicts laminar flow with a parabolic velocity profile. The Womersley number is used to characterize the velocity profile during pulsatile pressure conditions. The Womersley number is calculated using the values of fluid density ρ, dynamic viscosity μ, angular frequency ω, and the vessel radius **R**:

$$\mathbf{W_o = R(\rho\omega/\mu)^{1/2}} \tag{5}$$

When $\mathbf{W_o} < 1$, the flow tracks the oscillating pressure gradient, and the velocity profiles exhibit a parabolic shape. When $\mathbf{W_o} > 10$, the velocity profile is flat or plug-like, and the flow is phase-shifted relative to the oscillating pressure gradient. Values of $1 < \mathbf{W_o} < 10$ represents intermediate regimes (Manopoulos et al., 2020). For the surveyed non-biological studies of Liebau pumps listed under **Table 2**, typical $\mathbf{W_o}$ values exceed 10. In contrast, the two experimental attempts at creating BLPs (Azizgolshani, 2013; Li et al., 2019) described under see section "Published Attempts to Create Functional Biofabricated Liebau Pumps" had $\mathbf{W_o} < 10$. This was due to a combination of low frequency and small vessel diameters. In cases when solutions that mimic blood viscosity were used, the $\mathbf{W_o}$ values further declined. This was the case in our own experiments that tested the performance of the Liebau pump with physiologically relevant vessel dimensions, viscosity, and compression frequencies (Davtyan and Sarvazyan, 2021).

The Womersley number plays a role in calculating the mean flow rate **Q** from particle tracking, the latter method being one of the easiest ways to estimate the flow experimentally:

$$\mathbf{Q} = \boldsymbol{\pi}\mathbf{R}^2\mathbf{K_w v} \tag{6}$$

where **R** is the radius of the cylindrical vessel and **v** is the maximal linear velocity of the particles flowing midstream. Coefficient $\mathbf{K_w}$ enables one to account for different velocity profiles. It is equal to 0.5 when $\mathbf{Wo} < \mathbf{1}$ and the velocity profile is parabolic. When $\mathbf{Wo} > \mathbf{10}$, the $\mathbf{K_w}$ becomes close to 1, since when flow is plug-like, the velocity profile of flowing particles is nearly the same across the entire volume of the tube. For intermediate regimes when $\mathbf{1} < \mathbf{W_o} < \mathbf{10}$ an empirically derived formula can be used to derive coefficient $\mathbf{K_w}$**.** This formula was developed by Ponzini et al. (2010) and is included in **Supplementary Excel File**.

CHOICE OF VESSEL MATERIAL TO BUILD BIOFABRICATED LIEBAU PUMPS *EX VIVO*

To get closer to $\mathbf{F_n}$ within the physiological range of frequencies, i.e., 1–4 Hz, it is best to select highly stretchable materials with low Young modulus while having high tensile strength to prevent breakage. There are two possible approaches. The first approach is to excise tubular structures from an organism of choice and use them in their native, processed, or decellularized form. The most obvious choice appears to be pieces of arteries or veins. However, in their natural form, the values of Young modulus for blood vessels are still rather high. When stretched transversally, reported values of Young modulus for blood vessels span from 0.5 to 5 MPa (Riley et al., 1992; Egorov et al., 2008). When non-destructive decellularization protocols are being used, the elastic modulus of vessels changes very little (Daniel et al., 2005; Crapo et al., 2011). This is because the mechanical properties of vessels are mainly determined by interwoven collagen and elastin fibers. Other tubular structures that can be excised and used to create a compliant segment for BLPs include intestine (Herbert et al., 1993), ureter (Narita et al., 2008), or their components such as small-intestine submucosa, for example (Roeder et al., 1999). One can also consider additional treatments that can lower **E** values of these vessels while retaining their integrity, mild enzymatic treatment being one example (Trabelsi et al., 2020).

The second approach to creating BLP-compliant segments is to use the ever-expanding arsenal of biofabrication tools (Pashneh-Tala et al., 2016). Suitable tubular scaffolds can be created using casting, 3D printing, electrospinning, weaving, or other techniques (Chang and Niklason, 2017; Elomaa and Yang, 2017; Song et al., 2018). The range of biocompatible materials that can be used is vast, and they can be mixed or modified to achieve the desired stiffness (Bello et al., 2020). The Young modulus of unenforced simple hydrogels, such as gelatin, acrylamide, or agarose, is on the order of a few kPA (Chen et al., 2018; Lee et al., 2019). It can be enhanced by several orders of magnitude by including different additives (Le Goff et al., 2015; Yan et al., 2017). Collagen, elastin, and other extracellular matrix components are other obvious choices. Although pure collagen fibers are very stiff, with **E** reaching 1.2 GPa, the strength of structures made from collagen fibers can be adjusted by changing protein concentration, type, crosslinking, and inclusion of other ECM components (Gosline et al., 2002).

CREATION OF BIOFABRICATED LIEBAU PUMPS *IN VIVO*

The above-described strategies to approach $\mathbf{F_n}$ (i.e., by decreasing elastic modulus and **h/D** ratio, while increasing vessel length **L**) can work to create and test *ex vivo* BLPs. But what about creating BLPs *in vivo* by wrapping tissue engineered muscle around a vessel of choice? For medium-sized blood vessels, the **h/D** ratio is about 0.3 for arteries and 0.1 for veins. The lowest reported values of Young modulus for collagen-rich arteries and veins are about 0.2–0.5 MPa (Daniel et al., 2005). Therefore, if a 10 cm piece of vein with a diameter of 1 cm and an **E** of 0.2 MPa is used as a compliant segment of the Liebau pump, the Moens-Korteweg equation yields c = ∼4 m/s and $\mathbf{F_n}$ = 22 Hz (see **Supplementary Appendix** for formulas). The later value is too high for a pincher made from muscle cells. For smaller vessels, the $\mathbf{F_n}$ will be even higher. And if one estimates $\mathbf{F_n}$ values for an embryonic heart tube of a zebrafish by eyeballing its dimensions [200, 60, 20 μm for **L**, **D,** and **h,** respectively (Forouhar et al., 2006)], while assuming the lowest possible **E** of 2 kPA, the $\mathbf{F_n}$ will be > 2000 Hz, which is an impossible range of frequencies for biological pumps.

The above estimates of $\mathbf{F_n}$ seems to question the feasibility of creating *in vivo* BLPs while using a muscle ring as a pincher element. However, this is far from the case. Data shown in **Figure 3B** illustrate that despite being less efficient than their macro versions (i.e., **Figure 3A**), micro Liebau pumps working far from their $\mathbf{F_n}$ values generate flows that are about 10–30% of their peristaltic equivalents. Also, several modifications of Liebau pumps have been suggested. These modifications resemble features of embryonic hearts and parts of circulation in lower invertebrates. They can help to increase flow rates at frequencies lower than $\mathbf{F_n}$ and are considered next.

MODIFICATIONS TO INCREASE BIOFABRICATED LIEBAU PUMP OUTPUT

Previous paragraphs considered the simplest configuration of Liebau pumps that consisted of a single-walled cylindrical compliant segment with a single compression element. As we argued above, in this basic configuration BLPs with the length ranging from millimeters to several centimeters will yield miniscule flowrates when compressed with physiological frequencies. By mimicking scenarios that can be encountered *in vivo*, one can try to modify the basic configuration of the Liebau pump to increase the flow. One study, for example, documented the beneficial effect of kinks by showing that by bending compliant tubes in several places, one can significantly

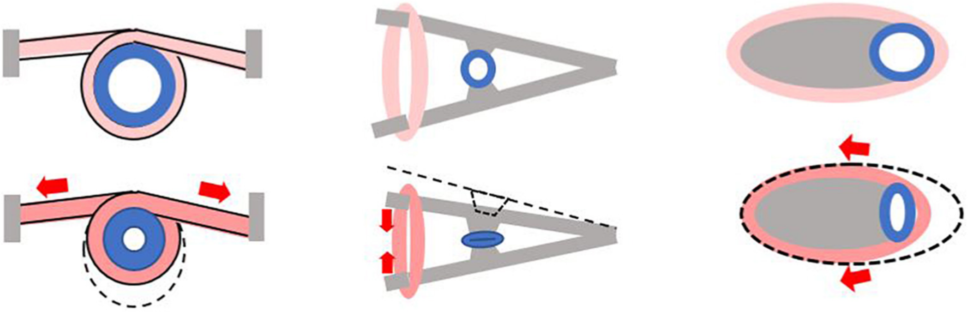

FIGURE 4 | Alternative ways to create a pincher from tissue engineered muscle. Gray color depicts stationary elements that can be created from bone-like or similar material. Pink color indicates tissue engineered muscle. Cross section of the compliant segment of Liebau pump is shown in blue. Each panel shows a pincher before (top) and during (bottom) contraction with red arrows depicting direction of muscle shortening.

increase its performance (Hiermeier and Männer, 2017). Another way to increase the mean flow rate was suggested by a theoretical study by Loumes et al. (2008). The authors tried to mimic the effects of cardiac jelly, which is present during the early stages of embryonic heart development. The proposed model predicted that the addition of a thick gelatinous layer to the inner wall of the complaint segment would greatly increase the amplitude of the pressure waves and increase the mean flow rates of the pump. Notably, in the presence of such a gelatinous layer, the vessel's lumen can be constricted to a larger degree using the same degree of outer layer shortening. The letter is particularly important for a pincher element made of striated muscle, which can only shorten to a ∼15% of its initial length. Another interesting approach to better mimic putative Liebau pumps was to add cavities before and after the pincher element (Kozlovsky et al., 2015). This was again a purely computational study, conclusions from which await experimental proof. An additional way to increase the force by which muscular band compresses the compliant tube can be to mimic the spiral structure of the cardiac wall by creating a pincher using multiple bands with alternating directions of the fibers (Torrent-Guasp et al., 2001).

One can also suggest building a Liebau pump using biological elements but without mimicking *in vivo* scenarios. This can be done by changing the position of the compression element relative to the vessel. Different configurations that can help to increase the degree of lumen compression can be envisioned (**Figure 4**). Although such configurations are unlikely to be considered in lieu of clinical treatments, one can imagine using them for organ-on-a-chip or similar applications.

RELATIVE EFFICIENCY OF LIEBAU PUMPS

Flow and pressure outputs of Liebau pumps are highly non-linear and depend on multiple factors, including those listed in **Tables 1**, **2**. Therefore, it is rather difficult to quantitively compare their energy efficiency to other types of pumping devices. As a rough estimate one can use a relationship between the maximal flowrate and the pump dimensions, an approach taken by Laser and Santiago to create a chart comparing a wide range of micropumps, including piezoelectric, thermopneumatic, electrostatic and electroosmotic devices (Laser and Santiago, 2004). The experimental data from **Table 2** and as well as evaluation by Meier (2011), places Liebau pumps on the top of that chart. Data shown **Figure 3** also suggest that at their optimal frequencies the output of Liebau pumps, particularly those on a centimeter scale, is comparable to their peristaltic counterparts. Interestingly, a significant increase in the flowrate can be achieved by the inclusion of the valves into the Liebau pump circuit (Moser et al., 1998). From the viewpoint of future clinical implementation though, addition of the valves makes little sense since their absence is probably the most beneficial feature of the Liebau pump design.

INSIGHTS FROM THE FIRST BIOFABRICATED LIEBAU PUMP ATTEMPT

Although the first published BLP attempt (Li et al., 2019) using tissue engineered rings of skeletal muscle around hydrogel tubes yielded negligible flow rates, it enabled the authors to make several interesting observations. Notably, such insights were never brought up by studies that built Liebau pumps from non-biological components or relied on simulations. Indeed, contraction of a ring of muscle cells wrapped around a vessel does not work like a mechanical pincher that compresses vessels in one dimension. Instead, the authors observed that in many cases, any significant contraction of the muscular ring led to an inward deformation of the vessel wall. Such "buckling" then impacted the calculation of a new radius of the tube as well as the degree of lumen compression. Also, the authors revealed that buckling had an unexpected effect on the flow rate-frequency relationship. When the tube was buckled, there was less resistance to the act of compression, so the degree of muscle shortening was higher at the same degree of electrical stimulation. Moreover, when stimulation frequency increased with electrical pulses arriving during relaxation, contraction amplitude decreased, giving rise to frequency dependence of contraction amplitude, i.e., the higher was the frequency, the lower was the amplitude of contraction. The authors argued that for the unbuckled case, restoring force of the elastic tube was high compared with the buckled tube, and contraction amplitude was less sensitive to the contraction frequency.

New insights, such as above, are expected from future attempts to build Liebau pumps using biological materials. We hope that this publication will encourage others to explore this fascinating phenomenon and stimulate additional experimental efforts to build valveless impedance pumps using biological materials.

CONCLUSION

Cumulative evidence from different labs point to physiological feasibility of Liebau-based valveless pumping warranting efforts to create such pumps using tissue engineering and other biofabrication tools. Such efforts will provide additional insights into performance of these pumps *in vivo* as well as further our understanding of the fundamental mechanisms driving blood flow during early development. Liebau-based biomimetic pumps can also serve as energy-efficient flow generators in organ-on-a-chip devices or be implanted to assist flow during various disease states.

AUTHOR CONTRIBUTIONS

NS conceived and wrote the manuscript.

FUNDING

This work was supported by the United States National Science Foundation EAGER award (#1927694).

ACKNOWLEDGMENTS

Rubina Davtyan is gratefully acknowledged for her help in compiling published values for **Table 2**.

SUPPLEMENTARY MATERIAL

The Supplementary Material for this article can be found online at: https://www.frontiersin.org/articles/10.3389/fphys.2021.770906/full#supplementary-material

REFERENCES

Anderson, R. H. (1981). Hearts and Heart-like Organs. Volume 1. Comparative anatomy and development. *J. Anat.* 133(Pt 1), 104.

Auerbach, D., Moehring, W., and Moser, M. (2004). An analytic approach to the Liebau problem of valveless pumping. *Cardiovasc. Eng.* 4, 201–207. doi: 10.1023/b:care.0000031549.13354.5e

Azizgolshani, H. (2013). *Tissue Engineering Active Biological Machines: Bio-Inspired Design, Directed Self-Assembly, and Characterization of Muscular Pumps Simulating the Embryonic Heart*. Ph.D. Thesis. California, CA: California Institute of Technology.

Babbs, C. F. (2010). Behavior of a viscoelastic valveless pump: a simple theory with experimental validation. *Biomed. Eng. Online* 9:42. doi: 10.1186/1475-925X-9-42

Bello, A. B., Kim, D., Kim, D., Park, H., and Lee, S. H. (2020). Engineering and functionalization of gelatin biomaterials: from cell culture to medical applications. *Tissue Eng. Part B Rev.* 26, 164–180. doi: 10.1089/ten.TEB.2019.0256

Bers, D. (2001). *Excitation-Contraction Coupling and Cardiac Contractile Force*, 2nd Edn. Berlin: Springer Science & Business Media.

Borzì, A., and Propst, G. (2003). Numerical investigation of the Liebau phenomenon. *Zeitschrift Angew Math. Phys.* 54, 1050–1072.

Breckwoldt, K., Letuffe-Brenière, D., Mannhardt, I., Schulze, T., Ulmer, B., Werner, T., et al. (2017). Differentiation of cardiomyocytes and generation of human engineered heart tissue. *Nat. Protoc.* 12, 1177–1197.

Bringley, T. T., Chilress, S., Vandenberghe, N., and Zhang, J. (2008). An experimental investigation and a simple model of a valveless pump. *Phys. Fluids* 20:33602.

Burton, R. A. B., Klimas, A., Ambrosi, C. M., Tomek, J., Corbett, A., Entcheva, E., et al. (2015). Optical control of excitation waves in cardiac tissue. *Nat. Photonics* 9, 813–816. doi: 10.1038/nphoton.2015.196

Carrier, R. L., Papadaki, M., Rupnick, M., Schoen, F. J., Bursac, N., Langer, R., et al. (1999). Cardiac tissue engineering: cell seeding, cultivation parameters, and tissue construct characterization. *Biotechnol. Bioeng.* 64, 580–589. doi: 10.1002/(sici)1097-0290(19990905)64:5<580::aid-bit8>3.0.co;2-x

Chang, W. G., and Niklason, L. E. (2017). A short discourse on vascular tissue engineering. *NPJ Regen. Med.* 2:7. doi: 10.1038/s41536-017-0011-6

Chen, R., Xu, X., Yu, D., Xiao, C., Liu, M., Huang, J., et al. (2018). Highly stretchable and fatigue resistant hydrogels with low Young's modulus as transparent and flexible strain sensors. *J. Mater. Chem. C. R. Soc. Chem.* 6:11193. doi: 10.1039/c8tc02583e

Crapo, P. M., Gilbert, T. W., and Badylak, S. F. (2011). An overview of tissue and whole organ decellularization processes. *Biomaterials* 32, 3233–3243. doi: 10.1016/j.biomaterials.2011.01.057

Cvetkovic, C., Raman, R., Chan, V., Williams, B. J., Tolish, M., Bajaj, P., et al. (2014). Three-dimensionally printed biological machines powered by skeletal muscle. *Proc. Natl. Acad. Sci. U.S.A.* 111, 10125–10130. doi: 10.1073/pnas.1401577111

Dai, W., Hale, S. L., and Kloner, R. A. (2006). Cardiac cells implanted within the outer aortic wall of rats generate measurable contractile force. *Regen. Med.* 1, 119–124. doi: 10.2217/17460751.1.1.119

Daniel, J., Abe, K., and McFetridge, P. S. (2005). Development of the human umbilical vein scaffold for cardiovascular tissue engineering applications. *ASAIO J.* 51, 252–261. doi: 10.1097/01.mat.0000160872.41871.7e

Davtyan, R., and Sarvazyan, N. A. (2021). Output of a valveless Liebau pump with biologically relevant vessel properties and compression frequencies. *Sci. Rep.* 11:11505. doi: 10.1038/s41598-021-90820-4

Egorov, V., Tsyuryupa, S., Kanilo, S., Kogit, M., and Sarvazyan, A. (2008). Soft tissue elastometer. *Med. Eng. Phys.* 30, 206–212. doi: 10.1016/j.medengphy.2007.02.007

Elomaa, L., and Yang, Y. P. (2017). Additive manufacturing of vascular grafts and vascularized tissue constructs. *Tissue Eng. Part B Rev.* 23, 436–450. doi: 10.1089/ten.TEB.2016.0348

Entcheva, E. (2013). Cardiac optogenetics. *Am. J. Physiol. Heart Circ. Physiol.* 304, H1179–H1191.

Entcheva, E., and Kay, M. W. (2020). Cardiac optogenetics: a decade of enlightenment. *Nat. Rev. Cardiol.* 18, 349–367. doi: 10.1038/s41569-020-00478-0

Forouhar, A. S., Liebling, M., Hickerson, A., Nasiraei-Moghaddam, A., Tsai, H. J., Hove, J. R., et al. (2006). The embryonic vertebrate heart tube is a dynamic suction pump. *Science* 312, 751–753. doi: 10.1126/science.1123775

Gosline, J., Lillie, M., Carrington, E., Guerette, P., Ortlepp, C., and Savage, K. (2002). Elastic proteins: biological roles and mechanical properties. *Philos. Trans. R Soc. B Biol. Sci.* 357, 121–132. doi: 10.1098/rstb.2001.1022

Herbert, S. T., Badylak, S. F., Geddes, L. A., Hillberry, B., Lantz, G. C., and Kokini, K. (1993). Elastic modulus of prepared canine jejunum, a new vascular graft material. *Ann. Biomed. Eng.* 21, 727–733. doi: 10.1007/BF02368651

Hickerson, A. I., and Gharib, M. (2006). On the resonance of a pliant tube as a mechanism for valveless pumping. *J. Fluid. Mech.* 555, 141–148. doi: 10.1017/s0022112006009220

Hickerson, A. I., Rinderknecht, D., and Gharib, M. (2005). Experimental study of the behavior of a valveless impedance pump. *Exp. Fluids* 38, 534–540. doi: 10.1007/s00348-005-0946-z

Hiermeier, F., and Männer, J. (2017). Kinking and torsion can significantly improve the efficiency of valveless pumping in periodically compressed tubular conduits. Implications for understanding of the form-function relationship of embryonic heart tubes. *J. Cardiovasc. Dev. Dis.* 4:19. doi: 10.3390/jcdd4040019

Jaffrin, M. Y., and Shapiro, A. H. (1971). Peristaltic pumping. *Annu. Rev. Fluid Mech.* 3, 13–37.

Johansen, K., Burggren, W., and Bourne, G. H. (1980). "Cardiovascular function in the lower vertebrates," in *Hear Hear Organs*, ed. G. H. Bourne (London: Academic Press), 61–117. doi: 10.1016/b978-0-12-119401-7.50009-8

Juhas, M., Engelmayr, G. C., Fontanella, A. N., Palmer, G. M., and Bursac, N. (2014). Biomimetic engineered muscle with capacity for vascular integration and functional maturation in vivo. *Proc. Natl. Acad. Sci. U.S.A.* 111, 5508–5513. doi: 10.1073/pnas.1402723111

Jung, E. (2007). A mathematical model of valveless pumping: a lumped model with time-dependent compliance, resistance, and inertia. *Bull. Math. Biol.* 69, 2181–2198. doi: 10.1007/s11538-007-9208-y

Jung, E., and Peskin, C. S. (2002). Two-dimensional simulations of valveless pumping using the immersed boundary method. *SIAM J. Sci. Comput.* 23, 19–45. doi: 10.1007/s12013-011-9157-9

Kang, H. W., Lee, S. J., Ko, I. K., Kengla, C., Yoo, J. J., and Atala, A. (2016). A 3D bioprinting system to produce human-scale tissue constructs with structural integrity. *Nat. Biotechnol.* 34, 312–319. doi: 10.1038/nbt.3413

Karabekian, Z., Ding, H., Stybayeva, G., Ivanova, I., Muselimyan, N., Haque, A., et al. (2015a). HLA Class I depleted hESC as a source of hypoimmunogenic cells for tissue engineering applications. *Tissue Eng. Part A* 21, 2559–2571. doi: 10.1089/ten.TEA.2015.0105

Karabekian, Z., Idress, S., Jamshidi, A., Posnack, N. G., Sarvazyan, N. A., Idrees, S., et al. (2015b). Downregulation of beta-microglobulin to diminish T-lymphocyte lysis of non-syngeneic cell sources of engineered heart tissue constructs. *Biomed. Mater.* 10:34101. doi: 10.1088/1748-6041/10/3/034101

Khodabukus, A., Madden, L., Prabhu, N. K., Koves, T. R., Jackman, C. P., Muoio, D. M., et al. (2019). Electrical stimulation increases hypertrophy and metabolic flux in tissue-engineered human skeletal muscle. *Biomaterials* 198, 259–269. doi: 10.1016/j.biomaterials.2018.08.058

Koti, P., Muselimyan, N., Mirdamadi, E., Asfour, H., and Sarvazyan, N. A. (2019). Use of GelMA for 3D printing of cardiac myocytes and fibroblasts. *J. 3D Print Med.* 3, 11–22. doi: 10.2217/3dp-2018-0017

Kozlovsky, P., Bryson-Richardson, R. J., Jaffa, A. J., Rosenfeld, M., and Elad, D. (2016). The driving mechanism for unidirectional blood flow in the tubular embryonic heart. *Ann. Biomed. Eng. Springer N. Y. LLC* 44:3069. doi: 10.1007/s10439-016-1620-8

Kozlovsky, P., Rosenfeld, M., Jaffa, A. J., and Elad, D. (2015). Dimensionless analysis of valveless pumping in a thick-wall elastic tube: application to the tubular embryonic heart. *J. Biomech.* 48:1652. doi: 10.1016/j.jbiomech.2015.03.001

Laser, D. J., and Santiago, J. G. (2004). A review of micropumps. *J. Micromech. Microeng.* 14:R35.

Le Goff, K. J., Gaillard, C., Helbert, W., Garnier, C., and Aubry, T. (2015). Rheological study of reinforcement of agarose hydrogels by cellulose nanowhiskers. *Carbohydr. Polym.* 116, 117–123. doi: 10.1016/j.carbpol.2014.04.085

Lee, D., Zhang, H., and Ryu, S. (2019). "Elastic modulus measurement of hydrogels," in *Cellulose-Based Superabsorbent Hydrogels. Polymers and Polymeric Composites: A Reference Series*, ed. M. Mondal (Cham: Springer), 865–884. doi: 10.1007/978-3-319-77830-3_60

Lee, V. C. C., Abakr, Y. A., and Woo, K. C. (2013). Valveless pumping using a two-stage impedance pump. *Front. Mech. Eng.* 8:311. doi: 10.1007/s11465-013-0270-x

Lee, V. C. C., Chai, C. H., Law, M. C., and Wee, S. K. (2017). On the analysis of impedance-driven reverse flow dynamics. *J. Eng. Sci. Technol.* 12, 451–459.

Li, Z., Seo, Y., Aydin, O., Elhebeary, M., Kamm, R. D., Kong, H., et al. (2019). Biohybrid valveless pump-bot powered by engineered skeletal muscle. *Proc. Natl. Acad. Sci. U.S.A.* 116, 1543–1548. doi: 10.1073/pnas.1817682116

Liebau, G. (1954). Uber ein ventilloses Pumpprinzip. *Naturwissenschaften* 41:327. doi: 10.1007/bf00644490

Liebau, G. (1955). Die Strömungsprinzipien des Herzens. *Z. Kreislaufforsch.* 44:677.

Longatti, P. (2018). The Liebau phenomenon: a translational approach to new paradigms of CSF circulation and related flow disturbances. *Child's Nerv. Syst.* 34, 227–233. doi: 10.1007/s00381-017-3653-1

Loumes, L., Avrahami, I., and Gharib, M. (2008). Resonant pumping in a multilayer impedance pump. *Phys. Fluids* 20:23013.

Ma, C., Peng, Y., Li, H., and Chen, W. (2021). Organ-on-a-Chip: a new paradigm for drug development. *Trends Pharmacol. Sci.* 42, 119–133. doi: 10.1016/j.tips.2020.11.009

Männer, J., Wessel, A., and Yelbuz, T. M. (2010). How does the tubular embryonic heart work? Looking for the physical mechanism generating unidirectional blood flow in the valveless embryonic heart tube. *Dev. Dyn.* 239, 1035–1046. doi: 10.1002/dvdy.22265

Manopoulos, C., Tsangaris, S., and Mathioulakis, D. (2020). Net flow generation in closed-loop valveless pumping. *Proc. Inst. Mech. Eng. Part C J. Mech. Eng. Sci.* 234:2126. doi: 10.1177/0954406220904110

Manopoulos, C. G., Mathioulakis, D. S., and Tsangaris, S. G. (2006). One-dimensional model of valveless pumping in a closed loop and a numerical solution. *Phys. Fluids* 18:17106.

Meier, J. (2011). *A Novel Experimental Study of A Valveless Impedance Pump for Applications at Lab-On-Chip, Microfluidic, and Biomedical Device Size Scales.* Ph.D. Thesis. California, CA: California Institute of Technology.

Moser, M., Huang, J., Schwarz, G., Kenner, T., and Noordergraaf, A. (1998). Impedance defined flow. Generalisation of William Harvey's concept of the circulation—370 years later. *Int. J. Cardiovasc. Med. Sci.* 1, 205–211.

Narita, Y., Kagami, H., Matsunuma, H., Murase, Y., Ueda, M., and Ueda, Y. (2008). Decellularized ureter for tissue-engineered small-caliber vascular graft. *J. Artif. Organs* 11, 91–99. doi: 10.1007/s10047-008-0407-6

Nguyen, T.-U., Bashur, C. A., and Kishore, V. (2016). Impact of elastin incorporation into electrochemically aligned collagen fibers on mechanical properties and smooth muscle cell phenotype. *Biomed. Mater.* 11:25008. doi: 10.1088/1748-6041/11/2/025008

Nunes, S. S., Miklas, J. W., Liu, J., Aschar-Sobbi, R., Xiao, Y., Zhang, B., et al. (2013). Biowire: a platform for maturation of human pluripotent stem cell-derived cardiomyocytes. *Nat. Methods* 10, 781–787.

Ottesen, J. T. (2003). Valveless pumping in a fluid-filled closed elastic tube-system: one-dimensional theory with experimental validation. *J. Math. Biol.* 46, 309–332. doi: 10.1007/s00285-002-0179-1

Pahlevan, N. M., and Gharib, M. (2013). In-vitro investigation of a potential wave pumping effect in human aorta. *J. Biomech.* 46, 2122–2129. doi: 10.1016/j.jbiomech.2013.07.006

Pashneh-Tala, S., MacNeil, S., and Claeyssens, F. (2016). The tissue-engineered vascular graft - Past, present, and future. *Tissue Eng. Part B Rev.* 22, 68–100. doi: 10.1089/ten.teb.2015.0100

Ponzini, R., Vergara, C., Rizzo, G., Veneziani, A., Roghi, A., Vanzulli, A., et al. (2010). Womersley number-based estimates of blood flow rate in doppler analysis: in vivo validation by means of phase-contrast MRI. *IEEE Trans. Biomed. Eng.* 57, 1807–1815. doi: 10.1109/TBME.2010.2046484

Radisic, M., Park, H., Shing, H., Consi, T., Schoen, F. J., Langer, R., et al. (2004). Functional assembly of engineered myocardium by electrical stimulation of cardiac myocytes cultured on scaffolds. *Proc. Natl. Acad. Sci. U.S.A.* 101, 18129–18134. doi: 10.1073/pnas.0407817101

Raman, R., Cvetkovic, C., Uzel, S. G. M., Platt, R. J., Sengupta, P., Kamm, R. D., et al. (2016). Optogenetic skeletal muscle-powered adaptive biological machines. *Proc. Natl. Acad. Sci. U.S.A.* 113, 3497–3502. doi: 10.1073/pnas.1516139113

Reeser, K., and Doiron, A. L. (2019). Three-dimensional printing on a rotating cylindrical mandrel: a review of additive-lathe 3D printing technology. 3D Print. *Addit. Manuf. Mary Ann. Liebert Inc.* 6, 293–307. doi: 10.1089/3dp.2019.0058

Riley, W. A., Barnes, R. W., Evans, G. W., and Burke, G. L. (1992). Ultrasonic measurement of the elastic modulus of the common carotid artery: the atherosclerosis risk in communities (aric) study. *Stroke* 23, 952–956. doi: 10.1161/01.str.23.7.952

Rinderknecht, D., Hickerson, A. I., and Gharib, M. (2005). A valveless micro impedance pump driven by electromagnetic actuation. *J. Micromech. Microeng.* 15:861. doi: 10.1088/0960-1317/15/4/026

Roeder, R., Wolfe, J., Lianakis, N., Hinson, T., Geddes, L. A., and Obermiller, J. (1999). Compliance, elastic modulus, and burst pressure of small-intestine submucosa (SIS), small-diameter vascular grafts. *J. Biomed. Mater. Res.* 47:65. doi: 10.1002/(sici)1097-4636(199910)47:1<65::aid-jbm9>3.0.co;2-f

Ronaldson-Bouchard, K., Yeager, K., Teles, D., Chen, T., Ma, S., Song, L. J., et al. (2019). Engineering of human cardiac muscle electromechanically matured to an adult-like phenotype. *Nat. Protoc.* 14, 2781–2817. doi: 10.1038/s41596-019-0189-8

Rosenfeld, M., and Avrahami, I. (2010). Net flow rate generation by a multi-pincher impedance pump. *Comput. Fluids* 39:1634. doi: 10.1016/j.compfluid.2010.05.016

Santhanakrishnan, A., and Miller, L. A. (2011). Fluid dynamics of heart development. *Cell Biochem. Biophys.* 61, 1–22. doi: 10.1007/s12013-011-9158-8

Santhanakrishnan, A., Nguyen, N., Cox, J. G., and Miller, L. A. (2009). Flow within models of the vertebrate embryonic heart. *J. Theor. Biol.* 259, 449–461. doi: 10.1016/j.jtbi.2009.04.020

Sarvazyan, N. (2014a). Creating biological pumps using engineered heart tissue. *Tissue Eng. Part A.* 20:S46.

Sarvazyan, N. (2014b). Thinking outside the heart: use of engineered cardiac tissue for treatment of chronic deep venous insufficiency. *J. Cardiovasc. Pharmacol. Ther.* 19, 394–401. doi: 10.1177/1074248413520343

Schuurman, W., Khristov, V., Pot, M. W., Van Weeren, P. R., Dhert, W. J. A., and Malda, J. (2011). Bioprinting of hybrid tissue constructs with tailorable mechanical properties. *Biofabrication* 3:21001. doi: 10.1088/1758-5082/3/2/021001

Song, H. H. G., Rumma, R. T., Ozaki, C. K., Edelman, E. R., and Chen, C. S. (2018). Vascular tissue engineering: progress, challenges, and clinical promise. *Cell Stem Cell* 22, 340–354. doi: 10.1016/j.stem.2018.02.009

Swift, L., Karimi, V., Velez, M., Simonyan, H., Patev, N., Posnack, N. G., et al. (2014). Engineered heart tissue to aid venous flow. *Tissue Eng. Part A.* 20, S119.

Takagi, S., and Takahashi, K. (1985). Study of a piston pump without valves: pumping effect and resonance in a pipe-capacity-system with a t-junction. *Bull. Japan Soc. Mech. Eng.* 28, 831–836.

Tandon, N., Cannizzaro, C., Chao, P.-H. G., Maidhof, R., Marsano, A., Au, H. T. H., et al. (2009). Electrical stimulation systems for cardiac tissue engineering. *Nat. Protoc.* 4, 155–173. doi: 10.1038/nprot.2008.183

Thomann, H. (1978). A simple pumping mechanism in a valveless tube. *Zeitschrift. Angew Math. Phys. ZAMP.* 29:169.

Timmermann, S., and Ottesen, J. T. (2009). Novel characteristics of valveless pumping. *Phys. Fluids* 21:53601.

Torrent-Guasp, F., Buckberg, G. D., Clemente, C., Cox, J. L., Coghlan, H. C., and Gharib, M. (2001). The structure and function of the helical heart and its buttress wrapping. I. The normal macroscopic structure of the heart. *Semin. Thorac. Cardiovasc. Surg.* 13, 301–319.

Trabelsi, O., Dumas, V., Breysse, E., Laroche, N., and Avril, S. (2020). In vitro histomechanical effects of enzymatic degradation in carotid arteries during inflation tests with pulsatile loading. *J. Mech. Behav. Biomed. Mater.* 103:103550. doi: 10.1016/j.jmbbm.2019.103550

Wen, C. Y., and Chang, H. T. (2009). Design and characterization of valveless impedance pumps. *J. Mech.* 25:345. doi: 10.1017/s1727719100002835

Yan, X., Chen, Q., Zhu, L., Chen, H., Wei, D., Chen, F., et al. (2017). High strength and self-healable gelatin/polyacrylamide double network hydrogels. *J. Mater. Chem. B* 5:7683. doi: 10.1039/c7tb01780d

Zawieja, D. C. (2009). Contractile physiology of lymphatics. *Lymphat Res. Biol.* 7, 87–96. doi: 10.1089/lrb.2009.0007

Zhang, B., Korolj, A., Lai, B. F. L., and Radisic, M. (2018). Advances in organ-on-a-chip engineering. *Nat. Rev. Mater.* 3, 257–278.

Zhang, D., Shadrin, I. Y., Lam, J., Xian, H.-Q., Snodgrass, H. R., and Bursac, N. (2013). Tissue-engineered cardiac patch for advanced functional maturation of human ESC-derived cardiomyocytes. *Biomaterials* 34, 5813–5820. doi: 10.1016/j.biomaterials.2013.04.026

Zhang, Y. S., Yue, K., Aleman, J., Mollazadeh-Moghaddam, K., Bakht, S. M., Yang, J., et al. (2017). 3D bioprinting for tissue and organ fabrication. *Ann. Biomed. Eng.* 45, 148–163. doi: 10.1007/s10439-016-1612-8

Zimmermann, W. H., Schneiderbanger, K., Schubert, P., Didié, M., Münzel, F., Heubach, J. F., et al. (2002). Tissue engineering of a differentiated cardiac muscle construct. *Circ. Res.* 90, 223–230. doi: 10.1161/hh0202.103644

Zislin, V., and Rosenfeld, M. (2018). Impedance pumping and resonance in a multi-vessel system. *Bioengineering* 5:63. doi: 10.3390/bioengineering5030063

Conflict of Interest: The author declares that the research was conducted in the absence of any commercial or financial relationships that could be construed as a potential conflict of interest.

frontiers in Physiology

ORIGINAL RESEARCH
published: 08 February 2022
doi: 10.3389/fphys.2021.817334

Variability of *in vivo* Sarcomere Length Measures in the Upper Limb Obtained With Second Harmonic Generation Microendoscopy

Amy N. Adkins*[1,2,3]*, Ryan M. Fong*[1,2]*, Julius P. A. Dewald*[1,4,5] *and Wendy M. Murray*[1,2,3,4,5]*

[1] Department of Biomedical Engineering, Northwestern University, Evanston, IL, United States, [2] Shirley Ryan AbilityLab, Chicago, IL, United States, [3] Edward Hines, Jr. VA Hospital, Hines, IL, United States, [4] Department of Physical Therapy and Human Movement Sciences, Northwestern University Feinberg School of Medicine, Chicago, IL, United States, [5] Department of Physical Medicine and Rehabilitation, Northwestern University Feinberg School of Medicine, Chicago, IL, United States

The lengths of a muscle's sarcomeres are a primary determinant of its ability to contract and produce force. In addition, sarcomere length is a critical parameter that is required to make meaningful comparisons of both the force-generating and excursion capacities of different muscles. Until recently, *in vivo* sarcomere length data have been limited to invasive or intraoperative measurement techniques. With the advent of second harmonic generation microendoscopy, minimally invasive measures of sarcomere length can be made for the first time. This imaging technique expands our ability to study muscle adaptation due to changes in stimulus, use, or disease. However, due to past inability to measure sarcomeres outside of surgery or biopsy, little is known about the natural, anatomical variability in sarcomere length in living human subjects. To develop robust experimental protocols that ensure data provide accurate representations of a muscle's sarcomere lengths, we sought to quantify experimental uncertainty associated with *in vivo* measures of sarcomere lengths. Specifically, we assessed the variability in sarcomere length measured (1) within a single image, along a muscle fiber, (2) across images captured within a single trial, across trials, and across days, as well as (3) across locations in the muscle using second harmonic generation in two upper limb muscles with different muscle architectures, functions, and sizes. Across all of our measures of variability we estimate that the magnitude of the uncertainty for *in vivo* sarcomere length is on the order of ∼0.25 μm. In the two upper limb muscles studied we found larger variability in sarcomere lengths within a single insertion than across locations. We also developed custom code to make measures of sarcomere length variability across a single fiber and determined that this codes' accuracy is an order of magnitude smaller than our measurement uncertainty due to sarcomere variability. Together, our findings provide guidance for the development of robust experimental design and analysis of *in vivo* sarcomere lengths in the upper limb.

Keywords: sarcomere length, second harmonic generation imaging, skeletal muscle, muscle architecture, sarcomere variability

Edited by:
Stefano Biressi,
University of Trento, Italy

Reviewed by:
Coen Ottenheijm,
VU Medical Center, Netherlands
Massimo Reconditi,
University of Florence, Italy

****Correspondence:***
Wendy M. Murray
w-murray@northwestern.edu

Specialty section:
This article was submitted to Striated Muscle Physiology, a section of the journal Frontiers in Physiology

Received: *17 November 2021*
Accepted: *27 December 2021*
Published: *08 February 2022*

Citation:
Adkins AN, Fong RM, Dewald JPA and Murray WM (2022) Variability of in vivo Sarcomere Length Measures in the Upper Limb Obtained With Second Harmonic Generation Microendoscopy. Front. Physiol. 12:817334. doi: 10.3389/fphys.2021.817334

INTRODUCTION

Whole muscle is made up of hundreds of thousands of sarcomeres arranged in series and parallel. The length of a muscle's sarcomeres is a primary determinant of a muscle's ability to contract and produce force (Gordon et al., 1966). In addition, when quantifying muscle architecture, sarcomere length is a critical parameter that is required to make meaningful comparisons of both the force-generating and excursion capacities of different muscles. With the advent of second harmonic generation (SHG) microendoscopy for measuring sarcomere length minimally invasively (Llewellyn et al., 2008), there are exciting and novel opportunities to measure sarcomere length *in vivo*.

Anatomical studies in cadavers, which involve dissection and measurement across multiple scales (whole muscles, fascicles, and sarcomeres), demonstrate that a major distinction among different skeletal muscles in the human body is the number of sarcomeres in series and parallel (Brand et al., 1981; Lieber et al., 1990; Lieber and Fridén, 2000). Serial sarcomere number (SSN) is a particularly important architectural parameter, as it describes the range of lengths over which a muscle can actively generate force and, given optimal sarcomere length, a measure of the fascicle length at which the muscle will produce its maximum isometric force. The number of parallel sarcomeres is proportional to the maximum isometric force a muscle can produce. In anatomical studies, SSN is commonly characterized by a muscle's optimal fascicle length (OFL), which is calculated as the ratio of fascicle and sarcomere lengths measured from a muscle's dissected fascicles, multiplied by optimal sarcomere length. Similarly, the number of sarcomeres in parallel is characterized by a muscle's physiological cross-sectional area (PCSA), which is calculated from the ratio of the muscle's volume and OFL, with a correction for the pennation angle of the fibers to estimate how much of the force-generating capacity is transmitted by the tendon. Measures of *in vivo* fascicle length and muscle volume have been made using safe and effective imaging techniques for decades. The novel capacity to make minimally invasive measures of sarcomere length *in vivo* provides new opportunities to study functionally meaningful muscle parameters (OFL and PCSA) and how they vary in living subjects across muscles, individuals, and due to alterations in muscle stimulus or use.

Due to the novelty of methods for sarcomere length measurement that do not involve surgery or biopsy, little is known about the natural, anatomical variability in sarcomere length in living human subjects. Such an understanding is critical for the development of robust experimental protocols that ensure data provide accurate representations of a muscle's sarcomere lengths. Animal muscle studies (e.g., Moo et al., 2016, 2017) and a single *in vivo* study on the tibialis anterior (Lichtwark et al., 2018) suggest that sarcomere length can vary considerably throughout a muscle. Importantly, the SHG microendoscopy method provides only a small field-of-view (82 μm × 82 μm, ∼20–35 sarcomeres in series) (Llewellyn et al., 2008; Sanchez et al., 2015). In addition, current protocols for processing SHG data utilize a method which provides a single measure—the mean sarcomere length—per image, precluding information about within fiber variability. To enable effective studies of how muscle sarcomere length may differ or change (e.g., across limbs, after an exercise intervention, following an injury, etc.), more information describing the natural anatomical variability, both across different locations in a single muscle and along a single muscle fiber, is needed.

In this study we aim to quantify experimental uncertainty associated with *in vivo* measures of sarcomere lengths made using second harmonic generation microendoscopy in two muscles of the upper limb (biceps brachii and flexor carpi ulnaris). Given the precision of the SHG imaging and measurement procedures established in the literature is small (∼30 nm) (Sanchez et al., 2015), we expect the primary sources of measurement uncertainty to include both natural anatomical variability of the lengths of the sarcomeres within these muscles and the random error associated with test-retest reliability using this method. In this study, we assessed the variability in sarcomere length measured (1) within a single image, along a muscle fiber, (2) across images captured within a single trial, across trials, and across days, as well as (3) across locations in the muscle. Quantifying the degree of experimental uncertainty for sarcomere length measures made using second harmonic generation microendoscopy will aid interpretation of these novel data, guide the design of future work aimed at detecting sarcomere length differences among different populations, and enable error propagation when sarcomere length measures are incorporated with other anatomical measures to calculate functionally meaningful muscle architectural parameter values.

MATERIALS AND METHODS

Data Collection

The 14 participants enrolled in this study provided informed consent; Northwestern University's Institutional Review Board approved this study's procedures. Imaging for both the biceps brachii and flexor carpi ulnaris (FCU) was completed under passive conditions, with participants seated. For biceps imaging, the participants arm was placed with the shoulder abducted 85°, elbow extended 25°, and wrist at neutral (0°), as verified by handheld goniometric measures. For the FCU, the limb was positioned with the elbow at 70° of flexion and the wrist at neutral (0°). Soft velcro straps were used to secure the arm after the joint angles were verified.

To image sarcomeres *in vivo*, a microendoscopic probe consisting of two 1.8 cm long, 20-gauge needles with beveled tips was inserted into the muscle of interest with its optical lenses aligned parallel to the fascicle direction. Insertion location of the probe was guided through palpation techniques and ultrasound imaging in the imaging limb posture. Ultrasound images were viewed in both the short and long axis planes of the muscle to identify key anatomical landmarks and to ensure both insertion in the correct muscle of interest and avoidance of major blood vessels, nerves, and bone. Once established, the appropriate location for probe insertion was marked on the skin.

As described previously (Adkins et al., 2021), a spring loaded injector was used to insert the microendoscopic probe into the muscle. Once inserted, images are acquired 0.3 cm superficial to the tip of the probe. Differences in muscle size and body composition among different participants means the exact depth that images are collected within the muscle can vary between subjects. For both the biceps brachii and FCU, we aimed to obtain images away from the inner tendon. For the biceps brachii, the distal nature of the inner tendon and the dimensions of the muscle and subcutaneous fat observed among our participants meant we could accomplish this while the full length of the probe needles (1.8 cm) were inserted in the muscle. Due to the longer central tendon, the smaller muscle belly size of the FCU, and its close proximity to the ulnar nerve, we needed to limit the insertion depth of the microendoscopic probe. For FCU, we modified imaging depth at the time of injection by adding custom spacers (thickness ranged from 0.2 to 0.7 cm) between the external surface of the skin and the base of the spring loaded injector.

Once the probe was placed as desired within the muscle belly, a second-harmonic generation microscope (Enspectra Health, Mountain View, CA, United States) was attached to it for imaging. In this implementation [probe design same as (Lichtwark et al., 2018; Adkins et al., 2021) as opposed to older design (Sanchez et al., 2015; Chen and Delp, 2016; Chen et al., 2016)], laser light travels down one of the probe's needles, interacts with the muscle tissue, and is then received by the other needle. The resulting images capture the intrinsic striation pattern (A-bands) of sarcomeres and have a field of view of 82 × 82 microns. Data were collected at 1.9 Hz for approximately 2–5 min (∼250–600 images per acquisition). The system was calibrated by the manufacturer using a precision Ronchi Ruling target with 10-micron line spacing to calculate the conversion factor (0.16 microns per pixel) for quantification of striation spacing from the images.

Variability Along Fiber

Current image processing methods for analysis of SHG images (mean sarcomere length code; MSLC) report a single mean sarcomere length value for an entire image (e.g., Sanchez et al., 2015; Adkins et al., 2021). Here, we developed and validated an image processing and analysis code (individual sarcomere length code: ISLC) which quantifies: the lengths of individual sarcomeres within an image, the mean length of these sarcomeres, and standard deviation in sarcomere length within the image. To verify the performance of the ISLC, realistic virtual phantoms were designed, tested for their similarity to real data, and then used to calculate and compare the accuracy and precision of the novel ISLC and the existing MSLC.

Individual Sarcomere Length Code

The image processing protocol developed in this study was designed to quantify the length of individual sarcomeres within an image, along the imaged fiber direction, using custom written MATLAB code. Specifically, the ISLC takes a Fast Fourier Transform (FFT) of each image and applies a threshold to reduce noise and clear the edges of the Fourier space. The inverse FFT (IFFT) is computed, and Canny edge detection is utilized to select the largest area in the image with sarcomeres (**Figure 1A**). Within the selected region, the fiber orientation is determined by binarizing the region and calculating the orientation relative to the horizontal axis of the box (**Figure 1B**). Sarcomere length is calculated along a single column of pixels as the pixel distance between pixel intensity peaks (A-bands), converted to microns (0.16 μm per pixel) and multiplied by the cosine of the detected angle to correct for angle of fiber orientation (**Figure 1C**). This analysis process is repeated for distinct columns of pixels at 2 μm intervals to enable the collection of sarcomere length data from separate myofibrils (Lieber, 2002; Moo et al., 2016).

Realistic Virtual Phantoms

Virtual phantoms were designed to closely mimic raw, *in vivo* data. A range of phantoms with sarcomere length averages and standard deviations representative of cadaveric data from the biceps brachii [data from Murray et al. (2000)] were generated using a series of normally distributed sinusoids (**Figure 2A**). To mimic observed raw SHG data, the image signal in the phantom was degraded by removing 70% of the pixels at random. A sinusoidal geometric transformation was applied to create fiber bending, and Gaussian white noise was added to capture similar signal quality (**Figures 2B,C**). To assess the phantoms' similarity to real data, the signal-to-noise ratio (SNR) for the phantoms was measured and then adapted to mimic the range of SNR values found in raw SHG images from the biceps brachii.

Determining Accuracy and Comparing Individual Sarcomere Length Code and Mean Sarcomere Length Code

Using 300 virtual phantom images with known sarcomere lengths, and varying image quality, the code's accuracy and precision were determined by comparing the ISLC output to the known phantom values. The accuracy and precision of the ISLC code developed in this study was defined from the differences between the "true" mean sarcomere lengths defined in the virtual phantoms and the mean sarcomere length values output from the ISLC. Accuracy was defined by the difference in means; precision was defined by the standard deviation of the differences. This analysis was repeated for the MSLC to enable direct comparison of the two methods. A Bland-Altman test was implemented to determine agreement between sarcomere lengths obtained using ISLC and sarcomere measurements obtained using MSCL.

Variability Across Images, Trials, and Days

Sarcomere length variability across different images from a single imaging trial (defined as a single needle insertion and microscope attachment) was assessed using the standard deviation of the mean sarcomere length from all processed images in the trial. For this study, we reanalyzed images originally collected for a separate study (Adkins et al., 2021) that were acquired in the non-paretic biceps of 7 individuals with chronic hemiparetic stroke and in the biceps from both the dominant and non-dominant limbs of 4 individuals with no neuromuscular impairments (**Table 1**). Therefore, SHG images were collected from the long head of the biceps brachii in 15 limbs. On average, we collected

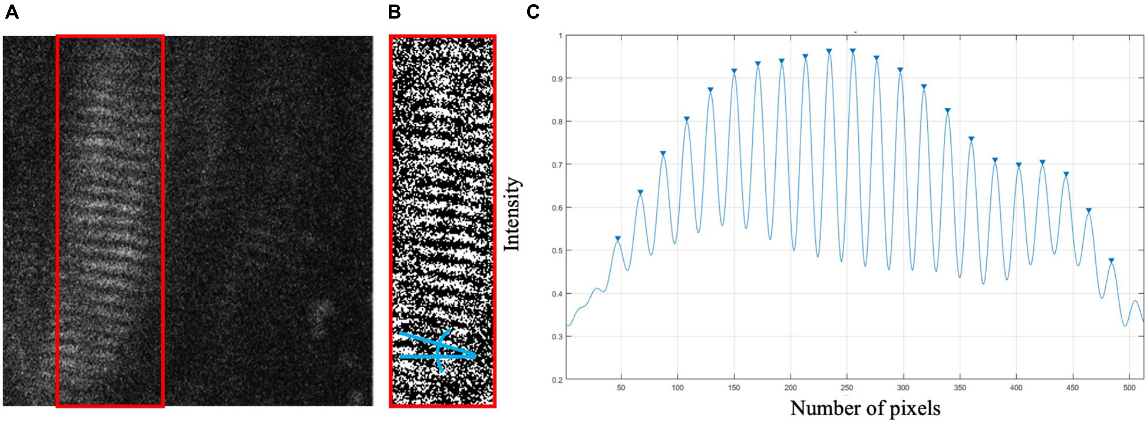

FIGURE 1 | (A) Sample raw SHG image of *in vivo* biceps brachii sarcomere data (512 pixels × 512 pixels, 82 μm × 82 μm). Canny edge detection selected region enclosed by red box. **(B)** Binarized selected region with blue lines indicating the angle relative to horizontal. **(C)** Pixel vs. intensity distribution where A-bands are represented by peaks.

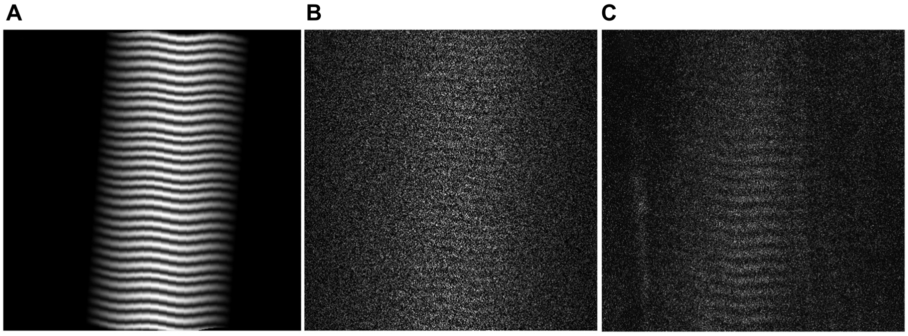

FIGURE 2 | (A) Virtual Phantom created with real sarcomere lengths and variability, distortion, and rotation. **(B)** Realistic Virtual Phantom with added noise. **(C)** Representative raw data from *in vivo* biceps brachii.

145 ± 108 images per trial. Mean sarcomere length per image was calculated using MSLC.

Images collected from 3 participants were analyzed to evaluate the variability in sarcomere lengths measured when two trials of data were collected in the same muscle (**Table 1**, different trials arise from a single needle insertion, but distinct microscope attachment). Across trials, there is a slight change in location or orientation of the probe within the muscle due to the removal and reattachment of the microscope on the probe. In some cases, we also apply slight pressure or other movements to the needle between trials. Because the needle is not removed and reinserted, we expect we are likely sampling from the same relatively small, localized area, but from different sarcomeres due to the probe movement. In total, we analyzed two trials of data collected from 5 distinct insertions, including insertions in both arms of two participants, and a single arm from a third participant. Variability between 2 trials of image data was quantified as the difference in the average sarcomere length per trial (i.e., the average value of the output of MSLC for all the images in that trial).

The variability in sarcomere lengths measured on different days (a minimum of 1 week apart) was assessed in the long head of the biceps brachii. Images collected from a single needle insertion in both limbs of 1 participant and from 4 insertion sites (at different locations in the muscle) from a single limb in a second participant were analyzed (**Table 1**). Because measurements were taken on different days, the location of the probe within the muscle across days is sensitive to replicability of arm position (which would effect the muscle-tendon length the images were collected in), identification of the location in the muscle where the needle should be inserted, and the process of probe insertion. In these evaluations, the investigator's intention was to perform each of these tasks consistently across days. Variability in the sarcomere lengths measured on 2 different days was quantified as difference in the average sarcomere length captured on "Day 1" and "Day 2" (i.e., the average value of the output of MSLC for all the images in the single trial of data collected from a given needle insertion location each day). In four of the repeated measures across days, the insertion location was marked on the limb and the distance between insertion locations was measured and determined to be less than 1 cm apart (average ± standard deviation, 0.54 ± 0.17 cm).

TABLE 1 | Participant demographic and participation information.

	Arm	Gender	Age	Stroke	Muscle	Location	Across images	Across trials	Across days	Across locations
*1	L	F	65	X	BB	1	X			
*2	R	F	63	X	BB	1	X			
*3	R	M	48	X	BB	1	X			
*4	L	M	60	X	BB	1	X			
*5	L	M	72	X	BB	1	X			
*6	R	M	62	X	BB	1	X			
*7	L	M	44	X	BB	1	X	X		
	R							X		
8	R	F	65	X	BB	1			X	
	L								X	
*9	R	F	53		BB	1	X			
	L						X			
*10	R	F	64		BB	1	X			
	L						X			
*11	R	M	62		BB	1	X			
	L						X			
*12	R	M	67		BB	1	X			
	L						X	X		
13	R	M	29		BB	4		1X	4X	4X
	L							1X		4X
	R				FCU	2				2X
	L									2X
14	L	F	28		BB	4				4X
		6F/8M	56 (14)		Total Comparisons		15	5	6	16

Age for all participants is reported as of the time at which the experimental data collection for that participant was completed.

The average and standard deviation of "Age" is given in the last row as "average (standard deviation)." For "Muscle"—BB stands for Biceps Brachii and FCU stands for Flexor Carpi Ulnaris.

**Indicates original data was collected from Adkins et al. (2021) and reanalyzed in this study for the purpose of understanding sarcomere variability.*

Variability in Different Locations in the Muscle

Sarcomere lengths in the biceps brachii were measured at distinct locations in the muscle in three arms of two individuals (1 female, 28 years; 1 male, 26 years) (**Figure 3**). Four insertions were made; insertions near the distal and proximal ends of the muscle belly (position 1 and 4), and two insertions in the center of the muscle belly approximately 1 cm apart (positions 2 and 3). In both arms of a single individual (male, 29 years old) sarcomere length measures were made at two locations along the flexor carpi ulnaris muscle; a proximal location where the fibers run longitudinally in the muscle, and a distal location where the fibers are pennated (**Figure 3**). Measurements of fascicle length of the long head of the biceps brachii and the flexor carpi ulnaris were obtained using extended field-of-view ultrasound (Acuson S2000 Ultrasound System, Siemens Medical Solutions United States, Inc., Mountain View, CA, United States) at the same joint posture sarcomere length was obtained (**Figure 4**). Ultrasound images were exported as uncompressed DICOM files and fascicles were measured using the segmented line tool in ImageJ (Wayne Rasband, National Institutes of Health, Bethesda, MD, United States).

RESULTS

Variability Along Fiber

The ISLC code developed in this study was accurate to 0.02 μm and precise to 0.02 μm. While the analysis from the virtual phantoms indicates the MSLC code was slightly less accurate than the ISLC (accuracy 0.03 μm, precision 0.02 μm), the Bland-Altman analysis (**Figure 5**) demonstrates that mean sarcomere lengths that result from the two analyses are comparable. There is a minimal bias between the two methods (−0.0025 μm; 95% limits-of-agreement = −0.0809–0.0759 μm), there is no observable systematic variance, and the measurements lay within the limits-of-agreement.

Variability Across Images, Trials, and Days

The mean sarcomere length observed in a single image varied across the multiple images that are captured in a single imaging trial (i.e., single needle insertion and microscope attachment), although this variability is relatively small. Across 15 trials, the standard deviation of the mean sarcomere length per image within a trial was 0.20 ± 0.07 μm. The magnitude of the

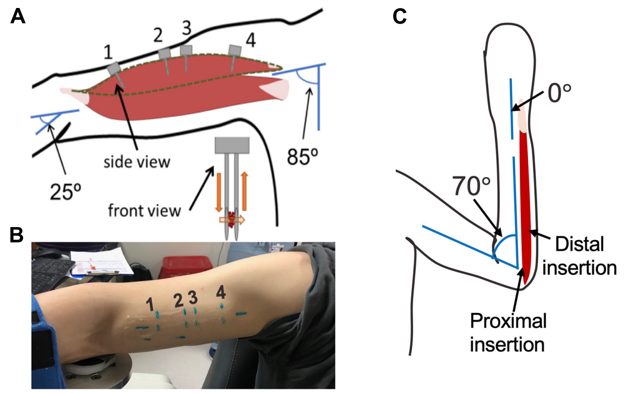

FIGURE 3 | (A) schematic of arm position and location of probe insertion in the long head of the Biceps Brachii. Illustration of probe showing the direction of laser light and interaction with muscle tissue (orange). **(B)** Picture of location of four probe insertions in one of the study participants. **(C)** Schematic of the elbow and wrist position and locations of the probe insertion in the flexor carpi ulnaris.

difference in mean sarcomere length measured in different trials (average ± standard deviation: trials: 0.18 ± 0.10 µm) was comparable to the variability across images and the difference in mean sarcomere length measured in the same muscle on different days (0.15 ± 0.13 µm). When standard deviations of sarcomere lengths within a single image were analyzed (from a single participant across all locations), variability within that image were on the same order (0.13 ± 0.02 µm) as those we report across images. Given this, and the fact the phantom study identified the ISLC and MSLC were of comparable accuracy, the MSLC was used for all *in vivo* sarcomere length data.

Variability Across Muscle

The uncertainty in sarcomere length that was introduced by sampling from various, distinct muscle locations was not larger than the variability in mean sarcomere length we observed across images within a single trial (i.e., needle insertion). For the biceps brachii, the difference in median sarcomere length across four locations was 0.15 ± 0.12 µm. For the flexor carpi ulnaris, the difference in median sarcomere length across two locations was 0.12 ± 0.13 µm. Standard deviations of images collected in a single trial and location averaged 0.18 ± 0.07 µm for the biceps and 0.34 ± 0.17 µm for the FCU. The largest difference in median sarcomere length between any two locations in a single muscle occurred in the biceps brachii of arm 3 between the proximal and center-proximal location (difference = 0.43 µm). Notably, for both muscles and for all arms evaluated, the maximum difference in median sarcomere length observed at different locations (c.f. **Figures 6**, **7** purple shaded region) was less than the range of sarcomere lengths observed in a single stick (colored probability distribution of each violin plot for each arm).

Summary/Functional Implications

Based on the sources of variability in sarcomere length measures in the upper limb muscles investigated in this study, we estimate the uncertainty (a lumped quantity that includes both the natural anatomical variability of sarcomere lengths within the muscle and experimental/random error) in sarcomere length associated with collecting SHG microendoscope images in a single imaging session from a single needle insertion within the muscle to be on the order of 0.25 µm (**Figure 8**). Because the variability observed across trials, probe insertions, and different days was not systematically larger than the variability observed in a single trial, we expect 0.25 µm, which was ∼7–8% of the average sarcomere lengths in the biceps brachii and FCU, provides a reasonable measure of natural anatomical variability of sarcomere lengths for these two muscles. Notably, this level of variability is an order of magnitude greater than the improvement in measurement accuracy obtained if the variability in sarcomere length within an image is considered along a muscle fiber (difference in accuracy between ISLC and MCLC ∼0.01*µm*). Given it is used in the calculation of functionally relevant architectural parameters, the uncertainty in sarcomere length measures we observed would yield uncertainty in calculations of optimal fascicle length and physiological cross-sectional area of ∼7–8%, independent of

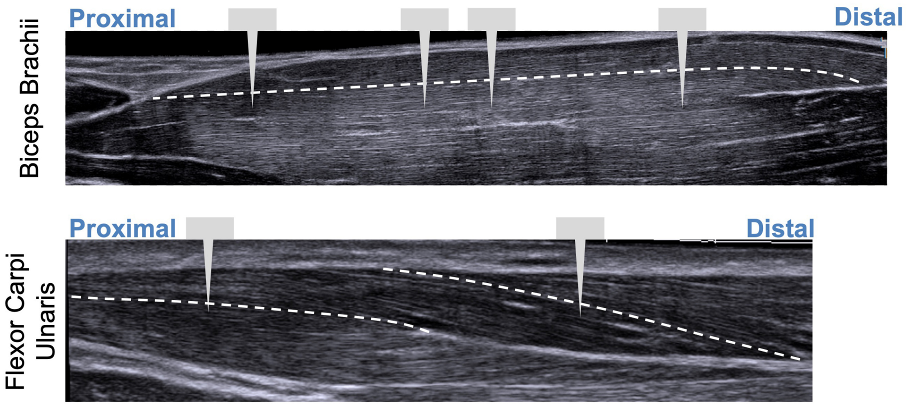

FIGURE 4 | Illustration showing extended field-of-view ultrasound images with approximate locations of probe insertions along the muscle. White dashed line represents fascicle paths.

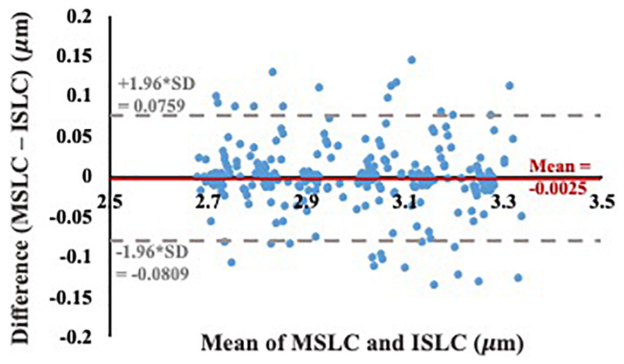

FIGURE 5 | Bland-Altman test of agreement between our individual sarcomere length code (ISLC) and the image processing method currently utilized in the literature, MSLC. The x-axis is the average of the MSLC and ISLC sarcomere length measurements and the y-axis is the difference between the sarcomere lengths calculated from the two methods. The solid red line indicates the bias (–0.0025 μm) and the dashed gray lines represent the lower (–0.0809 μm) and upper (0.0759 μm) limits-of-agreement (mean difference ± 1.96*standard deviation of the difference).

any experimental uncertainty in measurements of fascicle length or muscle volume.

DISCUSSION

We investigated both anatomical and experimental sources of variability in sarcomere length measures obtained *in vivo*, in the upper limb, using second harmonic generation microendoscopy. Based on assessments completed in two muscles in the upper limb that have different functions, size, and architectures, we estimate the magnitude of the uncertainty in such measures to be on the order of ∼0.25 μm, which we conclude is dominated by the anatomical variability of sarcomere lengths in these muscles, under these conditions, rather than from random error associated with our methods. Notably, we found that, in both a fusiform muscle (biceps brachii) and pennate muscle (flexor carpi ulnaris) of the upper limb, variability in sarcomere length within a single insertion is larger than the variability across locations in these muscles. We developed custom image processing code which takes measures of individual sarcomeres in an image, allowing for the quantification of sarcomere length variability along a muscle fiber and across myofibrils in a localized area (82 μm by 82 μm). We found that the variability in mean sarcomere length measures made using this ISLC was comparable to current processing methods (MSLC) and an order of magnitude smaller (∼0.02 μm) than the uncertainty in sarcomere length associated with all other sources investigated in this study (i.e., across images, trials, days, locations). Together, our findings provide guidance for the development of robust experimental design and analysis of *in vivo* sarcomere lengths in the upper limb.

The uncertainty in sarcomere length observed in this study (<8%), and its propagation through calculation of the most functionally meaningful muscle parameters (optimal fascicle length and PCSA), is smaller than differences reported in *in vivo* sarcomere length and fascicle length of various studies in the literature. This finding suggests that using SHG to detect *in vivo* sarcomere length adaptation is practical. For example, intraoperative measures of sarcomeres have been shown to be much longer in children with cerebral palsy (an injury of the brain during development) than sarcomere length estimates for Mathewson et al. (2015) (∼88%) or intraoperative measures (Lieber and Fridén, 2019) (∼46%) in typically developing children. In addition, following 3 weeks of Nordic hamstring training, a 17% increase in sarcomere length was found in the biceps femoris long head (Pincheira et al., 2021). Due to the relative ease of obtaining fascicle length measures as compared to sarcomere length measures *in vivo*, many studies have reported adaptation of fascicle length to altered use or stimulus. Previous studies in elbow flexors of individuals with chronic hemiparetic stroke report substantial decreases in fascicle length in extended joint postures [∼19% decrease in biceps brachii at 25° elbow flexion (Nelson et al., 2018), 15% decrease in brachialis at 10° elbow flexion (Li et al., 2007)]. Fascicle length in gastrocnemius medialis in individuals who regularly wear high heels were found to be 11% shorter than non-high heel wearers (Csapo et al., 2010). If these changes in fascicle length were due solely to changes in sarcomere length (i.e., a decrease in sarcomere length of 10–20%), our study suggests SHG microendoscopy would be able to reliably detect such changes. Notably, in a single individual who underwent a leg lengthening surgery (4 cm distraction) to correct a limb discrepancy, sarcomere length decreased by ∼15% while fascicle length increased by over 100% (Boakes et al., 2007). Together, these changes resulted in an overall increase in serial sarcomere number of 134.6% (Boakes et al., 2007), emphasizing the importance of measurement of both fascicle and sarcomere length to fully understand muscle function and plasticity.

Our data suggest the approach of measuring sarcomere lengths from a single insertion site in the muscle belly is appropriate for an understanding of average sarcomere length and variability in a fusiform (biceps brachii) and pennate (flexor carpi ulnaris) muscles of the upper limb. This finding will guide the development of future studies determining interlimb or interindividual differences in sarcomere length in the biceps brachii or flexor carpi ulnaris. For example, an *a priori* power analysis to determine the difference in sarcomere length between two dependent means (e.g., left and right arm) using SHG microendoscopy (standard deviation of 0.25 micrometers) would demonstrate that a power over 0.8 would be achieved with 10 participants with a detectable difference of 0.25 micrometers (effect size of 1) between limbs.

The mean sarcomere lengths observed in this study (3.04–3.97 μm) are substantially longer than optimal length (2.6–2.8 μm)(Gordon et al., 1966). These lengths are likely best explained by the joint postures in which data were collected, and that data collection occurs while the muscle is passive. In other studies in living human subjects, similar sarcomere lengths were observed under similar conditions. Most notably, in two different intraoperative studies, the native (prior to surgical tendon transfer) *in vivo* sarcomere lengths of the brachioradialis with the elbow fully extended were 3.90 ± 0.27 μm [$n = 8$; (Lieber et al., 2005)] and 3.7 ± 0.3 μm [$n = 12$; (Murray et al., 2006)].

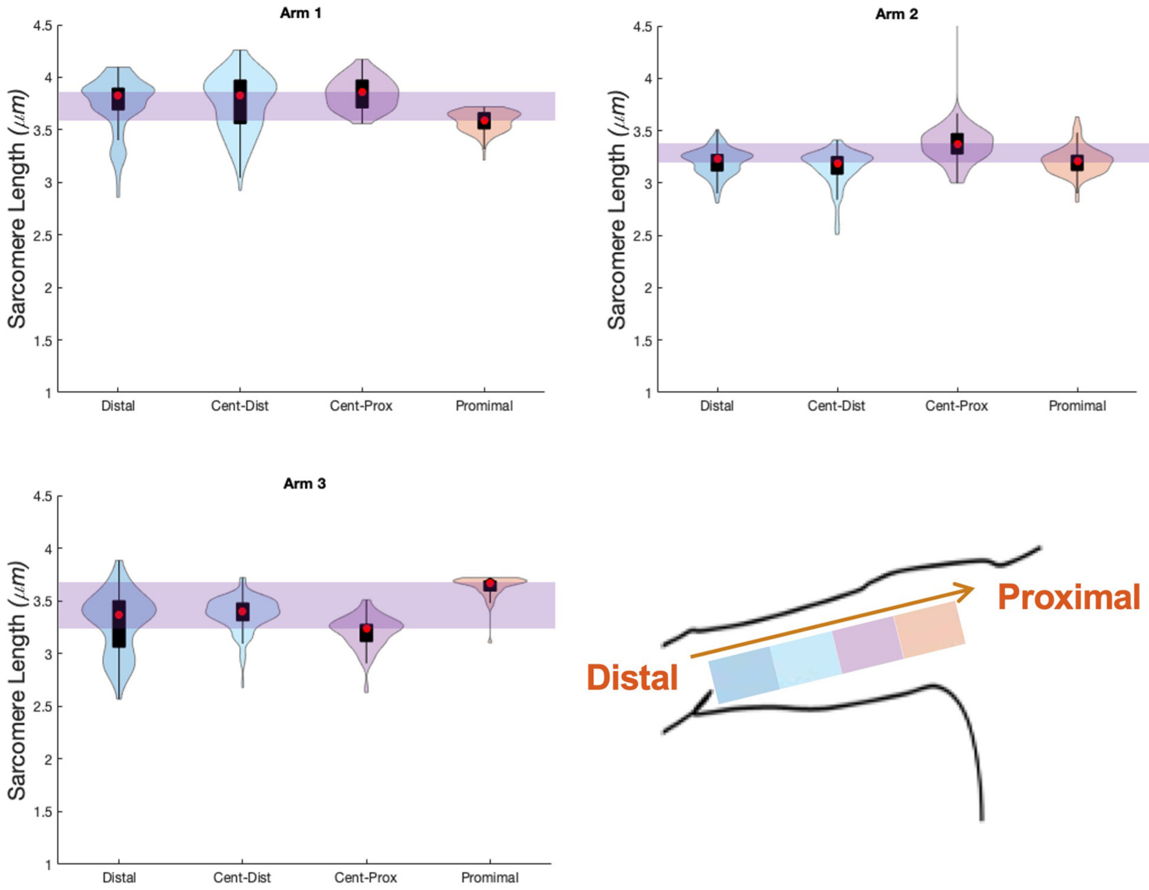

FIGURE 6 | Violin plots for 4 locations, and three arms showing median of data (red circle), interquartile range (black box plot), and probability density of data at each location (shaded violin shape). Arm 2 (right, dominant) and Arm 3 (left, non-dominant) are from a single individual.

Similarly, sarcomere lengths comparable to those we report here were reported for other muscles while the joint they crossed was positioned such that muscle-tendon lengths were relatively long. These *in vivo* studies include both intraoperative laser diffraction [e.g., extensor carpi radialis brevis lengths ranged from 3.1–3.9 μm in different participants (Lieber et al., 1994)] and *in vivo* microendoscopic imaging [e.g., soleus ∼3.0–4.2 μm (Chen and Delp, 2016), tibialis anterior 2.5–3.9 μm, (Lichtwark et al., 2018)]. Notably, when joint posture was repositioned in these same studies, SL decreased, and the length ranges included optimal length in these new joint postures [2.4–3.0 μm (Lieber et al., 1994), ∼2.5–3.5 μm (Chen and Delp, 2016), 2.3–3.8 μm, (Lichtwark et al., 2018)]. Sarcomere lengths substantially longer than optimal length have also been observed in the long head of the biceps brachii in cadaveric specimens (Murray et al., 2000). Finally, it is important to interpret these data with the understanding that data collection occurred while the muscles were passive. Due to the series elastic properties of muscle and tendon, sarcomere lengths will shorten to some degree during active force generation (Zajac, 1989).

In this study, we did not observe systematic differences in sarcomere lengths from the images collected from probe insertions at different locations along the length of the muscle belly. In isolated muscle fiber experiments, markedly shorter sarcomeres have been observed within single fibers at the at the extreme ends of the fibers, close to the fiber-tendon junction (Huxley and Peachey, 1961). Using these methods, the lengths of sarcomeres can be quantified at multiple locations in a single fiber, with the precise location of the measurement expressed as a displacement relative to a reference point on the fiber. Given the precision of these methods, data can also be collected very close to the fiber-tendon junction. Data in Huxley and Peachey (1961) suggest the shorter sarcomere lengths were only observed at a distance from the end of the fiber that was approximately ∼5% of total fiber length. While we sampled from very different locations in the muscle belly (cf., **Figure 3**), given the rigidity and size of the microscope, the geometry of the muscle belly near the muscle-tendon junction, and the lack of control we have in placing the probe precisely in the muscle belly using this imaging technique, we neither intended nor do we expect that we sampled from such an extreme end of the muscle belly. Other studies in which the sampling methodology is more similar to our methods than single fiber experiments (e.g., Moo et al., 2016) also present data without the systematic effects observed close to the muscle-tendon junction in single fiber data. The data we present here describe the level of uncertainty associated with

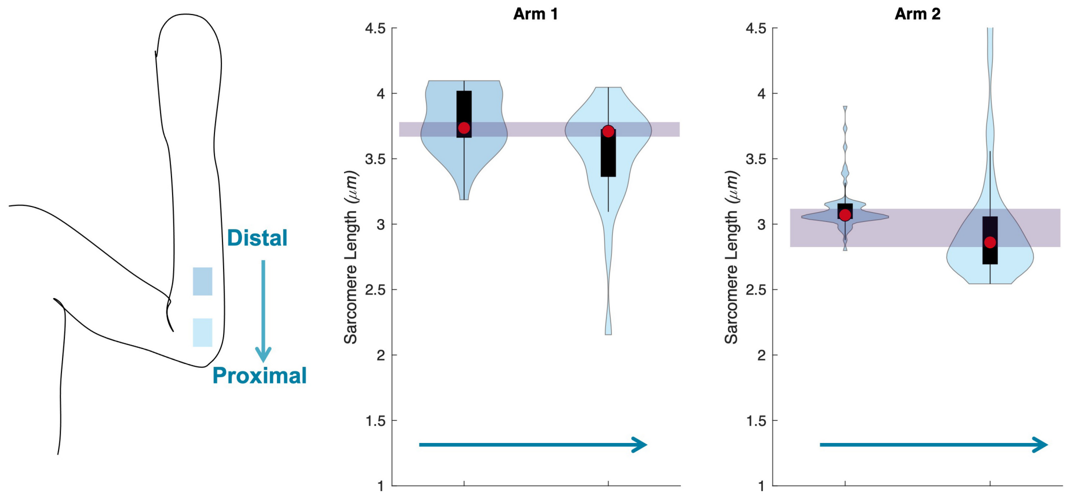

FIGURE 7 | Schematic of the two insertion locations (left) in the flexor carpi ulnaris., and three arms showing median of data (red circle), interquartile range (black box plot), and probability density of data at each location (shaded violin shape).

methodologies where random samples of sarcomere lengths are measured from different locations within a muscle's belly and will provide important guidance for interpretation of sarcomere length data measured *in vivo* in human participants.

This study provides insight which will be invaluable for the design, implementation, and analysis of future *in vivo* architectural studies aiming to explore muscle plasticity. However, there are several limitations in this work which should be considered. In particular, the relatively small cohort of individuals we evaluated limited our ability to make statistical conclusions. In addition, we only explore sarcomere length variability in a small number of muscles and at a single joint posture and contraction state per muscle. Future studies in these directions would be of interest. Notably, most previous *in vivo* muscle architectural studies demonstrate differences in fascicle length without normalizing to sarcomere length or make estimates of PCSA by using this non-normalized fascicle length. With the addition of sarcomere length differences across populations, following interventions, or impairment of the two most functionally relevant parameters of muscle (serial sarcomere length and PCSA) can be explicitly calculated. This work provides confidence in the ability to use SHG microendoscopy to make measures of *in vivo* sarcomere length to detect difference in functionally relevant muscle parameters on the order of 8% or greater.

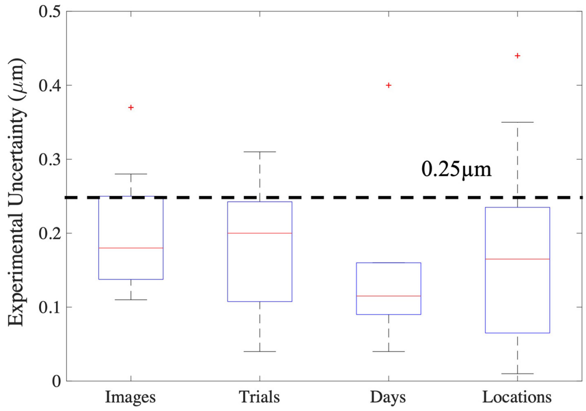

FIGURE 8 | Boxplots of the various sources of experimental uncertainty investigated in this study. The red line represents the median, the blue box extends from the 25th to the 75th percentile of the data, and the dashed error bars, referred to as whiskers, represent the range of all data excluding outliers (red "+"). For images the y-axis represents the standard deviation in mean sarcomere length across images. For all other x-axis elements, the y-axis represents the absolute difference in mean sarcomere length between trials, days, and locations.

DATA AVAILABILITY STATEMENT

The data supporting the conclusions of this article will be made available by the authors in Arch, Northwestern University Research and Data Repository (doi: 10.21985/n2-8mwv-mz5).

ETHICS STATEMENT

The studies involving human participants were reviewed and approved by Northwestern University Institutional Review Board. The patients/participants provided their written informed consent to participate in this study.

AUTHOR CONTRIBUTIONS

AA, RF, JD, and WM designed the research, performed the research, and wrote the manuscript. AA, RF, and WM analyzed the data. All authors contributed to the article and approved the submitted version.

FUNDING

This work is supported by the National Science Foundation (NSF) Graduate Research Fellowship Program under Grant No. DGE-1324585, the National Institutes of Health (NIH) R01 HD084009 and F31 AR076920, and the DeLuca Foundation Research Scholarship.

ACKNOWLEDGMENTS

We would like to thank the study participants, Vikram Darbhe and Jorie Budzikowski for assistance in data collection, and Zebra Medical Technologies (now Enspectra Health) for their support with data collection and image processing.

REFERENCES

Adkins, A. N., Dewald, J. P. A., Garmirian, L. P., Nelson, C. M., and Murray, W. M. (2021). Serial sarcomere number is substantially decreased within the paretic biceps brachii in individuals with chronic hemiparetic stroke. *Proc. Acad. Natl. Sci. U.S.A.* 118:e2008597118. doi: 10.1073/pnas.2008597118

Boakes, J. L., Foran, J., Ward, S. R., and Lieber, R. L. (2007). Case report: muscle adaptation by serial sarcomere addition 1 year after femoral lengthening. *Clin. Orthopaed. Relat. Res.* 456, 250–253. doi: 10.1097/01.blo.0000246563.58091.af

Brand, P. W., Beach, R. B., and Thompson, D. E. (1981). Relative tension and potential excursion of muscles in the forearm and hand. *J. Hand Surg. Am.* 6, 209–219. doi: 10.1016/s0363-5023(81)80072-x

Chen, X., and Delp, S. L. (2016). Human soleus sarcomere lengths measured using *in vivo* microendoscopy at two ankle flexion angles. *J. Biomech.* 49, 4164–4167. doi: 10.1016/j.jbiomech.2016.11.010

Chen, X., Sanchez, G. N., Schnitzer, M. J., and Delp, S. L. (2016). Changes in sarcomere lengths of the human vastus lateralis muscle with knee flexion measured using *in vivo* microendoscopy. *J. Biomech.* 49, 2989–2994. doi: 10.1016/j.jbiomech.2016.07.013

Csapo, R., Maganaris, C. N., Seynnes, O. R., and Narici, M. V. (2010). On muscle, tendon and high heels. *J. Exp. Biol.* 213, 2582–2588. doi: 10.1242/jeb.044271

Gordon, A., Huxley, A. F., and Julian, F. (1966). The variation in isometric tension with sarcomere length in vertebrate muscle fibres. *J. Physiol.* 184, 170–192. doi: 10.1113/jphysiol.1966.sp007909

Huxley, A. F., and Peachey, L. D. (1961). The maximum length for contraction in vertebrate straiated muscle. *J. Physiol.* 156, 150–165. doi: 10.1113/jphysiol.1961.sp006665

Li, L., Tong, K. Y., and Hu, X. (2007). The effect of poststroke impairments on brachialis muscle architecture as measured by ultrasound. *Arch. Phys. Med. Rehabil.* 88, 243–250. doi: 10.1016/j.apmr.2006.11.013

Lichtwark, G. A., Farris, D. J., Chen, X., Hodges, P. W., and Delp, S. L. (2018). Microendoscopy reveals positive correlation in multiscale length changes and variable sarcomere lengths across different regions of human muscle. *J. Appl. Physiol.* 125, 1812–1820. doi: 10.1152/japplphysiol.00480.2018

Lieber, R. L. (2002). *Skeletal Muscle Structure, Function & Plasticity: The Physiological Basis of Rehabilitation*. Philadelphia, PA: Lippincott Williams & Wilkins.

Lieber, R. L., Fazeli, B. M., and Botte, M. J. (1990). Architecture of selected wrist flexor and extensor muscles. *J. Hand Surg. Am.* 15A, 244–250. doi: 10.1016/0363-5023(90)90103-x

Lieber, R. L., and Fridén, J. (2000). Functional and clinical significance of skeletal muscle architecture. *Muscle Nerve* 23, 1647–1666. doi: 10.1002/1097-4598(200011)23:11<1647::aid-mus1>3.0.co;2-m

Lieber, R. L., and Fridén, J. (2019). Muscle contracture and passive mechanics in cerebral palsy. *J. Appl. Physiol.* 126, 1492–1501. doi: 10.1152/japplphysiol.00278.2018

Lieber, R. L., Loren, G. J., and Friden, J. (1994). In vivo measurement of human wrist extensor muscle sarcomere length changes. *J. Neurophysiol.* 71, 874–881. doi: 10.1152/jn.1994.71.3.874

Lieber, R. L., Murray, W. M., Clark, D. L., Hentz, V. R., and Fridén, J. (2005). Biomechanical properties of the brachioradialis muscle: implications for surgical tendon transfer. *J. Hand Surg.* 30, 273–282. doi: 10.1016/j.jhsa.2004.10.003

Llewellyn, M. E., Barretto, R. P. J., Delp, S. L., and Schnitzer, M. J. (2008). Minimally invasive high-speed imaging of sarcomere contractile dynamics in mice and humans. *Nature* 454, 784–788. doi: 10.1038/nature07104

Mathewson, M. A., Ward, S. R., Chambers, H. G., and Lieber, R. L. (2015). High resolution muscle measurements provide insights into equinus contractures in patients with cerebral palsy. *J. Orthopaed. Res.* 33, 33–39. doi: 10.1002/jor.22728

Moo, E. K., Fortuna, R., Sibole, S. C., Abusara, Z., and Herzog, W. (2016). *In vivo* sarcomere lengths and sarcomere elongations are not uniform across an intact muscle. *Front. Physiol.* 7:187. doi: 10.3389/fphys.2016.00187

Moo, E. K., Leonard, T. R., and Herzog, W. (2017). *In vivo* sarcomere lengths become more non-uniform upon activation in intact whole muscle. *Front. Physiol.* 8:1015. doi: 10.3389/fphys.2017.01015

Murray, W. M., Buchanan, T. S., and Delp, S. L. (2000). The isometric functional capacity of muscles that cross the elbow. *J. Biomech.* 33, 943–952. doi: 10.1016/s0021-9290(00)00051-8

Murray, W. M., Hentz, V. R., Fridén, J., and Lieber, R. L. (2006). Variability in surgical technique for brachioradialis tendon transfer: evidence and implications. *J. Bone Joint Surg. Am.* 88, 2009–2016. doi: 10.2106/JBJS.E.00973

Nelson, C. M., Murray, W. M., and Dewald, J. P. A. (2018). Motor impairment–related alterations in biceps and triceps brachii fascicle lengths in chronic hemiparetic stroke. *Neurorehabil. Neural Repair* 32, 799–809. doi: 10.1177/1545968318792618

Pincheira, P. A., Boswell, M. A., Franchi, M. V., Delp, S. L., and Lichtwark, G. A. (2021). Biceps femoris long head sarcomere and fascicle length adaptations after three weeks of eccentric exercise training. *bioRxiv* [Preprint] bioRxiv: 2021.2001.2018.427202, doi: 10.1016/j.jshs.2021.09.002

Sanchez, G. N., Sinha, S., Liske, H., Chen, X., Nguyen, V., Delp, S. L., et al. (2015). *In vivo* imaging of human sarcomere twitch dynamics in individual motor units. *Neuron* 88, 1109–1120. doi: 10.1016/j.neuron.2015.11.022

Zajac, F. E. (1989). Muscle and tendon: properties, models, scaling, and application to biomechanics and motor control. *Crit. Rev. Biomed. Eng.* 17, 359–411.

Author Disclaimer: Any opinions, findings, and conclusions or recommendations expressed in this material are those of the authors and do not necessarily reflect the views of the NSF, NIH, or DeLuca Foundation.

Conflict of Interest: The authors declare that the research was conducted in the absence of any commercial or financial relationships that could be construed as a potential conflict of interest.

frontiers in Physiology

ORIGINAL RESEARCH
published: 15 February 2022
doi: 10.3389/fphys.2021.817152

Feasibility, Efficacy, and Safety of Percutaneous Muscle Biopsies in Patients With Chronic Liver Disease

Jonathan I. Quinlan[1,2†], Amritpal Dhaliwal[1,3†], Felicity Williams[1,3], Sophie L. Allen[1,2], Leigh Breen[1,2,4], Carolyn A. Greig[1,2,4], Janet M. Lord[1,3,4], Matthew J. Armstrong[1,5] and Ahmed M. Elsharkawy[1,5]*

[1] NIHR Birmingham Biomedical Research Centre, University Hospitals Birmingham NHS Foundation Trust, University of Birmingham, Birmingham, United Kingdom, [2] School of Sport, Exercise and Rehabilitation Sciences, University of Birmingham, Birmingham, United Kingdom, [3] Institute of Inflammation and Ageing, University of Birmingham, Birmingham, United Kingdom, [4] MRC-Versus Arthritis Centre for Musculoskeletal Ageing Research, University of Birmingham, Birmingham, United Kingdom, [5] Liver Unit, Queen Elizabeth Hospital Birmingham, Birmingham, United Kingdom

Introduction: Sarcopenia is present in many chronic disease states including decompensated end stage liver disease (ESLD) and non-cirrhotic non-alcoholic fatty liver disease (NAFLD). Sarcopenia in ESLD can negatively impact quality of life and increase mortality. Despite this, very little is understood about the mechanisms of sarcopenia in these conditions. One key reason for this is the reluctance to undertake percutaneous muscle biopsies due to the perceived increased risks. ESLD can induce thrombocytopaenia and coagulopathy which significantly increases the risk of bleeding. In addition, patients with either NAFLD or ESLD often have co-morbidities that would require additional care and risk assessment. Thus, the aim of this study was to establish an effective and safe protocol for the implementation of percutaneous muscle biopsies in patients with NAFLD and ESLD.

Methods: A total of 47 patients with ESLD and 9 patients with non-cirrhotic NAFLD were recruited from the Liver Unit, Queen Elizabeth Hospital (Birmingham, United Kingdom). A total of 71 percutaneous vastus lateralis biopsies were attempted over two study visits. A vigorous safety screening occurred prior to and during each visit and a strict protocol was followed to mitigate against complications and risk.

Results: A total of 85% of patients consented to the muscle biopsy at either visit (48/56). A total of 9% of consented biopsies could not occur due to medical considerations, including high international normalised ratio (INR) ($n = 3$) and the use of aspirin ($n = 4$). Muscle tissue was obtained from 90% of attempts, with a mean average yield (wet weight tissue) of 98.1 ± 52.9 mg.

Conclusion: Percutaneous muscle biopsies are both feasible and yield sufficient tissue in an ESLD population. The procedure is effective for obtaining muscle tissue whilst also safe, with only one adverse event. This study provides evidence for the successful use of muscle biopsies in this population, even in consideration of disease specific complications, medications, and comorbidities.

Keywords: chronic liver disease (CLD), muscle biopsy, non-alcoholic fatty liver (NAFLD), end stage liver disease, liver disease

Edited by:
*Peter T. Wright,
University of Roehampton London,
United Kingdom*

Reviewed by:
*Benoit Smeuninx,
Monash University, Australia
Brandon Mitchell Roberts,
US Army Research Institute
of Environmental Medicine
(USARIEM), United States*

***Correspondence:**
*Ahmed M. Elsharkawy
ahmed.elsharkawy@uhb.nhs.uk*

† These authors have contributed equally to this work and share first authorship

Specialty section:
*This article was submitted to
Striated Muscle Physiology,
a section of the journal
Frontiers in Physiology*

Received: *17 November 2021*
Accepted: *14 December 2021*
Published: *15 February 2022*

Citation:
Quinlan JI, Dhaliwal A, Williams F, Allen SL, Breen L, Greig CA, Lord JM, Armstrong MJ and Elsharkawy AM (2022) Feasibility, Efficacy, and Safety of Percutaneous Muscle Biopsies in Patients With Chronic Liver Disease. Front. Physiol. 12:817152. doi: 10.3389/fphys.2021.817152

INTRODUCTION

The loss of muscle mass, function and quality is a condition known as sarcopenia (Cruz-Jentoft et al., 2019). Sarcopenia has typically been considered an age-related condition; however, it is also present in many chronic disease states. As such, sarcopenia can be subdivided into two categories: primary and secondary sarcopenia (Cruz-Jentoft et al., 2019). Primary sarcopenia is the result of the natural ageing process, i.e., largely occurs due to ageing alone. In contrast, secondary sarcopenia occurs due to a pre-existing condition or disease which consequently negatively impacts skeletal muscle. Secondary sarcopenia is often present in chronic disease states such as chronic liver disease (CLD); specifically non-alcoholic fatty liver disease (NAFLD) and end stage liver disease (ESLD). Indeed, sarcopenia is reported to be present in approximately 25–70% of ESLD patients (Kim et al., 2017) and negatively impacts quality of life, significantly increases mortality risk, and may adversely affect the outcome of liver transplantation (Carey et al., 2017). Despite these implications, the underlying mechanisms of sarcopenia within CLD remain relatively unknown.

To truly understand sarcopenia, it is imperative to understand the mechanistic drivers that underpin these changes in skeletal muscle. As such, a wealth of research outside the liver field has been based on percutaneous muscle biopsies to obtain muscle tissue and investigate the morphological, molecular, and genetic mechanisms of primary sarcopenia (Patel et al., 2015). While these studies often included older individuals (>65 years), the participants are typically "healthy" with minimal co-morbidities. As such, the muscle biopsy procedure in these non-clinical settings poses minimal risk and few complications. However, in clinically vulnerable cohorts there are many additional considerations and risks which must be mitigated, and, in many cases, there are contraindications for muscle biopsies (Wilson et al., 2017). Despite this, when a careful and considered approach is taken, percutaneous muscle biopsies can be completed in clinically challenging populations such as patients with cancer (MacDonald et al., 2015; Aversa et al., 2016) and those suffering from chronic inflammatory diseases (Dalakas, 2002; Van Langenberg et al., 2014; Boutrup et al., 2018). However, very few studies have investigated the molecular mechanisms of sarcopenia within patients with CLD using muscle biopsies (Tsien et al., 2015) and much of previous work is limited to cell and animal based models (Dasarathy et al., 2004, 2007). Thus, our understanding of the drivers of sarcopenia within CLD remains very limited. It is likely that the biological basis of these conditions and the consequent significant safety concerns has evoked caution.

Liver failure and coagulopathy present in ESLD and complications of CLD such as portal hypertension alter the usual clotting pathways, resulting in thrombocytopaenia and coagulopathy (Ginès et al., 2021). This results in an increased predisposition to bleeding and poor clotting. Other complications include hepatic encephalopathy (HE) which can affect cognition and the capacity to consent (Pantham and Mullen, 2017). In addition, as the liver is essential for glucose homeostasis, liver dysfunction can alter glucose uptake in both liver and skeletal muscle, increasing glycogenolysis and insulin resistance (Petrides and DeFronzo, 1989). CLD can often be accompanied by other co-morbidities, such as Diabetes Mellitus (Jepsen, 2014). Thus, these patients are often on a number of treatments, including insulin and oral hypoglycaemic medications which, if not correctly mitigated, pose significant complications for muscle biopsies. Specifically, prolonged fasting without dosage alterations or omissions can result in symptomatic hypoglycaemia, adverse events and consequently halting of the procedure (Hochberg et al., 2019). The stress response may further compound hypoglycaemia by decreasing serum glucose concentrations (Gibbons et al., 2012). In addition to medication concerns, within CLD, the presence of NAFLD is often associated with higher amounts of subcutaneous fat (Nishikawa et al., 2021), which can add an additional challenge to the subcutaneous muscle biopsy procedure. Therefore, the purpose of this study was to establish a safe and effective protocol for percutaneous muscle biopsies in patients with CLD, to instigate the necessary invasive mechanistic research.

MATERIALS AND METHODS

Patient Details

A total of 47 patients with ESLD and 9 patients with non-cirrhotic NAFLD. Patients were recruited from the Liver Unit, Queen Elizabeth Hospital (Birmingham, United Kingdom), as part of a larger, prospective observational study (ClinicalTrials.gov Identifier: NCT04734496). Within this study, multiple visits occurred, two of which included the possibility of a muscle biopsy (separated by 6 months). Full patient demographics alongside comorbidities and CLD related complications can be seen in **Table 1**. Primary aetiology and disease severity [as defined by Model for End Stage Liver Disease (MELD) score and Child-Pugh scoring] can be seen in **Table 2**. The study was approved by the Health Research Authority – West Midlands Solihull Research Ethics Service Committee Authority (REC reference: 18/WM/0167). All patients provided written informed consent.

Muscle Biopsy Protocol

Percutaneous muscle biopsies were obtained *via* the modified Bergström technique from mid vastus lateralis (VL) in fasted patients *via* full aseptic technique (Bergstrom, 1975). The biopsy site was obtained as 50% of the distance between the greater trochanter and mid patellar, and 50% between the medial and lateral borders of the VL (obtained *via* ultrasonography). The VL offers a safe option for muscle biopsies due to limited motor units and the lack of major blood vessels or nerves traversing the biopsy site (Andrew Shanely et al., 2014). In brief, the skin was cleaned with povidone-iodine antiseptic and approximately 5–10 ml of 1% lidocaine was utilised to fully anesthetise the biopsy site. A 5–8 mm incision was made through the skin, and any initial bleeding was stemmed by applying pressure with sterile gauze. A deeper incision was then made through the muscle fascia and into the muscle tissue, allowing a path for a 5 mm Bergström needle. Suction was applied to the Bergström needle *via* catheter and 100 ml syringe. Typically, three passes were attempted to

TABLE 1 | Patient characteristics, co-morbidities, and CLD related complications for both ESLD and non-cirrhotic NAFLD groups, as well as combined.

Mean (±SD)	**ESLD**	**Compensated NAFLD**	**Combined**
N	47	9	56
Age (years)	54.7 (10.4)	61.3 (7.9)	55.8 (10.2)
Sex (m/f)	31/16	6/3	31/16
Height (cm)	172.0 (11.9)	168.3 (8.4)	171.4 (11.5)
Weight (kg)	89.0 (21.4)	107.3 (33.2)	92.1 (24.3)
BMI (kg/m^2)	29.5 (6.5)	34.5 (8.0)	30.3 (6.9)
Body fat%	29.2 (10.7)	38.1 (13.3)	30.7 (11.5)
***N* (%)**	**ESLD**	**Compensated NAFLD**	**Combined**
Co-morbidities			
Diabetes Mellitus (DM)	12 (25)	4 (44)	16 (28)
DM (insulin dependent)	9 (19)	1 (11)	10 (18)
Chronic kidney disease	8 (17)	0	8 (14)
Chronic obstructive pulmonary disease	8 (17)	1 (11)	9 (14)
Cardiovascular disease	4 (8)	0	4 (7)
Hypertension	14 (30)	4 (44)	18 (32)
CLD related complications			
Hepatic encephalopathy	27 (56)	0 (0)	27 (48)
Portal hypertension	43 (91)	0 (0)	43 (76)

Characteristic data shown as mean average (±SD). Co-morbidity and CLD related complications data as N (% of respective group).

TABLE 2 | Disease aetiology for the liver disease group.

Liver disease aetiology	***N* (%)**	**MELD (±SD)**	**Child-Pugh score (±SD)**
Alcohol related liver disease	25 (45)	14.6 (4.9)	8.7 (1.1)
Cirrhotic NAFLD	6 (11)	12.4 (5.6)	7.0 (1.5)
Primary sclerosing cholangitis	9 (16)	11.6 (2.5)	6.3 (1.5)
Primary biliary cirrhosis	5 (9)	11.5 (1.7)	6.7 (0.9)
Other causes	2 (3)	10.5 (1.0)	6.0 (0.7)
Compensated NAFLD	9 (16)	N/A	N/A
Combined	56 (100)	13.2 (4.4)	7.7 (1.6)

Data shown as N (% of cohort) and as mean average (±SD) for MELD and Child-Pugh score.

obtain tissue, with a maximum of four passes. Operators would aim to obtain tissue within 15–30 s during each pass. Once completed, the wound was sealed, dressed and a cold compress was applied. Patients were supplied with a post biopsy aftercare leaflet and additional dressings were provided.

To ensure the safety of the patient and maximise the success of the biopsy procedure, we developed a detailed protocol which considered risk factors and established possible mitigation (**Figure 1**). Two weeks prior to their muscle biopsy visits, a medical doctor checked all medications including any antiplatelet, anticoagulation, insulin, or oral hypoglycaemic medications. We applied a strict ruling whereby no biopsy procedure would occur if pausing of any medication could incur significant risk (e.g., warfarin for venous thromboembolism). However, when feasible, medication was paused for a minimum of 3 days in advance of the biopsy visit, in accordance with drug half-life and national guidelines for gastroenterology endoscopic procedure (Veitch et al., 2016). In addition to anticoagulation and antiplatelet medication, a medical doctor also screened for insulin use and contacted patients in advance to advise on adjustment of their insulin doses the day prior to and day of the biopsy. This followed national guidelines for GI endoscopic procedure and radiology procedural guidelines (Runyon, 2009; Kurup et al., 2015; Veitch et al., 2016). For those with HE, only those who were deemed to have capacity to consent for the procedure were included. To ensure capacity and that the patient understood the procedure, consent was obtained on multiple occasions (prior to the visit, on arrival, and pre biopsy).

On the biopsy visit, a stringent safety checklist was utilised to ensure that every patient was adequately risk assessed. We devised a Local Safety Standards for Invasive Procedures (LocSSIP) checklist [similar to a World Health organization (WHO) checklist used in surgery] for performing the muscle biopsy procedure. The LocSSIP reconfirms capacity, consent, notes any allergies and medications, as well as confirming any medications that have been temporally paused for the procedure. At this stage, a pre-biopsy check of INR and platelets occurred, whereby a cut-off of INR $\geq$ 1.6 (normal value $<$ 1.2) and platelet count $\leq 30 \times 10^9$/L (normal range 50–450 $\times$ 10^9/L) would contraindicate biopsy; in concordance with national and local radiology guidance for procedures entailing a similar risk profile (Runyon, 2009; Kurup et al., 2015). If all safety concerns were satisfied, a point of care blood sugar (BM) check occurred, as those with diabetes and CLD are at an increased risk of hypoglycaemia due to fasting and liver dysfunction (Ginès et al., 2021). The cut-off point of <4.0 mmol/L was set as contraindication for muscle biopsy. Finally, as part of the wider study, ultrasonographic assessment of the VL occurred during each visit and as such helped identify the optimal muscle biopsy site. The captured images were also interpreted for VL size and the degree of subcutaneous adipose tissue and hence the depth from skin to muscle tissue (**Figure 2**). The scans also enabled assessment for any aberrant vessels, or potential complications. Although the procedure itself was "blind," the biopsy site was visually assessed for morphology and any possible contraindications. In addition to those mentioned above, other contraindications at the pre-biopsy check stage (**Figure 1**) would include any pre-existing swelling, infection or injury surrounding the proposed biopsy site or lower limb, systemic acute illness or haemodynamic instability. The protocol was to immediately stop the procedure if concerns were raised (from either the operator or patient).

RESULTS

Feasibility of Muscle Biopsies

As 56 patients were recruited, a maximum of 112 scheduled muscle biopsy visits could have occurred (i.e., 2 possible visits for each patient) (**Figure 3**). A total of 21 of these visits did not occur, primarily due to cancellations associated with COVID-19 or the patient undergoing recent liver transplantation, thus leaving 91 possible visits (**Figure 3**). In the visits that did occur, 85% of

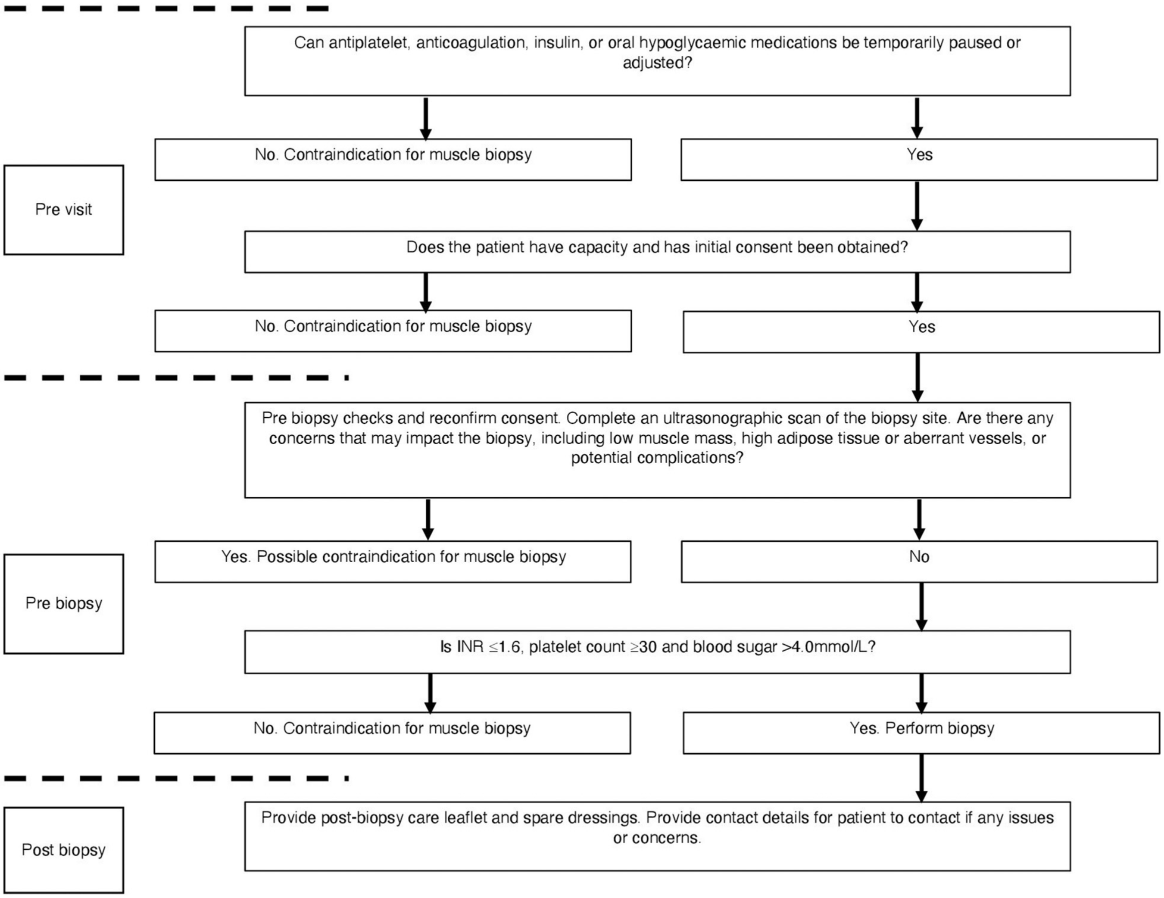

FIGURE 1 | Flowchart for safety considerations prior to muscle biopsy. Checks occur at pre-visit, pre-biopsy, and post-biopsy follow ups.

patients agreed to undergo a muscle biopsy (48/56), with only 13 biopsies not occurring due to patients declining. Including all visits whereby the patient agreed and provided consent, only 9% of biopsies could not occur due to medical considerations, including high INR and the use of aspirin (**Figure 3**).

Efficacy of Muscle Biopsies

A total of 71 muscle biopsies were consented and deemed safe to attempt; 64 of which were successful (i.e., yielded tissue) (90% of attempted) (**Figure 3**). The average yield of muscle tissue from all attempted biopsies (n = 71) was 89.5 ± 57.7 mg. However, if only successful biopsies are considered (n = 64), then the yield was 98.1 ± 52.9 mg (18–226 mg).

Haematology

The mean average platelet count for all patients (i.e., all patients included within the study, not just those consented to biopsy) was 126 ± 71 (range 27–380) and mean average INR was 1.3 ± 0.4 (range 0.9–3.2). Only one patient would have been below the platelet cut-off (<30), whilst six patients were above the INR cut-off (>1.6) for muscle biopsy. Whereas, if only those who consented to biopsy were considered, then no patient was below the platelet cut-off, and only three had high INR (**Figure 3**).

Adverse Events

A total of 71 muscle biopsies were performed, and we report only a single complication associated with the biopsy. Although the individual had an INR and platelet count within the acceptable range, a superficial haematoma at the site of biopsy occurred. The procedure itself was uneventful. The issue self-resolved within a week and did not require any medical management, or hospital admission. There were no reports of localised infection, or any other muscle biopsy associated complication post biopsy.

DISCUSSION

The data herein show that percutaneous biopsies of the VL are feasible, safe, and yielded muscle tissue in patients with CLD. Our safety protocol provided a stringent approach to the procedure which mitigated against, and significantly reduced the possible risk of adverse events. Thus, we believe that this study provides a platform to support future research into the mechanistic drivers of sarcopenia within CLD.

With regard to the feasibility of muscle biopsies, we showed that 85% of patients (48/56) agreed and consented to the procedure. As such, this meant that only 13 biopsies were missed

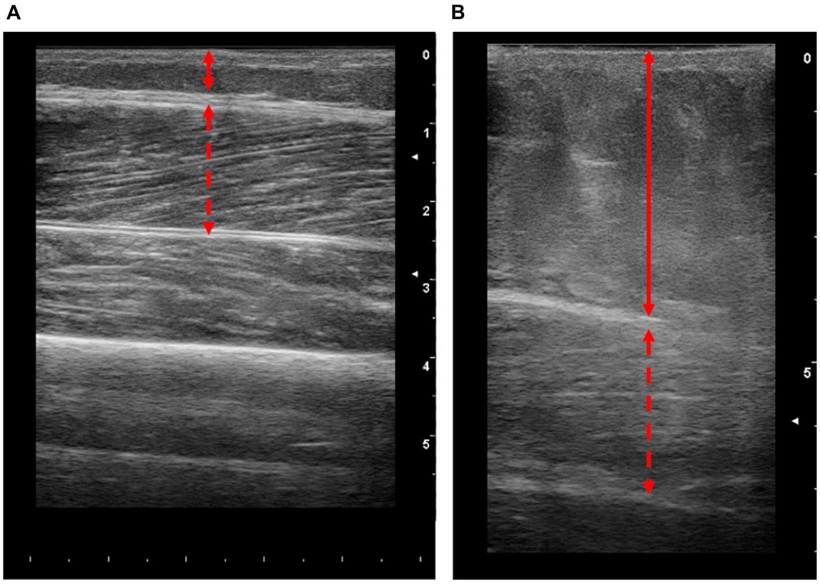

FIGURE 2 | Representative longitudinal ultrasound images of the vastus lateralis (VL) from patients with end stage liver disease. Images obtained from patients with lower **(A)** and higher **(B)** body fat percentages (10.5 and 46%, respectively). Solid lines represent the thickness of adipose tissue and dashed red arrow represents the thickness of the VL. Scale on the right-hand side of each image represents cm.

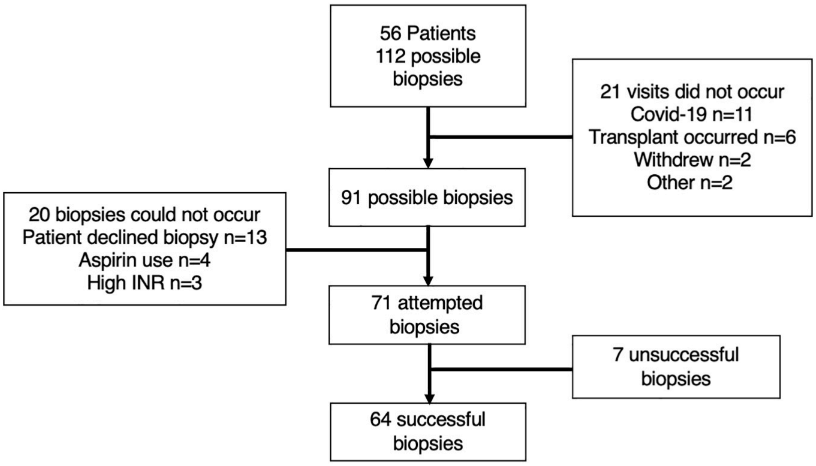

FIGURE 3 | Schematic representation of included patients and visits. The reasons for either the non-occurrence of visits, contraindications for biopsy and unsuccessful muscle biopsies are explained within the attached boxes.

due to lack of consent. It is worth noting that of the 8 patients who declined, 5 of these patients refused the biopsy at both visits (i.e., accounts for 10 of the 13 missed biopsies). Many investigators will attest to the challenge of recruitment for a voluntary invasive procedure, such that there will always be those who decline. Nonetheless, our data demonstrate that the concept of a muscle biopsy appears to be not overly daunting for those with CLD. It is possible that this patient group may have become accustomed to invasive procedures due to their diagnosis and treatment (i.e., liver biopsy, ascites drains, and regular blood tests). Importantly, within the consenting patients, only 7 (9%) were deemed unsafe to complete the procedure; due to coagulopathy, or in those unable to alter their anticoagulation/antiplatelet medication. Thus, even when stringent cut offs are utilised, the large majority of patients are eligible for the muscle biopsy procedure. Another potential concern for feasibility was the impact of HE on the patient's ability to consent. To navigate this issue, we ensured that consent was obtained on multiple occasions (i.e., prior to the visit, on arrival, and pre-biopsy). Nonetheless, despite ∼50% of patients having some degree of HE, we had no concerns due to lack of capacity to consent to the biopsy based on the clinical judgement of the research team.

A total of 71 muscle biopsies were consented to and deemed safe. A total of 90% of these attempts were successful (i.e., yielded muscle tissue). Unfortunately, seven attempted muscle biopsies were unsuccessful. It is worth noting that during this research study, junior colleagues were completing training on the muscle biopsy procedure and 3/7 of the unsuccessful procedures occurred due to this reason. One unsuccessful attempt was due to the patient feeling unwell and anxious following the anaesthetic, i.e., before an incision was made, so the procedure was aborted. Finally, the remaining three unsuccessful attempts included patients with high amounts of subcutaneous adipose tissue (mean body fat 41.2%), highlighting the procedural challenges associated with these populations. Indeed, as the procedure utilised a Bergström needle, there are practical limitations of this method, i.e., the limited needle length. Thus, whilst the needle itself may reach the muscle tissue; the procedure requires the needle window to be sufficiently within the muscle to obtain a sample. Therefore, in patients where subcutaneous adipose tissue is high, i.e., ∼5 cm adipose thickness (**Figure 2B**), the Bergström approach may not be suitable. As such, while ultrasound was not intentionally a component of the protocol, we suggest that the ultrasonographic assessment prior to biopsy is critical. Nonetheless, 64 muscle biopsies were successful with an average yield of 98.1 ± 52.9 mg (range of 18–226 mg). Molecular and RNA analysis of muscle tissue typically utilises ∼20 mg (Franchi et al., 2014) and ∼5–10 mg (Din et al., 2019) of wet weight tissue, respectively. Thus, all but one biopsy would be appropriate for western blot analysis, and all samples would be appropriate for RNA analysis. Collectively, this demonstrates that percutaneous muscle biopsies can be successful in patients with CLD.

Muscle biopsies have long been utilised for the molecular investigation of muscle tissue within a range of ages and conditions (Goodpaster et al., 2000; Tarnopolsky et al., 2011; Barthelemy et al., 2020). However, within any population there can be challenges associated with the muscle biopsy procedure. For example, in obese patients where adipose tissue is high (Tarnopolsky et al., 2011; Wang et al., 2011), or in individuals with low muscle mass such as both young and elderly patients (Ekblom, 2017; Wilson et al., 2018). The procedure can be further complicated when considering medication such as insulin and oral hypoglycaemia medications such as those with type 2 diabetes (Wang et al., 2011). Likewise, our study demonstrates that there are several safety considerations to mitigate in patients with CLD or NAFLD, specifically coagulopathy. There has been a reluctancy to perform muscle biopsies within this high-risk group. Surprisingly, we reported only one adverse event (haematoma), which is in line with previous research (Tarnopolsky et al., 2011). This highlights that appropriate patient selection, stringent pre biopsy preparation and good technique mitigates against potential risk. We also report no incidence of localised infection associated with the biopsy procedure. It is likely that the clear post procedure instructions were important to reduce the risk of complications and infection. In addition, patients had regular clinic visits as well as follow-up research visits; thus, if any issues arose, these could be reported and appropriately treated. For future research, we would recommend that a follow-up telephone call should be made in the case where follow-up visits do not occur. Finally, although we applied this safety protocol in specific ESLD and NAFLD groups, it is likely that the same safety protocol could be applied to other liver disease scenarios. Nonetheless, despite our success, to further improve the procedure a true ultrasound guided approach could be utilised to provide visual feedback during the biopsy.

CONCLUSION

We demonstrate that percutaneous muscle biopsies in patients with CLD are feasible and can yield sufficient muscle tissue. Indeed, only 15% of biopsies were declined by the patient, and 90% of the 71 attempted biopsies were successful with only one reported adverse event. It is likely that the success stems from the careful and considered approach to muscle biopsies in this population, considering medications, comorbidities, and mitigating against potential complications. As such, it provides grounds for further mechanistic work into the molecular drivers behind sarcopenia in CLD.

DATA AVAILABILITY STATEMENT

The raw data supporting the conclusions of this article will be made available by the authors, without undue reservation.

ETHICS STATEMENT

The studies involving human participants were reviewed and approved by the Health Research Authority – West Midlands Solihull Research Ethics Service Committee Authority (REC reference: 18/WM/0167). The patients/participants provided their written informed consent to participate in this study.

AUTHOR CONTRIBUTIONS

JQ, AD, FW, and SA acquired the data. JQ and AD completed further analysis of the data contained within the manuscript. JQ and AD jointly constructed initial and final drafts. JQ, AD, FW, LB, CG, JL, MA, and AE aided in the production of the protocol discussed within the manuscript. All authors edited and approved the final manuscript.

FUNDING

This work is supported by the National Institute for Health Research Birmingham Biomedical Research Centre at the University Hospitals Birmingham NHS Foundation Trust and the University of Birmingham (BRC-1215-20009).

ACKNOWLEDGMENTS

The authors would like to acknowledge the help and support of the Clinical Research Facility as well as the patient participants.

REFERENCES

Andrew Shanely, R., Zwetslo93.ot, K. A., Travis Triplett, N., Meaney, M. P., Farris, G. E., and Nieman, D. C. (2014). Human skeletal muscle biopsy procedures using the modified Bergström technique. *J. Vis. Exp.* 2014, 1–8. doi: 10.3791/51812

Aversa, Z., Pin, F., Lucia, S., Penna, F., Verzaro, R., Fazi, M., et al. (2016). Autophagy is induced in the skeletal muscle of cachectic cancer patients. *Sci. Rep.* 6, 1–11. doi: 10.1038/srep30340

Barthelemy, F., Woods, J. D., Nieves-Rodriguez, S., Douine, E. D., Wang, R., Wanagat, J., et al. (2020). A well-tolerated core needle muscle biopsy process suitable for children and adults. *Muscle Nerve* 62, 688–698. doi: 10.1002/mus.27041

Bergstrom, J. (1975). Percutaneous needle biopsy of skeletal muscle in physiological and clinical research. *Scand. J. Clin. Lab. Invest.* 35, 609–616.

Boutrup, R. J., Farup, J., Vissing, K., Kjaer, M., and Mikkelsen, U. R. (2018). Skeletal muscle stem cell characteristics and myonuclei content in patients with rheumatoid arthritis: a cross-sectional study. *Rheumatol. Int.* 38, 1031–1041. doi: 10.1007/s00296-018-4028-y

Carey, E. J., Lai, J. C., Wang, C. W., Dasarathy, S., Lobach, I., Montano-Loza, A. J., et al. (2017). A multicenter study to define sarcopenia in patients with end-stage liver disease. *Liver Transplant.* 23, 625–633. doi: 10.1002/lt.24750

Cruz-Jentoft, A. J., Bahat, G., Bauer, J., Boirie, Y., Bruyère, O., Cederholm, T., et al. (2019). Sarcopenia: revised European consensus on definition and diagnosis. *Age Ageing* 48, 16–31. doi: 10.1093/ageing/afy169

Dalakas, M. C. (2002). Muscle biopsy findings in inflammatory myopathies. *Rheum. Dis. Clin. North Am.* 28, 779–798. doi: 10.1016/S0889-857X(02)00030-3

Dasarathy, S., Dodig, M., Muc, S. M., Kalhan, S. C., and McCullough, A. J. (2004). Skeletal muscle atrophy is associated with an increased expression of myostatin and impaired satellite cell function in the portacaval anastamosis rat. *Am. J. Physiol. Liver Physiol.* 287, G1124–G1130. doi: 10.1152/ajpgi.00202.2004

Dasarathy, S., Muc, S., Hisamuddin, K., Edmison, J. M., Dodig, M., McCullough, A. J., et al. (2007). Altered expression of genes regulating skeletal muscle mass in the portacaval anastamosis rat. *Am. J. Physiol. Liver Physiol.* 292, G1105–G1113. doi: 10.1152/ajpgi.00529.2006

Din, U. S. U., Brook, M. S., Selby, A., Quinlan, J., Boereboom, C., Abdulla, H., et al. (2019). A double-blind placebo controlled trial into the impacts of HMB supplementation and exercise on free-living muscle protein synthesis, muscle mass and function, in older adults. *Clin. Nutr.* 38, 2071–2078. doi: 10.1016/j.clnu.2018.09.025

Ekblom, B. (2017). The muscle biopsy technique. Historical and methodological considerations. *Scand. J. Med. Sci. Sport.* 27, 458–461. doi: 10.1111/sms.12808

Franchi, M. V., Atherton, P. J., Reeves, N. D., Flück, M., Williams, J., Mitchell, W. K., et al. (2014). Architectural, functional and molecular responses to concentric and eccentric loading in human skeletal muscle. *Acta Physiol.* 210, 642–654. doi: 10.1111/apha.12225

Gibbons, C. H., Adler, G. K., Bonyhay, I., and Freeman, R. (2012). Experimental hypoglycemia is a human model of stress-induced hyperalgesia. *Pain* 153, 2204–2209. doi: 10.1016/j.pain.2012.06.030

Ginès, P., Krag, A., Abraldes, J. G., Solà, E., Fabrellas, N., and Kamath, P. S. (2021). Liver cirrhosis. *Lancet* 398, 1359–1376. doi: 10.1016/S0140-6736(21)01374-X

Goodpaster, B. H., Theriault, R., Watkins, S. C., and Kelley, D. E. (2000). Intramuscular lipid content is increased in obesity and decreased by weight loss. *Metabolism* 49, 467–472. doi: 10.1016/S0026-0495(00)80010-4

Hochberg, I., Segol, O., Shental, R., Shimoni, P., and Eldor, R. (2019). Antihyperglycemic therapy during colonoscopy preparation: A review and suggestions for practical recommendations. *United Eur. Gastroenterol. J.* 7, 735–740. doi: 10.1177/2050640619846365

Jepsen, P. (2014). Comorbidity in cirrhosis. *World J. Gastroenterol.* 20:7223. doi: 10.3748/wjg.v20.i23.7223

Kim, G., Kang, S. H., Kim, M. Y., and Baik, S. K. (2017). Prognostic value of sarcopenia in patients with liver cirrhosis: A systematic review and meta-analysis. *PLoS One* 12:1–16. doi: 10.1371/journal.pone.0186990

Kurup, A. N., Lekah, A., Reardon, S. T., Schmit, G. D., McDonald, J. S., Carter, R. E., et al. (2015). Bleeding rate for ultrasound-guided paracentesis in thrombocytopenic patients. *J. Ultrasound Med.* 34, 1833–1838. doi: 10.7863/ultra.14.10034

MacDonald, A. J., Johns, N., Stephens, N., Greig, C., Ross, J. A., Small, A. C., et al. (2015). Habitual myofibrillar protein synthesis is normalin patients with upper GI cancer cachexia. *Clin. Cancer Res.* 21, 1734–1740. doi: 10.1158/1078-0432.CCR-14-2004

Nishikawa, H., Enomoto, H., Nishiguchi, S., and Iijima, H. (2021). Sarcopenic obesity in liver cirrhosis: Possible mechanism and clinical impact. *Int. J. Mol. Sci.* 22, 1–13. doi: 10.3390/ijms22041917

Pantham, G., and Mullen, K. D. (2017). Practical issues in the management of overt hepatic encephalopathy. *Gastroenterol. Hepatol.* 13, 659–665.

Patel, H. P., White, M. C., Westbury, L., Syddall, H. E., Stephens, P. J., Clough, G. F., et al. (2015). Skeletal muscle morphology in sarcopenia defined using the EWGSOP criteria: findings from the Hertfordshire Sarcopenia Study (HSS). *BMC Geriatr.* 15:171. doi: 10.1186/s12877-015-0171-4

Petrides, A. S., and DeFronzo, R. A. (1989). Glucose and insulin metabolism in cirrhosis. *J. Hepatol.* 8, 107–114. doi: 10.1016/0168-8278(89)90169-4

Runyon, B. A. (2009). Management of adult patients with ascites due to cirrhosis: An update. *Hepatology* 49, 2087–2107. doi: 10.1002/hep.22853

Tarnopolsky, M. A., Pearce, E., Smith, K., and Lach, B. (2011). Suction-modified Bergström muscle biopsy technique: Experience with 13,500 procedures. *Muscle Nerve* 43, 716–725. doi: 10.1002/mus.21945

Tsien, C., Davuluri, G., Singh, D., Allawy, A., Ten Have, G. A. M., Thapaliya, S., et al. (2015). Metabolic and molecular responses to leucine-enriched branched chain amino acid supplementation in the skeletal muscle of alcoholic cirrhosis. *Hepatology* 61, 2018–2029. doi: 10.1002/hep.27717

Van Langenberg, D. R., Gatta, P., Della, Hill, B., Zacharewicz, E., Gibson, P. R., et al. (2014). Delving into disability in Crohn's disease: Dysregulation of molecular pathways may explain skeletal muscle loss in Crohn's disease. *J. Crohn's Colit.* 8, 626–634. doi: 10.1016/j.crohns.2013.11.024

Veitch, A. M., Vanbiervliet, G., Gershlick, A. H., Boustiere, C., Baglin, T. P., Smith, L. A., et al. (2016). Endoscopy in patients on antiplatelet or anticoagulant therapy, including Direct Oral anticoagulants: British Society of Gastroenterology (BSG) and European Society of Gastrointestinal endoscopy (ESGE) guidelines. *Gut* 65, 374–389. doi: 10.1136/gutjnl-2015-311110

Wang, Y., Simar, D., Anderberg, K., Mavros, Y., Kay, S., Zhao, R., et al. (2011). Muscle and adipose tissue biopsy in older adults with type 2 diabetes. *J. Diabet. Mellit.* 01, 27–35. doi: 10.4236/jdm.2011.13005

Wilson, D., Breen, L., Lord, J. M., and Sapey, E. (2018). The challenges of muscle biopsy in a community based geriatric population. *BMC Res. Notes* 11:1–6. doi: 10.1186/s13104-018-3947-8

Wilson, D., Jackson, T., Sapey, E., and Lord, J. M. (2017). Frailty and sarcopenia: The potential role of an aged immune system. *Ageing Res. Rev.* 36, 1–10. doi: 10.1016/j.arr.2017.01.006

Author Disclaimer: The views expressed are those of the author(s) and not necessarily those of the NHS, the NIHR or the Department of Health and Social Care.

Conflict of Interest: The authors declare that the research was conducted in the absence of any commercial or financial relationships that could be construed as a potential conflict of interest.

The reviewer BS declared a past collaboration with one of the authors, LB, to the handling editor.

frontiers in Physiology

METHODS
published: 23 February 2022
doi: 10.3389/fphys.2022.839139

Long-Term Cultivation of Human Atrial Myocardium

Maximilian J. Klumm[1,2†], Christian Heim[2†], Dominik J. Fiegle[1], Michael Weyand[2], Tilmann Volk[1] and Thomas Seidel[1*]

[1] Institute of Cellular and Molecular Physiology, Friedrich-Alexander-Universität Erlangen-Nürnberg, Erlangen, Germany,
[2] Department of Cardiac Surgery, Friedrich-Alexander-Universität Erlangen-Nürnberg, Erlangen, Germany

Organotypic culture of human ventricular myocardium is emerging in basic and translational cardiac research. However, few institutions have access to human ventricular tissue, whereas atrial tissue is more commonly available and important for studying atrial physiology. This study presents a method for long-term cultivation of beating human atrial myocardium. After written informed consent, tissues from the right-atrial appendage were obtained from patients with sinus rhythm undergoing open heart surgery with cardiopulmonary bypass. Trabeculae (pectinate muscles) prepared from the samples were installed into cultivation chambers at 37°C with a diastolic preload of 500 μN. After 2 days with 0.5 Hz pacing, stimulation frequency was set to 1 Hz. Contractile force was monitored continuously. Beta-adrenergic response, refractory period (RP) and maximum captured frequency (f_{max}) were assessed periodically. After cultivation, viability and electromechanical function were investigated, as well as the expression of several genes important for intracellular Ca^{2+} cycling and electrophysiology. Tissue microstructure was analyzed by confocal microscopy. We cultivated 19 constantly beating trabeculae from 8 patient samples for 12 days and 4 trabeculae from 3 specimen for 21 days. Functional parameters were compared directly after installation (0 d) with those after 12 d in culture. Contraction force was 384 ± 69 μN at 0 d and 255 ± 90 μN at 12 d ($p = 0.8$, $n = 22$), RP 480 ± 97 ms and 408 ± 78 ms ($p = 0.3$, $n = 9$), f_{max} 3.0 ± 0.5 Hz and 3.8 ± 0.5 Hz ($p = 0.18$, $n = 9$), respectively. Application of 100 nM isoprenaline to 11 trabeculae at 7 d increased contraction force from 168 ± 35 μN to 361 ± 60 μN ($p < 0.01$), f_{max} from 6.4 ± 0.6 Hz to 8.5 ± 0.4 Hz ($p < 0.01$) and lowered RP from 319 ± 22 ms to 223 ± 15 ms. CACNA1c (L-type Ca^{2+} channel subunit) and GJA1 (connexin-43) mRNA expressions were not significantly altered at 12 d vs 0 d, while ATP2A (SERCA) and KCNJ4 (Kir2.3) were downregulated, and KCNJ2 (Kir2.1) was upregulated. Simultaneous Ca^{2+} imaging and force recording showed preserved excitation-contraction coupling in cultivated trabeculae. Confocal microscopy indicated preserved cardiomyocyte structure, unaltered amounts of extracellular matrix and gap junctions. MTT assays confirmed viability at 12 d. We established a workflow that allows for stable cultivation and functional analysis of beating human atrial myocardium for up to 3 weeks. This method may lead to novel insights into the physiology and pathophysiology of human atrial myocardium.

Keywords: human atrium, calcium imaging, tissue culture, *in vitro*, confocal microscopy, gene expression, refractory period

Edited by:
Peter T. Wright,
University of Roehampton London,
United Kingdom

Reviewed by:
Sian Elizabeth Harding,
Imperial College London,
United Kingdom
Steven Baxter Marston,
Imperial College London,
United Kingdom

Correspondence:
Thomas Seidel
thomas.seidel@fau.de

[†] These authors have contributed equally to this work and share first authorship

Specialty section:
This article was submitted to
Striated Muscle Physiology,
a section of the journal
Frontiers in Physiology

Received: *19 December 2021*
Accepted: *25 January 2022*
Published: *23 February 2022*

Citation:
Klumm MJ, Heim C, Fiegle DJ,
Weyand M, Volk T and Seidel T (2022)
Long-Term Cultivation of Human Atrial
Myocardium.
Front. Physiol. 13:839139.
doi: 10.3389/fphys.2022.839139

INTRODUCTION

Organotypic long-term culture of adult human and animal cardiac tissue is emerging as a promising tool in basic and translational cardiac research (Fischer et al., 2019; Ou et al., 2019; Qiao et al., 2019; Watson et al., 2019; Perbellini and Thum, 2020). By preserving the multicellular structure and function of intact myocardium for up to several weeks *in vitro*, the technique bridges the gap between cell culture experiments on the one hand and *in vivo* studies using laboratory animals on the other. Myocardial tissue culture prevents the quick degradation and dedifferentiation occurring during culture of isolated adult cardiomyocytes (Banyasz et al., 2008), but still provides a level of control over physical and chemical stimuli that cannot be achieved *in vivo*. Another important advantage is that the technique can be used to cultivate fully differentiated human myocardial tissue obtained from explanted hearts or accrued during open heart surgery. Thus, the method provides an experimental platform for basic scientists to investigate, for example, the long-term effects of drugs on human cardiac tissue (Fischer et al., 2019; Miller et al., 2020). Other applications include the establishment of structure-function relationships in diseased human myocardium (Abu-Khousa et al., 2020), the investigation of viral myocardial infections (Bojkova et al., 2020), or the maturation of stem cell-derived human cardiomyocytes (Lu et al., 2021). Because stem-cell derived engineered heart tissues have not yet reached the differentiation, multicellularity and physiological properties of adult myocardium, the "heart in a dish" approach of myocardial tissue culture can currently be considered the most realistic *in vitro* model.

Earlier approaches to myocardial slices [reviewed in de Boer et al. (2009)] were useful mainly for short-term experiments (Han et al., 2002; Bussek et al., 2009) or used non-adult heart tissue (Bursac et al., 2003; Pillekamp et al., 2005). Mostly, however, tissues were not functionally stable for more than 24–48 h. Then, one study reported that ventricular slice cultivation on top of cell culture filters prolonged myocardial function and viability, possibly a result of preload applied through adhesion forces together with improved oxygen supply at the liquid-air interface (Brandenburger et al., 2012). However, the structure and function of the tissues still degraded over the course of several days, and for assessment of contractility slices had to be transferred from the filters to baths containing force transducers. This hampered repeated functional measurements over the cultivation period. In subsequent studies it was found that, in addition to a suitable culture medium, there are three important requirements for the longevity of human and animal ventricular slices: (1) the application of diastolic preload or stretch to obtain a physiological resting sarcomere length, (2) regular electrical stimulation causing contraction, and (3) convection of the culture medium (Fischer et al., 2019; Watson et al., 2019). Both studies used M199 as culture medium and carbon electrodes for electrical field stimulation. Watson et al. (2019) used a caliper to determine the strain necessary to achieve an optimal sarcomere length of approximately 2.2 μm and perfused the culture chamber with oxygen-enriched medium. Fischer et al. (2019) applied a preload of 0.66 mN/mm^2 and agitated the medium by placing culture chambers on a rocking platform. Other studies suggested similar solutions for electrical stimulation, preload, and convection or oxygen enrichment of the medium (Ou et al., 2019; Qiao et al., 2019).

Techniques for the cultivation of human ventricular slices are increasingly used in basic and translational studies addressing mechanisms of heart failure, a syndrome resulting mainly from ventricular dysfunction. However, if the described cultivation techniques could be applied also to human atrial tissue, this would constitute an *in vitro* model of comparable utility for studying atrial physiology and pathomechanisms, most prominently of atrial fibrillation. Similarly as described for ventricular slice culture, this could address the need for multicellular three-dimensional *in vitro* models of atrial myocardium (van Gorp et al., 2020) and complement stem-cell derived chamber-specific models (Zhao et al., 2019). Furthermore, because human atrial tissue can be easily obtained during open heart surgery with cardiopulmonary bypass, it is available to a larger number of laboratories than human ventricular tissue. Therefore, we asked whether it is possible to cultivate human atrial myocardium as reported for ventricular slices.

This study presents and evaluates a method for the long-term cultivation of human right-atrial trabeculae using the method reported by Fischer et al. (2019). It describes the preparation, culture conditions and several methods for the assessment of important functional parameters, such as contractile performance and kinetics, Ca^{2+} signaling, as well as gene expression and tissue microstructure before and after cultivation.

MATERIALS AND EQUIPMENT

Specifications of buffers, media, chemicals, reagents, antibodies, dyes, PCR primers, devices, and tools are provided in the **Supplementary Material**.

METHODS

Tissue Collection

Collection and use of patient tissue was approved by the ethics committee of the University of Erlangen-Nürnberg. All experiments followed the Declaration of Helsinki ethical principles. Tissues were donated after written informed consent by patients undergoing open heart surgery with cardiopulmonary bypass at the Cardiac Surgery Department of the University Hospital Erlangen, Germany. Patients with a history of atrial fibrillation were excluded from this study. Patient characteristics are presented in **Table 1**. Before insertion of a two-stage venous cannula for partial cardiopulmonary bypass, the tip of the right-atrial appendage (RAA) was resected after setting up purse-string sutures. The resected tissue, which would have been discarded otherwise, was immediately placed in cool (4°C) storage solution and transported to the laboratory on ice within 20 min.

TABLE 1 | Characteristics of patients who donated samples of the right atrial appendage.

Patient characteristics	
N	11
Age	67.1 ± 12.5 years
Male	10 (91%)
BMI	28.1 ± 6.1 kg/m^2
Sinus rhythm	11 (100%)
Surgery type	
CABG	9 (82%)
Aortic valve	2 (18%)
Hypertension	11 (100%)
Hypercholesterolemia	8 (72%)
Diabetes mellitus	4 (36%)
Coronary heart disease	10 (91%)
Myocardial infarction	4 (36%)
LVEF	55.6 ± 7.0%

BMI, body mass index; CABG, coronary artery bypass graft; LVEF, left-ventricular ejection fraction.

A video showing the tissue collection during surgery is available in the **Supplementary Material**.

Preparation of Trabeculae for Tissue Culture

An overview of the tissue processing steps is shown in **Figure 1**. The tissue was transferred to a 100 mm petri dish containing cold (4°C) storage solution with 30 mmol/l butanedione monoxime (BDM) and a sterile rubber pad for ease of processing (**Figure 1A**). BDM, an uncoupling agent, is used in many slicing protocols (e.g., Watson et al., 2017), and preparations of cardiac muscle strips (Mulieri et al., 1989) to reduce tissue damage. BDM is also used to improve cardiac and skeletal muscle function after long cold-storage periods (Stringham et al., 1994; van der Heijden et al., 2000) and to reduce reperfusion injury (Voigtlander et al., 1999). All processing steps were performed on a cooled plate on a laminar flow workbench. After a lateral incision the tissue was unfolded and secured with sterile cannulas pinned into the rubber pad (**Figure 1B**). Individual trabeculae were dissected using forceps, micro-scissors and, if necessary, magnifying glasses (**Figure 1C**). Typically, four to six trabeculae were retrieved from one single specimen (**Figure 1D**). For gene expression analysis one trabecula was snap-frozen in liquid nitrogen and stored at −80°C. The remaining trabeculae were prepared for installation into cultivation chambers of a commercially available cultivation system (InVitroSys, Germany) as previously described (Fischer et al., 2019). For this, trapezoid polyether holders with holes for mounting were glued to both endings of the trabecula (**Figures 1E,F**) with a 2-butyl cyanoacrylate tissue adhesive (Surgibond, SMI). Subsequently, the trabeculae were installed in the culture chambers filled with prewarmed (37°C) culture medium by mounting the plastic holders with forceps on two opposing metal wire posts inside the chambers (**Figure 1G**). The chambers were immediately placed on the cultivation platform in the incubator. A diastolic load of 500 μN was applied by retracting one of the wires manually with a hex key (**Figure 1H**). Up to 8 chambers were incubated in parallel. The incubator provided a constant temperature of 37°C, 5% CO_2 and 80–85% relative humidity. The rocker for medium agitation was set to 60 rpm, and electrical field stimulation was provided by carbon electrodes with 50 mA constant current and a 3 ms biphasic pulse. A biphasic pulse regiment (3 ms negative pulse, 1 ms pause, 3 ms positive pulse) is important to prevent electrochemical imbalance during long periods of electrical field stimulation. Otherwise, we found that electrolysis of the culture medium may occur, producing toxic chemicals and significant changes in pH. Stimulation frequency was set to 0.5 Hz for the first 48 h of culture. Twitch forces of trabeculae were continuously measured and recorded using a magnetic sensor mechanism and a flexible spring wire as described previously (Fischer et al., 2019). Stimulation time points were recorded in synchrony with the contraction data. After an adaptation period of 48 h the pacing frequency was set to 1 Hz.

A video showing all steps of trabecula preparation as well as a step-by-step protocol are available in the **Supplementary Material**.

Maintenance of Tissue Culture

Culture medium was partly exchanged with prewarmed fresh medium every 24–48 h. To compensate for evaporation, 0.8 ml were removed and 0.9 ml added every 24 h or 1.6 ml removed and 1.8 ml added every 48 h. After the first 24 h of culture, the preload was readjusted to 500 μN to account for viscoelasticity and plasticity of the tissue. On days two, seven and twelve, the beta-adrenergic response was investigated by adding 100 nM isoprenaline to the chambers. Directly before and 5 min after addition of isoprenaline, pacing protocols were performed. After 30–45 min, isoprenaline was washed out by completely replacing the medium. Except for four trabeculae from three patient samples, all trabeculae were removed from culture after 12 days. Trabeculae were then either fixed for immunofluorescence staining, frozen at −80°C for gene expression analyses, or used to assess viability or intracellular Ca^{2+} transients.

Analysis of Force Recordings

Force of contraction and contraction kinetics were analyzed as previously described (Abu-Khousa et al., 2020). **Figure 2** shows one contraction cycle with the diastolic force F_D, which is set by the preload and stretches the trabecula. After an electrical stimulus, the trabecula begins to contract, which deflects the flexible spring wire in the cultivation chamber. The deflection is registered by a magnetic field sensor and used to calculate the corresponding force with the spring constant of approximately 25 mN/mm. As threshold for the beginning of a contraction, 10% of the amplitude was used. At this point, the contraction duration was calculated (CD90). The time from 10% to the maximum force was defined as the time to peak force (TTP90). The time from the maximum back to 10% of the force was defined as time to relaxation (TTR90). Thus, CD90 equals TTP90 + TTR90. These

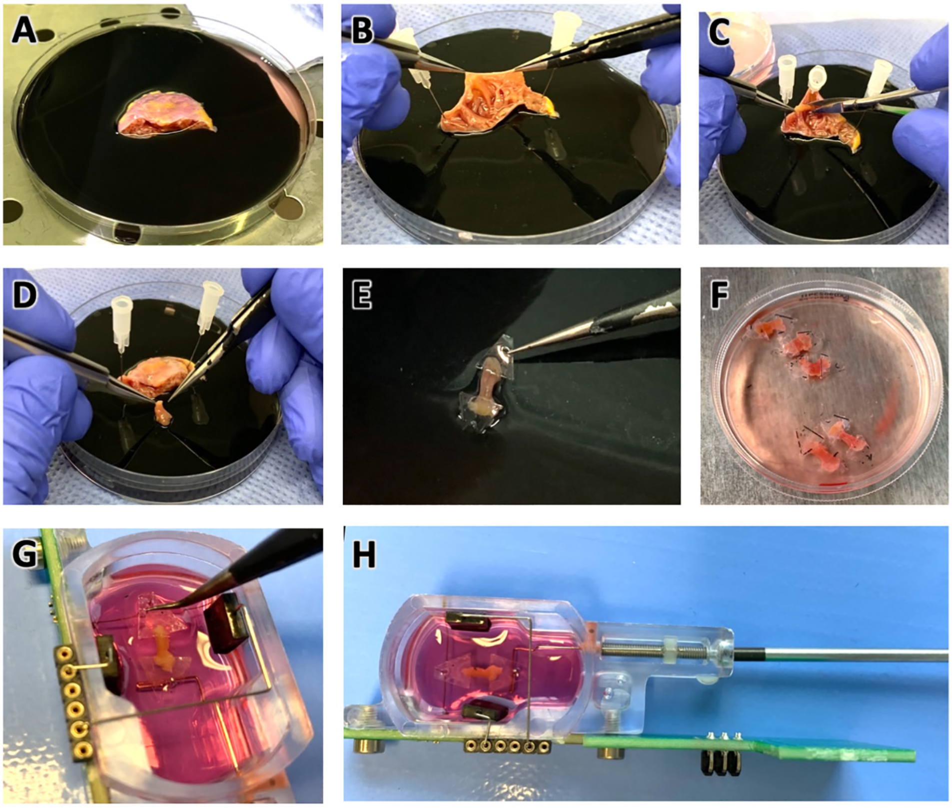

FIGURE 1 | Preparation of pectinate muscles (trabeculae) from right atrial appendage (RAA) samples for tissue culture. **(A)** RAA obtained during cardiac surgery, stored and transported in cold cardioplegic solution. Diameter of the petri dish is 100 mm. **(B)** Inspection of the RAA interior, displaying the typical trabecular meshwork. **(C)** Trabeculae were carefully dissected with a scalpel while fixing the tissue with pins on a rubber layer. **(D)** Excised trabecula. **(E)** Plastic triangles glued to the longitudinal ends of the trabecula. **(F)** Prepared trabeculae in cold Tyrode's solution containing BDM in a standard tissue culture petri dish. Diameter of the displayed dish is 60 mm. **(G)** Trabeculae were installed into cultivation chambers by mounting the plastic triangles on a spring wire (top) and a stiff wire (bottom). **(H)** Adjustment for trabecula length and setting of a defined preload is achieved by moving the stiff wire, which is attached to a bolt and nut, using a hex screwdriver. See also the **Supplementary Videos 1, 2**.

parameters were determined computationally, using custom-written Matlab functions (Mathworks, Matlab versions 2019a and higher). After downsampling the recorded data from 400 to 200 Hz with a mean filter, a central moving median filter of radius 10 and, subsequently, a central moving mean filter of radius 5 were applied to reduce noise. Only periods with the agitation rocker stopped were analyzed. First, the noise level was estimated by calculating the standard deviation and maximum amplitude at low pacing frequencies ($\leq$1 Hz) during 200 ms intervals before an electrical stimulus. Contraction durations were always shorter than 500 ms. Thus, during the 200 ms intervals directly before a stimulus, the fluctuations in the recorded sensor data stem exclusively from noise. Next, a peak detection was performed with the minimum peak height set to the maximum noise amplitude plus one standard deviation of the noise. Starting from each peak (F_{max}) a time window of ± 50% of the stimulus interval duration was analyzed to obtain the contraction amplitude ($F_{amp} = F_{max} - F_D$). F_D was defined as the minimum force within the interval and then subtracted from the signal. Moving backward in time from the peak, TTP90 was then obtained by identifying the time of first occurrence of a force $\leq$ 0.1 F_{amp} before the peak. Conversely, TTR90 was obtained by identifying the time of first occurrence of force $\leq$ 0.1 F_{amp} after the peak. CD90 was calculated as the sum of TTP90 and TTR90. The calculated parameters of all beats within an analyzed period were averaged and then considered representative for this period. For example, if the rocker was stopped for 2 s at a pacing frequency of 3 Hz, six contraction cycles were analyzed and the resulting mean parameters were representative for 3 Hz. The correct detection and analysis of beats was verified by inspection of the analyzed intervals and detected peaks and by comparison of the number of electrical stimuli with the number of detected beats. This way, it was also possible to decide whether a pacing frequency was captured.

Pacing Protocols to Determine Refractory Period and Maximum Frequency

Within 15 min of starting tissue culture (day 0) and on days 2, 7 and 12, pre-defined pacing protocols were performed to assess the refractory period (RP) and maximum captured frequency

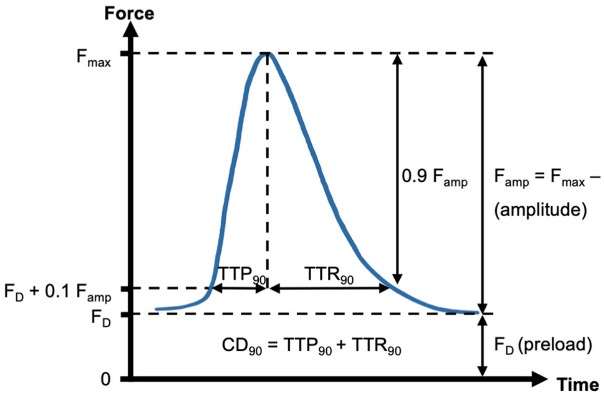

FIGURE 2 | Schematic of contraction analysis. Diastolic force (F_D, preload) and maximum force (F_{max}) were respectively determined from the minimum and maximum spring wire deflections during a contraction cycle, multiplied by the spring constant. The force of contraction was then identified with the resulting amplitude, $F_{amp} = F_{max} - F_D$. Contraction kinetics were assessed by using F_D + 10% of F_{amp} as a threshold for start and end of a contraction. Thus, the parameters contraction duration (CD_{90}), time to peak (TTP_{90}) and time to relaxation (TTR_{90}) were calculated.

($f_{\max}$). For this purpose, the trabeculae were paced with a baseline frequency of 0.5 Hz. After 22 s of normal pacing, three intertwined S2 beats followed with a defined S2 beat interval. After another 22 s of regular pacing at 0.5 Hz, trabeculae were stimulated with the frequency corresponding to the S2 beat interval for 6 s. For example, if the S2 beat interval was 500 ms, the corresponding pacing frequency was 2 Hz. This scheme was repeated with decreasing S2 beat intervals and accordingly increasing frequencies. The S2 beat intervals were (in ms): 750, 500, 400, 300, 275, 250, 240, 230, 220, 210, 200, 190, 180, 170, 160, 150, 140, 130, 120, 110, and 100. To evaluate contraction parameters at frequencies other than the baseline pacing rate, the stimulation frequency was increased successively from 0.2 to 5 Hz as follows (in Hz): 0.2, 0.5, 0.75, 1.0, 1.5, 2.0, 2.5, 3, 3.5, 4.0, 4.5, and 5.0. Each period lasted for 25 beats, for example, 25 s at 1 Hz and 5 s at 5 Hz. During Ca^{2+} imaging, modified versions of these protocols with fewer steps were used to reduce protocol durations. During all pacing protocols, the rocker of the culture platform was stopped intermittently for 2–10 s to record at least six consecutive contractions at the end of each stimulation period without any artifacts from medium agitation. These artifacts are caused by movements of the spring wire resulting from inertia and gravity and appear as low-frequency noise in the recorded data (see **Figure 5B** for an example). Thus, stopping the rocker briefly improves the signal-to-noise ratio. It was shown in previous work that stopping medium agitation has no effects for approx. 20–30 s (Fischer et al., 2019). Only contractions recorded during rocking-free periods were analyzed. The stimulation schedules of the protocols were defined with commands in a text file, which were read by the control software and then submitted to the controller/stimulation unit. The controller transferred a 400 Hz data stream including the force transducer data and the electrical stimulation times.

Contractions during the pacing protocols were identified by noise and peak analysis as described above. To decide whether a S2 beat was captured, the interval between the S2 stimulus and the following S1 stimulus was analyzed. If a peak, i.e., any positive slope above the minimum peak height, was detected, the stimulus was considered as captured. A second criterion was that all three S2 beats had to be captured. During the decreasing S2 stimulus intervals, the interval before the first occurrence of "not captured" was identified with the refractory period. To determine the maximum captured frequency, the last five stimuli of the high-frequency pacing train were analyzed applying the described approach for peak detection. If any of these five stimuli was not captured, the frequency was considered as not captured. The last captured frequency before the first occurrence of a non-captured frequency was identified with $f_{\max}$. By reviewing the contraction traces and detected peaks manually by researchers, it was ensured that the analysis program behaved as expected.

Parallel Registration of Contractile Force and Intracellular Ca^{2+}

Cultured trabeculae were mounted in a modified MyoDish culture chamber (InVitroSys) with a glass cover slip bottom. Culture medium was exchanged for Ca^{2+} imaging buffer. Calbryte 520-AM Ca^{2+} indicator (AAT Bioquest) was added at 10 μmol/l together with 0.1% Pluronic Acid F127 (Biotium) and incubated for 20 min at 37°C and agitation on a horizontal laboratory shaker. The chamber was then installed on an inverted microscope (Leica, DMIRB). For dye washout superfusion with Ca^{2+} imaging buffer (37°C) was initiated at 250 ml/h and maintained throughout the experiment. After 5 min the trabeculae were stimulated with pacing protocols for analysis of the force-frequency relationship (FFR), RP, and $f_{\max}$, using the MyoDish control unit. Simultaneously the trabecula was illuminated with a spectrum of 460–500 nm through a 5× lens (Leica, 0.15 HC PL FLUOTAR). Emitted light was collected after bandpass filtering 510–585 nm with a photomultiplier of a fluorescence imaging system (IonOptix). Contraction and Ca^{2+} signals were synchronized using the electrical simulation signal recorded with both acquisition systems.

Immunofluorescent Staining

Tissue was fixed either directly after procurement or after 12 days in culture with paraformaldehyde (PFA, 2% in phosphate buffered saline, PBS) for 30 min. After two washing steps in PBS (performed after all following steps) the specimens were embedded in Tissue Tek O.C.T. Compound (*Sakura*, 4583), frozen at −20°C and cut into 80 μm sections in longitudinal orientation. Subsequently, the tissue sections were stained with primary antibodies against connexin-43 (Cx43, 1:400) and alpha-actinin (aACT, 1:200) in PBS supplemented with 1% bovine serum albumin, 5% normal-goat-serum and 0.25% TritonX-100 for 24–48 h. Secondary antibodies goat-anti-rabbit AF555 (used for Cx43, 1:400) and goat-anti-mouse AF488 (used for alpha-actinin, 1:200) were incubated for 24–48 h while protected from light. In a last step, nuclear staining with DAPI and staining of the extracellular matrix with wheat germ agglutinin

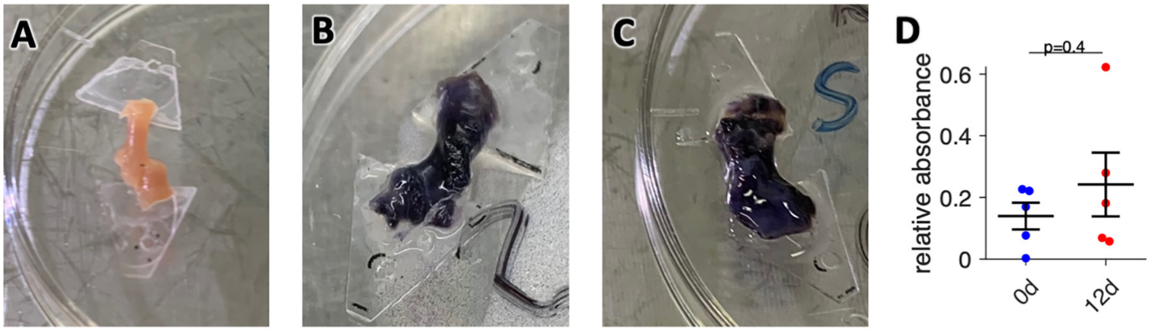

FIGURE 3 | Assessment of tissue viability. **(A)** Photograph of an unstained trabecula. Width of the plastic triangles is 7 mm. **(B)** Photograph of a fresh trabecula after incubation with the tetrazolium dye MTT for 15 min. The intensity of the dark purple color indicates the amount of MTT enzymatically reduced to formazan. **(C)** Photograph of a trabecula cultivated for 12 days after 15 min of MTT incubation from the same specimen as panel **(B)**. **(D)** Results from photometric analysis of the amount of formazan produced from MTT, normalized to total protein of fresh trabeculae (0 d) and trabeculae from matching specimens cultivated for 12 days (12 d). *N* = 5/5 trabeculae/samples. The unequal variances *t*-test was applied for statistical analysis.

(WGA) conjugated to AF647 was performed for 8–12 h. Stained tissue sections were then mounted on standard microscope slides in Fluoromount G mounting medium, covered with a coverslip and dried at room temperature for at least 24h while protected from light.

Confocal Microscopy and Image Analysis

Confocal microscopy and investigation of tissue microstructure was performed according to previously published methods (Seidel et al., 2016, 2017a,b; Abu-Khousa et al., 2020). Microscopy slides were mounted on the stage of an inverted confocal microscope (Zeiss, LSM780) and imaged with a 63× oil objective (Zeiss, Plan-Apochromat, 63×/1.4). Three-dimensional image stacks (1280 × 1280 × 100 voxels, voxel size 0.1 μm × 0.1 μm × 0.2 μm) of three randomly selected regions were scanned from each sample. After image acquisition, raw data were noise-filtered and deconvolved with the Richardson-Lucy method, using measured point spread functions, and corrected for depth-dependent signal attenuation (Seidel et al., 2016). Afterwards, the WGA, aACT, Cx43 and DAPI signals were separated from background by application of intensity thresholds calculated for each image stack. Global thresholds of image mode plus 1, 3, and 2 standard deviations were used for WGA, Cx43, and DAPI, respectively. The aACT signal showed large variation in intensity across image stacks. Therefore, a local threshold was used. This was achieved by application of a box mean filter with a dimension of 20 × 20 × 2 voxels and subsequent subtraction of the result from the original image. A threshold of mode + 1 standard deviation was then applied to the resulting image.

The amount of extracellular matrix was identified with the volume ratio of the segmented WGA signal (Emde et al., 2014; Seidel et al., 2017b). Similarly, gap junction density was estimated from the volume density of the Cx43 signal after application of a three-dimensional morphological opening filter with a radius of 0.2 μm to reduce speckle noise. Sarcomere density was estimated from the volume density of the segmented aACT signal. The aACT was also used as a myocyte marker to calculate the myocyte volume fraction. After watershed-based creation of intracellular and extracellular segments on the WGA signal inverted distance map (Seidel et al., 2013), those segments with an aACT content of at least 7.5% were classified as myocyte segments.

Viability Assay

Cellular viability of atrial tissue was assessed with MTT assay as described in earlier studies (Brandenburger et al., 2012). In brief, fresh or cultured trabeculae were washed once with assay buffer and then incubated in 2 ml assay buffer supplemented with 0.5 mg/ml 3-(4,5/dimethyl-2-thiayolyl)-2,5-diphenyl-2H-tetrazoliumbromide (MTT, Sigma) on the cultivation platform inside the incubator for 20 min, i.e., in the dark at 37°C, 5% CO_2 and 80–85% relative humidity. After that, the tissue was washed twice with assay buffer and dry-frozen at −80°C. For photometric analysis, reduced formazan was extracted from tissue by incubation in 1 ml dimethylsulfoxide (DMSO) at 37°C for 30 min and constant agitation at room temperature. The absorbance of the resulting supernatant was measured against DMSO in a microplate reader (Tecan, GENios) at 595 nm excitation. For normalization, total protein of the tissue was determined by lysis of the trabeculae after formazan extraction in 100 μl sodium hydroxide solution (0.5 M) for 30 min at 95°C. Lysed samples were then used for Bradford protein quantification assay. For this, samples were diluted 1:10 in Bradford reagent (BioRad) and measured against buffer in a microplate reader at 595 nm excitation. For absolute protein quantification a serial dilution of bovine serum albumin samples was used followed by linear regression for the calculation of total protein content of the samples. The formazan absorbance was then divided by the total protein, yielding the relative absorbance as an indicator of tissue viability.

Gene Expression Analysis

Quantitative real-time PCR (qPCR) was performed using total RNA extracted from frozen tissue samples that were stored at −80°C using NucleoSpin RNA-Kit (Macherey-Nagel), following the manufacturers' instructions. Tissue was processed with a T10 basic homogenizer (IKA) in the lysis buffer of the kit prior to all following steps. RNA was eluted in ultrapure water,

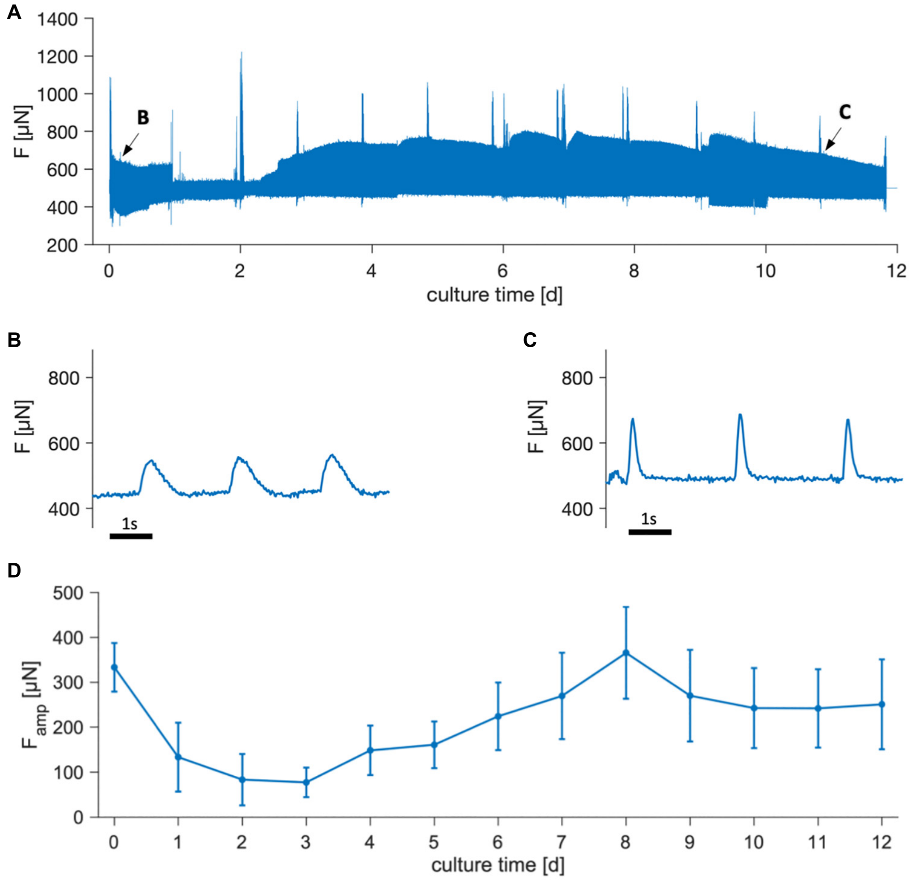

FIGURE 4 | Contraction force of trabeculae cultivated for 12 days. **(A)** Overview of an example showing the measured force, *F*. Spikes result from pacing protocols, addition of isoprenaline and medium exchanges. **(B,C)** Magnifications of periods indicated by arrows in panel **(A)**, showing single contractions. Pacing rate during the displayed periods was 0.5 Hz. Rocking for medium agitation was turned off, causing the amplitudes to appear smaller than at the corresponding time points in panel **(A)**. **(D)** Mean contraction force amplitudes, F_{amp}, of 22 trabeculae from 8 tissue samples. Error bars indicate SEM.

quantified and quality controlled by assessing A260/280 nm and A260/230nm ratios with a DS 11 + spectrophotometer (Denovix). 50 ng of total RNA was transcribed to cDNA with QuantiTect RT-Kit (Qiagen), including a DNAase digestion step for genomic DNA removal. The resulting cDNA was separated via gel electrophoresis to exclude genomic DNA contaminants and cDNA degradation. For real-time quantification, 50 ng cDNA was used in SYBR Select assay (Thermo Fisher Scientific) in a StepOnePlus thermocycler (Applied Biosystems) using the following protocol: Initiation: 50°C for 120 s, 95°C for 120 s, Amplification (40 cycles): 95°C for 15 s, 60°C for 60 s. The genes of interest and the reference genes were amplified with pairs of oligonucleotides as primers. Cycle threshold (C_t) values of triplicate reactions were averaged for each sample and non-template controls ensured the absence of contaminating DNA. Reaction efficiencies were calculated for every experiment from linear regression analysis of a template dilution serious (1:5, 1:25, 1:125, and 1:625). C_t value differences (ΔC_t) between treatment groups and the control group (fresh) were calculated and corrected for reaction efficiencies. Relative expression differences (ratios) were determined by normalization to values of the reference genes EEF2 and HPRT1, which were calculated accordingly (Pfaffl, 2001).

Statistics

If not otherwise indicated, data are presented as mean ± standard error of the mean (SEM). The paired, two-sided *t*-test was used to compare parameters obtained from the same trabecula, the Welch's (unequal variance), two-sided *t*-test was used to compare parameters from different trabeculae. Where required due to multiple comparisons of one parameter, the Holm-Bonferroni method was used to correct *p*-values. The level of significance (alpha) was set to 0.05.

RESULTS

Viability of Cultured Human Atrial Trabeculae

We prepared a total number of 38 trabeculae from 11 specimens obtained from 11 patients (**Table 1**). Of these, 33 (87%) produced contractions exceeding the sensor noise (>50 µN) in response to electrical stimulation immediately after bringing them into culture. The five non-beating trabeculae were removed. Five beating trabeculae were used within 30 min for viability assays, leaving 28 trabeculae. If after 2 days no response could be detected even after addition of isoprenaline, the trabeculae were removed and not included in any data analysis, which was the case in 5 trabeculae. Thus, after 12 d in culture, 23 trabeculae (82% of 28) were still beating. Of these, four trabeculae from three different specimens were kept in culture for a total of 21–22 days, while the other trabeculae were used at day 12 for functional, structural and molecular analyses. To assess general viability, we used an MTT assay, which indicates the activity of cellular NAD(P)H-dependent oxidoreductases reducing the nearly colorless tetrazolium dye MTT to the purple formazan (**Figure 3**). Thus, the amount of formazan produced is related to the metabolic activity and viability of the cells present in the tissue (Berridge et al., 2005). When comparing 5 trabeculae at 0 d with 5 trabeculae from matching specimens after 12 d in culture, we found no significant difference in relative absorbance, i.e., formazan produced in relation to total protein content was comparable (**Figure 3D**). This indicates that tissue viability of beating trabeculae was preserved during long-term culture.

Contractile Force During Culture

Figure 4 shows the contraction force of trabeculae cultivated for 12 days. In the example shown (**Figures 4A–C**) it is visible that contractility was relatively high directly after starting tissue culture, but then declined during the subsequent days. In some trabeculae, contraction was not detectable between days 1 and 3, but recovered to initial values within 1 week. Note that the trace shown in **Figure 4A** includes artifacts from tissue agitation, which add to the actively developed force. This explains why the beats presented in **Figures 4B,C** appear to have lower amplitudes than visible in the overview because the rocker was stopped. Spikes visible in the overview were caused due to transiently increased contractility after medium exchange, likely caused by brief changes in medium pH, and also due to periodically performed stimulation protocols or beta-adrenergic stimulation on days 2, 7, and 12. In **Figure 4D** the mean contraction amplitude of 22 trabeculae is presented over 12 days, showing a similar trend as in the example. Initial contraction force was reached after approximately 7 d and was then stable for the remaining time. Four trabeculae were kept in culture for 3 weeks, and contraction amplitudes did not significantly differ from day 12. From this we conclude that during the first days of culture contractility is reduced, but recovers within 1 week and then remains stable for at least the next 2 weeks.

Assessment of Refractory Period and Maximum Captured Frequency

Figure 5 displays an example of the pacing protocol used to assess RP and $f_{\max}$. The stimulation times were used to create the graph shown in **Figure 5A**, where the stimulus-to-stimulus intervals are displayed over time. It is visible on the logarithmic scale that the S2 beat intervals decreased with each period, and that each S2 beat period was followed by a brief period of stimulation with the corresponding frequency. **Figure 5B** shows the registered contraction data of an S2 beat period and the subsequent high-frequency stimulation intermitted by 22 s of baseline pacing at 0.5 Hz. The example also demonstrates how stopping the rocker reduced artifacts from medium agitation. To verify the relation of refractory period to action potential duration, we applied the highly selective IKr blocker dofetilide, which significantly prolongs the atrial action potential duration (APD) and refractory period (Gwilt et al., 1991; Sedgwick et al., 1992; Tsujimae et al., 2007). **Figure 5C** depicts the response to exactly the same stimulation sequence as displayed in **Figure 5B**, 15 min after addition of 100 nM dofetilide to the culture medium. At close inspection one can appreciate an increase in contractile force, presumably caused by increased Ca^{2+} influx due to APD prolongation, as well as a diminished response to the S2 stimulus. Furthermore, the high-frequency period (55–58 s) shows alternans, with each beat of high amplitude followed by a beat of markedly reduced amplitude. The effect of dofetilide becomes more evident when comparing the S2 beats under control conditions (**Figure 5D**) with those after application of the drug (**Figure 5F**). While the S2 beat at an interval of 750 ms was nearly unchanged when compared with the baseline beats under control conditions, it was hardly visible with dofetilide. According to the defined criteria, the refractory period in the shown example was 400 ms (control) and 500 ms (dofetilide), that is, dofetilide increased RP by approx. 25%, fitting well to clinical data (Gwilt et al., 1991). As expected, $f_{\max}$ was decreased after dofetilide application (**Figures 5E** vs. **G**). In the example it decreased from 5 to 2.5 Hz. These results demonstrate that RP and $f_{\max}$ as assessed by the chosen pacing protocols and criteria may indirectly detect changes in action potential duration.

Effects of Culture on Contraction Parameters, Refractory Period, and Maximum Captured Frequency

Figure 6 presents statistical data of contraction parameters, RP and $f_{\max}$ obtained from 22 trabeculae. **Figure 6A** shows that initial contraction forces at 0 d showed high variability, with values ranging from nearly 0 to 1200 μN. After 1 week of culture, variability was smaller, but the mean did not change significantly. This was also true after 12 d in culture. Analysis of contraction kinetics (**Figures 6B–D**) was restricted to trabeculae with amplitudes larger than 50 μN. Thus, the parameters of some trabeculae could not be evaluated at all time points, reducing the number of matching data points to 13. Mean CD90 was 367 ± 51 ms at 0 d, 309 ± 45 ms at 7 d and 414 ± 57 ms at 12 d, but differences were not statistically significant. Similarly, TTP90 and TTR90 did not differ at the investigated time points. Mean values ranged from 118—155 ms and 188–263 ms, respectively. However, with a contribution of approximately 35% to CD90, TTP90 was significantly shorter than TTR90 ($p < 0.0001$, paired t-test), fitting well to the observation that atrial contraction is about twofold faster than relaxation (Palka et al., 1996). RP showed high variance, especially at 0 d (**Figure 6E**) and did not change significantly over time. However, due to the chosen pacing protocol, the resolution was lower at long S2 beat intervals with

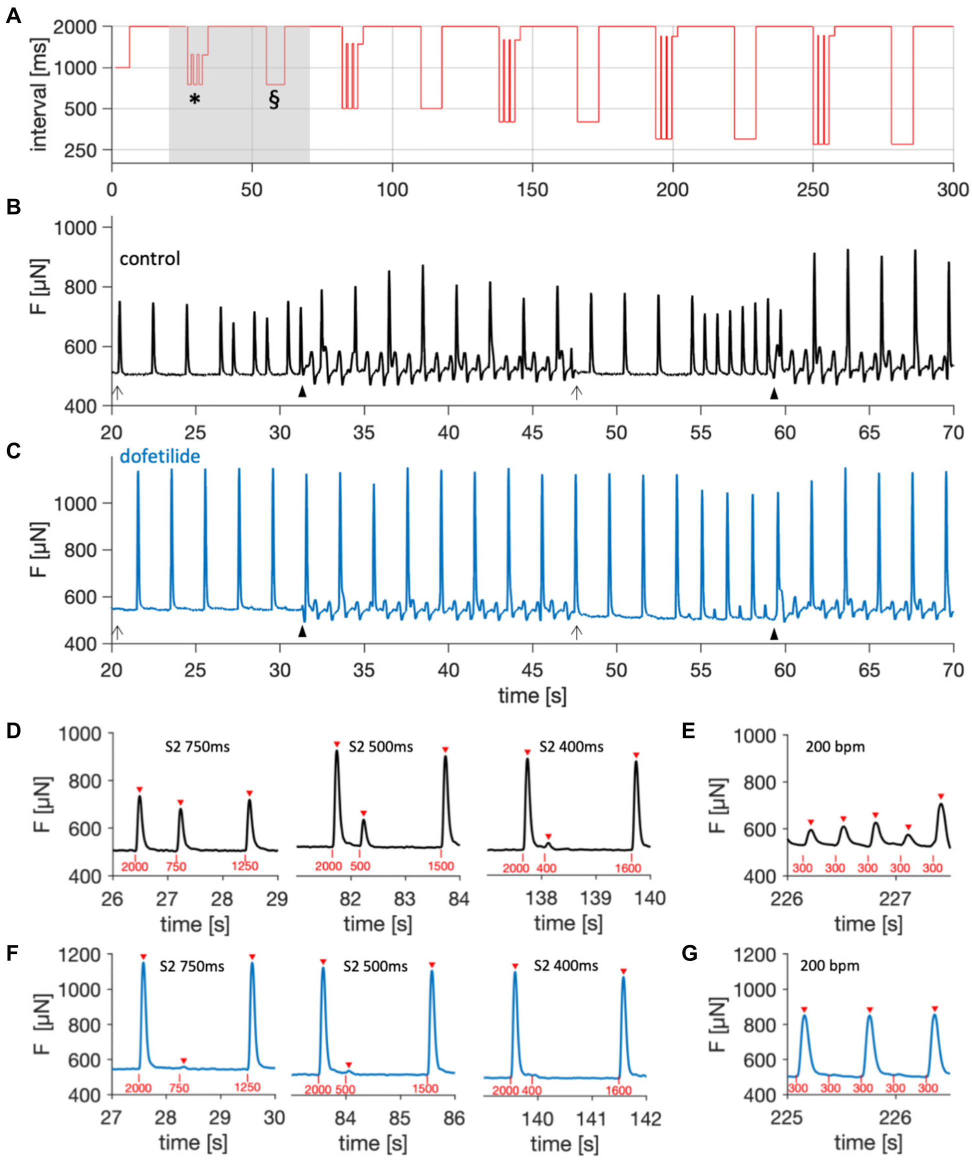

FIGURE 5 | Assessment of refractory period (RP) and maximum frequency captured (f_{max}). **(A)** Stimulation intervals during the pacing protocol, showing successive periods of decreasing interval lengths intermitted by 20-s periods with a baseline interval of 2000 ms. After each S1-S2 beat period (*), a period with constant pacing at the corresponding frequency (§) followed. Note the logarithmic *Y*-axis scale. **(B,C)** Force, *F*, measured during the period marked by the gray area in panel **(A)** of a trabecula **(B)** before, and **(C)** 15 min after treatment with 100 nM dofetilide. Closed arrow heads indicate the start of medium agitation by the rocker, causing shaking artifacts. Open arrow heads indicate rocker stop. **(D)** S1-S2 beat periods before addition of dofetilide (control) at S2 beat intervals of 750, 500, and 400 ms. Red triangles indicate detected contractions, red vertical bars and numbers indicate stimulation time points and intervals, respectively. **(E)** Period of pacing with 3.3 Hz (200 bpm) before addition of dofetilide (control). **(F)** S1-S2 beat periods after addition of dofetilide at S2 beat intervals of 750, 500, and 400 ms (same trabecula as **D,E**). **(G)** Period of pacing with 3.3 Hz (200 bpm) after addition of dofetilide.

relatively large steps from 750 to 500 ms and then to 400 ms. This may explain the large deviation of RP from the mean found in some trabeculae. Analysis of f_{max} (**Figure 6F**) revealed a tendency toward higher values at 7 d (5.2 ± 0.8 Hz) vs 0 d (3.0 ± 0.5 Hz) and 12 d (3.8 ± 0.5 Hz) without reaching statistical significance. Collectively, the data suggest that the variance between different trabecula is relatively high, but that culture of up to 12 d does not lead to significant changes in contraction parameters, RP or f_{max}.

Simultaneous Recording of Ca^{2+} Signals and Contraction

Because Ca^{2+} cycling in atrial cardiomyocytes is gaining increasing interest and is altered in atrial fibrillation (Hove-Madsen et al., 2004; Denham et al., 2018), we intended to demonstrate that cultivated trabeculae can be used for simultaneous recording of intracellular Ca^{2+} and contraction (**Figure 7**). After loading a trabecula that had been in culture

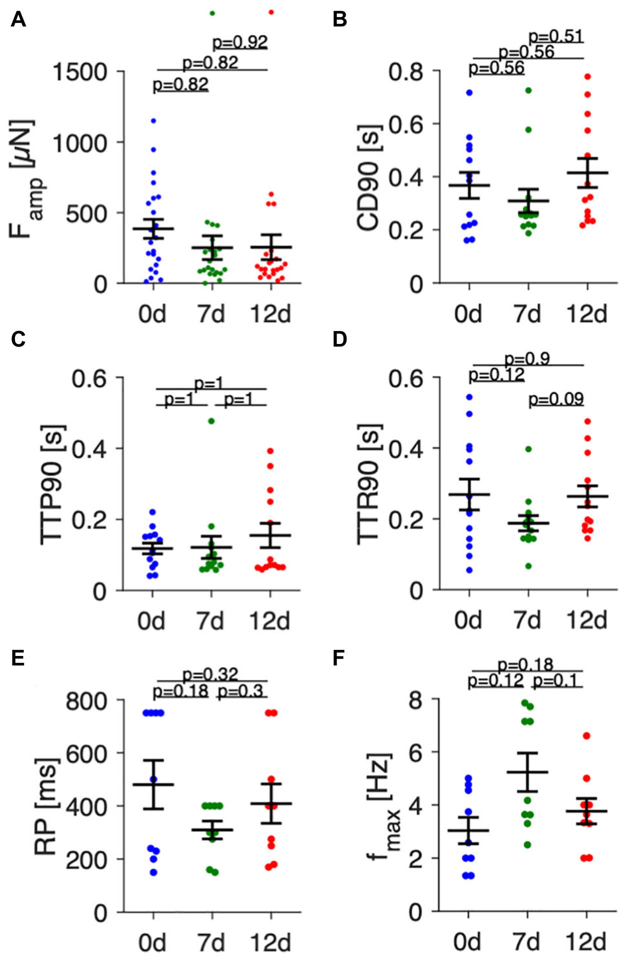

FIGURE 6 | Analysis of contraction amplitudes, kinetics and pacing response in fresh and cultivated trabeculae. **(A)** Contraction force amplitudes (F_{amp}) of fresh (0 d) trabeculae and trabeculae cultivated for 7 (7 d) and 12 days (12 d) at 1 Hz pacing. **(B)** Contraction duration (CD90), **(C)** time to peak (TTP90), and **(D)** time to relaxation (TTR90) at 1 Hz pacing. **(E)** Refractory period (RP), **(F)** Maximum frequency captured (f_{max}). *(N)* = 22/7 trabeculae/samples in panel **(A)**, 13/7 in panels **(B–D)**, and 9/6 in panels **(E,F)**. A paired, two-sided *t*-test with Holm-Bonferroni multiple-comparison correction was applied.

for 3 weeks with the Ca^{2+} indicator Calbryte, we placed the cultivation chamber on a microscope equipped with a perfusion system and a fitting excitation light source and emission filters. Using a 5× lens and a photomultiplier to record a sum signal of the whole trabecula and by capturing and recording the stimulation voltage pulses, we were able to synchronize the Ca^{2+} signal with the recorded force data. Starting from a baseline pacing frequency of 0.5 Hz, a stimulation sequence of increasing frequency was applied to investigate the behavior of contractility and the Ca^{2+} signal at frequencies up to 3 Hz (**Figure 7A**). Each frequency was held for 12 consecutive stimulation pulses. After the last 3 Hz stimulus, the pacing was decreased to 0.2 Hz, creating a pause of 5 s (post-rest beat). It is visible from the normalized traces in **Figure 7B** that the investigated trabecula displayed a negative force-frequency relationship (FFR), i.e., contraction and Ca^{2+} signal amplitudes were inversely related to pacing frequency. In the same experiment, 100 nM of the beta-1/2 receptor agonist isoprenaline was added to the perfusion buffer solution, which resulted in a nearly threefold increased contraction force and twofold increased Ca^{2+} signal. The FFR between 0.2 Hz and 1.5 Hz appeared less negative than under control conditions (**Figure 7C**), but showed a steeper negative slope at higher frequencies. Closer inspection of individual beats at different pacing rates revealed that the apparent difference in FFR at higher rates occurred because capture rate was increased in response to isoprenaline. While under control conditions only every second stimulus was captured starting at 2 Hz, each stimulus was captured after addition of isoprenaline (**Figures 7D,E**). Furthermore, when comparing the post-rest beats with the those recorded at 0.2 Hz, we observed that the relative increase of both contraction force and Ca^{2+} signal after the pause was higher under control conditions. This fits well to reports of a reduced post-rest response at high SERCA activity (Bluhm et al., 2000), because isoprenaline stimulates the SERCA. **Figure 7** also shows that Ca^{2+} signals and contractility can be investigated simultaneously in cultivated trabeculae and that trabeculae respond as expected to beta-adrenergic stimulation. Of note, some trabeculae used for Ca^{2+} imaging were placed back on the cultivation system and could be successfully kept in culture for several days after the imaging. This suggests that the used Ca^{2+} indicator does not exert toxic effects and allows for repeated assessment of Ca^{2+} signals within the same trabecula.

Effects of Beta-Adrenergic Stimulation on Contraction Parameters, Refractory Period, and Maximum Captured Frequency

In **Figure 8** we present data from 11 trabeculae that were treated with 100 nM isoprenaline at day 7 in culture. Contraction parameters, RP and f_{max} were evaluated directly before and 5 min after application of isoprenaline. Contractile force measured at 1 Hz (**Figure 8A**) increased by 114% from 168 ± 35 μN to 361 ± 60 μN ($p < 0.001$, paired *t*-test). CD90 decreased from 331 ± 47 ms to 209 ± 15 ms ($p < 0.05$), which predominantly resulted from a faster relaxation time (**Figures 8B–D**). RP decreased from 319 ± 22 ms to 223 ± 15 ms (**Figure 8E**), and f_{max} increased from 6.4 ± 0.6 Hz to 8.5 ± 0.4 Hz (**Figure 8F**), both being in accordance with shortened action potentials, increased excitability and accelerated mechanical response expected after beta-adrenergic stimulation. These results show that beta-adrenergic response is still present after 1 week in culture. They also let us conclude that the protocols used to determine RP and f_{max} are capable of detecting relevant differences.

Tissue Microstructure

To investigate effects of tissue culture on tissue and cardiomyocyte microstructure, we used immunofluorescent staining and confocal microscopy to compare four fresh trabeculae with four trabeculae from matching specimens (patients) after 12 d in culture (**Figure 9**). Fresh trabeculae displayed patches of fibrotic tissue and clearly visible Cx43

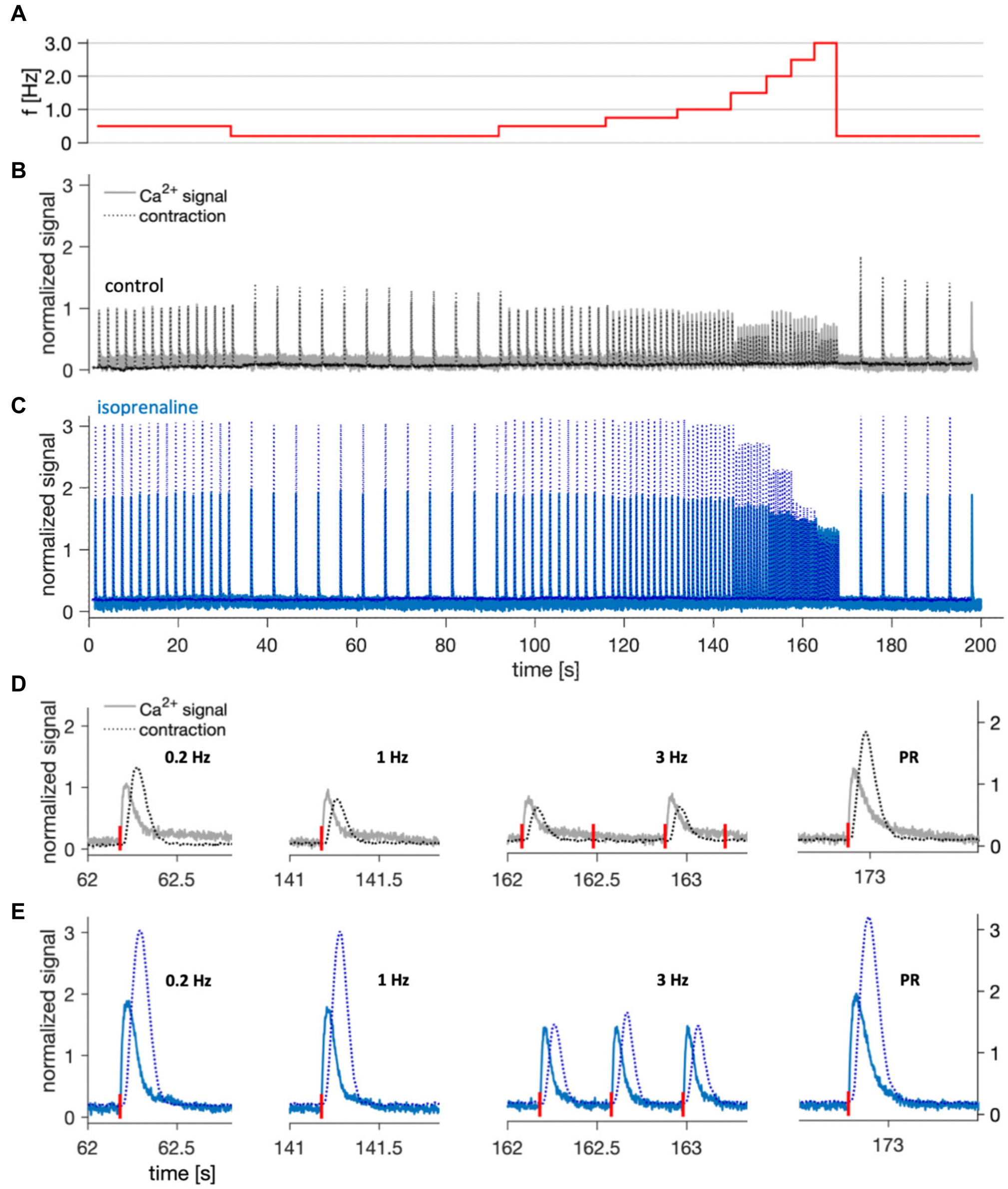

FIGURE 7 | Example of simultaneous Ca^{2+} signal and contraction recording at 37°C in a trabecula after 22 days in culture. **(A)** Stimulation frequencies applied during the imaging to assess the force-frequency response and post-rest beat. **(B)** Overlay of normalized Ca^{2+} signal (solid line) and contraction force (dotted line) recorded during the shown stimulation protocol under control conditions. After offset subtraction, both signals were normalized to the respective amplitude in response to the first stimulus (0.5 Hz). **(C)** The same trabecula 5 min after application of 100 nM isoprenaline. **(D,E)** Normalized single contractions and corresponding Ca^{2+} signals recorded at different stimulation frequencies, and the post-rest (PR) beat at 5 s after the last 3 Hz stimulus. Stimulation times are indicated by red vertical bars next to the *X*-axis. Shown traces are magnifications of panels **(B,C)**, respectively.

staining between cardiomyocyte borders (**Figure 9A**). Alpha-actinin (aACT) staining was visible in most cardiomyocytes and showed a regular sarcomere pattern (**Figure 9B**). The segmentation and classification of the imaged volume into cardiomyocytes and extracellular matrix (ECM) is presented in **Figure 9C**. Black regions indicate regions without any WGA or aACT signal, i.e., gaps in the tissue resulting from processing, cardiomyocytes without aACT staining, or other cell types, for example fibroblasts or endothelial cells. **Figures 9D–I** show two regions imaged in a trabecula from the same specimen (patient) that was cultivated for 12 d. In one region (**Figures 9D–F**), there was abundant Cx43 signal, similar to the fresh tissue and relatively weak but clearly visible aACT staining in most cardiomyocytes. The second region (**Figures 9G–I**) displayed only small clusters of Cx43, which were found not only at myocyte borders, but also intracellularly. The aACT signal intensity, however, was stronger. Quantitative analysis of the three-dimensional images indicated comparable amounts

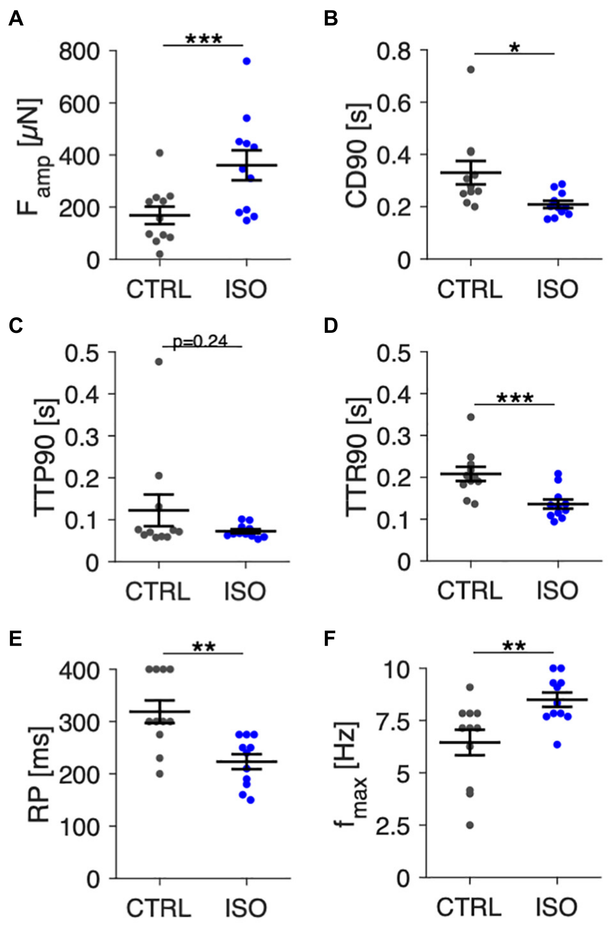

FIGURE 8 | Effect of beta-adrenergic stimulation by isoprenaline on contraction amplitudes, kinetics, and pacing response in trabeculae at 7 days in culture. **(A)** Contraction force amplitudes (F_{amp}) at control conditions (CTRL) and 5 min after addition of 100 nM isoprenaline (ISO), 1 Hz pacing. **(B)** Contraction duration (CD90), **(C)** time to peak (TTP90), and **(D)** time to relaxation (TTR90) at 1 Hz pacing. **(E)** Refractory period (RP), **(F)** Maximum frequency captured (f_{max}). N = 11/3 trabeculae/samples. A paired t-test was applied. $^*p < 0.05$, $^{**}p < 0.01$, $^{***}p < 0.001$.

of ECM, myocytes, Cx43 and aACT in fresh and cultivated trabeculae (**Figure 9J**). This allows the conclusion that tissue culture preserved cardiomyocyte and tissue microstructure and did not cause additional fibrosis.

Expression of Genes Related to Ca^{2+} Cycling and Electrophysiology

Finally, we selected several genes that encode proteins important for cardiomyocyte Ca^{2+} cycling and electrophysiology and analyzed the mRNA expression of these genes by quantitative RT-PCR (**Figure 10**). After analyzing expression levels in 8 fresh trabeculae and 8 cultivated trabeculae from matched specimens (patients), we found that the CACNA1c subunit of the L-type Ca^{2+} channel had a trend toward lower expression after 12 d of culture, although statistical significance was not reached (p = 0.08). However, mRNA expression of ATP2A, the gene encoding the sarcoplasmic/endoplasmic reticulum calcium ATPase 2 (SERCA2) was significantly downregulated. GJA1, encoding Cx43, did not change significantly, but showed higher variance in cultivated trabeculae, which confirmed the results from confocal microscopic analysis of Cx43. We also investigated two subunits of the inwardly rectifying potassium channels that have been reported to be altered in atrial fibrillation (Deshmukh et al., 2015). The mRNA expression of KCNJ4, encoding Kir2.3, was downregulated by half, while KCNJ2, encoding Kir2.1, was about threefold upregulated. These data show that gene expression is altered in culture. They also demonstrate that it is possible to extract enough RNA from fresh and cultivated trabeculae to perform gene expression analysis with standard qPCR.

DISCUSSION

Due to non-negligible differences between human and animal cardiac physiology, testing hypotheses or verifying results on human cardiac cells and tissues is important. However, living human myocardium is difficult to obtain and may be even more difficult to use because the amount, quality, and variability of the specimens are often insufficient for conclusive experiments, especially those requiring preservation of cells or tissues over longer periods. As novel methods for stable long-term culture of human ventricular myocardium were recently presented, the question arose whether the principle of these techniques could be applied to human atrial tissue. Our results show that trabeculae (pectinate muscles) prepared from human right-atrial appendages can be maintained in culture in a commercially available device for up to 3 weeks under constant electrical stimulation with a frequency of 1 Hz, which corresponds to the human resting heart rate. We show that, although there is an initial transient decline in function, structure and function of trabeculae cultured for nearly 2 weeks are comparable to those of non-cultured (fresh) trabeculae. Furthermore, we describe a set of methods that can be used to acquire important functional parameters.

Tissue Preparation and Viability in Culture

When comparing the presented method with that published for ventricular slices (Fischer et al., 2019), less time is needed for the preparation because the atrial tissue does not need to be cut into slices with a vibratome. Instead, trabeculae can be dissected with scissors and a scalpel. This makes the method not only faster, but also less expensive. Another advantage is that human atrial tissue can be obtained regularly during open heart surgery by removal of the RAA tip for insertion of the atrial cannula of the heart-lung machine (Boldt et al., 2004; Nummi et al., 2017). In contrast, sufficient amounts of ventricular tissue can be obtained only during implantation of ventricular assist device or after heart transplantation (Seidel et al., 2017a). We did not investigate if sliced atrial myocardium would be similarly or even better suited for tissue culture. However, in two pilot experiments where the wall of the RAA was sliced, we were not able to create

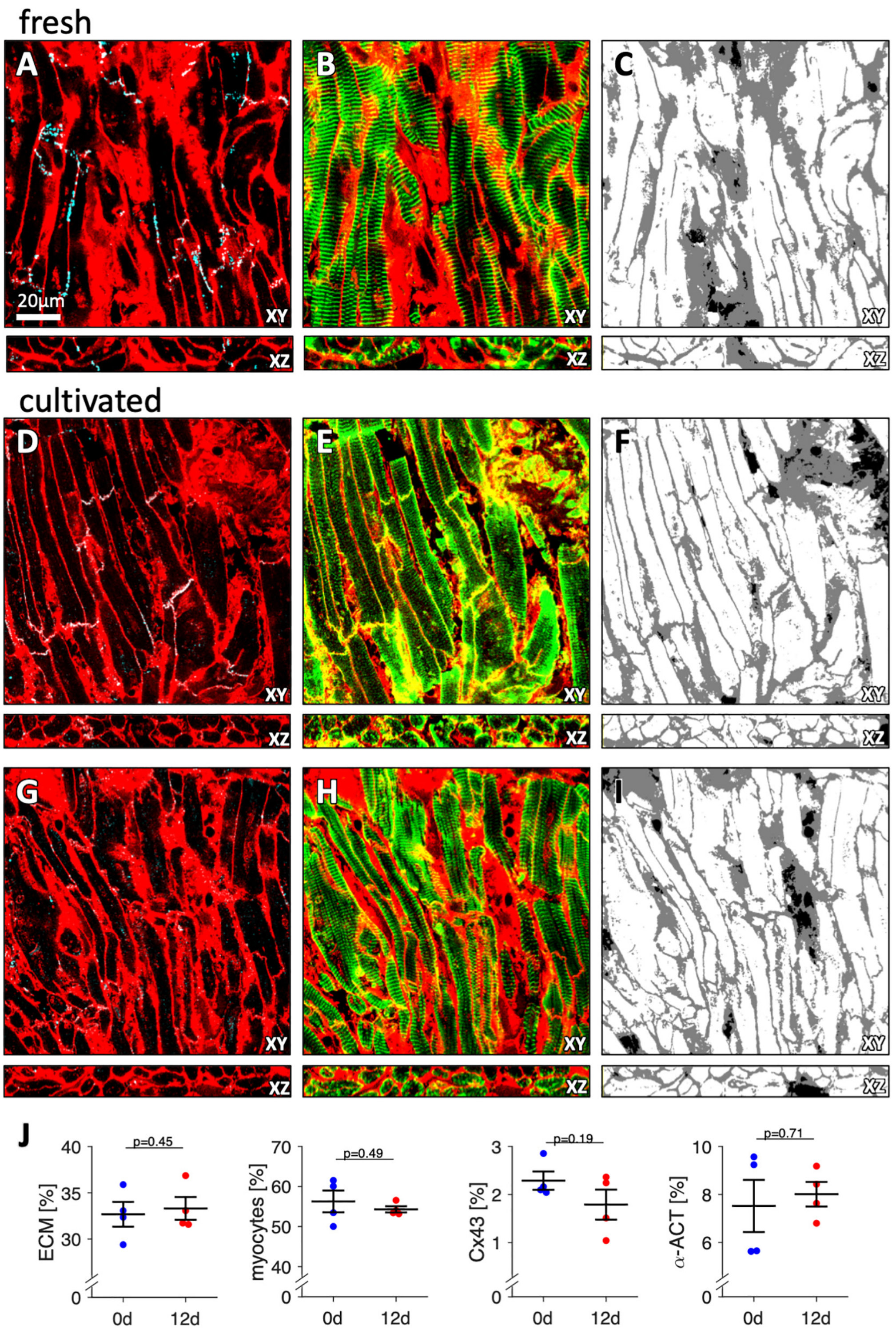

FIGURE 9 | Three-dimensional microscopic images of fresh and cultured trabeculae stained with WGA for the extracellular matrix and with antibodies against Cx43 and alpha-actinin. **(A)** XY- and XZ-view of the WGA (red) and Cx43 signal (cyan) of a fresh (non-cultivated) trabecula. Note that the overlay of the signals appears white. The scale bar applies to all images. **(B)** XY- and XZ-view of the WGA (red) and alpha-actinin signal (green) of the same region shown in panel **(A)**. Note that the overlay of the signals appears yellow. **(C)** Extracellular matrix (gray) and myocytes (white) after computational segmentation and classification of the image stack shown in panels **(A,B)**. **(D–F)** Images of a trabecula cultured for 12 d presented in analogy to panels **(A–C)**. **(G–I)** Images of the same trabecula as in panels **(D–F)** from a different region, presented in analogy to panels **(A–C)**. **(J)** Volume fractions of the extracellular matrix (ECM), myocytes, Cx43, and alpha-actinin (α-ACT). The results from three image stacks of each sample were averaged and treated as one data point. Paired, two-sided *t*-test. *N* = 4 trabeculae from 4 specimens (patients).

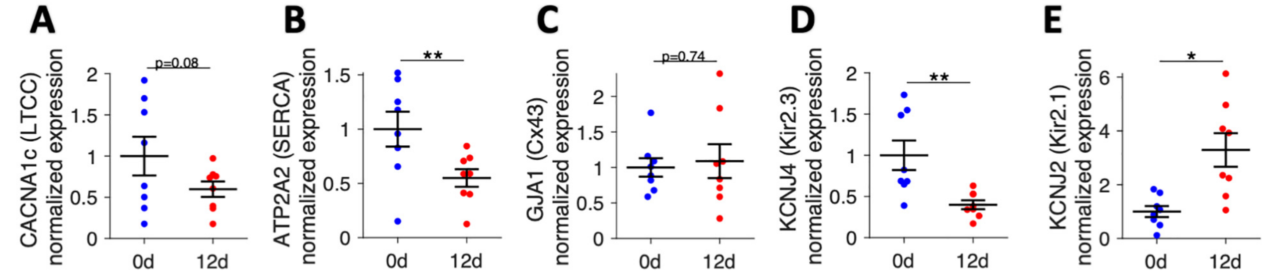

FIGURE 10 | mRNA expression of genes related to Ca^{2+} cycling and electrophysiology analyzed by quantitative RT-PCR in fresh trabeculae (0 d) and trabeculae cultivated for 12 days (12 d). **(A)** CACNA1c subunit of the L-type Ca^{2+} channel (LTCC), **(B)** ATP2A2, encoding the sarcoplasmic/endoplasmic reticulum calcium ATPase 2 (SERCA2), **(C)** GJA1, encoding connexin-43 (Cx43), **(D)** KCNJ4, encoding the Kir2.3 subunit of the inwardly rectifying potassium channel, and **(E)** KCNJ2, encoding the Kir2.1 subunit of the inwardly rectifying potassium channel. $N = 8/8$ trabeculae/samples. A paired, two-sided *t*-test was applied. $^{*}p < 0.05$, $^{**}p < 0.01$.

slices of sufficient quality because of the irregular cardiomyocyte orientation and trabeculated structure. It could be investigated in future studies if the free wall of whole atria obtained, for instance, after a heart transplantation is better suited for slicing with a vibratome. The success rate in our study was close to 75%, that is 7–8 of 10 prepared trabeculae responded to electrical stimulation after at least 12 d in culture. This is in the range of success rates reported by other studies using human myocardium (Fischer et al., 2019; Fiegle et al., 2020). A distinct difference to ventricular slice culture was that we never observed initial tonic contracture, which has been reported to be a sign of tissue damage in human ventricular myocardium. It is possible that atrial tissue behaves differently when damaged or that hypercontracture did not occur because we had significantly shorter storage times than reported for ventricular tissue samples that were shipped on ice (Fischer et al., 2019).

Contractility and Estimated Wall Stress

The changes in contractility observed over culture time (see **Figure 4**) resembled those reported for ventricular slices, with an initial decay and subsequent recovery. However, recovery occurred faster, because initial contraction amplitudes were regained after approximately 1 week, in contrast to 2–3 weeks reported for ventricular slices (Fischer et al., 2019). The decline and recovery of contractility could reflect adaptation of the tissue to culture conditions, including auxotonic contraction, a different extracellular milieu or cessation of catecholaminergic stimulation. A major difference in comparison to ventricular slices was visible when considering absolute contraction forces. Although some trabeculae produced forces higher than 1 mN (**Figure 6A**), most trabeculae reached contraction forces of 300–500 μN, which was about 10-fold smaller than in ventricular slices (Fischer et al., 2019; Abu-Khousa et al., 2020) and smaller than in other studies measuring isometric force in RAA trabeculae (Guo et al., 1983; Brixius et al., 1997). In the loaded state, most trabeculae exhibited a width of 1–2 mm and a height of 0.5–1 mm, resulting in an estimated cross-sectional area of 0.5–2 mm^2. This yields a wall stress of about 0.15–1 mN/mm^2, which is low when compared to the wall stress of up to 10mN/mm^2 reported for isometric force measurements in human RAA trabeculae (Brixius et al., 1997). However, the mentioned studies (Guo et al., 1983; Brixius et al., 1997) measured isometric forces, which are commonly greater than forces developed during isotonic or auxotonic contraction as measured here. In fact, the ratio of wall stress during auxotonic contraction estimated here to isometric wall stress reported by other studies in RAA myocardium (≈1:10) is similar to the ratio of auxotonic wall stress measured in human ventricular slices [1–3 mN/mm^2 (Fischer et al., 2019; Abu-Khousa et al., 2020)] to isometric wall stress in human ventricular muscle strips [10–20 mN/mm^2 (Mulieri et al., 1992)]. Contraction duration CD90 found immediately after installation and after 12 d of culture (367 ± 50 and 414 ± 57 ms) and relative contributions of TTP90 (118 ± 16 and 155 ± 35 ms) were close to values found in other studies on RAA trabeculae [twitch time 433 ms and TTP 110 ms (Brixius et al., 1997)] and shorter than in human ventricular muscle strips [CD 634–747 ms and TTP 157–167 ms (Mulieri et al., 1992)].

Assessment of Contraction Parameters, Refractory Period, and Maximum Captured Frequency

Our results show that the protocols and computational analyses used to assess contraction force, TTP90, TTR90, CD90, RP and f_{max} are sensitive enough to detect the changes expected after beta-adrenergic stimulation (see **Figure 8**). This finding also supports the conclusion from **Figure 6** that trabecula function was similar at 0 d and after 12 d in culture, because no differences were found using the same analysis that detected differences after beta-adrenergic stimulation. However, while the interpretation of contraction amplitude and kinetic parameters TTP90, TTR90 and CD90 is straight-forward – they respectively correspond to actively developed force, contraction velocity, relaxation velocity and total duration of a contraction – it is more complicated to interpret RP and f_{max}. The results shown in **Figure 5** indicate that RP increases when an APD-prolonging drug (dofetilide) is applied (Tsujimae et al., 2007). In turn, the results in **Figures 7**, **8** indicate that isoprenaline, which has been shown to significantly decrease APD under steady-state conditions at normal to high extracellular Ca^{2+} (Munakata et al., 1982), decreases RP. Thus, the RP as assessed here seems to correlate with APD. This may also explain the data in **Figure 7D**, where at 3 Hz every other stimulus is captured although Ca^{2+} levels are already at baseline, suggesting that electrical excitability has not recovered yet, whereas after addition of isoprenaline, each stimulus is captured (**Figure 7E**). Still, it is important to note that the RP reported here cannot be set equal to the electrical refractory period or even APD, because a mechanical, not an electrical signal was measured. One should keep in mind that the threshold for considering an electrical stimulus as captured or non-captured was chosen somewhat arbitrarily. We considered each stimulus followed by a force increase larger than the noise level as captured. Another possibility would be to define a minimum amplitude that must be reached, for example 50% of the S1 beat. Such changes in definition would shift the refractory periods to larger intervals, but likely preserve the relative changes. Thus, it is important to define a fixed criterion as done here and apply this to all tissues investigated. The definition used here fits best to the absolute refractory period. Using a larger threshold, for instance 90% of the S1 beat, might be closer to the relative refractory period. Similar considerations apply to $f_{\max}$. The number of beats that had to be successively captured was arbitrarily set to 5, and, again, we considered very small beats as captured as long as they significantly exceeded the noise level. This may explain the relatively high values found for $f_{\max}$ (see **Figures 6F**, **8F**). Modifications of the presented protocol for RP assessment could be smaller steps of the S2 beat at high S2 beat intervals. In our protocol, we used steps from 750 ms to 500 ms and then to 400 ms, which reduced the resolution of RP determination in trabeculae with high RP values (**Figure 6E**). To investigate how well the presented protocol works to detect the actual electrical refractory period and action potential frequency, one could design experiments with parallel voltage recording, for example using voltage sensitive dyes (Lang et al., 2011) or sharp electrodes (Peinkofer et al., 2017).

Calcium Imaging

The Ca^{2+} indicator used here (Calbryte 520-AM) was recommended in other protocols describing Ca^{2+} imaging in human cardiac tissue (Borysova et al., 2021). According to the manufacturer it has a reported dissociation constant (K_D) of 1200 nM. This would lead to a nearly linear relationship between the expected intracellular Ca^{2+} concentrations of 200–1000 nM (Backx et al., 1995) and the fluorescence signal. In **Figure 7** the Ca^{2+} signal increased nearly twofold after addition of 100 nM of isoprenaline and also showed a clear increase during the post-rest beat. This is as expected from experimental and modeling studies reporting a 1.5- to 2-fold increase in intracellular Ca^{2+} after beta-adrenergic stimulation (Lyon et al., 2020) and suggests that the indicator was not saturated. Hence, relative changes in Ca^{2+} transient amplitude as well as Ca^{2+} transient kinetics can be studied with the presented approach. High-affinity Ca^{2+} indicators, for example Fluo-3 or Fluo-4, have been used frequently in preparations of intact hearts (Johnson et al., 1999; Kaneko et al., 2000). However, earlier studies suggest these dyes may saturate within the physiological range of intracellular Ca^{2+} (Stout and Reynolds, 1999; Kong and Fast, 2014). After Ca^{2+} imaging, we placed two trabeculae back into the incubator and were able to retain culture for several days without obvious negative effects. This would allow for repeated Ca^{2+} imaging in the same trabecula or slice. Although not investigated systematically here, other studies also reported low toxicity and repeated measurements with Calbryte (Liao et al., 2021). For several reasons, however, it is not reasonable to compare absolute values of the Ca^{2+} signal between different trabecula. First, it is unknown how the thickness of the tissue in the imaged region influences the signal. Second, variations in loading efficiency may have large effects on signal intensity. Future studies might use ratiometric Ca^{2+} indicators or combine Ca^{2+} indicators with additional dyes for voltage imaging.

Tissue and Cardiomyocyte Microstructure

We used three-dimensional confocal microscopy to assess culture-induced changes in cardiomyocyte structure and tissue composition. Our results suggest that tissue culture preserved cardiomyocytes and did not cause fibrosis or heavy fibroblast proliferation, which can become problematic and may require pharmacological interventions in cardiomyocyte cultures (Boateng et al., 2003). It is possible that the intact tissue structure prevents fibroblast activation or that growth factors necessary for fibroblast activation are missing because serum-free culture medium was used. It would be interesting to investigate in future studies if and how fibrosis can be induced. Confocal data also indicate preserved gap junctions and sarcomeres, although some variations in staining efficiency of aACT and volume density of Cx43 were observed (**Figure 9**).

Limitations

A limitation of the method is that the used tissues were obtained from patients suffering from cardiac diseases. Thus, although only patients with sinus rhythm were included, the results presented may differ in atrial trabeculae from healthy hearts. In some countries, however, healthy donor hearts are available for research through dedicated organizations.

During the first 2 weeks of culture, the function of trabeculae was not stable, but showed a transient decline and approached initial values after 12 days. This may reflect adaptation to culture conditions, which differ in several aspects from *in vivo* conditions, for example, hormonal stimulation, oxygen pressure, force-length-relationship during contraction or electrical stimulation. We observed mRNA downregulation of Ca^{2+} handling proteins, such as SERCA. This was also reported for ventricular slices (Fischer et al., 2019), where after 4 weeks in culture, gene expression partially returned to the non-cultured level. Our study suggests that this may apply also to human atrial tissue. Therefore, depending on the experimental setup and research question, for instance short-term or long-term drug effects, it can be appropriate to wait until stabilization of functional parameters before treatment or to treat immediately after installation in culture. In any case, time-matched controls should be used to account for culture-induced effects.

Summary and Outlook

The method presented here describes an *in vitro* model of beating intact human atrial myocardium that can be readily implemented provided that RAA tissue is available. Because the atrial tissue is functionally and structurally stable for at least 3 weeks, we expect that the model can be used to study long-term drug and hormonal effects, mechanical and electrical stimuli to elucidate general atrial physiology and mechanisms of disease. It is also conceivable that the high stability will enable toxicity screening, drug discovery, co-culture with stem-cell derived cardiomyocytes, and gene delivery or silencing. These applications might be particularly useful to investigate the most common disease of the human atrium, which is atrial fibrillation.

DATA AVAILABILITY STATEMENT

The raw data supporting the conclusions of this article will be made available by the authors, without undue reservation.

ETHICS STATEMENT

The studies involving human participants were reviewed and approved by Ethics Committee of the University of Erlangen-Nürnberg. The patients/participants provided their written informed consent to participate in this study.

AUTHOR CONTRIBUTIONS

MK, DF, and TS performed experiments, analyzed the data, and drafted the manuscript. CH and MK performed patient education, and acquired patient samples and patient data. TS, TV, CH, and MW designed the study. All authors critically revised the manuscript.

FUNDING

This work was supported by intramural funds.

ACKNOWLEDGMENTS

For excellent technical support, we would like to thank Celine Grüninger, Lorenz McCargo, Philipp P. Müller, and the OR staff.

SUPPLEMENTARY MATERIAL

The Supplementary Material for this article can be found online at: https://www.frontiersin.org/articles/10.3389/fphys.2022.839139/full#supplementary-material

REFERENCES

Abu-Khousa, M., Fiegle, D. J., Sommer, S. T., Minabari, G., Milting, H., Heim, C., et al. (2020). The degree of t-system remodeling predicts negative force-frequency relationship and prolonged relaxation time in failing human myocardium. *Front. Physiol.* 11:182. doi: 10.3389/fphys.2020.00182

Backx, P. H., Gao, W. D., Azan-Backx, M. D., and Marban, E. (1995). The relationship between contractile force and intracellular [Ca2+] in intact rat cardiac trabeculae. *J. Gen. Physiol.* 105, 1–19. doi: 10.1085/jgp.105.1.1

Banyasz, T., Lozinskiy, I., Payne, C. E., Edelmann, S., Norton, B., Chen, B., et al. (2008). Transformation of adult rat cardiac myocytes in primary culture. *Exp. Physiol.* 93, 370–382. doi: 10.1113/expphysiol.2007.040659

Berridge, M. V., Herst, P. M., and Tan, A. S. (2005). Tetrazolium dyes as tools in cell biology: new insights into their cellular reduction. *Biotechnol. Annu. Rev.* 11, 127–152. doi: 10.1016/S1387-2656(05)11004-7

Bluhm, W. F., Kranias, E. G., Dillmann, W. H., and Meyer, M. (2000). Phospholamban: a major determinant of the cardiac force-frequency relationship. *Am. J. Physiol. Heart Circ. Physiol.* 278, H249–H255. doi: 10.1152/ajpheart.2000.278.1.H249

Boateng, S. Y., Hartman, T. J., Ahluwalia, N., Vidula, H., Desai, T. A., and Russell, B. (2003). Inhibition of fibroblast proliferation in cardiac myocyte cultures by surface microtopography. *Am. J. Physiol. Cell Physiol.* 285, C171–C182. doi: 10.1152/ajpcell.00013.2003

Bojkova, D., Wagner, J. U. G., Shumliakivska, M., Aslan, G. S., Saleem, U., Hansen, A., et al. (2020). SARS-CoV-2 infects and induces cytotoxic effects in human cardiomyocytes. *Cardiovasc. Res.* 116, 2207–2215. doi: 10.1093/cvr/cvaa267

Boldt, A., Wetzel, U., Lauschke, J., Weigl, J., Gummert, J., Hindricks, G., et al. (2004). Fibrosis in left atrial tissue of patients with atrial fibrillation with and without underlying mitral valve disease. *Heart* 90, 400–405. doi: 10.1136/hrt.2003.015347

Borysova, L., Ng, Y. Y. H., Wragg, E. S., Wallis, L. E., Fay, E., Ascione, R., et al. (2021). High spatial and temporal resolution Ca(2+) imaging of myocardial strips from human, pig and rat. *Nat. Protoc.* 16, 4650–4675. doi: 10.1038/s41596-021-00590-6

Brandenburger, M., Wenzel, J., Bogdan, R., Richardt, D., Nguemo, F., Reppel, M., et al. (2012). Organotypic slice culture from human adult ventricular myocardium. *Cardiovasc. Res.* 93, 50–59. doi: 10.1093/cvr/cvr259

Brixius, K., Pietsch, M., Hoischen, S., Muller-Ehmsen, J., and Schwinger, R. H. (1997). Effect of inotropic interventions on contraction and Ca2+ transients in the human heart. *J. Appl. Physiol.* 83, 652–660. doi: 10.1152/jappl.1997.83.2.652

Bursac, N., Papadaki, M., White, J. A., Eisenberg, S. R., Vunjak-Novakovic, G., and Freed, L. E. (2003). Cultivation in rotating bioreactors promotes maintenance of cardiac myocyte electrophysiology and molecular properties. *Tissue Eng.* 9, 1243–1253. doi: 10.1089/10763270360728152

Bussek, A., Wettwer, E., Christ, T., Lohmann, H., Camelliti, P., and Ravens, U. (2009). Tissue slices from adult mammalian hearts as a model for pharmacological drug testing. *Cell. Physiol. Biochem.* 24, 527–536. doi: 10.1159/000257528

de Boer, T. P., Camelliti, P., Ravens, U., and Kohl, P. (2009). Myocardial tissue slices: organotypic pseudo-2D models for cardiac research & development. *Future Cardiol.* 5, 425–430. doi: 10.2217/fca.09.32

Denham, N. C., Pearman, C. M., Caldwell, J. L., Madders, G. W. P., Eisner, D. A., Trafford, A. W., et al. (2018). Calcium in the pathophysiology of atrial fibrillation and heart failure. *Front. Physiol.* 9:1380. doi: 10.3389/fphys.2018.01380

Deshmukh, A., Barnard, J., Sun, H., Newton, D., Castel, L., Pettersson, G., et al. (2015). Left atrial transcriptional changes associated with atrial fibrillation susceptibility and persistence. *Circ. Arrhythm. Electrophysiol.* 8, 32–41. doi: 10.1161/CIRCEP.114.001632

Emde, B., Heinen, A., Godecke, A., and Bottermann, K. (2014). Wheat germ agglutinin staining as a suitable method for detection and quantification of fibrosis in cardiac tissue after myocardial infarction. *Eur. J. Histochem.* 58:2448. doi: 10.4081/ejh.2014.2448

Fiegle, D. J., Volk, T., and Seidel, T. (2020). Isolation of human ventricular cardiomyocytes from vibratome-cut myocardial slices. *J. Vis. Exp.* 159:e61167. doi: 10.3791/61167

Fischer, C., Milting, H., Fein, E., Reiser, E., Lu, K., Seidel, T., et al. (2019). Long-term functional and structural preservation of precision-cut human myocardium under continuous electromechanical stimulation *in vitro*. *Nat. Commun.* 10:117. doi: 10.1038/s41467-018-08003-1

Guo, Z. G., Levi, R., Aaronson, L. M., and Gay, W. A. (1983). The isolated human pectinate muscle: a reliable preparation of human cardiac tissue. *J. Pharmacol. Methods* 9, 127–135. doi: 10.1016/0160-5402(83)90004-9

Gwilt, M., Arrowsmith, J. E., Blackburn, K. J., Burges, R. A., Cross, P. E., Dalrymple, H. W., et al. (1991). UK-68,798: a novel, potent and highly selective class III antiarrhythmic agent which blocks potassium channels in cardiac cells. *J. Pharmacol. Exp. Ther.* 256, 318–324.

Han, J., Kim, N., Joo, H., and Kim, E. (2002). Ketamine abolishes ischemic preconditioning through inhibition of K(ATP) channels in rabbit hearts. *Am. J. Physiol. Heart Circ. Physiol.* 283, H13–H21. doi: 10.1152/ajpheart.01064.2001

Hove-Madsen, L., Llach, A., Bayes-Genis, A., Roura, S., Rodriguez Font, E., Aris, A., et al. (2004). Atrial fibrillation is associated with increased spontaneous calcium release from the sarcoplasmic reticulum in human atrial myocytes. *Circulation* 110, 1358–1363. doi: 10.1161/01.CIR.0000141296.59876.87

Johnson, P. L., Smith, W., Baynham, T. C., and Knisley, S. B. (1999). Errors caused by combination of Di-4 ANEPPS and Fluo3/4 for simultaneous measurements of transmembrane potentials and intracellular calcium. *Ann. Biomed. Eng.* 27, 563–571. doi: 10.1114/1.198

Kaneko, T., Tanaka, H., Oyamada, M., Kawata, S., and Takamatsu, T. (2000). Three distinct types of Ca(2+) waves in langendorff-perfused rat heart revealed by real-time confocal microscopy. *Circ. Res.* 86, 1093–1099. doi: 10.1161/01.res.86.10.1093

Kong, W., and Fast, V. G. (2014). The role of dye affinity in optical measurements of Cai(2+) transients in cardiac muscle. *Am. J. Physiol. Heart Circ. Physiol.* 307, H73–H79. doi: 10.1152/ajpheart.00751.2013

Lang, D., Sulkin, M., Lou, Q., and Efimov, I. R. (2011). Optical mapping of action potentials and calcium transients in the mouse heart. *J. Vis. Exp.* 55:3275. doi: 10.3791/3275

Liao, J., Patel, D., Zhao, Q., Peng, R., Guo, H., and Diwu, Z. (2021). A novel Ca(2+) indicator for long-term tracking of intracellular calcium flux. *Biotechniques* 70, 271–277. doi: 10.2144/btn-2020-0161

Lu, K., Seidel, T., Cao-Ehlker, X., Dorn, T., Batcha, A. M. N., Schneider, C. M., et al. (2021). Progressive stretch enhances growth and maturation of 3D stem-cell-derived myocardium. *Theranostics* 11, 6138–6153. doi: 10.7150/thno.54999

Lyon, A., Dupuis, L. J., Arts, T., Crijns, H., Prinzen, F. W., Delhaas, T., et al. (2020). Differentiating the effects of beta-adrenergic stimulation and stretch on calcium and force dynamics using a novel electromechanical cardiomyocyte model. *Am. J. Physiol. Heart Circ. Physiol.* 319, H519–H530. doi: 10.1152/ajpheart.00275.2020

Miller, J. M., Meki, M. H., Ou, Q., George, S. A., Gams, A., Abouleisa, R. R. E., et al. (2020). Heart slice culture system reliably demonstrates clinical drug-related cardiotoxicity. *Toxicol. Appl. Pharmacol.* 406:115213. doi: 10.1016/j.taap.2020.115213

Mulieri, L. A., Hasenfuss, G., Ittleman, F., Blanchard, E. M., and Alpert, N. R. (1989). Protection of human left ventricular myocardium from cutting injury with 2,3-butanedione monoxime. *Circ. Res.* 65, 1441–1449. doi: 10.1161/01.res.65.5.1441

Mulieri, L. A., Hasenfuss, G., Leavitt, B., Allen, P. D., and Alpert, N. R. (1992). Altered myocardial force-frequency relation in human heart failure. *Circulation* 85, 1743–1750. doi: 10.1161/01.cir.85.5.1743

Munakata, K., Dominic, J. A., and Surawicz, B. (1982). Variable effects of isoproterenol on action potential duration in guinea-pig papillary muscle: differences between nonsteady and steady state; role of extracellular calcium concentration. *J. Pharmacol. Exp. Ther.* 221, 806–814.

Nummi, A., Nieminen, T., Patila, T., Lampinen, M., Lehtinen, M. L., Kivisto, S., et al. (2017). Epicardial delivery of autologous atrial appendage micrografts during coronary artery bypass surgery-safety and feasibility study. *Pilot Feasibility Stud.* 3:74. doi: 10.1186/s40814-017-0217-9

Ou, Q., Jacobson, Z., Abouleisa, R. R. E., Tang, X. L., Hindi, S. M., Kumar, A., et al. (2019). Physiological biomimetic culture system for pig and human heart slices. *Circ. Res.* 125, 628–642. doi: 10.1161/CIRCRESAHA.119.314996

Palka, P., Lange, A., Fleming, A. D., Fenn, L. N., Bouki, K. P., Shaw, T. R., et al. (1996). Age-related transmural peak mean velocities and peak velocity gradients by Doppler myocardial imaging in normal subjects. *Eur. Heart J.* 17, 940–950. doi: 10.1093/oxfordjournals.eurheartj.a014977

Peinkofer, G., Hescheler, J., and Halbach, M. (2017). Murine short axis ventricular heart slices for electrophysiological studies. *J. Vis. Exp.* 124:55725. doi: 10.3791/55725

Perbellini, F., and Thum, T. (2020). Living myocardial slices: a novel multicellular model for cardiac translational research. *Eur. Heart J.* 41, 2405–2408. doi: 10.1093/eurheartj/ehz779

Pfaffl, M. W. (2001). A new mathematical model for relative quantification in real-time RT-PCR. *Nucleic Acids Res.* 29:e45. doi: 10.1093/nar/29.9.e45

Pillekamp, F., Reppel, M., Dinkelacker, V., Duan, Y., Jazmati, N., Bloch, W., et al. (2005). Establishment and characterization of a mouse embryonic heart slice preparation. *Cell. Physiol. Biochem.* 16, 127–132. doi: 10.1159/000087739

Qiao, Y., Dong, Q., Li, B., Obaid, S., Miccile, C., Yin, R. T., et al. (2019). Multiparametric slice culture platform for the investigation of human cardiac tissue physiology. *Prog. Biophys. Mol. Biol.* 144, 139–150. doi: 10.1016/j.pbiomolbio.2018.06.001

Sedgwick, M. L., Rasmussen, H. S., and Cobbe, S. M. (1992). Clinical and electrophysiologic effects of intravenous dofetilide (UK-68,798), a new class III antiarrhythmic drug, in patients with angina pectoris. *Am. J. Cardiol.* 69, 513–517. doi: 10.1016/0002-9149(92)90996-c

Seidel, T., Dräbing, T., Seemann, G., and Sachse, F. B. (2013). "A semi-automatic approach for segmentation of three-dimensional microscopic image stacks of cardiac tissue," in *Proceedings of the 7th International Conference Lecture Notes in Computer Science*, Vol. 7945, ed. S. Ourselin (London: Springer), 300–307.

Seidel, T., Edelmann, J. C., and Sachse, F. B. (2016). Analyzing remodeling of cardiac tissue: a comprehensive approach based on confocal microscopy and 3D reconstructions. *Ann. Biomed. Eng.* 44, 1436–1448. doi: 10.1007/s10439-015-1465-6

Seidel, T., Navankasattusas, S., Ahmad, A., Diakos, N. A., Xu, W. D., Tristani-Firouzi, M., et al. (2017a). Sheet-Like remodeling of the transverse tubular system in human heart failure impairs excitation-contraction coupling and functional recovery by mechanical unloading. *Circulation* 135, 1632–1645. doi: 10.1161/CIRCULATIONAHA.116.024470

Seidel, T., Sankarankutty, A. C., and Sachse, F. B. (2017b). Remodeling of the transverse tubular system after myocardial infarction in rabbit correlates with local fibrosis: a potential role of biomechanics. *Prog. Biophys. Mol. Biol.* 130, 302–314. doi: 10.1016/j.pbiomolbio.2017.07.006

Stout, A. K., and Reynolds, I. J. (1999). High-affinity calcium indicators underestimate increases in intracellular calcium concentrations associated with excitotoxic glutamate stimulations. *Neuroscience* 89, 91–100. doi: 10.1016/s0306-4522(98)00441-2

Stringham, J. C., Paulsen, K. L., Southard, J. H., Mentzer, R. M. Jr., and Belzer, F. O. (1994). Prolonging myocardial preservation with a modified University of Wisconsin solution containing 2,3-butanedione monoxime and calcium. *J. Thorac. Cardiovasc. Surg.* 107, 764–775.

Tsujimae, K., Suzuki, S., Murakami, S., and Kurachi, Y. (2007). Frequency-dependent effects of various IKr blockers on cardiac action potential duration in a human atrial model. *Am. J. Physiol. Heart Circ. Physiol.* 293, H660–H669. doi: 10.1152/ajpheart.01083.2006

van der Heijden, E. P., Kroese, A. B., Werker, P. M., de With, M. C., de Smet, M., Kon, M., et al. (2000). Improving the preservation of isolated rat skeletal muscles stored for 16 hours at 4 degrees C. *Transplantation* 69, 1310–1322. doi: 10.1097/00007890-200004150-00017 van Gorp, P. R. R., Trines, S. A., Pijnappels, D. A., and de Vries, A. A. F. (2020). Multicellular *in vitro* models of cardiac arrhythmias: focus on atrial fibrillation. *Front. Cardiovasc. Med.* 7:43. doi: 10.3389/fcvm.2020.00043

Voigtlander, J., Leiderer, R., Muhlbayer, D., and Habazettl, H. (1999). Time-dependent efficacy of initial reperfusion with 2,3 butanedione monoxime (BDM) on release of cytosolic enzymes and ultrastructural damage in isolated hearts. *Thorac. Cardiovasc. Surg.* 47, 244–250. doi: 10.1055/s-2007-1013152

Watson, S. A., Duff, J., Bardi, I., Zabielska, M., Atanur, S. S., Jabbour, R. J., et al. (2019). Biomimetic electromechanical stimulation to maintain adult myocardial slices *in vitro*. *Nat. Commun.* 10:2168. doi: 10.1038/s41467-019-10175-3

Watson, S. A., Scigliano, M., Bardi, I., Ascione, R., Terracciano, C. M., and Perbellini, F. (2017). Preparation of viable adult ventricular myocardial slices from large and small mammals. *Nat. Protoc.* 12, 2623–2639. doi: 10.1038/nprot.2017.139

Zhao, Y., Rafatian, N., Feric, N. T., Cox, B. J., Aschar-Sobbi, R., Wang, E. Y., et al. (2019). A platform for generation of chamber-specific cardiac tissues and disease modeling. *Cell* 176, 913–927.e18. doi: 10.1016/j.cell.2018.11.042

Conflict of Interest: TS is shareholder of InVitroSys GmbH.

The remaining authors declare that the research was conducted in the absence of any commercial or financial relationships that could be construed as a potential conflict of interest.

frontiers in Physiology

METHODS
published: 03 March 2022
doi: 10.3389/fphys.2022.817205

Preparing Excitable Cardiac Papillary Muscle and Cardiac Slices for Functional Analyses

***Bradley M. Palmer*[1]* and Stephen P. Bell[2]**

[1]Department of Molecular Physiology and Biophysics, University of Vermont, Burlington, VT, United States, [2]Department of Medicine, University of Vermont, Burlington, VT, United States

While the reductionist approach has been fruitful in understanding the molecular basis of muscle function, intact excitable muscle preparations are still important as experimental model systems. We present here methods that are useful for preparing cardiac papillary muscle and cardiac slices, which represent macroscopic experimental model systems with fully intact intercellular and intracellular structures. The maintenance of these *in vivo* structures for experimentation *in vitro* have made these model systems especially useful for testing the functional effects of protein mutations and pharmaceutical candidates. We provide solutions recipes for dissection and recording, instructions for removing and preparing the cardiac papillary muscles, as well as instruction for preparing cardiac slices. These instructions are suitable for beginning experimentalists but may be useful for veteran muscle physiologists hoping to reacquaint themselves with macroscopic functional analyses.

Keywords: cardiac, excitable, force, slice, papillary, muscle

Edited by:
Peter T. Wright,
University of Roehampton London,
United Kingdom

Reviewed by:
Benedict Reilly-O'Donnell,
Imperial College London,
United Kingdom
Gregory Milburn,
University of Kentucky College of
Medicine, United States

****Correspondence:***
Bradley M. Palmer
bmpalmer@uvm.edu

Specialty section:
This article was submitted to
Striated Muscle Physiology,
a section of the journal
Frontiers in Physiology

Received: *17 November 2021*
Accepted: *09 February 2022*
Published: *03 March 2022*

Citation:
Palmer BM and Bell SP (2022)
Preparing Excitable Cardiac Papillary
Muscle and Cardiac Slices for
Functional Analyses.
Front. Physiol. 13:817205.
doi: 10.3389/fphys.2022.817205

INTRODUCTION

The middle of the last century witnessed a dramatic turn in the muscle physiology field toward the molecular. A recent historical review suggests that the early 1970s marks a time when protein biochemistry of muscle contraction overtook the previously conventional approaches to understanding muscle function (Szent-Györgyi, 2004). The field at the molecular level has advanced tremendously since then, especially with the advent of molecular genetics techniques. With these new tools, select mutations in muscle proteins could be produced, and the functional consequences at the molecular level assessed. In this way, the molecular basis of muscle function could be examined one protein at a time and with the precision of one amino acid at a time.

Yet inferring macroscopic muscle performance from molecular-level results is not always straightforward. For example, a single point mutation in cardiac myosin known to underlie the development of a cardiomyopathy can cause little to no observed effect in molecular function, and the result would often go unpublished. Perhaps more confusing are those cases when a mutation in a seemingly ancillary muscle protein, for example, muscle LIM protein in the sarcomeric Z-disk, can cause a significant cardiomyopathy (Morita et al., 2005). These examples serve to support the importance of examining intact muscle function even in the age of molecular manipulations. Hence the value of transgenic mouse models, which allowed the examination of protein mutations in the context of an intact working muscle (Fatkin et al., 1999).

The examination of the cardiac slice has recently gained deserved attention due to the ease with which a slice can be generated and maintained (Pitoulis et al., 2020). Cardiac slices can remain viable for weeks and even months (Watson et al., 2017; Fischer et al., 2019). With this muscle model system, viral transfections of proteins are possible thus minimizing the developmental of compensatory secondary effects that mutations may cause in the transgenic animals (Moretti et al., 2020). For this and many other reasons, the cardiac slice is likely to become an important model system for examining macroscopic muscle function due to molecular-level manipulations including response of pharmaceuticals.

This methods paper describes how to prepare a cardiac papillary muscle and cardiac slice for examination with a conventional force transducer and length controller. We provide details related to the instruments required that would allow a beginning muscle experimentalist or a starting laboratory to prepare these experimental model systems. We do not provide details related the apparatus used to examine muscle function nor details related to specific protocols to examine muscle function. The procedures provided here are illustrated using rat heart but are also applicable to other species, such as mouse, guinea pig, ferret, and rabbit, and other muscle types, such as cardiac trabeculae, cardiac strips prepared from endo- or epicardium, and skeletal muscles with intact tendons.

MATERIALS AND METHODS

Papillary Muscle Preparation

We will not describe how to anesthetize the rat and remove the heart. Please seek out instruction from your institutional veterinarian. All procedures and use of animals described here adhere to the Guidelines of the American Physiological Society and have been reviewed and approved by the Institutional Animal Care and Use Committee of the University of Vermont. A video demonstration of dissecting the left ventricle and removing the papillary muscles can be found at this link.[1]

Have ready a small beaker (~50 ml) filled about halfway with Dissection Solution chilled to 0–4°C. Also have ready a small shallow glass container with a silicon bottom also filled about halfway with Dissection Solution and sitting on the cooling plate. Make sure the solutions are being bubbled with 100% O_2.

After the heart has been removed, place the heart into the small beaker. Using forceps, hold the atria and vessels above the base of the heart and shake the ventricles in the beaker to wash away as much blood as possible. Then place the heart into the shallow dish on the cooling plate. Removing and transferring the heart from the animal to the small beaker and then to the shallow dish on the cooling plate should be done quickly but without rushing and take under 1 min.

Exposing the Endocardium

The following sections are facilitated by use of the dissection microscope. Nevertheless, many experimentalists can expose the endocardium without use of the microscope. It is important that the tasks are performed accurately but also as quickly as possible without rushing. Using a pair of forceps and a pair of scissors, trim away the atria, valves and blood vessels that lie above the base of the ventricles. Once the atria have been trimmed away, the openings to the right and left ventricles can be seen at the base of the heart. If there is any blood obscuring your view, use transfer pipettes to remove blood and refill the volume with fresh dissection solution. The right ventricle can be identified by its thin wall, and it is opening at the base is crescent-shaped (**Figure 1A**). The opening of the left ventricle is circular and surrounded by thick muscular walls (**Figure 1A**). Removing the atria and exposing the base of the heart should be done in under 1 min after the heart is placed in the shallow dish.

Using forceps, hold the free wall of the right ventricle and trim it away to expose the septum. Now hold the remaining left ventricle with the septum pointing up. Place a scissors blade (~10–20 mm long) into the left ventricular cavity and cut down the center of the septum from the base to the apex. Cutting down the center of the septum will assure that the papillary muscles are not damaged by the scissors. Removing the right ventricular free wall and cutting down the septum should be done in under 2 min.

Removing the Papillary Muscles

Taking a few dissection pins, pin down both sides of the now cut septum to expose the endocardium. It is sometimes useful to pin down the apex, too, although in this photo the apex has been cut open prior to pinning. In **Figure 1B**, the heart is oriented with the apex to the right and base to the left. The anterior and posterior papillary muscles are now visible. In this orientation, the anterior papillary muscle is at the top of the image, and the posterior papillary muscle, which is typically thicker than the anterior papillary muscle, is at the bottom.

Now cut out the papillary muscles using a finer pair of scissors with a ~2–4 mm blade. It is very important not to hold the muscles with the forceps. Pinching or pulling the muscle will damage it and render it useless for later physiological analysis. Cut along the length of the papillary muscle to release it from the rest of the endocardium (**Figure 1C**). Once the papillary muscles have been removed, place them into another glass or clear plastic container holding the omega clips, looped suture, and bubbled dissection solution. Removing the papillary muscles should require 2-4 min.

Clipping a Papillary Muscle

Trim away any excess endocardium from the papillary muscle being careful to grab only the tissue to be cut away and not to grab the papillary muscle with the forceps. Trimming does not need to be perfect, but good enough to assure a reasonably cylindrical muscle. Place the muscle in the dish with its long

---

[1] https://www.youtube.com/watch?v=VBaOjrf0NlU

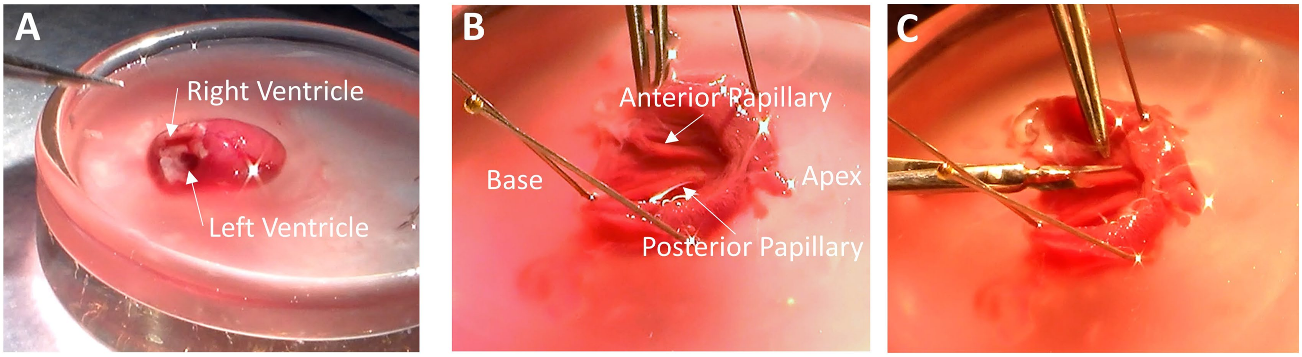

FIGURE 1 | Removing Papillary Muscles. **(A)** With the atria trimmed away, the base of the heart is exposed, and the ventricles can be easily identified. The right ventricular cavity is crescent-shaped, and its free wall is thin. The left ventricular cavity is more circular in shape, and the walls are thick. **(B)** After removing the right ventricle and cutting down the septum, the endocardium is exposed with the anterior and posterior papillary muscles visible. **(C)** Remove the papillary muscles by cutting gently along the length of the muscle while being sure not to pull on muscle with the forceps.

axis running back and forth away from your position. Bring an omega clip and a suture loop into the field. The resting distance between the feet should be narrower than the diameter of the muscle. Using two forceps, gently pull apart the feet of the omega clips and then placed the feet over the end of the muscle. Upon letting go of the feet, the spring action of the omega clip will recoil and maintain its position on the muscle during suturing. Grab one foot of the omega clip and lift it off the bottom and slip the loop over the head of the omega clip. Pull on the ends of the suture so the knot is tightened near the feet of the omega clip (**Figure 2A**). It is important that the suture be tight, but not over-tightened, which can cut into the muscle. The excess suture is then cut away. Repeat the process for the other end of the muscle. A video demonstration of clipping and mounting the papillary muscles can be found at this link.[2]

Note that, by the time the muscle is clipped, only the muscle between the clips will be characterized for function. The muscle at the point of the clipping, that is, between the feet, is considered connective. Whatever damage may occur to muscle function between the feet should not affect the recorded muscle function unless the damage includes cutting of the muscle.

Mounting a Papillary Muscle

Carry the small dish with the clipped muscle to the chamber. Adjust the distance between the platinum hooks using the manual micromanipulator so the hooks are slightly closer together than the distance between the two heads of the omega clips. Make sure the chamber is already filled with Recording Solution. Using forceps, pick up the muscle by a suture and carry it to the chamber. Place one omega clip over one hook and then place the other omega clip over the other hook (**Figure 2B**). The reader may wish to skip ahead to section "Preparing to Record Functional Data" to continue with recording force from a papillary muscle.

Cardiac Slice Preparation

The preparation of a cardiac slice begins with exposing the endocardium. The methods outlined above for exposing the endocardium should be followed. It is also possible to remove the papillary muscles and use the remaining left ventricle for the preparation of the cardiac slice. A video demonstration of preparing, clipping, and mounting a cardiac slice can be found at this link.[3]

Making a Cardiac Slice

An excellent description of cardiac slice preparation can be found in Watson et al. (2017), which provides a detailed account of reagents, procedures, and expectations. A vibratome is used to slice thin layers of the cardiac tissue. The vibratome will vibrate its blade back and forth while traveling forward and slicing the tissue. It is important that the vibratome allow for adjustments to vibration amplitude and speed of travel, whose values will be addressed below. Standard safety razors are adequately sharp for cutting the tissue.

There must be a platform or stage for the heart to be glued down. In **Figure 3A**, the stage is a glass slide about 45 mm long and 25 mm wide. This size stage is large enough for hearts from small mammals (up to size of a rabbit), but a larger stage and blade would be necessary if slicing hearts or larger heart sections from pigs or humans. A thin layer of a cyanoacrylate adhesive (Histoacryl, Braun) is applied to the glass. The left ventricle, which has already been cut down its septum, is then dabbed onto paper or gauze to remove excess solution from the epicardium. The tissue must still be wet, but not dripping with solution. The left ventricle is then laid onto the glue and pressed down with forceps for about 20–40 s (**Figure 3B**), after which the epicardium is glued to the glass and the endocardium exposed. Note that, while the left ventricle has been kept cold, the glass slide is not chilled at this point. We have found the glue is less adherent if the glass is chilled prior to forming a seal between tissue and glass.

Once glued down, put cold and oxygenated Dissection Solution onto the tissue with a transfer pipette. As solution starts to fill the chamber, excess glue will tend to float. Use a transfer pipette to remove the excess glue from the solution

---

[2] https://www.youtube.com/watch?v=-ktp0mMNj1g

[3] https://www.youtube.com/watch?v=3WcKLTUFPfw

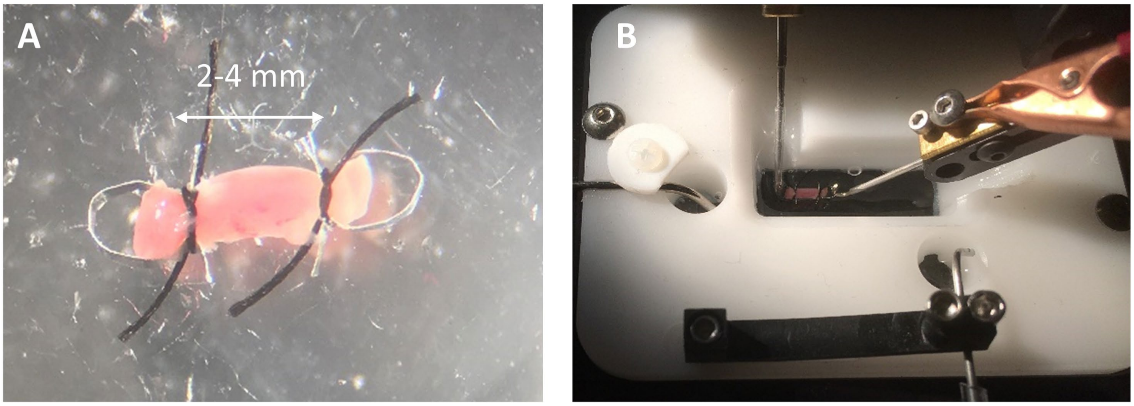

FIGURE 2 | Clipping and Mounting Papillary Muscle. **(A)** A clipped rat cardiac papillary muscle is about 2–4 mm long. **(B)** The omega clips are placed over the hooks of the measurement apparatus and perfused with solution.

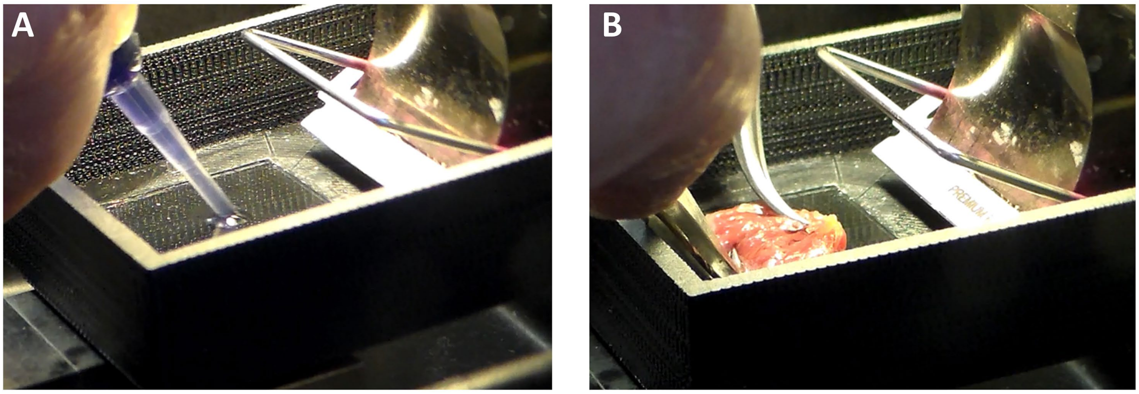

FIGURE 3 | Cardiac Slice Preparation. **(A)** A cyanoacrylate glue (Histoacryl, Braun) is applied to the stage on which the heart will adhere. **(B)** The epicardium is pressed against the glue to leave the endocardium exposed for slicing with the vibratome.

and continue to fill the chamber with fresh solution. Once the chamber is about half filled, ice or iced water can be placed around the stage. Be careful that ice does not get into the Dissection Solution bathing the tissue. To maintain viability, bubble with 100% O_2.

The height of the blade should now be adjusted to assure that the blade will cut 0.5–1 mm below the surface of the endocardium. Turn on the vibratome, and the blade will slowly move across the tissue while vibrating. The settings for each vibratome and each laboratory will vary. Reasonable settings should include a relatively high amplitude of vibration and slow speed of travel. We typically use a vibration amplitude of ~1 mm peak to peak with vibration frequency ~200 Hz and travel speed ~5 mm per min or slower. With such slow travel, cutting one slice will take several minutes.

The first slice is usually not useable, as it will retain the uneven surface of the endocardium. The blade is then retracted. If the slice is still tethered to the left ventricle, remove the tethers with small scissors and remove the slice with forceps being careful not to pull on the tissue. The relative blade height is then adjusted by raising the tissue stage a distance that will define the thickness of the next slice. Typically, the thickness of each slice is between 0.2 and 0.4 mm. The next slice or two may also be unusable due to uneven surfaces. When the cut exposes a flat surface, the subsequent slices are useable. Place the slices into cold, oxygenated Dissection Solution. The creation of 3–5 slices can take approximately 30 min depending on the size of the heart and the cutting speed chosen. The yield from a single rat heart is typically on the order of 3–10 intact useable cardiac slices depending on the size of the heart and the thickness of the slices.

Short Term Viability of a Cardiac Slice

We examined the viability of myocytes within cardiac slices with Thermo Fisher Scientific LIVE/DEAD Cell Imaging Kit 488/570, which uses 488 nm and 570 nm excitation wavelengths to excite calcein with emission at 510 nm and bobo-3 with emission at 605 nm. The calcein channel, displayed in green, indicates live intact myocytes, and the bobo-3 channel, displayed in red, indicates DNA and DNA fragments. **Figure 4A** demonstrates a high fraction

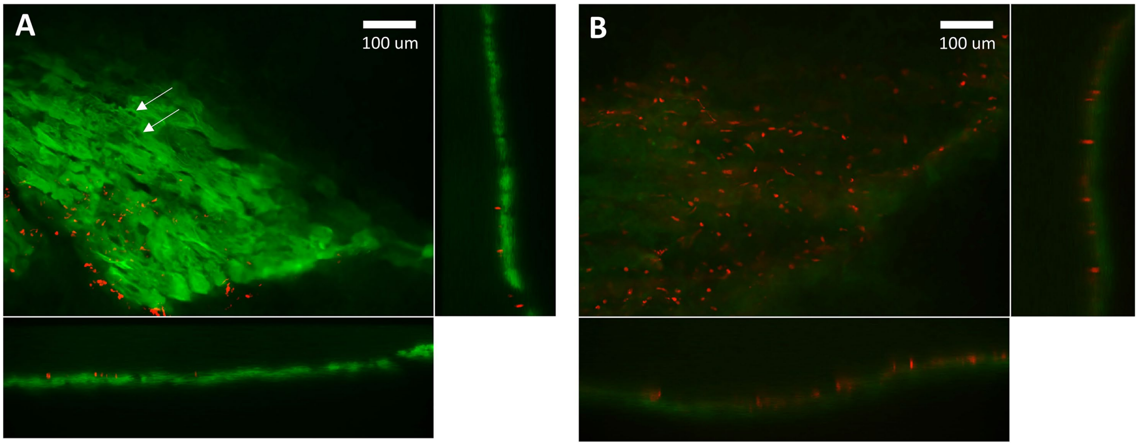

FIGURE 4 | Confocal microscopy imaging of cell viability after slicing. **(A)** Green indicates cytosol of intact myocytes within a cardiac slice. Red indicates detection of DNA, which is only possible if the membrane has been disrupted. The localized absence of green within a myocyte indicates intact nuclei (arrows). DNA fragments and disrupted membranes appear limited to the edge of the slice where a razor blade was used to cut the tissue. We estimate 40% intact myocytes on the edges and effectively 100% intact for myocytes further than 30 mm from an edge. **(B)** Red indicates DNA detected in "dead" myocytes whose membranes have been disrupted by detergent. The absence of green further attests to a lack of intact membranes. Settings used for acquisition and display of these two images were the same.

of intact myocytes, whose cytosol volumes are shown in green, for myocytes away from the slice edge. A smattering of DNA or DNA fragments, shown in red, are apparent near the edges. **Figure 4B** demonstrates the expected image for myocytes that have been disrupted, in this case by the detergent Triton X-100 at 0.1% concentration by volume exposed for 30 min at room temperature. We estimate the fraction of intact viable myocytes along an edge to be 40% upon examining tissue with 20 µm depth from the edge, and the fraction of intact myocytes away from the edge is effectively 100%. For a typical slice 300 µm thick and 8 mm wide, total cross-sectional area is 2.4 mm^2 with 0.33 mm^2 attributed to edges and 2.07 mm^2 away from edges. The net viability of myocytes within a typical slice was therefore estimated at 92%, which is consistent with the estimate reported by Watson et al. (2017). The effective cross-sectional area, which is necessary for normalizing force to calculate tension, is therefore 2.2 mm^2 for this example.

We have found that cardiac slices can be maintained on a cooling plate at 0–4°C and bubbled with 100% O_2 for up to 24 h. The long-term maintenance of cardiac slices over days, weeks, and months requires equipment, strategies, and techniques not described here and is beyond the scope of this paper.

Clipping a Cardiac Slice

The small, triangularly shaped clips are required to attach the slice to the recording apparatus. We use laser cut acrylic 0.5 mm thick and 10 mm wide at its broadest, but the clips can also be 3D printed and made of various plastics.

Applying the clips to a cardiac slice requires a well-lit area, a dissection microscope, a larger glass slide, a new razor blade, a tube of cyanoacrylate adhesive (Histoacryl, Braun), a couple triangularly shaped clips, and two pairs of forceps (**Figure 5A**). Start by examining the slices through the microscope and choosing one that looks to have a fully intact and even surface.

Place a slice onto the glass and add oxygenated Dissection Solution to cover the slice. Gently flatten the slice onto the glass surface using forceps. Be careful not to pull on the muscle. Using the microscope, find the primary orientation of the muscle fibers in the slice. In the example of **Figure 5B**, the orientation is left to right. Using the razor blade, cut the tissue parallel and perpendicular with the orientation of the muscle fibers to produce a rectangle. The length of the rectangle running parallel with the fibers can be between 5 and 10 mm long. The width of the tissue can be between 5 and 10 mm. Once the rectangle has been made, remove excess solution from around the tissue. The tissue should be moist, but not wet, for the clip to be glued to the tissue.

Put some glue on a hard surface, such as another razor blade. Using forceps, take a clip and dip the broad end into the glue. Dab off excess glue and place it onto the end of the rectangularly shaped slice. Do the same for the other clip on the other end of the slice. After 20–40 s, the glue will adhere. Dissection Solution can then be reapplied to the tissue. Do not yet pick up a clip, as it may be adhered to the glass. First, push the tissue to assure none of the tissue is adhered to the glass surface prior to lifting it. Then return the tissue to the storage dish making sure it is submerged in the Dissection Solution (**Figure 5C**).

Mounting a Cardiac Slice

Carry the small dish with the clipped muscle the chamber. Adjust the distance between the platinum hooks using the manual micromanipulator so the hooks are slightly closer together than the distance between the ends of the clips. Also make sure the solution in the chamber is just covering the hooks and that the chamber is not full.

Pick up the muscle by one of the clips using forceps and carry it to the chamber. Put the end of a clip onto a hook

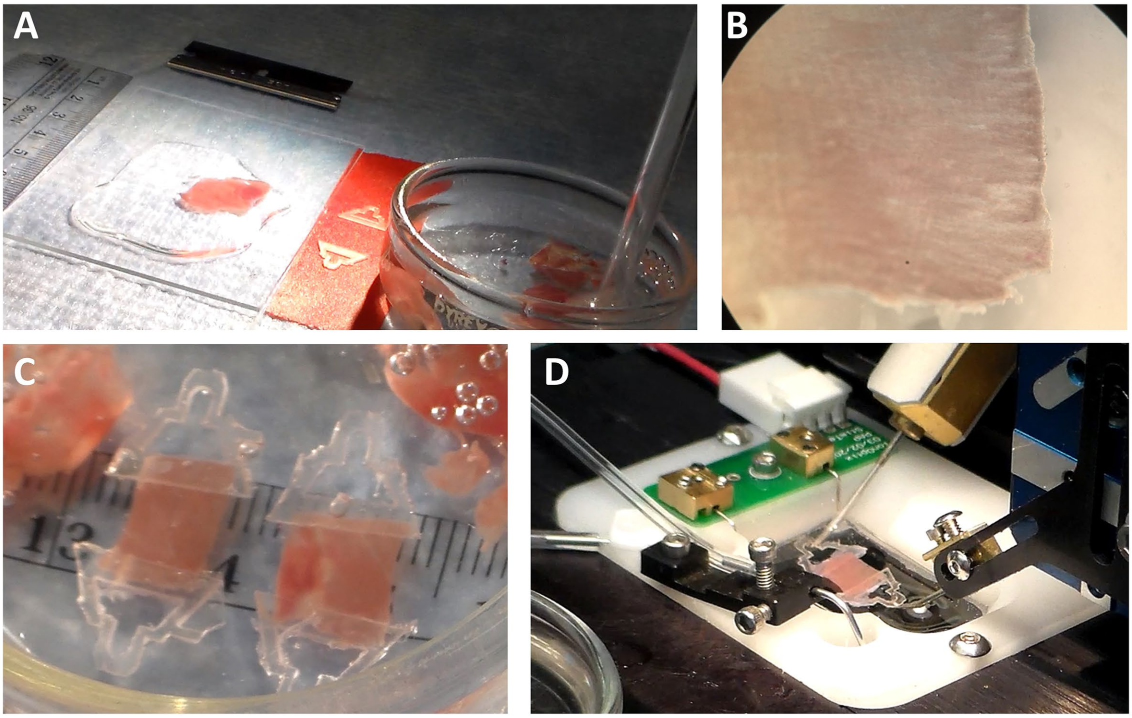

FIGURE 5 | Clipping a Cardiac Slice. **(A)** The area required for clipping must be well lit surrounded by the necessary materials. **(B)** Fiber orientation must be detected using a dissection microscope. In this example, the fibers are running left to right. The lines running up and down are either creases from the cutting action of the blade and can be reduced with slower cutting speed. **(C)** Examples of clipped slices show the dimensions are roughly 10 mm long × 5–8 mm wide x 0.3 mm thick. **(D)** The clips permit the slice to be mounted into the recording apparatus.

attached to the length controller. Lay the tissue into the chamber to minimize the effects of surface tension, which will tend to force the tissue to the surface. Position the second clip over the other hook attached to the force transducer (**Figure 5D**). Once the tissue is in the chamber, use the manual micrometer to increase the distance between the hooks. Once there is some tension on the tissue, add additional solution to bring the chamber to a volume that covers the slice. A transfer pipette is useful to place solution on top of the slice in the chamber.

PREPARING TO RECORD FUNCTIONAL DATA

Setup Before Recording

At this point, the muscle should be slack on the hooks. The Recording Solution should be bubbled with 100% O_2 and can now be circulated through the chamber. The Recording Solution should be flowing at about 1–4 ml/min so that the chamber volume is exchanged every minute or two. The outflow from the chamber should go into waste for at least 5 min to assure that any residual Dissection Solution released from the muscle will be discarded. After those 5 min have passed, the Recording Solution can be recirculated to save solution volume.

The in-line solution heater can be turned on if a temperature higher than room temperature is desired. The new temperature will be stabilized within about 5 min of turning on the heating element. The aspirator height should be checked and adjusted if necessary to assure the muscle is submerged in the solution.

The stimulator should be set up to deliver a bipolar pulse to minimize electrolysis issues, between 1 and 5 ms in duration, and 1–100 V amplitude. Please note that the voltage amplitude of the stimulus will depend on the type of stimulator used. Some stimulators will activate muscle with as little as 1 V, while other stimulators may require as much as 30 V or more. This is because some instruments have low output impedance and cannot deliver sufficient stimulating current at low voltage. Start the voltage amplitude at a low value to assure that the threshold voltage will be discovered as stimulus amplitude is raised.

With the muscle loaded and no stimulation applied, adjust the length between the hooks to assure there is no tension on the muscle and the muscle is slack. Adjust the zero point of the force transducer so that zero force is recorded under this condition.

Adjusting Stimulation Voltage and Frequency

Using the manual micromanipulator, slowly lengthen the distance between the hooks to assure there is some tension on the muscle. In the case of the papillary muscle, this will also assure there is a good electrical connection between the muscle and the stimulus. Turn on the stimulator in repeat mode. Starting with a low stimulating voltage, raise voltage to 1.5 times the stimulating threshold voltage. If the Dissection Solution is still washing out of the muscle, this washing out can often be visualized as an increase in twitch force for a few minutes as the BDM is removed from the muscle.

The stimulation frequency that allows for full relaxation between twitches can range from 0.2 to 10 Hz depending on the species, muscle type, and experimental conditions. For rat cardiac muscle at room temperature, a stimulation frequency of 1–3 Hz is reasonable. Human samples at room temperature function well at 0.2–1 Hz but may not be able to relax fully at higher frequencies up to 3 Hz, corresponding to 180 bpm, unless temperature is raised to 37°C. Samples from mouse heart at room temperature will function well at 1.5–3 Hz. Higher frequencies as high as 10 Hz can be achieved with mouse cardiac muscle at higher temperatures. Be aware that heart samples, especially from the smaller mammals, may spontaneously contract if the stimulation frequency is too low. In those cases, it is best to stimulate with a higher frequency that captures the muscle and gradually reduce stimulation frequency over 10–30 min until the muscle is stimulated at the desired frequency.

Adjusting Starting Muscle Length

Once the stimulation voltage and frequency have been established and the Dissection Solution has washed out, the starting muscle length can be established. If the sarcomere pattern is not regularly visible, as is usually the case for papillary muscle, the initial muscle length can be established by stretching the muscle until the peak generated force is maximized. Starting from nearly slack muscle, the sarcomere length can be expected to be in the vicinity of 1.7–1.9 μm. As the muscle is lengthened, the sarcomere length will lengthen and systolic force will increase, which represents the ascending limb of the force–sarcomere length relationship. The optimal muscle length, often termed L_{max}, can be found by lengthening the muscle until the highest developed force is achieved while maintaining the lowest possible diastolic force. In **Figure 6A**, the muscle is lengthened, and the developed force is found to rise with each incremental increase in length. This procedure should be repeated until there is no more rise in developed force with increasing length.

The optimal length coincides with sarcomere length approximately between 2.1 and 2.3 μm, which is the plateau region of the cardiac muscle force–sarcomere length relationship (de Tombe and ter Keurs, 2016). There are two factors that most influence the force–sarcomere length relationship and therefore optimal sarcomere length: (i) the fractional overlap of the thick and thin filaments, which is 100% within this range of sarcomere lengths, and (ii) whatever unidentified mechanism is further responsible for length-dependent activation in striated muscle (de Tombe and ter Keurs, 2016). The range of sarcomere lengths that corresponds to the optimal length can therefore be broad and will not correspond to a single sarcomere length for all preparations and conditions.

Sarcomeres are usually visible in cardiac slices thinner than ~250 μm (**Figure 6B**) and in skeletal muscle with a linear long axis, that is, not pennate. If possible, it is best to establish a sarcomere length by visualizing the sarcomere length using light microscopy as the initial step in the experimental procedure. We have found that diastolic sarcomere length can be routinely monitored in the cardiac slice, but systolic sarcomere length cannot be followed reliably. Fractional changes in whole muscle length are then in proportion to the fractional change in sarcomere length. Thus, establishing sarcomere length for a corresponding muscle length is an important initial step.

It should be noted that several attributes of the twitch force may change over time. The twitch force will generally rise slowly over the next hour and the diastolic force will generally hold steady or will slowly drop. If the diastolic force rises over time, it may be due to solution pH. We have found that even a temporary rise in pH will cause an irreversible rise in diastolic force. The changes in function that occur over time will depend upon species, muscle type, temperature, and stimulation frequency. The experimentalist must check to be sure that pH is maintained throughout the experiment.

MATERIALS AND EQUIPMENT

Basic laboratory supplies must be available including glassware, double-distilled 18 MΩ water (ddH$_2$O), refrigerator, pH meter, stir plate, ice, 100% O$_2$ with regulator at 35 kPa (5 psi), tubing, and bubbling stones to deliver O$_2$.

Solutions

The solutions used in the preparation and examination of intact muscle are crucial to recording excitable muscle function. There are many solutions that have been used successfully. We provide here only one set of solutions that are useful for testing, demonstration, and practice. The user could use these solutions to answer many experimental questions, but ultimately must select solutions that will be most applicable for the physiological processes under investigation.

The Dissection Solution outlined in **Table 1** is a HEPES-based, low Ca^{2+} Krebs-Ringer Solution useful for muscle preparation and not for recording muscle function. The Recording Solution outlined in **Table 2** is a HEPES-based Krebs-Ringer Solution useful for functional analyses. Both solutions were proposed by Dr. Pieter de Tombe for use in investigating papillary muscles (de Tombe and Little, 1994). The use of HEPES rather than sodium bicarbonate as the buffering system makes it easier to maintain pH *in vitro*. However, be aware that many physiological processes rely upon bicarbonate, which is present *in vivo*.

The presence of 2,3-Butanedione Monoxime (BDM) in the Dissection Solution prevents muscle contraction during the dissection process and therefore preserves the muscle during preparation (Mulieri et al., 1989). The BDM will wash out of the muscle prior to recording function. Make the solutions according to the steps below.

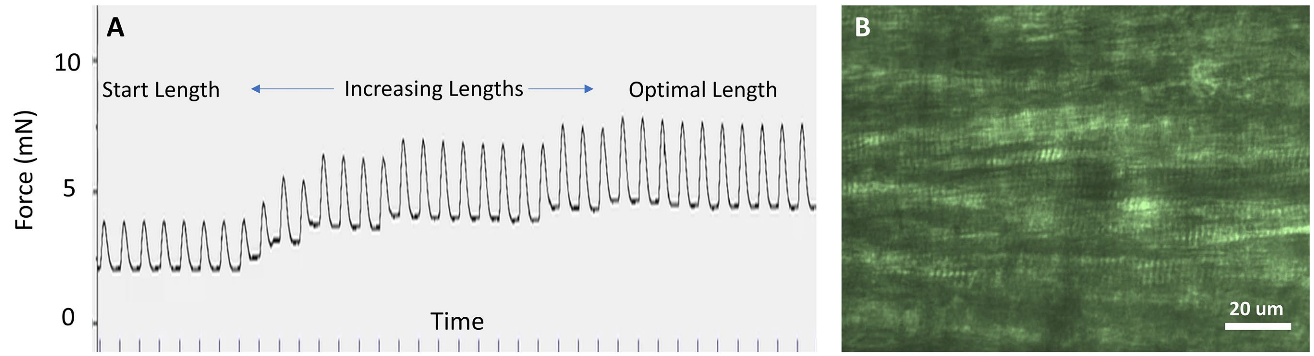

FIGURE 6 | Starting muscle length. **(A)** When sarcomeres are not visible, the optimal muscle length can be determined by lengthening the muscle until the peak twitch force (systolic minus diastolic force) is maximized while the diastolic force is minimized. In this example, stimulation was repeated at 1 Hz. **(B)** In cardiac slices of ~0.2 mm thickness, sarcomeres are clearly visible using light microscopy and can be used to adjust sarcomere length. In this example, sarcomere length is 2.0 μm.

TABLE 1 | Dissection solution.

	2 L	1 L	500 ml	250 ml
NaCl (137 mM)	16.00 g	8.00 g	4.00 g	2.00 g
KCl (5.4 mM)	0.80 g	0.40 g	0.20 g	0.10 g
$CaCl_2$ (0.2 mM)	0.40 ml	0.20 ml	0.10 ml	0.05 ml of 1 M Stock
$MgCl_2$ (1.0 mM)	2.00 ml	1.00 ml	0.50 ml	0.25 ml of 1 M Stock
Glucose (10 mM)	3.60 g	1.80 g	0.90 g	0.45 g
HEPES (10 mM)	4.80 g	2.40 g	1.20 g	0.60 g
BDM (30 mM)	6.0 g	3.0 g	1.5 g	0.75 g

This solution is useful for dissection and muscle preparation only and typically maintained cold ~ 4°C and oxygenated with 100% O_2. Final concentrations are given in parentheses.

1. Put ~90% of specified volume of ddH_2O into a beaker or Erlenmeyer flask.
2. Add stir bar and stir.
3. Add each component listed in the table.
4. pH Dissection Solution to 7.35–7.40 at ~4°C (on ice) with NaOH.
5. pH Recording Solution to 7.35–7.40 at the temperature that will be used during recording with NaOH. Do not use KOH, which will add unwanted K^+.
6. Take out the stir bar and pour into volumetric flask. Add ddH_2O to final volume.
7. Filter and pour into clean, closable glass container.
8. Label (e.g., Krebs+HEPES+BDM or Krebs+HEPES+1.8Ca^{2+}) and date
9. Close the container and store at 4°C.

When the solutions are needed for tissue dissection and data recording, be sure to bring the solutions to their respective temperatures, check pH and adjust if applicable, and bubble with 100% O_2 prior to use. When long dissection periods are expected (e.g., >5 min), bubble with 100% O_2 continuously. These solutions are best used fresh but can be kept at 4°C for up to 1 or 2 weeks.

TABLE 2 | Recording solution.

	2 L	1 L	500 ml	250 ml
NaCl (137 mM)	16.00 g	8.00 g	4.00 g	2.00 g
KCl (4.5 mM)	0.68 g	0.34 g	0.17 g	0.09 g
$CaCl_2$ (1.8 mM)	3.60 ml	1.80 ml	0.90 ml	0.45 ml of 1 M Stock
$MgCl_2$ (1.0 mM)	2.00 ml	1.00 ml	0.50 ml	0.25 ml of 1 M Stock
Glucose (10 mM)	3.60 g	1.80 g	0.90 g	0.45 g
HEPES (10 mM)	4.80 g	2.40 g	1.20 g	0.60 g

This solution is useful for recording function, such as twitch force, and can be used over a range of temperatures 15–40°C and must be oxygenated with 100% O_2.

Other Considerations Regarding Solutions

The presence of Ca^{2+} in the Recording Solution is essential for cardiac muscle, which requires extracellular Ca^{2+} to induce muscle contraction. The extracellular Ca^{2+} concentration can change depending upon the function under investigation and the species. Higher concentrations of extracellular Ca^{2+} (often reported up to 2.5 mM) will induce higher peak systolic force but can also induce higher diastolic force, which is undesirable. The experimentalist should be wary of this caveat and choose the extracellular Ca^{2+} concentration carefully.

In humans, the total plasma calcium is on the order of 2.2–2.6 mM and about half (1.1–1.3 mM) is in the form of ionic calcium (Pagana and Pagana, 2014). Anecdotally, the concentration of Ca^{2+} often appears in published studies to mimic more closely the total plasma calcium rather than ionic, for example, 2.4 mM in Runte et al. (2017). The range of total plasma calcium in mouse is dependent upon the mouse strain and encompasses 2.1–2.7 mM (Tordoff et al., 2007). The range of total plasma calcium for rats, rabbits, and other small mammals falls within the ranges of human and mouse, although the normal range for guinea pig can span 1.3–3.0 mM (Washington and Van Hoosier, 2012). The use of 1.8 mM Ca^{2+} as noted in **Table 2** is a good starting point. Reasonable systolic and diastolic function would be expected, but this concentration should be adjusted according to the experimentalists needs and the physiology under investigation.

Those processes that require bicarbonate may be less physiological if using the HEPES-based solutions. For example, a HEPES-based solution resulted in a lower intracellular pH (~7.2) compared to a bicarbonate-HEPES solution (~7.3), and whole heart function was reduced (Imahashi et al., 2007). Bicarbonate can be added to the solution recipes in **Tables 1** and **2**, but sodium balance must be maintained. For example, the addition of 25 mM sodium bicarbonate ($NaHCO_3$) will require a concomitant reduction of 25 mM NaCl. And it will be necessary to bubble the solution with 95% O_2-5% CO_2 before and during the pH'ing process and to maintain pH during recording.

Stations

Three stations that must be available: a gross dissection station, a muscle preparation station, and a recording station.

The gross dissection station is used to anesthetize and euthanize the animal subject and allows for removing the heart humanely. We will not provide information here about anesthetizing and euthanizing an animal or about removing the heart. Those procedures typically require training with a local veterinarian or physiologist, whose guidance will depend upon local laws and accepted practices of the experimentalist's country, professional societies, and institution where the work is performed.

The muscle preparation station allows the experimentalist to remove the papillary muscles from the left ventricle and prepare the papillary muscles for recording and will be described below.

The recording station allows the recording of functional data from the papillary muscle and will also be described.

Muscle Preparation Station

The muscle preparation station must provide the following (**Figure 7**): (a) excellent lighting, (b) dissection microscope (10X magnification may be sufficient, but variable magnification up to 60X is preferable), (c) cooling plate and circulator (can be substituted with ice if a cooling plate and circulator are not available), (d) bubbling stone for delivering gases, (e) at least one shallow glass dish with a clear silicon or rubber bottom and dissection pins filled half way with Dissection Solution, (f) small scissors (~10–20 mm blade), (g) smaller scissors (~2–4 mm blade), (h) at least two pairs of forceps, (i) at least two platinum omega-shaped clips in a small glass or clear plastic dish, (j) 7-O silk suture with at least two double-thrown loops also in the dish, and (k) laboratory tissues. It is also important to have transfer pipettes, ice bucket, and additional Dissection Solution readily available.

Recording Station

The recording station typically includes the following (**Figure 8**): (a) force transducer, length adjuster and chamber, (b) inverted microscope with 20X, 25X, or 40X fluorescence objective, (c) bridge amplifier for force transducer, (d) electronic interface and computer required for data collection, (e) stimulator, (f) motor controller, (g) peristaltic circulating pump, (h) tubing for delivery and withdrawal of circulating solution, (i) in-line heater to warm the solution prior to delivery to chamber, (j) rack for holding beakers or tubes

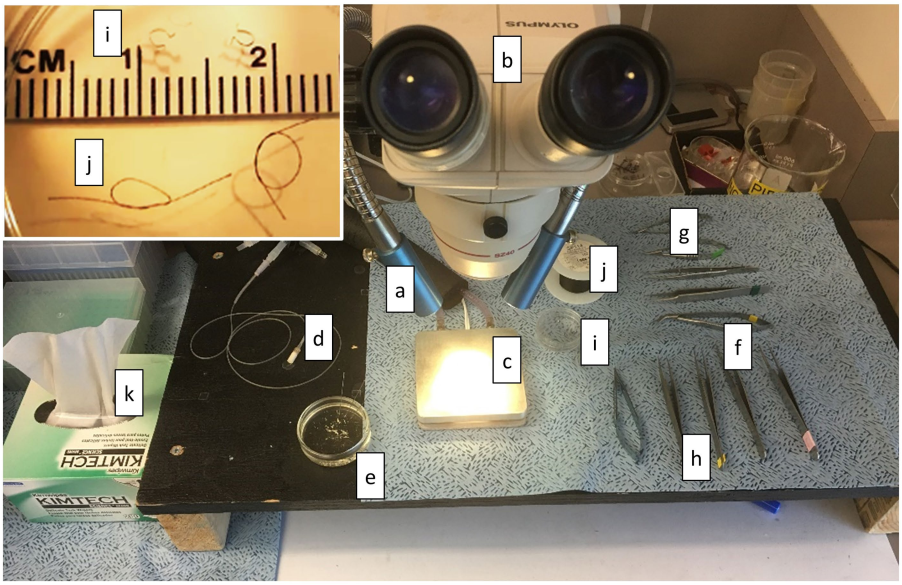

FIGURE 7 | Muscle Preparation Station. The equipment and tools required to prepare muscle are shown here. (a) lighting, (b) dissection microscope, (c) cooling plate and circulator, (d) bubbling stone for delivering gases, (e) at least one shallow glass dish with a clear silicon or rubber bottom and dissection pins filled half way with Dissection Solution, (f) small scissors (~10–20 mm blade), (g) smaller scissors (~2–4 mm blade), (h) at least two pairs of forceps, (i) at least two platinum omega-shaped clips in a small glass or clear plastic dish (see inset), (j) 7-O silk suture with at least two double-thrown loops also in the dish (see inset), and (k) laboratory tissues.

FIGURE 8 | Recording Station. The equipment and tools required to record data associated with muscle function are shown here. (a) chamber fitted with force transducer and length adjuster, (b) inverted microscope with 20X, 25X, or 40X fluorescence objective, (c) bridge amplifier for force transducer, (d) electronic interface and computer required for data collection, (e) stimulator, (f) motor controller, (g) peristaltic circulating pump, (h) tubing for delivery and withdrawal of circulating solution, (i) in-line heater to warm the solution prior to delivery to chamber, (j) rack for holding beakers or tubes containing perfusion solutions, (k) bubbling stone to deliver gases to the perfusion solutions.

containing perfusion solutions, (k) bubbling stone to deliver gases to the perfusion solutions. It is also important to have transfer pipettes and additional Recording Solution available. It is useful to have magnifying glasses, sometimes called jeweler's magnifiers, for loading muscle into the chamber. Standard 1.75X magnification with 35 mm (14 in) focal length is recommended.

DISCUSSION

The cardiac papillary muscle has been studied for decades and represents a staple experimental model system for studying cardiac muscle physiology (de Tombe and Little, 1994). Similar linear preparations, such as cardiac trabeculae or strips, can be examined using similar methods provided the tissue consists of cells oriented in parallel along the long axis of the preparation (Chung et al., 2017; Runte et al., 2017). The cardiac slice is relatively new, at least in its widespread adoption (Pitoulis et al., 2020), and represents a robust model system that can remain viable for weeks (Fischer et al., 2019; Moretti et al., 2020). Both types of model systems, linear preparations and cardiac slices, can be subjected to length changes that mimic the cardiac pressure–volume relationship (Taberner et al., 2011). Furthermore, due to its longevity, the cardiac slice can be subjected to a specified pressure–volume profile long enough to undergo cardiac remodeling that mimics the *in vivo* response to pressure overload or volume overload (Pitoulis et al., 2021). The cardiac slice, again due to its longevity, can also support transfections of novel or mutant proteins. In these ways, the cardiac slice offers some advantages over linear preparations and isolated cardiac myocytes as a versatile experimental model system. The cardiac slice also offers routine visualization of sarcomere length, which is not possible in papillary muscles or whole hearts. It is likely that the cardiac slice will become the model system of choice as more laboratories begin to take advantage of its broad utility and relative ease of preparation (Watson et al., 2017).

Both the linear preparations and cardiac slices can be loaded with fluorescent dyes to examine calcium regulation (Runte et al., 2017) or action potential (Pitoulis et al., 2020). Action potentials over an entire cardiac slice can also be recorded with an array of microelectrodes (Halbach et al., 2006). With the various methods and assays available using the model systems presented here, several physiological phenomena could be explored. For example, the effects of sarcomere length on calcium dynamics or action potential can be examined; the effects of extracellular inorganic phosphate on cardiac function can be examined; the effects of protein mutations on length-dependent force activation can be examined in an intact muscle sample. These are just a few examples of the many possible experiments that could be performed with these models. We anticipate that several more physiological questions, protocols, and experimental measurement tools will arise as these model systems become more widely employed.

Limitations of These Model Systems

While the linear preparation and the cardiac slice have much to offer, there are a few limitations the experimentalist should be aware of. For example, recording fluorescence from these preparations will often be accompanied by motion artifact. In the case of isolated myocytes, the field of view and depth of field can be chosen to encompass the entire myocyte, and total fluorescence from a single myocyte is negligibly affected by its motion. This is not the case in the more macroscopic preparations, although reasonably useful fluorescence signals are possible if care is taken to physically stabilize the sample in the field of view.

Papillary muscle and other linear preparations can experience a lack of metabolites at their core due to diffusion limitations. This phenomenon can hinder or prevent muscle performance when metabolite demands are high (Han et al., 2011). For this reason, linear preparations on the order of 200 mm diameter or smaller are required when high function and high stimulation rates are expected (Han et al., 2011). Again, the cardiac slice with a thickness under 250 μm will mitigate much of the issue related to diffusion limits.

Conclusion

With the growing use of molecular methods to probe muscle physiology at the protein and sub-protein levels, there is a generation of muscle physiologists without much if any first-hand experience collecting function data at a level higher than the molecular. Yet the methods and skills required to collect functional data from macroscopic muscle preparations, like the papillary muscle or cardiac slice, are well established, clearly valuable, and still accessible to anyone willing to try. Much of the value in examining the macroscopic preparation stems from the preservation of *in vivo* structures that are lost or modified when single myocytes or molecules are isolated. The data collected with these model systems make for relatively easy translation to whole heart function and should be considered important components of assessing cardiac muscle function due to protein modification or response to drugs. With that need in mind, we have provided here some of the most basic methods for cardiac muscle preparation that are suitable for beginners and intermediate experimental physiologists.

DATA AVAILABILITY STATEMENT

The original contributions presented in the study are included in the article/supplementary material, further inquiries can be directed to the corresponding author.

ETHICS STATEMENT

The animal study was reviewed and approved by University of Vermont.

AUTHOR CONTRIBUTIONS

BP and SB contributed to develop the methods presented in this article and revised the manuscript, read, and approved the submitted version. BP wrote the first draft of the manuscript. SB contributed the figures. All authors contributed to the article and approved the submitted version.

FUNDING

This work was supported by National Institutes of Health (R44HL137603, BP) and by National Science Foundation (1660908, BP). Confocal microscopy was performed at the Microscopy Imaging Center at the University of Vermont (RRID# SCR_018821) using a Nikon A1R-ER point scanning confocal microscope supported by NIH award number 1S10OD025030-01 from the National Center for Research Resources. The authors are grateful for the expert technical assistance of Nicole Bouffard.

REFERENCES

Chung, C. S., Hoopes, C. W., and Campbell, K. S. (2017). Myocardial relaxation is accelerated by fast stretch, not reduced afterload. *J. Mol. Cell. Cardiol.* 103, 65–73. doi: 10.1016/j.yjmcc.2017.01.004

de Tombe, P. P., and Little, W. C. (1994). Inotropic effects of ejection are myocardial properties. *Am. J. Physiol. Heart Circ. Physiol.* 266, 1202–1213.

de Tombe, P. P., and ter Keurs, H. E. (2016). Cardiac muscle mechanics: sarcomere length matters. *J. Mol. Cell. Cardiol.* 91, 148–150. doi: 10.1016/j.yjmcc.2015.12.006

Fatkin, D., Christe, M. E., Aristizabal, O., McConnell, B. K., Srinivasan, S., Schoen, F. J., et al. (1999). Neonatal cardiomyopathy in mice homozygous for the Arg403Gln mutation in the alpha cardiac myosin heavy chain gene. *J. Clin. Invest.* 103, 147–153. doi: 10.1172/JCI4631

Fischer, C., Milting, H., Fein, E., Reiser, E., Lu, K., Seidel, T., et al. (2019). Long-term functional and structural preservation of precision-cut human myocardium under continuous electromechanical stimulation in vitro. *Nat. Commun.* 10:117. doi: 10.1038/s41467-018-08003-1

Halbach, M., Pillekamp, F., Brockmeier, K., Hescheler, J., Müller-Ehmsen, J., and Reppel, M. (2006). Ventricular slices of adult mouse hearts--a new multicellular in vitro model for electrophysiological studies. *Cell. Physiol. Biochem.* 18, 1–8. doi: 10.1159/000095132

Han, J. C., Taberner, A. J., Kirton, R. S., Nielsen, P. M., Archer, R., Kim, N., et al. (2011). Radius-dependent decline of performance in isolated cardiac muscle does not reflect inadequacy of diffusive oxygen supply. *Am. J. Physiol. Heart Circ. Physiol.* 300, H1222–H1236. doi: 10.1152/ajpheart.01157.2010

Imahashi, K., Mraiche, F., Steenbergen, C., Murphy, E., and Fliegel, L. (2007). Overexpression of the Na^+/H^+ exchanger and ischemia-reperfusion injury in the myocardium. *Am. J. Physiol. Heart Circ. Physiol.* 292, H2237–H2247. doi: 10.1152/ajpheart.00855.2006

Moretti, A., Fonteyne, L., Giesert, F., Hoppmann, P., Meier, A. B., Bozoglu, T., et al. (2020). Somatic gene editing ameliorates skeletal and cardiac muscle failure in pig and human models of Duchenne muscular dystrophy. *Nat. Med.* 26, 207–214. doi: 10.1038/s41591-019-0738-2

Morita, H., Seidman, J., and Seidman, C. E. (2005). Genetic causes of human heart failure. *J. Clin. Invest.* 115, 518–526. doi: 10.1172/JCI24351

Mulieri, L. A., Hasenfuss, G., Ittleman, F., Blanchard, E. M., and Alpert, N. R. (1989). Protection of human left ventricular myocardium from cutting injury with 2,3-butanedione monoxime. *Circ. Res.* 65, 1441–1449. doi: 10.1161/01.RES.65.5.1441

Pagana, K., and Pagana, T. J. (eds.) (2014). *Mosby's Manual of Diagnostic and Laboratory Tests. 5th Edn.* (St. Louis, Missouri: Elsevier Mosby).

Pitoulis, F. G., Nunez-Toldra, R., Xiao, K., Kit-Anan, W., Mitzka, S., Jabbour, R. J., et al. (2021). Remodelling of adult cardiac tissue subjected to physiological and pathological mechanical load in vitro. *Cardiovasc. Res.* 118, 814–827. doi: 10.1093/cvr/cvab084

Pitoulis, F. G., Watson, S. A., Perbellini, F., and Terracciano, C. M. (2020). Myocardial slices come to age: an intermediate complexity in vitro cardiac model for translational research. *Cardiovasc. Res.* 116, 1275–1287. doi: 10.1093/cvr/cvz341

Runte, K. E., Bell, S. P., Selby, D. E., Häußler, T. N., Ashikaga, T., LeWinter, M. M., et al. (2017). Relaxation and the role of calcium in isolated contracting myocardium from patients with hypertensive heart disease and heart failure with preserved ejection fraction. *Circ. Heart Fail.* 10:e004311. doi: 10.1093/cvr/cvab084

Szent-Györgyi, A. G. (2004). The early history of the biochemistry of muscle contraction. *J. Gen. Physiol.* 123, 631–641. doi: 10.1085/jgp.200409091

Taberner, A. J., Han, J. C., Loiselle, D. S., and Nielsen, P. M. (2011). An innovative work-loop calorimeter for in vitro measurement of the mechanics and energetics of working cardiac trabeculae. *J. Appl. Physiol. (1985)* 111, 1798–1803. doi: 10.1152/japplphysiol.00752.2011

Tordoff, M. G., Bachmanov, A. A., and Reed, D. R. (2007). Forty mouse strain survey of voluntary calcium intake, blood calcium, and bone mineral content. *Physiol. Behav.* 91, 632–643. doi: 10.1016/j.physbeh.2007.03.027

Washington, I. M., and Van Hoosier, G. (2012). "Chapter 3 – clinical biochemistry and hematology," in *The Laboratory Rabbit, Guinea Pig, Hamster, and Other Rodents*. eds. K. A. Stevens, M. A. Suckow and R. P. Wilson (Netherlands: Elsevier Science, 2012), 57–116.

Watson, S. A., Scigliano, M., Bardi, I., Ascione, R., Terracciano, C. M., and Perbellini, F. (2017). Preparation of viable adult ventricular myocardial slices from large and small mammals. *Nat. Protoc.* 12, 2623–2639. doi: 10.1038/nprot.2017.139

Conflict of Interest: BP is employed by IonOptix, a manufacturer of equipment and software used in examine cardiac myocytes and small intact muscle preparations.

The remaining author declares that the research was conducted in the absence of any commercial or financial relationships that could be construed as a potential conflict of interest.

frontiers in Physiology

ORIGINAL RESEARCH
published: 25 March 2022
doi: 10.3389/fphys.2022.828144

Monoclonal Antibodies as Probes to Study Ligand-Induced Conformations of Troponin Subunits

Monica Rasmussen[1] *and Jian-Ping Jin*[1,2]*

[1]*Department of Physiology, Wayne State University School of Medicine, Detroit, MI, United States,* [2]*Department of Physiology and Biophysics, University of Illinois at Chicago, Chicago, IL, United States*

Striated muscle contraction and relaxation is regulated by Ca^{2+} at the myofilament level *via* conformational modulations of the troponin complex. To understand the structure–function relationship of troponin in normal muscle and in myopathies, it is necessary to study the functional effects of troponin isoforms and mutations at the level of allosteric conformations of troponin subunits. Traditional methodologies assessing such conformational studies are laborious and require significant amounts of purified protein, while many current methodologies require non-physiological conditions or labeling of the protein, which may affect their physiological conformation and function. To address these issues, we developed a novel approach using site-specific monoclonal antibodies (mAb) as molecular probes to detect and monitor conformational changes of proteins. Here, we present examples for its application in studies of two subunits of troponin: the Ca^{2+}-binding subunit, TnC, and the tropomyosin-binding/thin filament-anchoring subunit, TnT. Studies using a high-throughput microplate assay are compared with that using localized surface plasmon resonance (LSPR) to demonstrate the effectiveness of using mAb probes to assess ligand-induced conformations of troponin subunits in physiological conditions. The assays utilize relatively small amounts of protein and are free of protein modification, which may bias results. Detailed methodologies using various monoclonal antibodies (mAbs) are discussed with considerations for the optimization of assay conditions and the broader application in studies of other proteins as well as in screening of therapeutic reagents that bind a specific target site with conformational and functional effects.

Keywords: protein conformation, ELISA, LSPR, monoclonal antibody, high-throughput screening, troponin, ligand-protein binding

Edited by:
Jose Renato Pinto,
Florida State University, United States

Reviewed by:
Joanna Moraczewska,
Kazimierz Wielki University of Bydgoszcz, Poland
Henry G. Zot,
University of West Georgia, United States

****Correspondence:***
Jian-Ping Jin
jpjin@uic.edu

Specialty section:
This article was submitted to Striated Muscle Physiology, a section of the journal Frontiers in Physiology

Received: *03 December 2021*
Accepted: *25 February 2022*
Published: *25 March 2022*

Citation:
Rasmussen M and Jin J-P (2022) Monoclonal Antibodies as Probes to Study Ligand-Induced Conformations of Troponin Subunits. Front. Physiol. 13:828144. doi: 10.3389/fphys.2022.828144

INTRODUCTION

The troponin complex plays a crucial role in regulating striated muscle contraction and relaxation by allosterically modulating the configuration of tropomyosin (TM) on the actin thin filament, thus regulating myosin cross-bridge cycling (Gordon et al., 2000). Troponin is a heterotrimer consisting of troponin C (TnC, Ca^{2+}-binding subunit), troponin I (TnI, actomyosin ATPase inhibitory subunit), and troponin T (TnT, TM-binding subunit). Muscle contraction starts with initial conformational changes in TnC upon Ca^{2+} binding, which confers further conformational changes in TnI and TnT to release the inhibition of myosin ATPase and permit the movement of TM for cross-bridge formation (Zhang et al., 2011). Owing to the essential nature of the allosteric functions of troponin subunits in muscle contraction and relaxation, understanding their structure-conformation relationship and the conformational states relevant to muscle contraction and relaxation is vital to understanding how striated muscle functions.

Two homologous genes encode muscle-fiber type specific TnC isoforms, one expressed in fast skeletal muscle and the other in cardiac and slow skeletal muscles. Both isoforms contain four E-F hand divalent metal ion binding sites, two high affinity sites in the C-terminal domain that competitively bind both Ca^{2+} and Mg^{2+}, and two low affinity sites in the N-terminal domain that favor binding of Ca^{2+} (Robertson et al., 1981). The two TnC isoforms differ in that all ion-binding sites are active in fast skeletal muscle TnC, while one of the N-terminal sites (Site 1) in cardiac/slow skeletal muscle TnC is inactive (van Eerd and Takahashi, 1975; Putkey et al., 1991). In both isoforms, the N and C domains are connected by a linker region which forms an alpha helical arrangement in fast skeletal TnC but is less well-resolved in the X-ray crystallography structure of cardiac/slow skeletal muscle TnC, suggesting this region may be highly flexible in the latter isoform (Vinogradova et al., 2005). In muscle cells, the C domain metal-binding sites are constantly occupied by Mg^{2+}, whereas the rising cytosolic Ca^{2+} ions during muscle activation preferentially bind the N domain of TnC to initiate the conformational changes that confer contraction (Grabarek, 2011). Experimental data suggest that Mg^{2+} may be able to compete to some degree with Ca^{2+} for binding to the N domain of TnC though it cannot initiate conformational changes (Potter and Gergely, 1975; Leavis and Kraft, 1978; Rayani et al., 2021).

Three TnT isoforms exist in fast skeletal, slow skeletal, and cardiac muscles, respectively (Wei and Jin, 2016). The N-terminal domain of TnT is a hypervariable region with a highly diverged structure among isoforms and undergoes alternative splicing during muscle development (Jin et al., 2008). The N-terminal structural variations have been shown to modulate the conformation and function of the middle and C-terminal conserved regions of TnT (Biesiadecki and Jin, 2002; Zhang et al., 2006). An intriguing feature of the N-terminal variable region of avian fast skeletal muscle TnT is an alternatively spliced Glu and His rich segment uniquely expressed in adult pectoral muscles of the avian orders of *Galliformes* (Jin and Smillie, 1994; Ogut and Jin, 1998). This N-terminal variable segment of *Galliformes* fast skeletal muscle TnT contains repeating [H(E/A)EAH] motifs designated the Tx segment (Smillie et al., 1988), which has been shown to bind transition metal ions (Jin and Smillie, 1994). While this unique feature is not present in muscles of other species and is therefore not required for the basic function of troponin T, research from our lab has previously demonstrated that binding of Zn^{2+} to the N-terminal domain of chicken fast skeletal muscle TnT alters the local and global molecular conformations with functional impacts (Ogut and Jin, 1996; Wang and Jin, 1998).

Traditional approaches to study folded protein structure include methods such as X-ray crystallography, nuclear magnetic resonance spectroscopy, circular dichroism, and Förster resonance energy transfer (FRET). These methods often demand large amounts of purified protein at high concentration and highly specialized equipment, or they require external labeling of the protein, which can interfere with the very native structure seeking to be investigated (Alberts et al., 2002; Liu and Hsu, 2005; Raicu and Singh, 2013). The now widespread availability of computational models has expanded the ability to model protein structure *in silico*, but such methods still rely on experimentally determined conformation data and the need for empirical validation through biochemical and biophysical studies (Bhasin and Raghava, 2006). Therefore, there remains a need to assess native protein conformation and physiological structure–function relationship through assays that can be readily performed in the laboratory of individual investigators.

Antibodies are ubiquitously used in research laboratories. The binding of an antibody (immunoglobulin) to an antigen protein is a protein–protein interaction dependent on the 3-D conformational fit between the topology of the epitope and the variable region of the antibody. The affinity of an antibody to an antigen reflects the degree of structural fit (**Figure 1**). Generation of antibodies *in vivo* is mediated by antigen presenting cells, which process an immunogen and present it in the form of short peptides to activate B cells (Avalos and Ploegh, 2014). Therefore, antibodies generated by various forms of immunogens, such intact proteins, either denatured or native, as well as protein fragments or synthetic peptides can potentially be useful as conformational probes as long as their epitopes are related to the conformation-sensitive structures of a desired protein. Hybridoma technology has expanded the ability to produce site-specific monoclonal antibodies (mAbs) (Köhler and Milstein, 1975), allowing for the production of reagents which recognize various antigenic epitopes with high specificity.

It is widely recognized that the high throughput enzyme-linked immunosorbant assay (ELISA) (Plested et al., 2003), typically performed in a 96-well microtiter plate, can rapidly titrate and quantitatively compare antibody-protein bindings. The ELISA method is easily adaptable to a wide array of study designs, among which we have explored its novel application in mAb protein conformational studies (**Figure 2**; Wang and Jin, 1998; Jin and Root, 2000; Chong and Jin, 2009).

Localized surface plasmon resonance (LSPR) is a technique which takes advantage of the oscillations of conduction band electrons in a metallic nanoparticle following stimulation by irradiated light. When probed with a light wave, the electron cloud will oscillate in a predictable manner, which will further shift with local changes at the surface of the nanoparticle. By functionalizing the nanoparticle, various proteins can be bound to the surface, and interactions with other proteins will disrupt the resonant wavelength in a quantitative manner (Petryayeva and Krull, 2011). This method can analyze a bound protein of interest using specific mAbs, in which empirical antibody–antigen binding data can be fit to a model to estimate association (K_a) and dissociation (K_d) constants. By using LSPR in conjunction

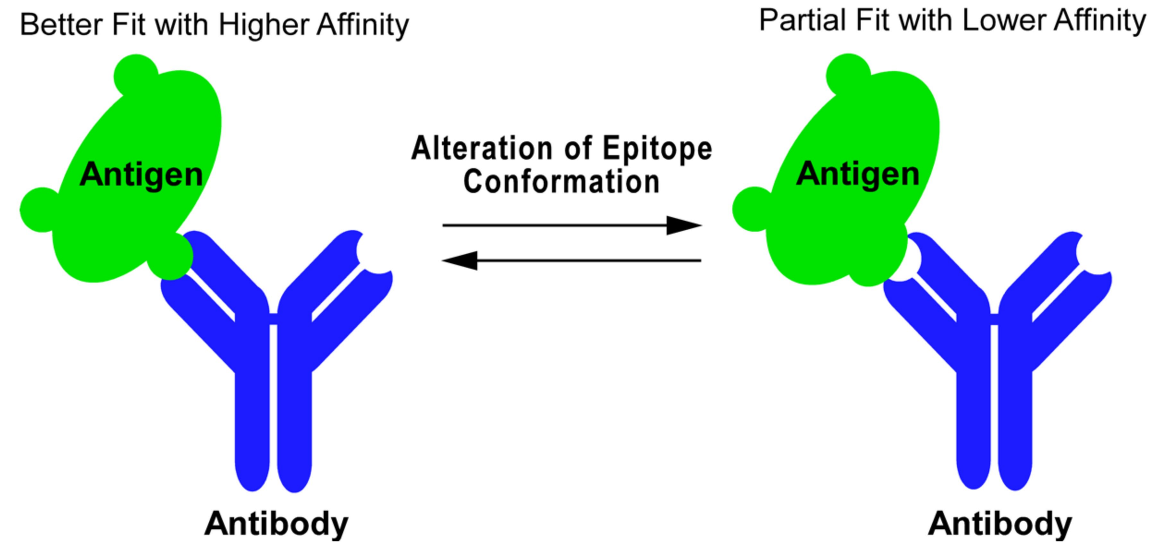

FIGURE 1 | Antibody as probe to detect protein conformational change. Antibody–antigen binding is a protein–protein interaction whose affinity is determined by 3-D structural fitting of the antigenic epitope and the variable region of antibody. Changes in the epitope conformation can be reflected in the antibody binding affinity, where an alteration of the epitope conformation can shift an antibody–antigen interaction from a better fit with higher affinity (left) to a partial fit with lower affinity (right) and vice versa.

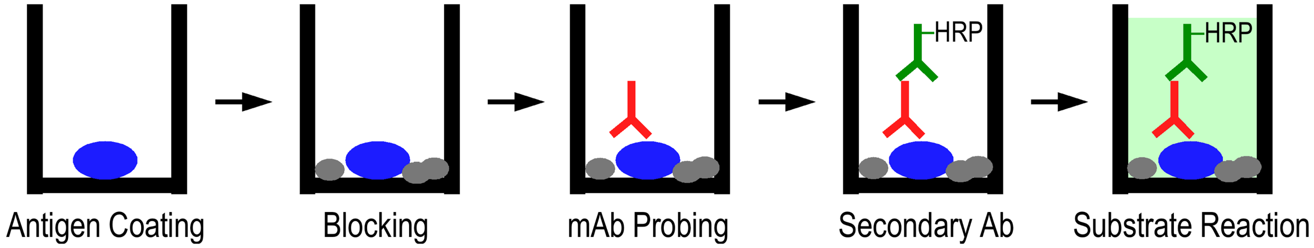

FIGURE 2 | ELISA-based mAb epitope analysis. Protein of interest was coated on a microtiter plate in a buffer containing the desired additives, which can be used as the buffer throughout the entire assay or modified in later steps. After blocking the plate, the mAb conformational probe was incubated in serial dilutions, followed by washes and incubation with horse radish peroxidase (HRP)-conjugated secondary antibody. After final washes, the binding of mAb probes was detected *via* H_2O_2-ABTS colorimetric substrate reaction and recording the development of absorbance at 420 nm.

with a high-throughput method like ELISA, a fuller picture of antibody–antigen binding can be efficiently studied (**Figure 3**).

In the present work, we employed a diverse range of site-specific mAbs to assess conformations of TnC and TnT for functional significance, with a focus on quantifying ligand-induced changes upon ion binding. We investigated Ca^{2+}-induced changes in the molecular conformation of TnC at regions related to the E-F hand domains, as well as remote ligand-induced effects. We also explored how binding of transition metal ions to the N-terminal Tx segment affect local and overall conformation of avian pectoral muscle TnT. Site-specific mAbs are employed based on their epitope locations in TnC or TnT. LSPR is utilized to understand changes in TnC structure upon Ca^{2+} binding. We further discussed the utility of site-specific mAbs to investigate protein conformation, with an emphasis on optimization of assay conditions and the applicability of mAb analysis of protein conformational differences and changes for broader use in other systems, including the screening of therapeutic reagents that bind a specific target site with conformational and functional effects.

MATERIALS AND METHODS

Proteins Used in Study

Recombinant chicken fast skeletal TnC and mouse cardiac/slow skeletal muscle TnC were expressed in BL21(DE3)pLysS *Escherichia coli* and purified as previously reported (Jin et al., 2007). Recombinant chicken fast skeletal muscle TnT8e16 protein was expressed in BL21(DE3)pLysS *E. coli* and purified as previously reported (Ogut and Jin, 1998). Recombinant chicken fast skeletal muscle TnT1 fragment 1–165 (N165) was expressed in BL21(DE3)pLysS *E. coli* and purified as previously reported (Ogut and Jin, 1996).

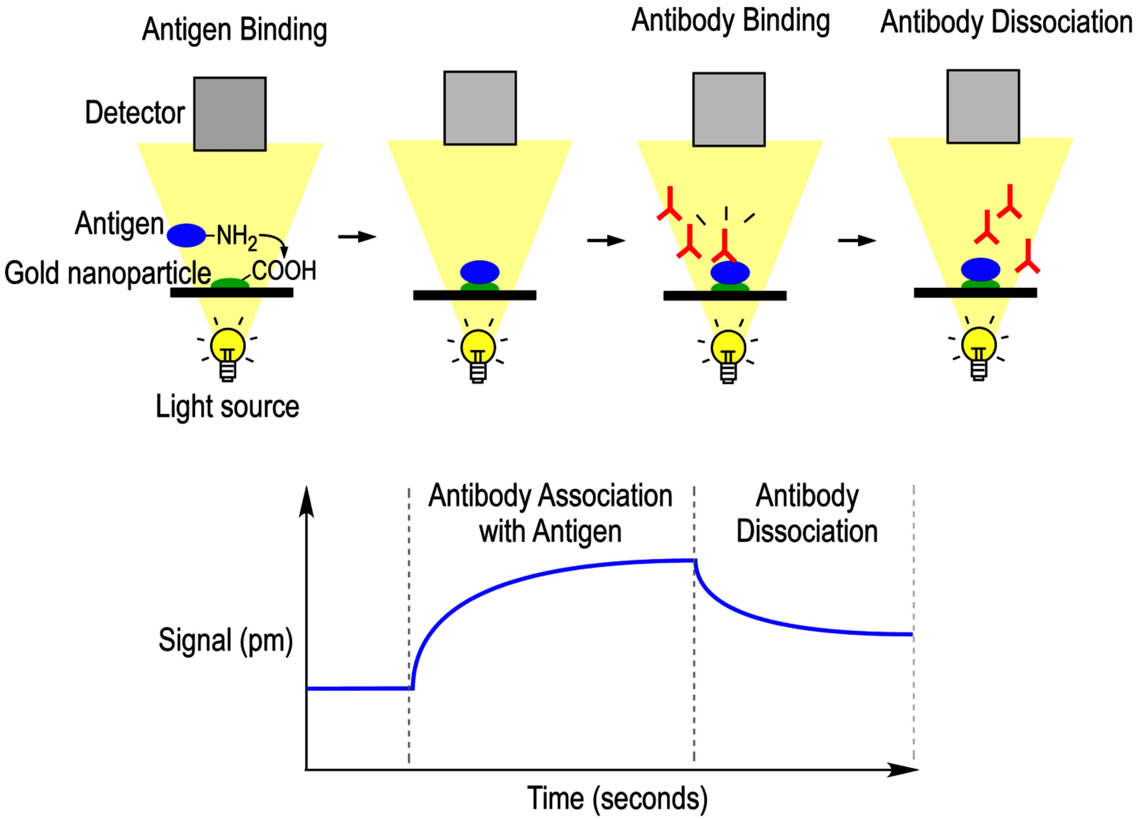

FIGURE 3 | Localized surface plasmon resonance-based mAb epitope analysis. Protein of interest was attached to a carboxy-functionalized gold nanoparticle *via* covalent bonding with lysine residues. The protein was permitted to equilibrate in running buffer, and then the mAb probe diluted in the same buffer was permitted to flow over the chip and interacts with the protein. Interactions were measured *via* local changes in refractive index that are reflected in optical signal detection. Running buffer was then flushed over the chip to promote mAb dissociation. The resulting signal measured by the optical detector is plotted against time to calculate antibody association and dissociation rate constants.

Concentrations of protein stocks were determined using Bradford reagent (BioRad) with a linear fit standard curve of serial dilutions of bovine serum albumin (BSA). Absorbances were determined at $A_{595\ nm}$ using an automated microplate reader (BioTek Synergy H1).

Monoclonal Antibodies Used in Study

Development and immunological characterization of anti-TnC and anti-TnT mAbs were completed using the methods reported previously (Wang and Jin, 1998). Briefly, Balb/c mice were immunized with purified antigen using a short term protocol including a primary injection with Freund's complete adjuvant and three daily pre-fusion boosts without adjuvant. Two days after the final boost, spleens cells were harvested and fused with SP2/0 mouse myeloma cells. Hybridoma clones were screened using ELISA against the antigen protein immobilized on 96-well microplate. The antibody-secreting hybridomas were subcloned three or more times to establish stable cell lines for use in the production of mAb-enriched mouse ascites fluid.

Anti-chicken fast skeletal muscle TnC mAbs 4E7, 2C3, and 2D10 were prepared as reported previously, through immunization with purified chicken fast skeletal muscle TnC (Jin et al., 2007). Anti-chicken fast skeletal muscle TnT mAbs 6B8, 3E4, 3H12, and 4C3 were prepared as described previously through immunization with purified chicken breast muscle TnT or leg muscle TnT (Wang and Jin, 1998). An anti-Tx peptide mAb 3C11 was produced as reported previously through immunization with a Tx3 peptide fused to ApoE protein with Freund's complete adjuvant (Liu, 2016).

To partially purify mAbs from mouse ascites fluid, saturated ammonium sulfate solution was added dropwise to 1 ml of ascites fluid to arrive at 30% saturation. The mixture was permitted to equilibrate at 4°C with mixing for 1 h and then was centrifuged at 20,000 × *g* at 4°C for 15 min. The supernatant was collected, and the volume was measured. Saturated ammonium sulfate solution was added dropwise to the 30% saturation supernatant to arrive at 60% saturation, equilibrated at 4°C for 1 h, and centrifuged at 20,000 × *g* at 4°C for 15 min. The resulting pellet containing enriched IgG was collected and resuspended in phosphate buffered saline (PBS) for use.

SDS-PAGE and Western Blotting

TnC and TnT proteins were analyzed *via* SDS-PAGE and Western blotting to determine the recognition by specific mAbs.

Briefly, purified proteins in SDS-PAGE sample buffer were resolved on 14% Laemmli gel with an acrylamide-to-bisacrylamide ratio of 180:1 and were visualized using Coomassie blue R250 staining or electrically transferred to nitrocellulose membrane using a semi-dry apparatus (Bio-Rad). The membranes were blocked with Tris-buffered saline (TBS) containing 1% BSA, followed by incubation in TBS containing 0.05% Tween-20 (TBS-T), 0.1% BSA, and pre-titrated concentrations of mAbs at 4°C overnight. Membranes were washed using TBS containing 0.5% Triton X-100 and 0.1% SDS, and incubated with alkaline phosphatase-conjugated anti-mouse IgG secondary antibody (Santa Cruz) in TBS-T + 0.1% BSA at room temperature for 1 h. Membranes were washed again and developed in 5-bromo-4-chloro-3-indolyl-phosphate/nitro blue tetrazolium (BCIP/NBT) to visualize the target protein bands.

Microtiter Plate Antibody Epitope Analysis of TnC and TnT Conformational Changes

As outlined in **Figure 2**, antibody epitope analysis using solid-phase ELISA was performed to assess changes in protein conformations *via* titration of antibody-protein binding affinities. To study the troponin subunits, a standard buffer mimicking the intracellular ionic environment (10 mM Tris–HCl, pH 8.0, and 100 mM KCl) was used with assay-specific additives described below. All assays were run in 96-flat bottom well microplates in triplicate.

To study Ca^{2+}/Mg^{2+}-dependent conformations of fast TnC, purified chicken fast skeletal muscle TnC was coated on microtiter plates at 2 μg/ml, 100 μl per well, in the standard buffer plus either 0.1 mM ethylene glycol tetraacetic acid (EGTA), 0.1 mM $CaCl_2$, 3 mM $MgCl_2$ + 0.1 mM EGTA, or 3 mM $MgCl_2$ + 0.1 mM $CaCl_2$, at 4°C overnight. Plates were washed three times 5 min each using the standard buffer with the corresponding assay-specific additives plus 0.05% Tween-20 to remove unbound protein, and the remaining plastic surface was blocked using 1% BSA in the washing buffer for 30 min. The immobilized protein was then incubated with serial dilutions of ascites fluid of anti-fast TnC mAbs 2C3, 4E7, or 2D10 in standard buffer plus 0.1% BSA, 0.05% Tween-20, and the assay-specific additives at 100 μl per well at room temperature for 2 h. Same as above, the plates were washed and further incubated with horse radish peroxidase (HRP)-conjugated anti-mouse secondary antibody (Santa Cruz) at room temperature for 1 h. Washed again to remove unbound secondary antibody, H_2O_2–2,2′-azinobis (3-ethylbenzthiazolinesulfonic acid; ABTS) substrate was added at 100 μl per well for color development at room temperature for 30 min. $A_{420\ nm}$ of each assay well was measured at a series of time points using an automated microplate reader (BioTek Synergy H1). Values in the linear range of color development were used to construct affinity titration curves after background subtraction.

To study the effects of transition metal binding to the N-terminal Tx element of avian pectoral muscle fast TnT on local and global molecular conformation, purified chicken fast TnT8e16 was coated at 4 μg/ml in the standard buffer containing 0.1 mM ethylenediaminetetraacetic acid (EDTA) or 0.1 mM $ZnCl_2$. Microplate epitope analyses were performed as above using mAbs 3C11, 3E4, 4C3, 2C8, or 3H12.

Localized Surface Plasmon Resonance Epitope Analysis of Antibody Kinetics

As illustrated in **Figure 3**, LSPR was employed to study TnC epitope conformation *via* determining the binding kinetic rate constants of mAbs. Chicken fast skeletal muscle TnC was covalently immobilized on a carboxyl sensor chip of the Open SPR™ instrument (Nicoya Lifesciences, Canada), using 1-ethyl-3-(3-dimethylaminopropyl)carbodiimide (EDC) and N-hydroxysuccinimide (NHS) to activate the carboxyl groups by producing an activated NHS-ester intermediate, which was then displaced by primary amines from lysine groups of the protein of interest. A 200 μl injection of fast TnC at 50 μg/ml in sodium acetate buffer pH 5 was allowed to bind to the chip over 5 min at a flow rate of 20 μl/min, followed by a blocking solution (Nicoya Lifesciences, Canada) to block any remaining activated esters on the chip.

To study antibody binding to the immobilized protein, ammonium sulfate-enriched mAb stock was diluted in the running buffer at 50 and 10 μg/ml to a negligible amount of ammonium sulfate. The mAb was permitted to bind to the immobilized protein over 300 s at a flow rate of 20 μl/min, followed by fresh running buffer for 180 s at 20 μl/min to allow for dissociation. The chip was regenerated with 3 M KCl (or HCl, pH 1.5, if salt was not sufficient to promote full regeneration). If a buffer change was required, the buffer was perfused through the instrument at 20 μl/min for 10 min for complete solution exchange. The data were retrieved and analyzed using TraceDrawer software, and the curves were fit to a one-to-one model to estimate binding constants (Myszka et al., 1997; Önell and Andersson, 2005; Rich and Myszka, 2010).

The effect of Ca^{2+} on TnC conformation was studied in buffers at pCa 10.0, 9.0, 8.0, 7.5, 7.0, 6.5, 6.3, 6.0, 5.5, 5.0, 4.5, and 4.0 prepared by mixing pCa 10.0 and 4.0 buffers [10 mM piperazine-N,N′-bis(2-ethanesulfonic acid) pH 7, 100 mM KCl, 3 mM $MgCl_2$, 10 mM EGTA, 3 μM, or 10.06 mM $CaCl_2$] calculated using the UC Davis Ca-Mg-ATP-EGTA v1.0 computer program[1] and mixed at various ratios as described previously (Feng and Jin, 2020).

RESULTS

Conformational Effects of Ca^{2+} and/or Mg^{2+} Binding to N and C Domains of Fast Skeletal Muscle TnC Detected Using mAb ELISA

Domain-specific anti-chicken fast skeletal muscle TnC mAbs 4E7, 2C3, and 2D10 were employed to assess conformational

---

[1] https://somapp.ucdmc.ucdavis.edu/pharmacology/bers/maxchelator/CaMgATPEGTA-NIST.htm

changes of fast TnC induced by the binding of Ca^{2+} and Mg^{2+}. The epitope locations of the mAbs have been previously reported (Jin et al., 2007), with 4E7 and 2C3 against the N domain fragment (amino acids 1–91) and 2D10 against the C domain fragment (amino acids 89–163; **Figure 4A**). Chicken fast skeletal TnC contains 4 E-F hand metal-binding sites: the high-affinity C domain sites bind Mg^{2+} or Ca^{2+}, while the low-affinity N domain sites preferentially bind Ca^{2+} (**Figure 4B**; Vinogradova et al., 2005; Sehnal et al., 2021). The three mAbs were used as probes in an ELISA microtiter plate solid-phase assay to assess changes in fast TnC conformation with Ca^{2+} and/or Mg^{2+} binding and with an EGTA control for the metal-free apo form.

The ELISA mAb titration curve in **Figure 5A** shows that fast TnC at the physiological activation state (two-Mg^{2+} and two-Ca^{2+}) exhibits significantly higher affinity for 4E7 in comparison to that of the EGTA-apo state. Occupation of the C domain metal binding sites by Ca^{2+} further increases the affinity to mAb 4E7 (**Figure 5A**). The Mg^{2+}-only relaxation state shows an intermediately higher binding affinity than that of apo state (**Figure 5A**). The results, therefore, indicate that the binding of Ca^{2+} to the N domain of TnC during muscle activation reconfigures the N domain conformation in a detectable manner *via* change of mAb 4E7 affinity. The effects of four-Ca^{2+} vs. Ca^{2+} + Mg^{2+} on increasing mAb 4E7 affinity further demonstrate a cross talk between the C and N domains.

The anti-C domain mAb 2D10 shows higher affinity than that of the metal free-apo state in the presence of either Ca^{2+} alone or $Ca^{2+} + Mg^{2+}$ ions (**Figure 5B**), indicating structural effects regardless of which ion occupies the C domain binding sites. The detectable difference between the Mg^{2+} only state and the Ca^{2+} + Mg^{2+} state (**Figure 5B**) indicates a Ca^{2+}-N domain binding-induced conformational change in the C domain.

In contrast, the affinity of mAb 2C3 was not dramatically affected by the binding of Ca^{2+} and Mg^{2+} as compared to the EGTA-apo state (**Figure 5C**). In addition to confirming consistent coating of TnC protein on the microtiter plate regardless of metal additives, the result suggests that the mAb 2C3 epitope may lie in the central helical linker region near the end of the N domain peptide of fast skeletal TnC (**Figure 4A**) and may be conformationally independent of the four metal ion-binding sites.

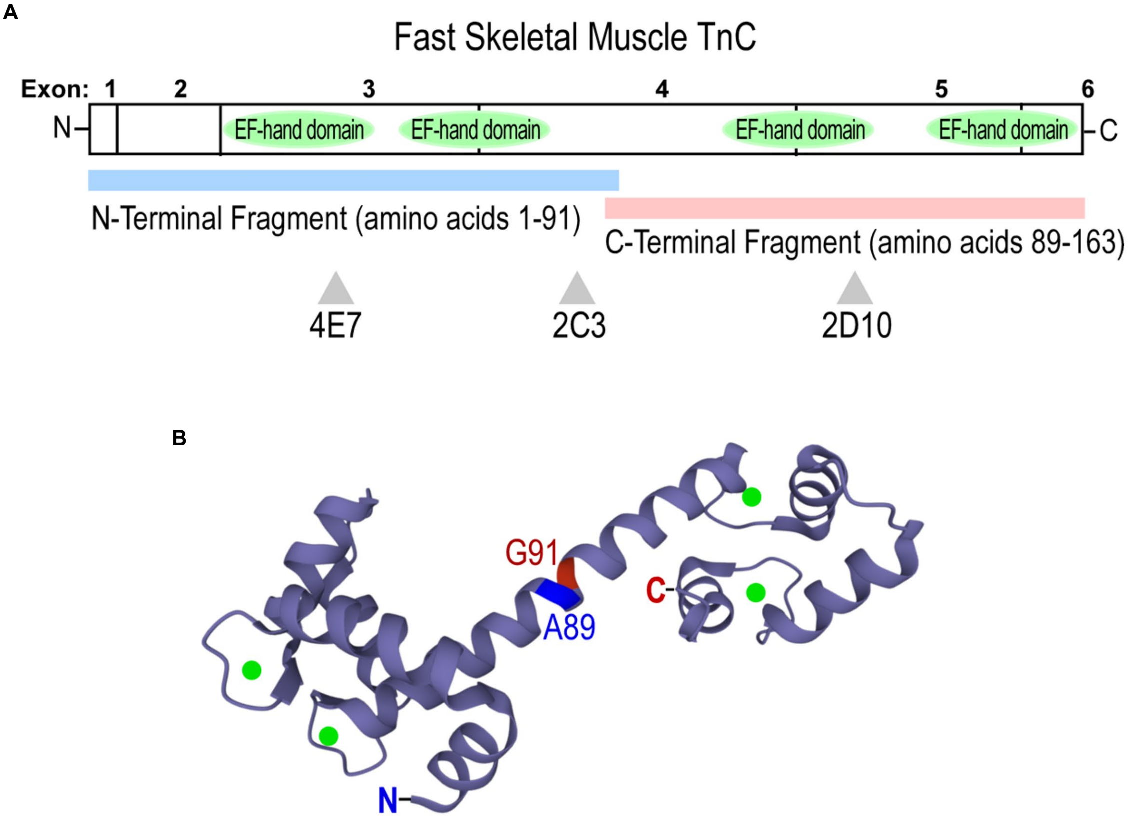

FIGURE 4 | Structure of chicken (*Gallus gallus*) fast skeletal muscle TnC. **(A)** A linear map showing locations of epitopes recognized by anti-TnC mAbs 4E7, 2C3, and 2D10 used as conformational probes in the present study. Fast TnC consists of N and C terminal domains containing four E-F hand Ca^{2+}-binding motifs, along with a central helical linker to connect the domains. N-terminal (amino acids 1–91) and C-terminal (89–163) fragments were employed to map epitopes of the mAbs. **(B)** A crystal structure of fast TnC in the Ca^{2+}-saturated state (PDB: 1YTZ; Ca^{2+} ions are present as green spheres). The N and C termini, and the boundary of the N- and C-terminal fragments used for mAb epitope mapping are indicated.

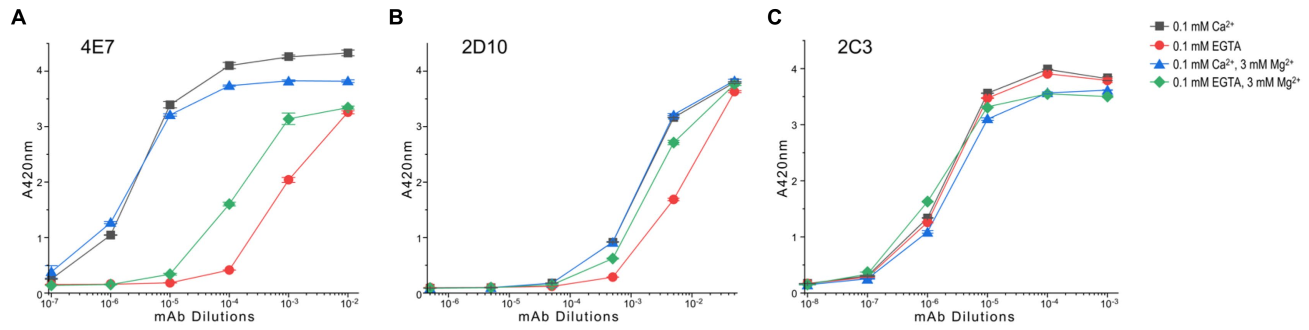

FIGURE 5 | Conformational effect of Ca^{2+} and/or Mg^{2+} binding to fast TnC detected in microtiter plate ELISA. **(A)** The ELISA titration curves show that mAb 4E7 against the N domain of fast TnC exhibits a low affinity in the metal-free condition. The presence of Mg^{2+}, which binds to the C domain sites, significantly increased the affinity of mAb 4E7, indicating an effect on the N-domain conformation. Binding of Ca^{2+} to the N-domain sites in the presence of 3 mM Mg^{2+} further increased the affinity of mAb 4E7. The highest affinity of mAb 4E7 was seen in the four-Ca^{2+} state, indicating that the occupations of the C domain sites by Ca^{2+} or Mg^{2+} have different conformational effect on fast TnC. **(B)** mAb 2D10 against the C domain of fast TnC shows higher affinities in the four-Ca^{2+} or Ca^{2+} + Mg^{2+} state than that of Mg^{2+} alone while the metal free-apo state has the lowest affinity, indicating both ions bind to the C-domain with similar conformational effect whereas Ca^{2+} binding to the N domain increases the affinity for mAb 2D10. **(C)** mAb 2C3 detected a conformation-independent epitope that displays similar affinity for fast TnC in the presence or absence of Ca^{2+} and Mg^{2+} ions.

Ca^{2+} Sensitivity of Fast Skeletal Muscle TnC Titrated With LSPR

Using mAbs 2C3 and 4E7 in LSPR infused with buffers containing 3 mM Mg^{2+} and differing [Ca^{2+}], mAb 2C3 affinity to fast skeletal muscle TnC is nearly identical at pCa 9.0 and 4.0 (**Figure 6A**), consistent with the results from the ELISA titrations. mAb 4E7, on the other hand, shows a low association rate with fast skeletal muscle TnC at pCa 9.0 with a dramatic increase at pCa 4.0 (**Figure 6B**). Infusing mAb-free buffer to promote dissociation quickly returns the pCa 9.0 curve to baseline, conditions which mimic the post-wash endpoint readings in ELISA.

Over the range from pCa 10.0 to 4.0, a shift in mAb 4E7 affinity is observed with [Ca^{2+}] at and above pCa 8.0 (**Figure 6C**). The Ca^{2+}-induced conformational changes at the mAb 4E7 epitope, reflected by the equilibrium dissociation constant K_D, mirror the equilibrium endpoint measured in ELISA. While B_{max}, the maximum possible binding to the fast TnC chip, increases with increasing [Ca^{2+}], K_D decreases, reflecting a higher affinity of mAb 4E7 for fast TnC in the Ca^{2+}-bound state. In our previous work using skinned cardiac muscle fiber preparations with similar buffer conditions, pCa 5.8 is approximately the concentration of half maximal force activation, indicating a Ca^{2+} concentration sufficient to induce TnC conformational changes that instigate muscle contraction (Wong et al., 2019). Of note, both measures of antibody kinetics, B_{max} and K_D, reach an equilibrium value at approximately pCa 7.0. The results implicate that fast TnC can be sufficiently "primed" at this pCa prior to the fiber activation of contraction at pCa 5.8, similar to the four-state model of calcium regulation of muscle contraction proposed in a previous study of cardiac muscle (Sun and Irving, 2010).

The results of an ELISA pCa titration of mAb 4E7 binding to fast TnC further validate the results observed in LSPR (**Figure 6D**), where 4E7 shows a dramatic increase in affinity from pCa 10 to 7.5 followed by a gradual decrease to reach a plateau level at pCa 5.5. With the presence of two Ca^{2+} binding sites in the N domain of fast TnC, we posit that the early phase of mAb 4E7 epitope conformational change from pCa 10 to 7.5 may be reflective of one vs. two Ca^{2+} state binding, whereas the second phase conformational change between pCa 7.5 and 5.5 induces myofilament activation and force production, though more work needs to be done to further validate this hypothesis.

Conformational Effect of Transition Metal Ion Binding to Tx-Segment of Avian Pectoral Muscle TnT

Site specific mAbs 3C11, 3E4, 2C8, 4C3, and 3H12 against the pectoral splice form of chicken fast skeletal muscle TnT were employed to assess conformational changes with metal ion binding. Previous characterizations have shown that mAb 3C11 is specific to the metal binding Tx peptide, mAb 3E4 is against an epitope lying in the adjacent exon 7-encoded linker region, and mAb 2C8 epitope lies downstream in the exons 10–11 encoded segment (**Figure 7A**; Wang and Jin, 1998; Jin and Chong, 2010; Liu, 2016). The Western blots and ELISA titrations against intact TnT8e16 and the T1 segment of chicken fast skeletal TnT1, N165, further determined the epitope locations of the anti-TnT mAbs used in the present study. mAb 2C8, used as a positive control, recognizes the N165 peptide and displays equal reactivity to N165 and TnT8e16 in both Western blot and ELISA (**Figures 7B,C**). mAbs 3C11 and 4C3 showed similar reactive pattern to TnT8e16 and N165 in ELISA and thus also possess epitopes within the T1 segment. N165 lacks the exon 7-encoded segment, and thus mAb 3E4 displays reactivity to TnT8e16 but not to N165. Both mAbs 3C11 and 4C3 lacked strong reactivity to N165 in Western blot, suggesting low affinity under the SDS-PAGE denaturing conditions as compared to

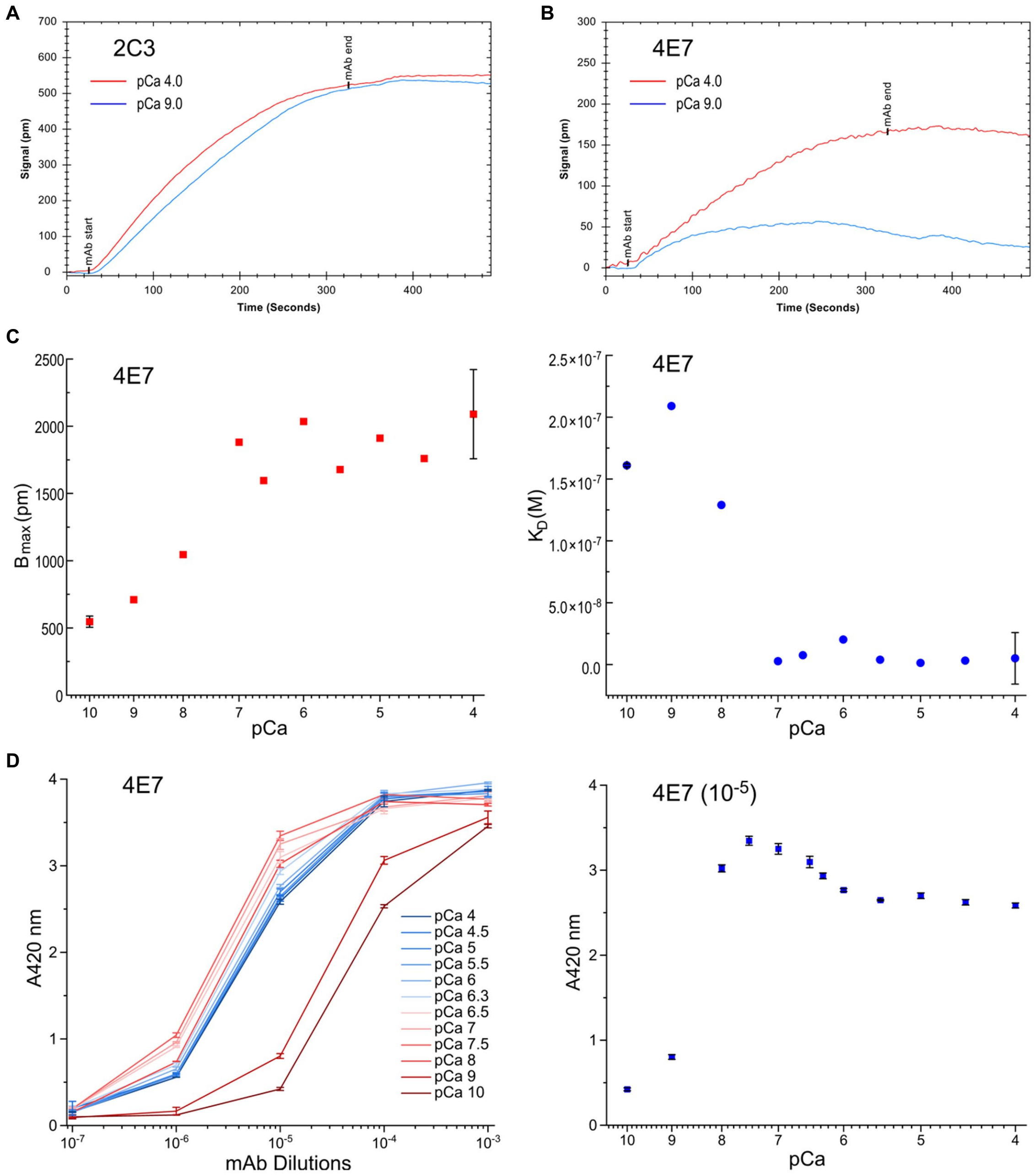

FIGURE 6 | Conformational effect of Ca^{2+} binding to fast TnC detected in quantitative LSPR assay. **(A)** Changes in buffer pCa did not affect the binding of mAb 2C3, consistent with the observation in ELISA that mAb 2C3 binding to fast TnC remains constant regardless of ion binding. In addition, the binding signal of mAb 2C3 confirms constant protein coating on the LSPR chip. **(B)** In contrast, the binding of mAb 4E7 against the N domain of fast TnC changes with the change in pCa. A significant decrease in association rate and increase in dissociation rate at pCa 9.0 vs. pCa 4.0 are detected, indicating weaker binding of the mAb probe in the Ca^{2+}-free state. **(C)** The physiological range pCa titration curve of mAb 4E7 binding with LSPR indicates that fast TnC changes conformation when [Ca^{2+}] increases. The maximum binding of mAb 4E7 to the fast TnC chip, B_{max}, increased in a gradual manner to a plateau level when [Ca^{2+}] reached pCa 7.0, while K_D, the equilibrium dissociation constant, started to decrease when [Ca^{2+}] increases to pCa 8.0 and rapidly minimized at pCa 7.0. **(D)** The ELISA titration curves of mAb 4E7 binding to fast TnC at the same range of pCa (left panel) show a dramatic increase in affinity from pCa 10.0 to pCa 8.0. At sub-saturated concentration of mAb 4E7 (10^{-5} dilution, right panel), the [Ca^{2+}] titration curve reveals three-phases of binding affinity changes: A rapid increase from pCa 10 to 7.5, a small decrease from pCa 7.5 to 5.5, and a plateau above pCa 5.5.

the native conformation observed in ELISA. mAb 3H12 does not react to N165 in Western blot or ELISA, indicating its epitope is outside of the T1 segment in the C-terminal T2 region.

Binding affinities of those mAb probes to TnT8e16 were compared between the Zn^{2+}-bound and EDTA-apo states to investigate the metal-Tx binding-induced conformational changes.

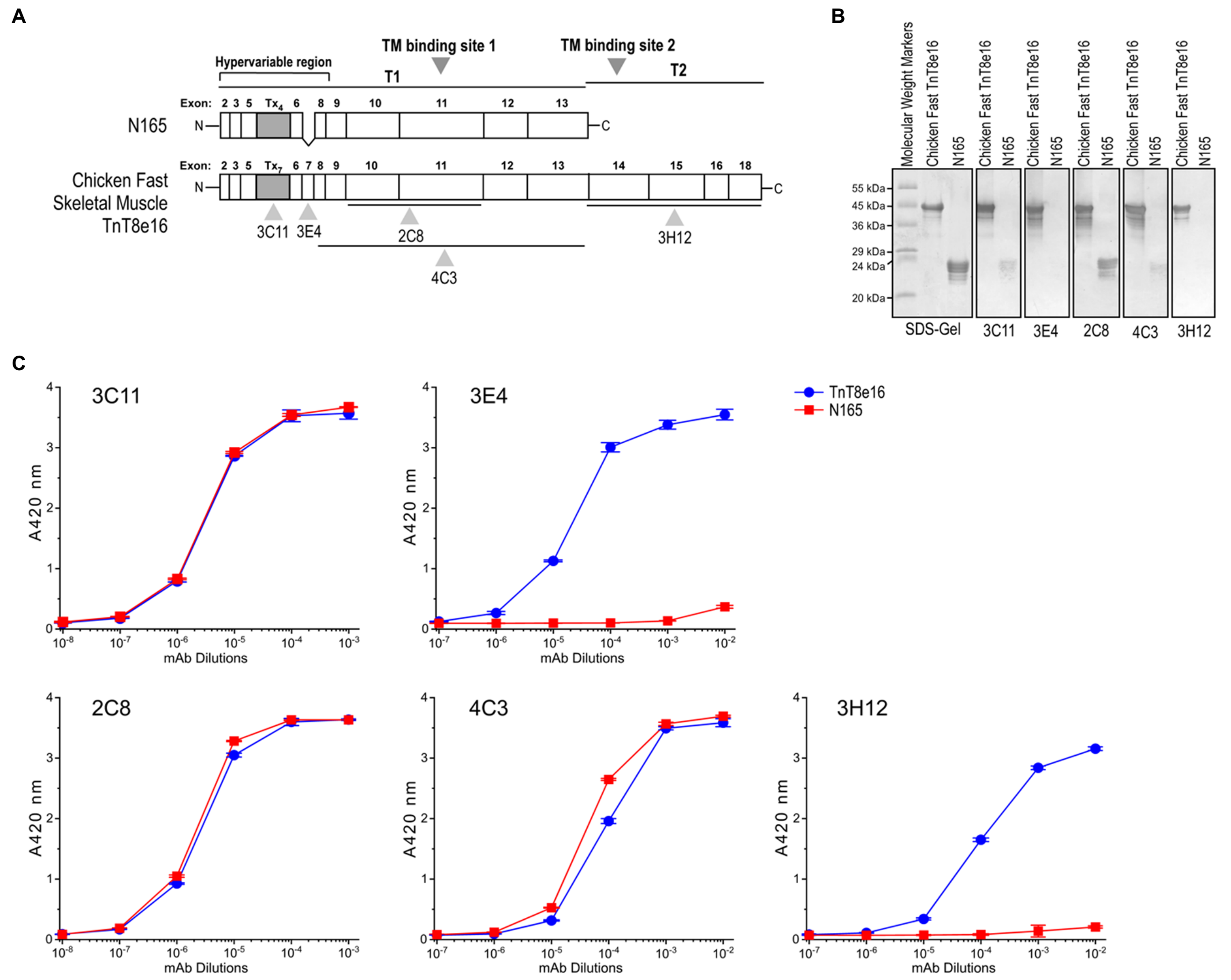

FIGURE 7 | Linear structure of chicken fast skeletal muscle TnT8e16 and epitope mapping of anti-TnT mAbs. **(A)** Locations of the epitopes recognized by anti-TnT mAbs used in the present study are indicated on a linear map of chicken fast TnT8e16. The Tx segment of chicken fast TnT, consisting of seven repeated H(E/A) EAH transition metal binding motifs, is encoded by alternatively-spliced exons. **(B)** Western blotting and **(C)** ELISA using intact chicken TnT8e16 and N-terminal T1 fragment N165 demonstrated that mAbs 2C8, 4C3, and 3C11 epitopes are contained within the N165 peptide, while the 3H12 epitope is outside of N165. mAb 3E4 had no reaction with N165 due to the lack of exon 7-encoded segment, serving as a background control.

Owing to the large number of site-specific mAbs available, we were able to map conformational changes directly at the Tx segment as well as highlight ligand-induced effects felt further from this domain. mAb 3C11 displayed a clear detection of the local conformational effect of Zn^{2+} binding on the Tx cluster, whereby which the affinity of mAb 3C11 was significantly decreased relative to the EDTA-apo control (**Figure 8A**), as previously observed in other anti-Tx mAbs (Wang and Jin, 1998). The binding of mAb 3E4 against a closely downstream epitope also displayed a decrease in affinity with Zn^{2+} binding, though the effect was less dramatic, indicating a propagated conformational change (**Figure 8B**).

Interestingly, mAbs 2C8 and 4C3 recognizing epitopes further downstream detected similarly increased affinities to TnT8e16 in metal-Tx-bound state than that to the EDTA-apo state (**Figures 8C,D**). This effect suggests the entire T1 segment may be highly flexible and responds with metal ion binding to change conformation and function.

The results also indicate that mAbs raised during immunizations may differentiate to have their variable regions fit with either metal-bound or metal-free state of TnT8e16. Since the antigenic epitopes are presented to the B lymphocytes in short peptides, and the 2C8 and 4C3 epitopes are remote from the N-terminal Tx segment (**Figure 7A**), the yield of mAbs with higher affinity for the metal bound state indicates that the metal-Tx binding induced conformational reconfiguration in the middle region of avian pectoral muscle TnT reflects an intrinsic property present in isolated antigenic peptides.

In contrast, the affinity of mAb 3H12 did not change with the binding of Zn^{2+} to the N-terminal Tx element (**Figure 8E**).

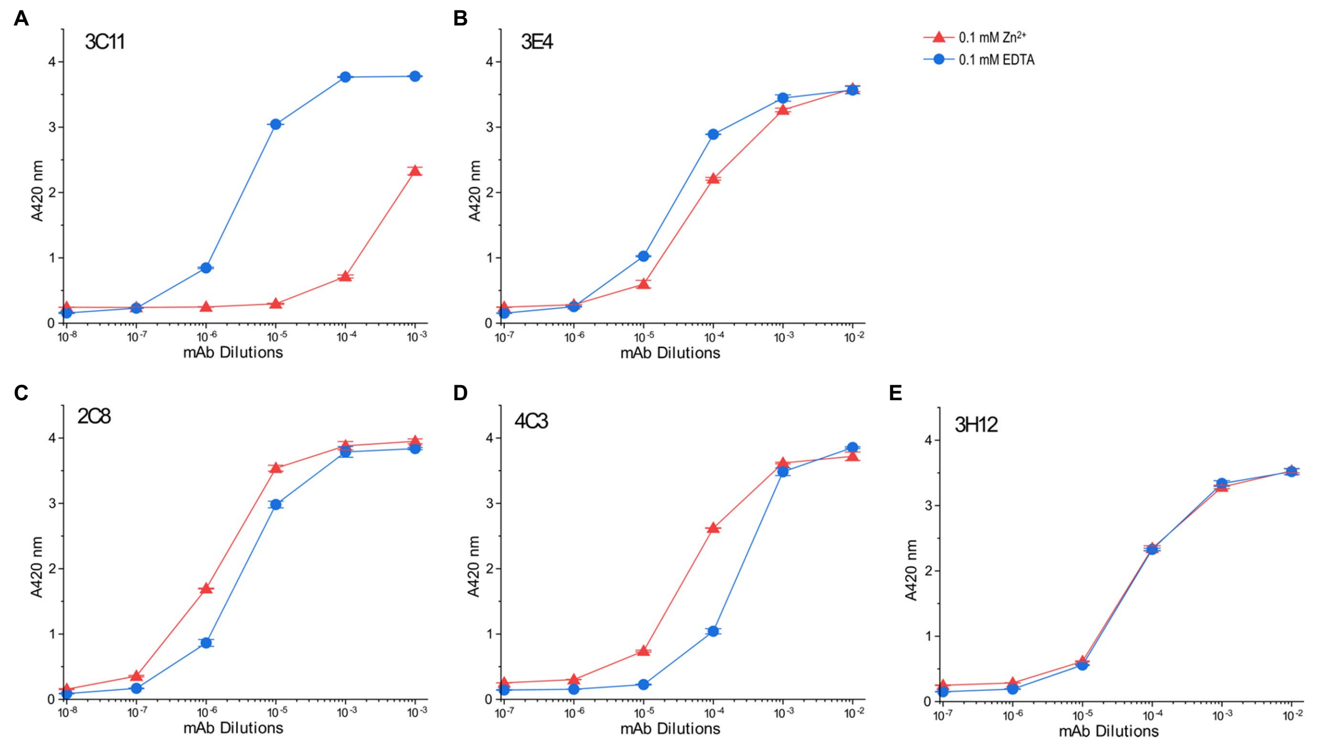

FIGURE 8 | Conformational effect of metal ion binding to chicken fast skeletal muscle TnT8e16 detected by ELISA epitope analysis. **(A)** Zn^{2+}-binding to the N-terminal Tx segment of TnT8e16 resulted in a dramatic decrease in the affinity of anti-Tx mAb 3C11 as compared to the ethylenediaminetetraacetic acid (EDTA) control. **(B)** mAb 3E4 raised against an epitope related the exon 7-encoded segment downstream of the Tx metal binding site also showed decreased affinity with the binding of Zn^{2+}, though less dramatic, reflecting conformational effects propagated from the metal-Tx binding. **(C)** Zn^{2+} binding to the Tx segment enhanced the binding of mAb 2C8 against the exons 10–11 encoded segment further downstream in comparison to the EDTA control. **(D)** mAb 4C3 shows an effect similar to that of mAb 2C8. **(E)** mAb 3H12 against an epitope in the T2 domain of TnT8e16 remote from the Tx segment did not detect any Zn^{2+} binding-induced conformational change. In addition to reflecting that the T2 domain of TnT may conform largely independent of the N-terminal variable region, the result served as a protein coating control.

The epitope of mAb 3H12 is contained within the C-terminal T2 segment, remote from the Tx region, implying that the C-terminal T2 domain conforms independently of the T1 domain and is insensitive to metal ion-Tx-binding induced conformational changes. The results of mAb 3H12 binding also confirm consistent protein coating regardless of buffer conditions, serving as a control and validating the ELISA system for use in the comparison of anti-TnT8e16 mAbs.

DISCUSSION

The methods and results described the present study highlight the utility of mAbs as site-specific probes to study protein conformation and changes. Our goal is to provide a framework for designing experiments, which measure changes both locally at the effector site as well as at remote allosteric regions. We employed two subunits of the troponin complex, TnC and TnT, to test the effects of metal ligand binding and demonstrate this novel approach in ELISA and LSPR. Several points on the methodology as well as findings on TnC and TnT structure–function relationships are summarized as follows.

mAbs As Conformational Probes to Study Protein Structure–Function Relationships

The use of antibodies to measure epitopic structure and conformational changes of proteins has many advantages. Typically, only small amounts of protein are required for such assays, and no protein labeling is required, avoiding bias in the results. Furthermore, the results of our study illustrate how mAb-based structural epitope assays can be designed in both high throughput, semi-quantitative (ELISA), and kinetically quantitative (LSPR) manners. Of particular interest is whether protein structure and conformation, when perturbed, change in a gradual or quantum fashion. For example, the pattern of changing affinity of anti-TnC mAbs with changes in pCa shown in the present study may reflect how troponin conformation responds to the rising of intracellular Ca^{2+} during the activation of muscle contraction. Although the results may be reflective of an averaging effect at the surface of the microtiter plate or LSPR chip, whereby which at threshold pCa levels, some TnCs are Ca^{2+}-bound while others are not, the condition is similar to that of TnC immobilized in myofilament and is therefore physiologically informative.

Crucial to the execution of the approaches is the availability of a range of mAbs raised against different portions of the protein of interest. With the advent of hybridoma technology, there is an ability to raise a large number of hybridoma clones in a single immunization and then screen for mAbs of various epitope specificity. Many commonly available mAbs against various proteins of interests can also be evaluated for use as conformational probes in the approaches described in the present study.

The immunogenicity of epitope structure of proteins may limit the ability to develop mAbs against certain parts of a protein, and there is a need to map the epitopes recognized by available mAbs in order to design an informative study. Still, once characterized, specific mAbs possess high utility and can be adapted to many study designs. To further optimize study design, one can take advantage of the high-throughput nature of ELISA to perform a broad screening of available mAbs, mapping epitopes, optimizing dilutions, and testing a large range of biochemical, physiological, and pathological conditions which may alter protein structure. LSPR can be of complementary use to provide a quantitative measurement of antibody affinity once study conditions have been determined, and the data in tandem give a holistic picture of a given protein's structure and serve to independently validate results. Main features of the ELISA and LSPR approaches are summarized in **Table 1**.

Ca^{2+} and Mg^{2+} Modulate Local and Remote Conformational Changes in TnC

TnC belongs to the calmodulin family of Ca^{2+}-binding proteins, and the data obtained in the present study demonstrate how Ca^{2+} binding to the N domain of fast TnC induces conformational modulations which can be clearly displayed as changes in the affinity of mAb 4E7 (**Figure 5A**). LSPR data confirm the results of ELISA with quantitative antibody association and dissociation rates (**Figure 6**).

An interesting observation is that Mg^{2+} binding to the C domain sufficiently flexes the N domain to induce measurable changes (**Figure 5A**). On the other hand, Ca^{2+} binding to the N domain does not dramatically alter the molecular conformation of C domain, as shown by the relatively small change in the affinity of mAb 2D10 (**Figure 5B**). It is also worth noting that while the conformational cross talk between the N and C domains of fast TnC is anticipated to transmit *via* the central helical linker (**Figure 4B**), the helix *per se* seems to have no significant change in epitopic conformation as shown by the lack of change in mAb 2C3 affinity (**Figure 5C**).

Since it is not possible through our studies, both ELISA and LSPR, to distinguish the ligand-induced conformational changes of a single protein, we must consider our data to be the result of an averaging of the population of TnC's bound and reflective of TnC-Ca^{2+} binding at equilibrium, whereby which at an intermediate pCa, some TnC's may be ion-bound while others are not. In our work, we consider that TnC-Ca^{2+} binding during muscle fiber activation arising from the increase cytosolic Ca^{2+} models a similar situation, with muscle fiber activation resulting from the conformational change of multiple troponin repeats along the thin filament. Our observed feature of the three phase responses of fast TnC to rising [Ca^{2+}] (**Figure 6D**) may reflect the contractile kinetics of myofilaments with physiological and pathological significance.

TABLE 1 | Comparison of advantages and disadvantages of ELISA vs. localized surface plasmon resonance (LSPR) technology.

ELISA	LSPR
Higher through-put using microplates	Lower through-put
Provides only endpoint monoclonal antibodies (mAb) binding	Provides estimation of mAb kinetic on- and off-rates
Buffer change possible in each step of assay	Buffer change possible in each step of assay
Assays run on multiple mAb populations in parallel	Assays run on single mAb population that is regenerated
No plate regeneration necessary	Background signal reduction and chip regeneration optimization crucial for quality data
Uses standard microplate readers and lower cost microtitering plates	Requires specialized instrument and higher cost LSPR chips
Useful for broad screening of multiple assay conditions and mAbs	Useful for quantitative and kinetic validation of single mAb-antigen interaction

The Unique Transition Metal Binding Cluster Tx in Avian Flight Muscles and Potentially Functional Role of Metal-Ion Induced Conformational Modulation

Adult pectoral muscle-specific fast skeletal muscle TnT in *Galliformes* birds, represented by chicken TnT8e16, contains a unique transition metal ion binding Tx segment that can be targeted to induce local and remote conformational changes in TnT. Using a battery of site-specific anti-TnT8e16 mAbs, we were able to investigate epitopic conformational changes at five different points (**Figure 7A**) for how metal ion-Tx binding alters the structure and function of TnT.

While the dramatically decreased affinity of the anti-Tx mAb 3C11 in 0.1 mM $ZnCl_2$ (**Figure 8A**) confirms previous observation that metal binding significantly alters the local conformation of the Tx segment, mAb 3E4 against a nearby epitope (**Figure 7A**) detected a weaker secondary effect propagated from the Tx site (**Figure 8B**), demonstrating the conformational modulatory role of Tx-metal binding.

Monoclonal antibodies 2C8 and 4C3 against epitopes in the middle region of TnT (**Figure 7A**) both detected metal binding-induced conformational changes (**Figures 8C,D**). In contrast to the metal-binding induced decreases in the affinities of anti-Tx mAb 3C11 and mAb 3E4 against a nearby epitope, the binding of Zn^{2+} to the N-terminal Tx segment induced increased affinities for mAbs 2C8 and 4C3. This finding suggests that Zn^{2+} binding to the Tx segment likely increases the flexibility of the middle region of TnT, allowing increased compliance and fitting to the variable region of the mAb probes. The alternative splicing regulated Tx segment is specifically expressed adult avian flight muscles. The data may imply that the trace amount of Zn^{2+} in avian pectoral muscle cells may bind to Tx to produce a remote conformational effect on the function of the TM binding site 1 in the T1 region with functional importance, a hypothesis worth further investigation.

The anti-T2 region mAb 3H12 did not detect any conformational change (**Figure 8E**). Therefore, the N-terminal originated conformational modulations seem predominantly through changes in the T1 region (**Figure 7A**).

High Throughput ELISA mAb Epitope Confirmational Analysis

Enzyme-linked immunosorbent assay is a high throughput, well-established methodology platform using microtiter plates of 96- or 384-well format of which the former is commonly used with standard plate readers. Even with manual operations, a trained operator can readily handle 4–6 plate in daily assays of several hundreds of samples or testing conditions. The steps of microtiter plate ELISA can be automated by using a plate washer and a multi-channel sample handler to maximize the high throughout benefit.

The ELISA mAb conformational analysis described in the present study provides a generally practical approach to conduct high throughput investigation on protein structure–function relationships and ligand-induced functional changes in various proteins. The assay can be done in physiological buffers to mimic *in vivo* conditions. One valuable feature of the microtiter plate assay is that the buffer and environmental conditions can be different for the protein coating, ligand binding, antibody incubation, and washing steps to compensate for the solubility of reagents and optimal temperature and pH of the reactions. Specific interactions identified using high throughput ELISA screening can be further investigated using more quantitative or high resolution but low throughput approaches for in depth characterization.

Broader Applications

Protein conformation is directly related to function. The mAb epitope conformational analysis approach can be considered for various applications in addition to myofilament protein studies. For example, while the current work focused on ligand-induced changes in the ion-binding subunits of troponin, N-terminal phosphorylation of cardiac TnI is a well-documented phenomenon with functional effects (Solaro et al., 1976), and phospho-specific mAbs have been developed to assess phosphorylation states (Al-Hillawi et al., 1998). Previous work from our lab has shown that N-terminal phosphorylation or restrictive truncation induced conformational changes in a remote region of cardiac TnI are detectable *via* an mAb probe (Akhter et al., 2012). Future directions may focus on understanding how TnI conformation changes with phosphorylation and what role this plays in the inhibitory function of cardiac TnI.

Pathogenic mutations represent another avenue with implications for human health. Disease-causing mutations in a protein may not be directly at the functional site responsible for the disease phenotype but instead may act through remote or global conformational effects. Therefore, one can use mAb conformational analysis to detect such effect of pathogenic mutations of a protein and obtain insights into possible therapeutic intervention.

Comparing the mAb epitope analysis with other methods for conformational studies, as well as combining ELISA's high throughput nature with LSPR kinetic analysis, another example for broader applications of the mAb epitope conformational analysis is drug screening. With a conformationally sensitive mAb against the target protein, ELISA can sensitively detect conformational changes induced by ligand binding. The sensitivity can be increased by using combinations of two or more mAbs against different epitopes or use a polyclonal antibody at proper dilution. Upon identification of promising compounds that induce conformational changes in the target protein, biochemical, cellular, and organ level functional studies can be conducted to further select candidates for therapeutic development.

DATA AVAILABILITY STATEMENT

The original contributions presented in the study are included in the article/supplementary material; further inquiries can be directed to the corresponding author.

AUTHOR CONTRIBUTIONS

MR designed and conducted the experiments, analyzed results, drafted the manuscript and figures, and edited and approved the submission. J-PJ conceived the research, designed the experiments, drafted the manuscript and figures, and edited and approved the submission. All authors contributed to the article and approved the submitted version.

FUNDING

This study was supported in part by grants from the National Institutes of Health (HL127691 and HL138007 to J-PJ).

ACKNOWLEDGMENTS

We thank Dr. Han-Zhong Feng for providing the pCa buffers.

REFERENCES

Akhter, S., Zhang, Z., and Jin, J. P. (2012). The heart-specific NH_2-terminal extension regulates the molecular conformation and function of cardiac troponin I. American journal of physiology. *Heart Circ. Physiol.* 302, H923–H933. doi: 10.1152/ajpheart.00637.2011

Alberts, B., Johnson, A., Lewis, J., Raff, M., Roberts, K., and Walter, P. (2002). *Molecular Biology of the Cell. 4th Edn.* New York: Garland Science.

Al-Hillawi, E., Chilton, D., Trayer, I. P., and Cummins, P. (1998). Phosphorylation-specific antibodies for human cardiac troponin-I. *Eur. J. Biochem.* 256, 535–540. doi: 10.1046/j.1432-1327.1998.2560535.x

Avalos, A. M., and Ploegh, H. L. (2014). Early BCR events and antigen capture, processing, and loading on MHC class II on B cells. *Front. Immunol.* 5:92. doi: 10.3389/fimmu.2014.00092

Bhasin, M., and Raghava, G. P. S. (2006). Computational methods in genome research. *Appl. Mycol. Biotechnol.* 6, 179–207. doi: 10.1016/S1874-5334(06)80011-0

Biesiadecki, B. J., and Jin, J.-P. (2002). Exon skipping in cardiac troponin T of turkeys with inherited dilated cardiomyopathy. *J. Biol. Chem.* 277, 18459–18468. doi: 10.1074/jbc.M200788200

Chong, S. M., and Jin, J.-P. (2009). To investigate protein evolution by detecting suppressed epitope structures. *J. Mol. Evol.* 68, 448–460. doi: 10.1038/jid.2014.371

Feng, H.-Z., and Jin, J.-P. (2020). High efficiency preparation of skinned mouse cardiac muscle strips from cryosections for contractility studies. *Exp. Physiol.* 105, 1869–1881. doi: 10.1113/EP088521

Gordon, A. M., Homsher, E., and Regnier, M. (2000). Regulation of contraction in striated muscle. *Physiol. Rev.* 80, 853–924. doi: 10.1152/physrev.2000.80.2.853

Grabarek, Z. (2011). Insights into modulation of calcium signaling by magnesium in calmodulin, troponin C and related EF-hand proteins. *Biochem. Biophys. Acta* 1813, 913–921. doi: 10.1016/j.bbamcr.2011.01.017

Jin, J.-P., and Chong, S. M. (2010). Localization of the two tropomyosin-binding sites of troponin T. *Arch. Biochem. Biophys.* 500, 144–150. doi: 10.1016/j.abb.2010.06.001

Jin, J.-P., Chong, S. M., and Hossain, M. M. (2007). Microtiter plate monoclonal antibody epitope analysis of Ca^{2+}- and Mg^{2+}-induced conformational changes in troponin C. *Arch. Biochem. Biophys.* 466, 1–7. doi: 10.1016/j.abb.2007.07.021

Jin, J.-P., and Root, D. D. (2000). Modulation of troponin T molecular conformation and flexibility by metal ion binding to the NH_2-terminal variable region. *Biochemistry* 39, 11702–11713. doi: 10.1021/bi9927437

Jin, J.-P., and Smillie, L. B. (1994). An unusual metal-binding cluster found exclusively in the avian breast muscle troponin T of Galliformes and Craciformes. *FEBS Lett.* 341, 135–140. doi: 10.1016/0014-5793(94)80256-4

Jin, J.-P., Zhang, Z., and Bautista, J. A. (2008). Isoform diversity, regulation, and functional adaptation of troponin and calponin. *Crit. Rev. Eukaryot. Gene Expr.* 18, 93–124. doi: 10.1615/critreveukargeneexpr.v18.i2.10

Köhler, G., and Milstein, C. (1975). Continuous cultures of fused cells secreting antibody of predefined specificity. *Nature* 256, 495–497. doi: 10.1038/256495a0

Leavis, P. C., and Kraft, E. L. (1978). Calcium binding to cardiac troponin C. *Arch. Biochem. Biophys.* 186, 411–415. doi: 10.1016/0003-9861(78)90453-8

Liu, R. (2016). Calponin and Cytoskeleton Dynamics in Macrophage Functions and the Pathogenesis of Atherosclerosis. Dissertation. Detroit (MI): Wayne State University.

Liu, H. L., and Hsu, J. P. (2005). Recent developments in structural proteomics for protein structure determination. *Proteomics* 5, 2056–2068. doi: 10.1002/pmic.200401104

Myszka, D. G., Morton, T. A., Doyle, M. L., and Chaiken, I. M. (1997). Kinetic analysis of a protein antigen-antibody interaction limited by mass transport on an optical biosensor. *Biophys. Chem.* 64, 127–137. doi: 10.1016/S0301-4622(96)02230-2

Ogut, O., and Jin, J.-P. (1996). Expression, zinc-affinity purification, and characterization of a novel metal-binding cluster in troponin T: metal-stabilized α-helical structure and effects of the NH_2-terminal variable region on the conformation of intact troponin T and its association. *Biochemistry* 35, 16581–16590. doi: 10.1021/bi961712y

Ogut, O., and Jin, J.-P. (1998). Developmentally regulated, alternative RNA splicing-generated pectoral muscle-specific troponin T isoforms and role of the NH_2-terminal hypervariable region in the tolerance to acidosis. *J. Biochem.* 273, 27858–27866. doi: 10.1074/jbc.273.43.27858

Önell, A., and Andersson, K. (2005). Kinetic determinations of molecular interactions using Biacore—minimum data requirements for efficient experimental design. *J. Mol. Recognit.* 18, 307–317. doi: 10.1002/jmr.745

Petryayeva, E., and Krull, U. J. (2011). Localized surface plasmon resonance: nanostructures, bioassays and biosensing—A review. *Anal. Chim. Acta* 706, 8–24. doi: 10.1016/j.aca.2011.08.020

Plested, J. S., Coull, P. A., and Gidney, M. A. J. (2003). ELISA. *Methods Mol. Med.* 71, 243–262. doi: 10.1385/1-59259-321-6:243

Potter, J. D., and Gergely, J. (1975). The calcium and magnesium binding sites on troponin and their role in the regulation of myofibrillar adenosine triphosphatase. *J. Biol. Chem.* 250, 4628–4633. doi: 10.1016/S0021-9258(19)41347-1

Putkey, J. A., Liu, W., and Sweeney, H. L. (1991). Function of the N-terminal calcium-binding sites in cardiac/slow troponin C assessed in fast skeletal muscle fibers. *J. Biochem.* 266, 14881–14884. doi: 10.1016/s0021-9258(18)98558-3

Raicu, V., and Singh, D. R. (2013). FRET spectrometry: a new tool for the determination of protein quaternary structure in living cells. *Biophys. J.* 105, 1937–1945. doi: 10.1016/j.bpj.2013.09.015

Rayani, K., Seffernick, J., Li, A. Y., Davis, J. P., Spuches, A. M., van Petegem, F., et al. (2021). Binding of calcium and magnesium to human cardiac troponin C. *J. Biol. Chem.* 296:100350. doi: 10.1016/j.jbc.2021.100350

Rich, R. L., and Myszka, D. G. (2010). "Extracting kinetic rate constants from binding responses," in *Label-Free Biosensors: Techniques and Applications*. ed. M. Cooper (Cambridge: Cambridge University Press), 85–109.

Robertson, S. P., Johnson, J. D., and Potter, J. D. (1981). The time-course of Ca^{2+} exchange with calmodulin, troponin, parvalbumin, and myosin in response to transient increases in Ca^{2+}. *Biophys. J.* 34, 559–569. doi: 10.1016/S0006-3495(81)84868-0

Sehnal, D., Bittrich, S., Deshpande, M., Svobodová, R., Berka, K., Bazgier, V., et al. (2021). Mol* viewer: modern web app for 3D visualization and analysis of large biomolecular structures. *Nucleic Acids Res.* 49, W431–W437. doi: 10.1093/nar/gkab314

Smillie, L. B., Golosinska, K., and Reinach, F. C. (1988). Sequences of complete cDNAs encoding four variants of chicken skeletal muscle troponin T. *J. Biol. Chem.* 263, 18816–18820. doi: 10.1016/s0021-9258(18)37355-1

Solaro, R. J., Moir, A. J. G., and Perry, S. V. (1976). Phosphorylation of troponin I and the inotropic effect of adrenaline in the perfused rabbit heart. *Nature* 262, 615–617. doi: 10.1038/262615a0

Sun, Y.-B., and Irving, M. (2010). The molecular basis of the steep force–calcium relation in heart muscle. *J. Mol. Cell. Cardiol.* 48, 859–865. doi: 10.1016/j.yjmcc.2009.11.019

van Eerd, J.-P., and Takahashi, K. (1975). The amino acid sequence of bovine cardiac troponin-C. Comparison with rabbit skeletal troponin-C. *Biochem. Biophys. Res. Commun.* 64, 122–127. doi: 10.1016/0006-291X(75)90227-2

Vinogradova, M. V., Stone, D. B., Malanina, G. G., Karatzaferi, C., Cooke, R., Mendelson, R. A., et al. (2005). Ca^{2+}-regulated structural changes in troponin. *Proc. Natl. Acad. Sci. U. S. A.* 102, 5038–5043. doi: 10.1073/pnas.0408882102

Wang, J., and Jin, J.-P. (1998). Conformational modulation of troponin T by configuration of the NH_2-terminal variable region and functional effects. *Biochemistry* 37, 14519–14528. doi: 10.1021/bi9812322

Wei, B., and Jin, J.-P. (2016). TNNT1, TNNT2, and TNNT3: isoform genes, regulation, and structure-function relationships. *Gene* 582, 1–13. doi: 10.1016/j.gene.2016.01.006.TNNT1

Wong, S., Feng, H.-Z., and Jin, J.-P. (2019). The evolutionarily conserved C-terminal peptide of troponin I is an independently configured regulatory structure to function as a myofilament Ca^{2+}-desensitizer. *J. Mol. Cell. Cardiol.* 136, 42–52. doi: 10.1016/J.YJMCC.2019.09.002

Zhang, Z., Akhter, S., Mottl, S., and Jin, J.-P. (2011). Calcium-regulated conformational change in the C-terminal end segment of troponin I and its binding to tropomyosin. *FEBS J.* 278, 3348–3359. doi: 10.1111/j.1742-4658.2011.08250.x

Zhang, Z., Biesiadecki, B. J., and Jin, J.-P. (2006). Selective deletion of the NH_2-terminal variable region of cardiac troponin T in ischemia reperfusion by myofibril-associated μ-calpain cleavage. *Biochemistry* 45, 11681–11694. doi: 10.1021/bi060273s

Conflict of Interest: The authors declare that the research was conducted in the absence of any commercial or financial relationships that could be construed as a potential conflict of interest.

frontiers | Frontiers in Physiology

ORIGINAL RESEARCH
published: 01 April 2022
doi: 10.3389/fphys.2022.834705

Targeting Muscle-Resident Single Cells Through *in vivo* Electro-Enhanced Plasmid Transfer in Healthy and Compromised Skeletal Muscle

Francesca Florio[1,2], Silvia Accordini[1], Michela Libergoli[1,2] and Stefano Biressi[1,2]*

[1] Department of Cellular, Computational and Integrative Biology (CIBIO), University of Trento, Trento, Italy, [2] Dulbecco Telethon Institute at University of Trento, Trento, Italy

Skeletal muscle is composed of syncytial muscle fibers, and by various mononucleated cellular types, such as muscle stem cells, immune cells, interstitial and stromal progenitors. These cell populations play a crucial role during muscle regeneration, and alterations of their phenotypic properties have been associated with defective repair and fibrosis in aging and dystrophic muscle. Studies involving *in vivo* gene modulation are valuable to investigate the mechanisms underlining cell function and dysfunction in complex pathophysiological settings. Electro-enhanced transfer of plasmids using square-wave generating devices represents a cost-effective approach that is widely used to transport DNA to muscle fibers efficiently. Still, it is not clear if this method can also be applied to mononuclear cells present in muscle. We demonstrate here that it is possible to efficiently deliver DNA into different muscle–resident cell populations *in vivo*. We evaluated the efficiency of this approach not only in healthy muscle but also in muscles of aging and dystrophic animal models. As an exemplificative application of this method, we used a strategy relying on a reporter gene-based plasmid containing regulatory sequences from the *collagen 1 locus*, and we determined collagen expression in various cell types reportedly involved in the production of fibrotic tissue in the dystrophic settings. The results enclosed in this manuscript reveal the suitability in applying electro-enhanced transfer of plasmid DNA to mononucleated muscle-resident cells to get insights into the molecular events governing diseased muscle physiology.

Keywords: muscle stem cells, endothelial cells, fibroadipogenic progenitors, electroporation, collagen, muscular dystrophy, aging

Edited by:
Radbod Darabi,
University of Texas Health Science Center at Houston, United States

Reviewed by:
Antonio Serrano,
Pompeu Fabra University, Spain
Lucas Robert Smith,
University of California, Davis, United States
Yvan Torrente,
University of Milan, Italy

Correspondence:
Stefano Biressi
stefano.biressi@unitn.it

Specialty section:
This article was submitted to Striated Muscle Physiology, a section of the journal Frontiers in Physiology

Received: *13 December 2021*
Accepted: *25 February 2022*
Published: *01 April 2022*

Citation:
Florio F, Accordini S, Libergoli M and Biressi S (2022) Targeting Muscle-Resident Single Cells Through in vivo Electro-Enhanced Plasmid Transfer in Healthy and Compromised Skeletal Muscle. Front. Physiol. 13:834705. doi: 10.3389/fphys.2022.834705

INTRODUCTION

The basic functional cell units of skeletal muscle are the myofibers, which consists of single elongated multinucleated cells formed during development following proliferation and fusion process of muscle progenitor cells (Biressi et al., 2007; Bryson-Richardson and Currie, 2008; Comai and Tajbakhsh, 2014). Following injury, the skeletal muscle has a remarkable capacity to regenerate and restore its physiological tissue architecture and functionality. Skeletal muscle regeneration consists of several highly coordinated cellular processes, which lead to the formation of tissue similar to the uninjured muscle (Kuang and Rudnicki, 2008; Baghdadi and Tajbakhsh, 2018). Muscle regeneration requires the orchestrated contribution of at least two different classes of cellular players in the tissue: (1) the muscle stem cells (also known as muscle satellite cells, MuSCs), which are quiescent in uninjured muscle, but become activated after an injury, proliferate and eventually fuse to differentiate into new myofibers (Scharner and Zammit, 2011); (2) support cells, which consist of a heterogeneous group of cells found in the interstitial spaces between myofibers or associated to the vasculature (Wosczyna and Rando, 2018). They include tissue-resident cells and cells infiltrating from the circulation, and the disruption of their normal contributions has been associated with incomplete regeneration. This aspect is highlighted by mesenchymal stromal cells, called fibroadipogenic progenitors (FAPs), which are required for muscle regeneration and maintenance (Joe et al., 2010; Uezumi et al., 2010; Wosczyna et al., 2019). Moreover, experiments conducted by multiple groups have identified endothelial cells, pericytes and different subpopulations of immune cells, including macrophages, eosinophils and regulatory T cells, as necessary components for proper MuSCs function and effective muscle restoration (Shen et al., 2008; Burzyn et al., 2013; Heredia et al., 2013; Kostallari et al., 2015; Lemos et al., 2015; Latroche et al., 2017; Liu et al., 2017; Verma et al., 2018).

The homeostatic importance of skeletal muscle regeneration appears clear when considering physiological aging or genetic pathologies such as muscular dystrophies. Both intrinsic and extrinsic cues negatively impact MuSCs regenerative properties in old muscles (Muñoz-Cánoves et al., 2020; Rando and Jones, 2021). MuSCs from dystrophic muscles reportedly present several abnormalities (Morgan and Cohen, 1974; Ionasescu and Ionasescu, 1982; Blau et al., 1983; Delaporte et al., 1984, 1990; Jasmin et al., 1984; Melone et al., 1999; Furling et al., 2001; Alexakis et al., 2007; Rhoads et al., 2013; Biressi et al., 2014; Dumont et al., 2015; Pessina et al., 2015). The functional interactions between MuSCs and support cells and among different subpopulations of inflammatory and stromal cells also appear to be compromised in aging and diseased muscle (Villalta et al., 2009; Mozzetta et al., 2013; Wang et al., 2015). These alterations are likely contributing to the defective regeneration and lead to the chronic accumulation of inert fibrotic tissue that is observable in aging and dystrophic muscle (Serrano and Munoz-Canoves, 2010). Little is known about the mechanisms underlining fibrosis in diseased muscle tissue, and different cellular sources have been reported to contribute to the excessive accumulation of extracellular matrix components. FAPs (or their derivatives) have been proposed as major contributors (Uezumi et al., 2011; Mueller et al., 2016). However, an increasing amount of evidence indicates that other cell types can potentially contribute to fibrosis. MuSCs have the propensity to adopt fibrogenic phenotypes in the setting of both aged and dystrophic muscle (Brack et al., 2007; Biressi et al., 2014; Pessina et al., 2015). This parallels a similar behavior documented for endothelial cells and cells belonging to the hematopoietic lineage in the dystrophic settings (Pessina et al., 2015; Wang et al., 2016).

The *in vivo* alteration of gene expression is a powerful tool to investigate muscle biology, including the properties of MuSCs and other muscle cell populations. Genetic or pharmacological down- and up-regulation of various genes have been widely exploited to get insights into the basic mechanisms controlling productive regeneration in healthy muscle and pathological defective repair. Therapeutic gene expression and nucleic acid delivery have been induced in different animal models to restore physiological gene expression and counteract the progression of various muscle genetic diseases, and recently also entered the clinical arena (Bengtsson et al., 2016; Chamberlain and Chamberlain, 2017; Schneider and Aartsma-Rus, 2021). Genetic manipulation by transient or stable transfer of nucleic acids in the tissues of live organisms has been applied to skeletal muscle by different approaches, involving both viral vectors and non-viral strategies (Braun, 2008; Hollinger and Chamberlain, 2015). Among the non-viral strategies, electro-enhanced plasmid transfer (i.e., electroporation) has gained a special position over the last three decades due to its simplicity, safety, and cost-effectiveness that perfectly suit the time and practical constraints typical of the academic research. *In vivo* electro-enhanced plasmid transfer consists of a physical method of gene delivery relying on the cellular uptake of plasmid DNA facilitated by an electric field transmitted by electrodes placed on each side of the injection site and connected to a square-wave pulse generator (Somiari et al., 2000; Bloquel et al., 2004; Sokołowska and Błachnio-Zabielska, 2019). Specialized technical skills or complex instrumentation are not needed to electroporate skeletal muscle. Therefore, it is not surprising that electro-enhanced plasmid delivery has become one of the elective methods to be used in gain- or loss-of-function studies targeting skeletal muscle, particularly at the preclinical laboratory level.

Noteworthy, the great majority of the studies in this field have been centered on the delivery of nucleic acids to multinucleated muscle fibers, and little focus has been given to the mononucleated cells that are coexisting with mature fibers in the muscle tissue. Lentiviral vectors have been reported to target muscle stem cells (Kobinger et al., 2003; Kimura et al., 2010; Jonuschies et al., 2014). Nevertheless, conflicting information is available for non-viral delivery methods, such as electroporation (Peng et al., 2005; Wong et al., 2005). Despite circumstantial evidence in immune and interstitial cells, a systematic quantification of the efficiency of electro-enhanced plasmid transfer to muscle-resident mononucleated cells that are different from MuSCs still needs to be performed (Dupuis et al., 2000; Grønevik et al., 2003; Ratanamart et al., 2010). Through a cytofluorimetric analysis based on well-established lineage markers, we demonstrate here that it is possible to target various defined mononucleated cell subtypes (i.e., FAPs, endothelial cells, cells of the hematopoietic lineage, MuSCs) that reside in skeletal muscles by using an electro-enhanced plasmid delivery protocol. Notably, we characterized the process of electro-enhanced DNA transfer to mononucleated cells in healthy muscle and muscles affected by alterations in structure and function, such as muscles of aging and dystrophic animal models. Moreover, by applying a strategy relying on the electroporation of a reporter gene-expressing plasmid, we determined the extent of collagen expression in various cell types present in fibrotic dystrophic and old muscles. The results enclosed in this manuscript reveal the suitability of electro-enhanced DNA delivery in targeting muscle-resident cells to get insights into the cellular and molecular events governing diseased muscle physiology.

MATERIALS AND METHODS

Mice

Animals were maintained with access to food and water *ad libitum* and kept at a constant temperature on a 12:12 h light/dark cycle. *C57BL/6J* mice (The Jackson Laboratory, no. 000664) were used as *wild type* animals. B6Ros.Cg-$Dmd^{mdx-4Cv/J}$ mice (The Jackson Laboratory, no. 002378, herein referred to as mdx^{4Cv}) were used as dystrophic mice. Animal care and experimental procedures were conducted in accordance with the Ethical Committee of the University of Trento and were approved by the Italian Ministry of Health (Authorization No. 62/2020-PR).

In vivo Gene Transfer and Electroporation

Tibialis anterior (*TA*) muscles were electroporated as previously described with minor modifications (Magarò et al., 2021). Briefly, mice were anesthetized by inhaled isoflurane, the hindlimb skin was shaved and disinfected with 70% ethanol. Plasmids were injected with a 0.5 ml insulin syringe through a 27-gauge needle into *TA* muscles in a constant volume of 40 μL. Plasmid DNA was purified using endofree plasmid kits (Qiagen) and dissolved in sterile PBS at the concentration of 2 μg/μL. The following expression vectors were used: pCMV-LacZ (Clontech), pEGFP-N3 (Clontech, hereinafter referred to as GFP), ptdTomato-N1 (Clontech, hereinafter referred to as tdTomato), pOBCol2.3-GFPemd (hereinafter referred to as Col1-GFP). pOBCol2.3-GFPemd was a gift from David Rowe (Addgene plasmid # 110210[1]). For specific experiments a mix of GFP- and tdTomato-expressing plasmids (in 10:1 ratio) or a mix of Col1-GFP- and tdTomato- expressing plasmids (in 10:1 ratio) was injected. Unless otherwise stated, PBS was injected in samples used as negative controls. Platinum plated 5 mm tweezer-style electrodes (BTX) were then applied over the muscle to encompass the injection area. Electrode jelly was used on the electrode plates to ensure conduction. Current was delivered 5 min after DNA injection as a constant current, square-wave pulse with a digital Stimulator (Intracel TSS20 Ovodyne electroporator combined with Intracel EP21 current amplifier). The characteristics of the electric field applied were 200 V/cm, 20 ms amplitude, 1 Hz, eight consecutive pulses. Two series of pulses were applied, one on the most proximal part of the *TA* and the other on the most distal one. An analgesic was administered subcutaneously at the end of the procedure. Animals were kept warm until recovery, and then returned to their cages. When indicated, mdx^{4Cv} *TA* muscles were injected with 25 μl of bovine hyaluronidase (H-4272; Sigma) at the concentration of ∼0.4 U/l in saline 2 h prior to plasmid injection and electroporation, as previously described (McMahon et al., 2001; Gollins et al., 2003; Molnar et al., 2004).

Muscle Injury

Mice were anesthetized with isoflurane, hindlimb skin was shaved, and 50 μl of cardiotoxin from *Naja pallida* snake venom (Latoxan) resuspended at the concentration of 0.1 mg/ml in PBS were injected into the mid-belly of *TA* muscles. Depending on the experiment, muscle damage was induced 1.5 days prior to electroporation or 1 week after electroporation.

Immunofluorescence

For immunofluorescence studies, muscles were fixed for 4 h using 0.5% paraformaldehyde and transferred to 30% sucrose overnight. Muscles were frozen in optimum cutting temperature compound (OCT) (Histo-Line Laboratories). Cryosections (8 μm) were fixed with 4% paraformaldehyde for 10 min at room temperature, and processed for immunofluorescence according to standard protocols with primary antibodies (rabbit anti-GFP, Invitrogen, 1: 500; rat anti-mouse F4/80, Biolegend, 1:50) followed by incubation with Alexa Fluor 488/594 donkey secondary antibodies (Invitrogen). Incubation for 10 min with 10 μg/ml Hoechst in PBS was used to stain the nuclei. Samples were mounted using Fluroshield histology mounting medium (Sigma).

X-Gal Staining

X-gal staining was used to detect the LacZ reporter gene expression after pCMV-LacZ plasmid injection and electroporation. Muscles were dissected 1 or 3 weeks after electroporation and fixed in 4% paraformaldehyde at 4°C for 15 min, then washed in PBS and stained at 37°C for 3-5 h in X-gal buffer [1 mg/ml 5 bromo-4-chloro-3-indolyl-β-D-galactoside, 5 mM $K_4Fe(CN)_6$, 5 mM $K_3Fe(CN)_6$, 2 mM $MgCl_2$ in PBS]. When the β-galactosidase (β-gal) was expressed by the muscles, a typical blue color was observed. The X-gal buffer was removed and muscles were washed in PBS prior to images acquisition.

Imaging

X-gal images were acquired using an optical stereomicroscope (MZ10F; Leica) and processed using LAS X software (Leica). The GFP and tdTomato intensities of dissected muscles and *in vivo* muscle were acquired using the Bruker *In Vivo* Xtreme I imaging system. Prior to the *in vivo* analysis, mice were anesthetized by inhaled isoflurane, the hindlimb skin was shaved and the animals were placed inside the instrument with the *TA* facing the camera. The GFP and tdTomato intensities were then evaluated with the Bruker MISE software as number of photons/sec/mm^2. Immunofluorescence images were acquired using a Zeiss Axio Observer Z1 optical microscope equipped with a monochrome camera (AxioCam 503 mono D).

Muscle Single Cells Isolation and Fluorescence-Activated Cell Sorting Analysis

Hindlimb muscles from young *C57BL/6J* (∼2 months-old), adult *C57BL/6J* (∼1 year-old), old *C57BL/6J* (∼24-26 months-old) and adult mdx^{4Cv} (∼1 year-old) mice were dissected 1,

---

[1] http://n2t.net/addgene:110210; RRID:Addgene_110210

2 or 3 weeks after the *in vivo* gene transfer and processed as previously described to obtain mononucleated cells (Liu et al., 2015). Muscles were washed in Wash Medium (Ham's F-10 supplemented with 10% FBS, 1% L-glutamine and 1% penicillin-streptomycin), added to Muscle Dissociation Buffer [500 U/ml collagenase II (Worthington Biochemical Corporation) prepared in Ham's F-10], minced with scissor, incubated in a 37°C water bath with agitation (70 rpm) for 40 min. After incubation samples were centrifuged at 500g for 5 min, and the pellet was dissolved in dispase (11 U/ml, GIBCO) and collagenase II (2000 U/ml) and triturated with a 10-ml serological pipette. Samples were incubated in a 37°C water bath with agitation (70 rpm) for 20 min, then passed through 18- and 19-gauge needles by using a 10-ml syringe to allow mechanical dissociation into single cells. Samples were centrifuged at 500g for 10 min at 4°C, the pellet was resuspended and filtered through a 40-μm nylon cell strainer (Euroclone), centrifuged at 500g for 10 min at 4°C, then resuspended in Wash Medium. Cells were incubated on a rotating wheel (10 rpm) for 45 min at 4°C with primary antibodies to mark FAPs, MuSCs, hematopoietic and endothelial cells. A list of fluorescence-activated cell sorting (FACS) antibodies used is enclosed in **Supplementary Table 1**. Samples were washed, APC Streptavidin (1:100, BioLegend) was added and samples were incubated on a rotating wheel (10 rpm) for 20 min at 4°C, then washed and resuspended in a sorting buffer (Wash Medium + PBS with 1.5 mM EDTA, 2% BSA, 1% L-glutamine and 1% penicillin-streptomycin, 1:1 ratio). Samples were finally filtered through cell strainer cap tubes (Thermo Fisher Scientific).

FACSAria III cell sorter (BD Biosciences) was used to analyze the uptake of the electroporated plasmids in mononucleated muscle cells. Physical parameters as forward scatter (FSC) and side scatter (SSC) were used to exclude cell clumps and debris. Hematopoietic cells were identified by positive selection with anti-CD45 antibody, endothelial cells were identified by positive selection with anti-CD31 antibody or negative selection with anti-CD45 antibody followed by positive selection with anti-CD31 antibody, MuSCs were identified by negative selection with anti-CD31, anti-CD45, anti-sca1 antibodies and positive selection with anti-vcam antibody (Liu et al., 2015), FAPs were identified by negative selection with anti-CD31 and anti-CD45 antibodies and positive selection with anti-sca1 antibody (Liu et al., 2015) (**Supplementary Figure 1A**). Control samples (i.e., sample injected with PBS and electroporated or samples not electroporated) were used in the FACS analysis to set gates specifically for *C57BL/6J* or mdx^{4Cv} samples to calculate the percentage of electroporated cells within each cell population. In the experiments with the Col1-GFP and tdTomato plasmids mix, a control sample was used to set the tdTomato^{+ve} (TOM^{+ve}) cells gates within each cell populations. TOM^{+ve} cells (i.e., electroporated cells) were then analyzed for the GFP expression (i.e., collagen1-GFP expression). The median values of the tdTomato and GFP intensities within the cell populations were calculated using the FlowJo software. The tdTomato intensity was used as a normalizer. For specific experiments, MuSCs, FAPs, and CD31^{+ve} cells were processed after sorting for RNA extraction and real time polymerase chain reaction (RT-PCR).

RNA Extraction and Quantitative Real-Time PCR

Total RNA was extracted from FACS isolated cells using TRIzol Reagent (Invitrogen) according to manufacturer's instructions. RNA was quantified using NanoDrop spectrophotometer and reverse transcribed using High Capacity cDNA Reverse Transcription Kit (Thermo Fisher Scientific). Gene expression was measured by quantitative RT-PCR using SYBR Green Master Mix (Thermo Fisher Scientific) and a C1000 Touch thermocycler-CFX96 Real Time System (Biorad). Primers spanning exon-exon junctions were used (col1a1 Fw: TCC GGC TCC TGC TCC TCT TA; col1a1 Rev: GTA TGC AGC TGA CTT CAG GGA TGT). The level of each transcript was measured using mouse HPRT (hypoxanthine-guanine phosphoribosyltransferase) mRNA levels as normalizer (mHPRT Fw: AAC TGG AAA GAA TGT CTT GAT TGT; mHPRT Rev: GAA TTT CAA ATC CAA CAA AGT CTG G).

Statistical Analysis

Unless otherwise stated, experiments presented here were repeated at least three times and quantitative data are presented as mean ± SEM. Statistical analysis was performed using GraphPad Prism 8. Unpaired Parametric Student's *t*-test (two-tailed) was performed for comparison between two groups. Statistical significance is expressed with the p-value (p), which is reported in each graph.

RESULTS

In vivo Electroporation of Skeletal Muscles' Mononuclear Cells

A major aim of this work is to describe to which extent mononucleated cells present in skeletal muscles are susceptible to electro-enhanced plasmid transfer. With this goal we injected a GFP-expressing plasmid in the *TA* muscle of adult *C57BL/6J* mice, we electroporated the injected muscles, and we measured the GFP intensity through the Bruker *In Vivo* Xtreme I imaging system at different time points after the plasmid injection. In agreement with previous reports, this approach resulted in a strong GFP signal 1 week after plasmid delivery (**Figure 1A** and **Supplementary Figure 2A**), which indicated that the electroporation effectively led to the plasmids uptake in the muscles. Moreover, our *in vivo* imaging analysis showed a clear GFP signal in the electroporated *C57BL/6J* mice compared to the negative controls from 1.5 days up to 6 weeks after electroporation, indicating a long-term permanence of the plasmid in electroporated muscles (**Supplementary Figures 2B,H**). After having assessed that our *in vivo* electroporation effectively leads to the plasmid uptake in the hindlimb muscles, we aimed to get insights on the specific cells that are capable of receiving and expressing the electroporated plasmid. A histological analysis performed on muscle sections of electroporated *C57BL/6J* mice revealed effective plasmid uptake by muscle fibers and by nearby mononucleated cells (**Figure 1B** and **Supplementary Figure 3A**).

A fraction of the targeted mononucleated cells resulted positive for the macrophage marker F/480. Nevertheless, numerous effectively electroporated mononucleated cells were F/480^{-ve} (**Figure 1B** and **Supplementary Figure 3A**). To further investigate the nature of these cells, we injected a tdTomato-expressing plasmid in the *TA* of adult *C57BL/6J* and electroporated the same muscles. Three weeks after the electroporation, muscles were dissected and enzymatically digested to obtain a suspension of mononucleated cells. Mononucleated cells were stained with antibodies directed against surface markers for the identification of specific cell populations by FACS analysis (**Supplementary Figure 1A**). Our cytofluorimetric analysis revealed that up to 31.0% of the total mononucleated cells expressed the plasmid (**Figure 1C**). Within the single cells, up to 29.9% of CD45^{+ve} cells, 41.9% of CD31^{+ve} cells, 53.4% of FAPs and 25.5% of MuSCs expressed the electroporated plasmid (**Figures 1D–G**). Differences among subpopulations were not statistically significant ($p > 0.05$). Negligible fluorescence was observed in control muscles injected with PBS and electroporated (**Figures 1C–G**). Plasmid uptake by muscle mononucleated cells was clear as early as 1.5 days after electroporation (**Supplementary Figures 2C–G**). This analysis demonstrates that, in addition to syncytial muscle fibers, it is possible to effectively target various muscle mononucleated cells through electro-enhanced plasmid transfer.

To further characterize the properties of electro-enhanced plasmid transfer to muscle mononucleated cells, we evaluated the efficiency of plasmid uptake after simultaneous injection of two distinct plasmids. *In vitro* co-electroporation of myotubes with two different plasmids results in the preferential uptake of both plasmids by the same cells (Sandri et al., 2003). In order to assess whether this preferential uptake is occurring also in mononucleated cells after electroporation *in vivo*, we injected adult *C57BL/6J* muscles with a mix of GFP- and tdTomato- expressing plasmids. The FACS analysis performed 1 week after the electroporation revealed that 80.7 to 95.9% of TOM^{+ve} cells also expressed the GFP plasmid in all the analyzed cell populations (i.e., total single cells, CD45^{+ve}CD31^{+ve} cells, FAPs and MuSCs), suggesting that those cells that are effectively electroporated have the tendency to uptake both plasmids (**Figures 1H–K** and **Supplementary Figures 3B–D** for negative controls).

In vivo Electroporation of Injured Muscles

Pre-treatement with muscle-damaging agents reportedly reduces the efficiency of whole muscle electroporation (Gollins et al., 2003). To assess if tissue damage could also affect plasmid uptake by mononucleated cells, we electroporated *C57BL/6J* muscles with the GFP-expressing plasmid 1.5 days after intramuscular injection of cardiotoxin. As expected, 6 days after electroporation, the GFP intensity measured *in vivo* through the Bruker *In Vivo* Xtreme I imaging system was reduced in the cardiotoxin-treated mice compared to uninjured mice (**Figure 2A**). This protocol also resulted in a significant decrease in the electroporation efficiency of all analyzed mononucleated cell populations (i.e., total single cells, CD45^{+ve} cells, CD31^{+ve} cells, and FAPs) except MuSCs, for which the analysis gave variable results (**Figures 2B–F**). Intriguingly, a comparable low efficiency of electroporation (1.9 ± 1.0% for total single cells, 1.4 ± 0.6% for CD45^{+ve} cells, 2.3 ± 2.4% for CD31^{+ve} cells, 3.5 ± 3.6% for FAPs, and 1.9 ± 1.7% for MuSCs) was also observed when cardiotoxin was injected 1 week after electroporation and the FACS analysis was performed after 2 additional weeks. This observation suggests that the integrity of the muscle is crucial for the electroporation outcome.

In vivo Electroporation of Dystrophic Muscles

The *mdx*^{4Cv} mouse model is one of the most widely used animal models to study Duchenne muscular dystrophy (DMD) (van Putten et al., 2020). Duchenne muscular dystrophy is characterized by chronic fiber necrosis and regeneration (Ciciliot and Schiaffino, 2010). Accumulation of fibrotic tissue characterizes *mdx*^{4Cv} muscles as compared with age-matched controls, and collagen depositions is becoming conspicuous with age paralleling muscle deterioration (Pastoret and Sebille, 1995). Other than contributing to the dystrophic phenotype, muscle fibrosis potentially represents a physical barrier to the effective exogenous material uptake, including drugs and cells which are meant for the disease treatment (Gargioli et al., 2008). In order to assess if and how efficiently we were able to deliver an expression vector in the *mdx*^{4Cv} muscles we injected a β-gal expressing plasmid (**Figure 3A**) and a GFP-expressing plasmid (**Figure 3B**) in adult *C57BL/6J* and *mdx*^{4Cv} hindlimbs by applying the electroporation protocol. Our analysis of the GFP intensity performed 1 week after electroporation revealed clear GFP signals in both the *C57BL/6J* and the *mdx*^{4Cv} muscles *in vivo* (**Figure 3B**). Intriguingly, the GFP intensity in the *mdx*^{4Cv} mice was significantly reduced compared to the aged-matched *C57BL/6J* mice (**Figure 3B**). A similar trend was apparent also after whole–mount X-gal staining of muscles injected with β-gal-expressing plasmids and collected 3 weeks after electroporation (**Figure 3A**). The presence of individual fibers characterized by strong X-gal staining suggests that once plasmids are taken up by dystrophic fibers they might be maintained for several weeks (**Figure 3A**).

We next decided to investigate the extent of plasmid uptake in mononuclear cells by electroporating tdTomato-expressing plasmids in dystrophic muscles (**Figures 3C–G**). In keeping with our whole muscles' analysis (**Figures 3A,B**) the percentage of cells which received the exogenous plasmid was significantly lower in *mdx*^{4Cv} mice compared to the aged-matched *C57BL/6J* mice for all the analyzed cell populations. Up to 5.1% of the entire single cell population (**Figure 3C**), 6.0% of CD45^{+ve} cells (**Figure 3D**) 10.1% of CD31^{+ve} cells (**Figure 3E**), 12.0% of FAPs (**Figure 3F**) and 4.9% of MuSCs (**Figure 3G**) expressed the tdTomato vector after the electroporation in *mdx*^{4Cv}. Altogether, these results indicate that the dystrophic muscle is intrinsically different in terms of efficiency of plasmid uptake upon electroporation.

Hyaluronidase pre-treatment is reportedly increasing the efficiency of whole muscle electroporation both in *wild type* and *mdx* mice (McMahon et al., 2001; Gollins et al., 2003;

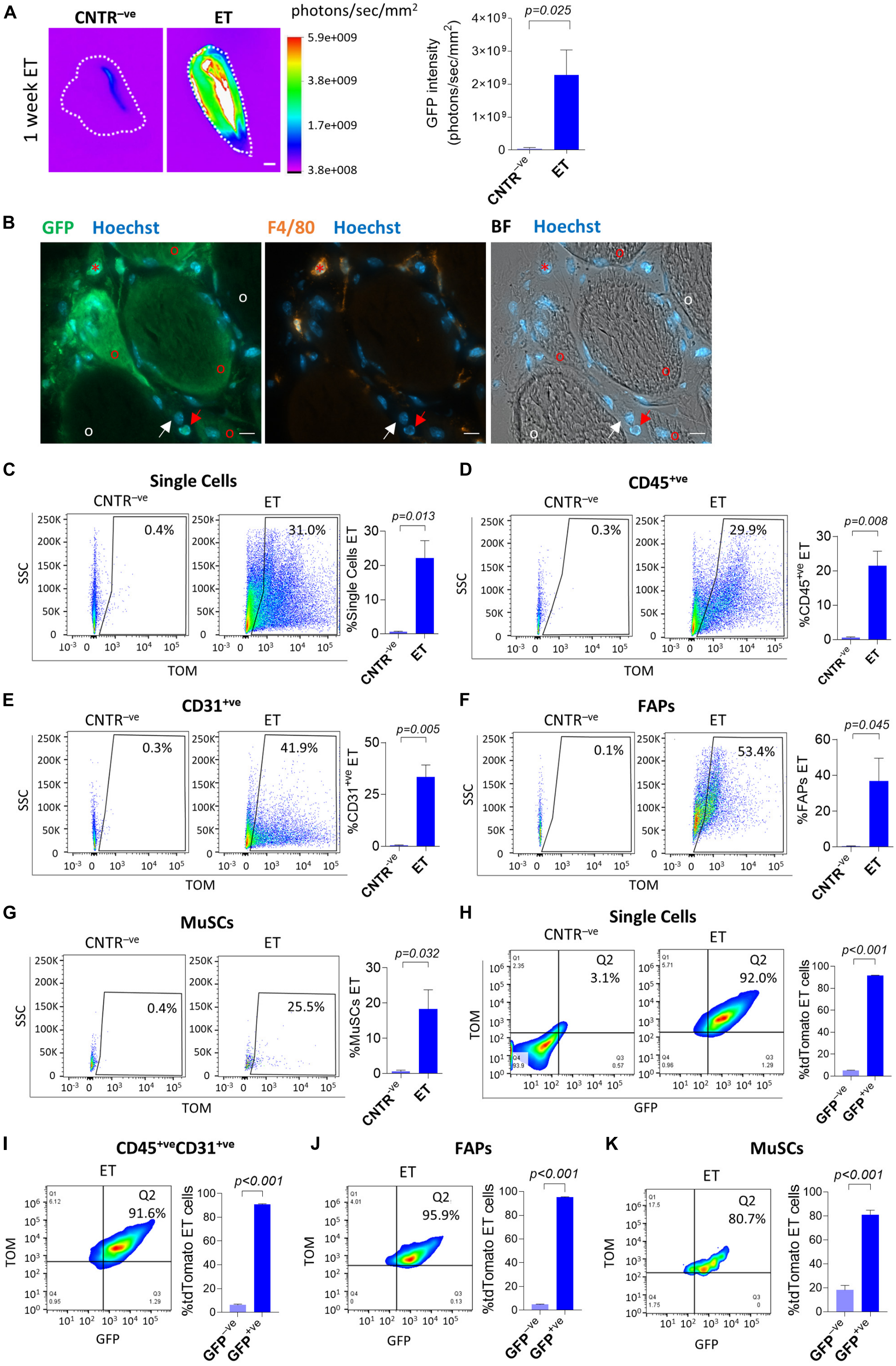

FIGURE 1 | *In vivo* electroporation of whole muscles and single cells. **(A)** GFP intensity measurement (photons/sec/mm^2) of whole *gastrocnemius* (CNTR^{-ve}) or *TA* (ET) from ~12 months-old *C57BL/6J* mice injected with GFP plasmid and electroporated (ET) or not injected nor electroporated (CNTR^{-ve}). Scale bar: 2.5 mm.

(Continued)

FIGURE 1 | White color in the figure indicates photons/sec/mm^2 > 5.9e+009. Refer also to **Supplementary Figure 2A** for the corresponding muscles reflectance images. The analysis was performed using Bruker *In Vivo* Xtreme I imaging system. Muscles were collected 1 week after electroporation and scanned *ex vivo*. *N* = 5 (CNTR^{-ve}), *N* = 6 (ET). **(B)** Representative immunofluorescence of *TA* from ∼8 months-old *C57BL/6J* mice injected with GFP plasmid and electroporated. Muscles were stained with anti-GFP (green), anti-F4/80 (orange) antibodies, and Hoechst (blue). The analysis was performed 1 week after electroporation. BF: Bright Field. Scale bar: 10 μm. Note the presence of electroporated (GFP^{+ve}) F4/80^{+ve} cells (red asterisks), * and F4/80^{-ve} mononucleated muscle cells (red arrows) nearby electroporated (GFP^{+ve}) muscle fibers (red circles). White arrows and circles are, respectively, marking examples of non-electroporated (GFP^{-ve}) F4/80^{-ve} mononucleated muscle cells and muscle fibers. *N* = 3. Refer to **Supplementary Figure 3A** for additional images collected from different mice. **(C–G)** Representative FACS plot (left) and quantification (right) of electroporated (ET, TOM^{+ve}) single cells **(C)**, CD45^{+ve} **(D)**, CD31^{+ve} **(E)**, FAPs **(F)** and MuSCs **(G)** from *TA* of ∼5 months-old *C57BL/6J* mice injected with PBS (CNTR^{-ve}) or with tdTomato plasmid (ET) and electroporated. The analysis was performed 3 weeks after electroporation. *N* = 3. **(H–K; left)** Representative FACS plot showing in Q2 TOM^{+ve}GFP^{+ve} cells in single cell **(H)**, CD45^{+ve}CD31^{+ve} cell **(I)**, FAPs **(J)** and MuSCs **(K)** populations from *TA* of ∼4 months-old *C57BL/6J* mice electroporated with GFP/tdTomato plasmid mix and identified as effectively electroporated with tdTomato plasmid (ET) as shown in panels **(C–G)**. CNTR^{-ve} [shown only in **(H)**] represents non-electroporated cells of *TA* injected with PBS and electroporated. The analysis was performed 1 week after electroporation. Refer also to **Supplementary Figures 3B–D** for CNTR^{-ve} FACS plot of **(I–K)**. **(H–K; right)** Quantification of the GFP^{+ve} fraction of single cells **(H)**, CD45^{+ve}CD31^{+ve} cells **(I)**, FAPs **(J)**, and MuSCs **(K)** effectively electroporated with tdTomato plasmid (ET) in *TA* of ∼4 months-old *C57BL/6J* mice injected with a GFP/tdTomato plasmids mix and electroporated. The analysis was performed 1 week after electroporation. *N* = 3. FAPs: CD45^{-ve}CD31^{-ve}sca1^{+ve} cells; MuSCs: CD45^{-ve}CD31^{-ve}sca1^{-ve}vcam^{+ve} cells.

Molnar et al., 2004). To assess if this approach could also increase plasmid uptake by mononucleated cells, we electroporated dystrophic muscles with plasmids expressing reporter genes after pre-conditioning with hyaluronidase. As expected, 1 week after electroporation, the GFP intensity measured *in vivo* and on dissected muscles through the Bruker *In Vivo* Xtreme I imaging system resulted higher in the hyaluronidase-treated mice compared to mice not injected with hyaluronidase (**Figure 4A** and **Supplementary Figure 4A**). Importantly, this protocol also resulted in a significant increase in the electroporation efficiency of mononucleated cells (**Figures 4B–F**). To further characterize the properties of electroporation in mononucleated cells of dystrophic tissues, we evaluated if the co-electroporation with two different plasmids results in the preferential uptake of both plasmids by the same cells as previously shown for *wild type* muscles. The FACS analysis performed 1 week after the electroporation with a mix of GFP- and tdTomato-expressing plasmids revealed that also in the *mdx*^{4Cv} muscles, the great majority of TOM^{+ve} cells expressed GFP in all the analyzed cell populations (**Figures 4G–K** and **Supplementary Figures 4B–E** for negative controls). This aspect is not influenced by hyaluronidase, as similar results were obtained without hyaluronidase pre-conditioning (not shown). Altogether, these data highlight the possibility to effectively target the mononucleated cells in the dystrophic muscles.

In vivo Electroporation of Old Muscles

Both dystrophic and aging muscles are characterized by excessive accumulation of fibrotic tissue, but only dystrophic tissues are actively regenerating in the absence of external damaging events. To get insights into the relative contribution of fibrosis and regeneration-associated cellular turnover to the reduced electroporation efficiency observed in dystrophic muscles, we directed our attention to old mice. We evaluated the efficiency of *in vivo* plasmid electroporation by analyzing both whole muscles and muscle mononucleated cells in old (∼2 years-old) and young (∼2 months-old) *C57BL/6J* mice (**Figure 5**). Expression from a β-gal-expressing plasmid was readily observed 1 week after electroporation at both ages (**Figure 5A**). Interestingly, the β-gal expression appeared more intense in the old muscles compared to the young mice (**Figure 5A**). This observation was confirmed by an independent experiment in which a tdTomato-expressing vector was electroporated. Although the difference was not statistically significant, 1 week after electroporation the tdTomato intensity measured through the Bruker *In Vivo* Xtreme I imaging system resulted slightly higher in the old mice compared to the young mice (**Figures 5B,C**). Two weeks after the electroporation the plasmid was still expressed in both old and young muscles, but at comparable levels (**Figures 5B,C**). The FACS analysis showed that the electroporated vector was effectively delivered in the muscle mononucleated cells in both young and old muscles (**Figures 5D–H**). Two weeks after the *in vivo* electroporation 12.4 to 23.3% of the whole mononucleated cell population (**Figure 5D**), 6.7 to 13.4% of CD45^{+ve} population (**Figure 5E**), 14.8 to 32.5% of CD31^{+ve} population (**Figure 5F**), 23.6 to 48.8% of FAPs (**Figure 5G**) and 11.7 to 31.6% of MuSCs (**Figure 5H**) were effectively expressing the vector in both the young and old muscles. Altogether, these data indicate that despite the presence of fibrosis, the efficiency of electro-enhanced plasmid transfer in old muscle is not reduced compared to the situation in young adults.

Study of Collagen 1 Expression in Muscle Single Cells Through *in vivo* Electroporation

Our data indicate that the electroporation can deliver with different yet satisfactory efficiency an exogenous DNA vector in both healthy and compromised (i.e., dystrophic and old) muscles at the mononucleated cell level. This possibility opens to the *in vivo* investigation of the behavior of muscle mononucleated cells with unprecedented simplicity. As a proof of principle, we decided to take advantage of the electroporation protocol to investigate the involvement of various mononucleated cells to the accumulation of fibrotic tissue in dystrophic and aging muscle. Collagens are one of the major components of muscle extracellular matrix and, within all the different members of collagen superfamily, collagen 1 is the most abundant in the skeletal muscles (McKee et al., 2019). With the goal to study collagen 1 expression in muscle mononucleated cells we used the *in vivo* electroporation of a plasmid expressing the reporter gene GFP under the control of a portion of the

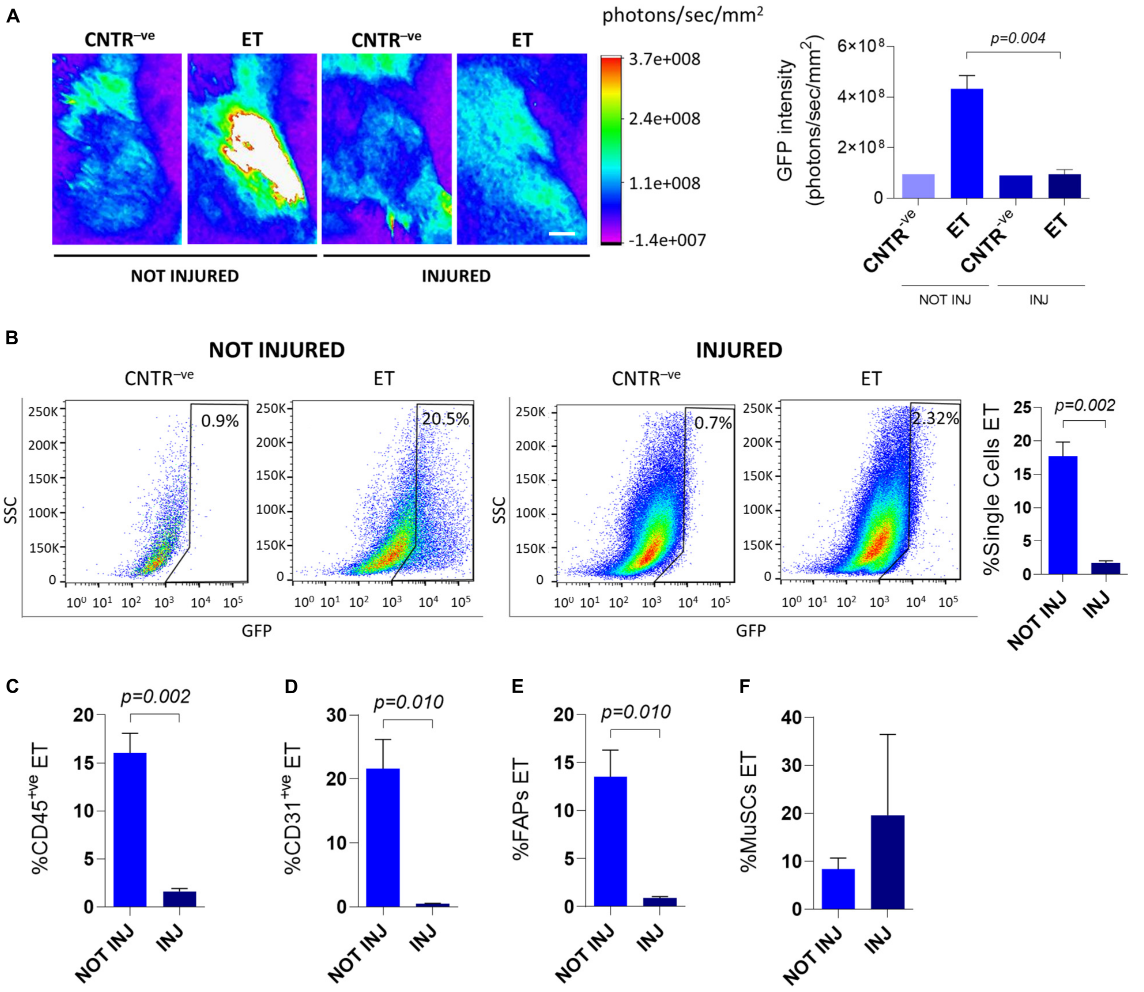

FIGURE 2 | *In vivo* electroporation of injured muscles**. (A)** Representative Bruker *In Vivo* Xtreme I images (left) and GFP intensity measurement (photons/sec/mm^2) (right) of *TA* muscles from ~8 months-old *C57BL/6J* mice uninjured (NOT INJ) or injected with cardiotoxin (INJ). Mice were injected with PBS (CNTR^{-ve}) or GFP plasmid (ET) and electroporated 1.5 days after cardiotoxin injection. Scale bar: 2.5 mm. White color in the figure indicates photons/sec/mm^2 > 3.7e+008, Muscles were analyzed 5 days after electroporation. *N* = 3 (ET), *N* = 1 (CNTR^{-ve}). **(B)** Representative FACS plot (left) and quantification (right) of electroporated (ET, GFP^{+ve}) single cells from *TA* of ~8 months-old *C57BL/6J* mice uninjured (NOT INJ) or injected with cardiotoxin (INJ). Mice were injected with PBS (CNTR^{-ve}) or GFP plasmid (ET) and electroporated 1.5 days after the cardiotoxin injection. The analysis was performed 6 days after electroporation. *N* = 3 (ET). **(C–F)** Quantification of electroporated (ET) CD45^{+ve} cells **(C)**, CD31^{+ve} cells **(D)**, FAPs **(E)** and MuSCs **(F)** from *TA* of the same mice as in panel **(B)**. All CNTR^{-ve} gates were set on control samples (i.e., sample injected with PBS and electroporated). The percentage of ET cells in each CNTR^{-ve} gate was < 1% for all the analyzed cell populations.

collagen 1 promoter (Col1-GFP) (Kalajzic et al., 2002). Our observation indicating that two plasmids can be efficiently co-electroporated in the same cells in both dystrophic and *wild type* muscles (see above) allowed the use of a second plasmid expressing tdTomato under the control of the constitutive CMV promoter to normalize for the differences in the efficiencies of DNA transfer between dystrophic and *wild type* muscles. We therefore electroporated a mix of Col1-GFP and tdTomato plasmids in *TA* muscles of age-matched *C57BL/6J* and *mdx^{4Cv}* mice. Two weeks after electroporation the muscles were dissected and digested to mononucleated cells. The GFP and tdTomato fluorescence intensities were measured by FACS. The level of GFP expression from the collagen 1 promoter was higher in the CD31^{+ve} cells (**Figure 6A**) and FAPs (**Figure 6B**) of the *mdx^{4Cv}* muscles compared to the *C57BL/6J* after normalization with the corresponding tdTomato intensity. A similar trend, although not statistically significant, was also observed for MuSCs (**Figure 6C**). To corroborate these results, we investigated in parallel the mRNA levels of *collagen1a1* by quantitative PCR. Overall, the quantification of *collagen1a1* transcripts paralleled the results obtained with the plasmid expressing the reporter from the collagen promoter, although the difference was statistically significant only for FAPs (**Figures 6G–I**). This observation is in keeping with data reported in previous studies (Biressi et al., 2014; Pessina et al., 2015), and therefore confirmed the suitability of our electroporation-based approach to investigate the features of mononuclear cells in dystrophic tissues.

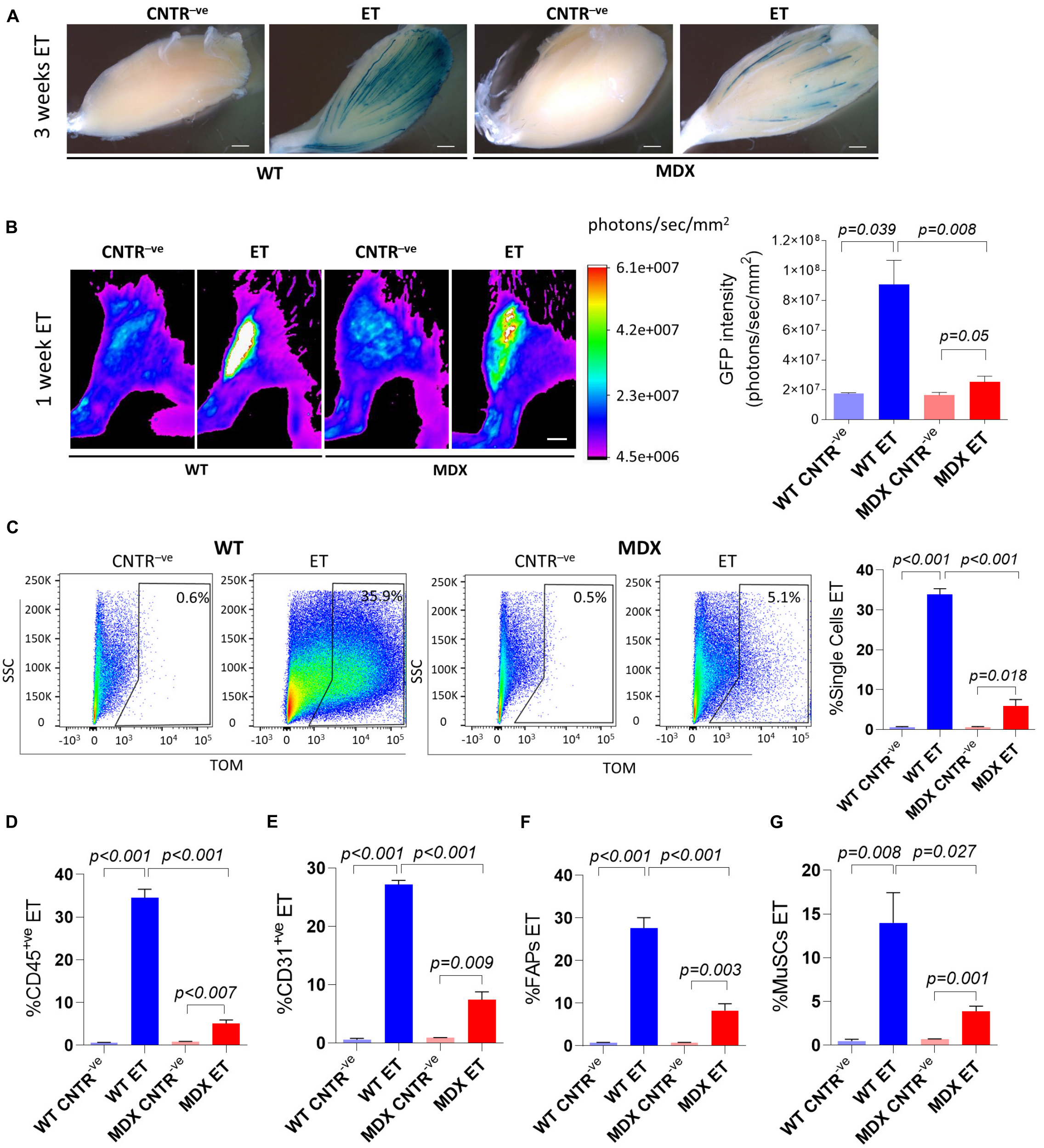

FIGURE 3 | *In vivo* electroporation of dystrophic muscles. **(A)** Whole-mount X-gal staining of not electroporated (CNTR^{-ve}) and electroporated (ET) *TA* muscles from ∼16 months-old *C57BL/6J* (WT) and *mdx*^{4Cv} (MDX) mice. β-gal plasmid was injected in muscles prior electroporation. Muscles were collected 3 weeks after electroporation. *N* = 2. Scale bar: 0.85 mm. **(B)** Representative Bruker *In Vivo* Xtreme I images (left) and GFP intensity measurement (photons/sec/mm^2) (right) of *TA* muscles from 12–14 months-old *C57BL/6J* (WT) and *mdx*^{4Cv} (MDX) mice injected with β-gal (CNTR^{-ve}) or GFP plasmid (ET) and electroporated. Scale bar: 2.5 mm. White color in the figure indicates photons/sec/mm^2 > 6.1e+007. Muscles were analyzed 1 week after electroporation. *N* = 2 (WT CNTR^{-ve}), *N* = 4 (WT ET; MDX ET), *N* = 6 (MDX CNTR^{-ve}). **(C)** Representative FACS plot (left) and quantification (right) of electroporated (ET, TOM^{+ve} or GFP^{+ve}) single cells from *TA* of ∼6–9 months-old *C57BL/6J* (WT) and *mdx*^{4Cv} (MDX) mice injected with tdTomato or GFP plasmid and electroporated (ET). CNTR^{-ve} samples are hindlimb untreated muscles or muscles injected with PBS and electroporated. The analysis was performed 1 week after electroporation. *N* = 4. **(D–G)** Quantification of electroporated (ET) CD45^{+ve} cells (*N* = 3) **(D)**, CD31^{+ve} cells (*N* = 3) **(E)**, FAPs (*N* = 4) **(F)** and MuSCs (*N* = 4) **(G)** from muscles of the same mice as in panel **(C)**. All CNTR^{-ve} gates were set on control samples. The percentage of ET cells in each CNTR^{-ve} gate was < 1% for all the analyzed cell populations.

The same experiment was also performed to compare young and old *C57BL/6J* muscle mononucleated cells. We did not observe a significant increase in GFP expression from the *collagen 1* promoter in the old CD31^{+ve} cells (**Figure 6D**), FAPs (**Figure 6E**), and MuSCs (**Figure 6F**) compared to their young counterparts. In line with these results, our mRNA expression analysis on FACS-isolated CD31^{+ve} cells (**Figure 6G**) and FAPs (**Figure 6H**) from old and young muscles showed

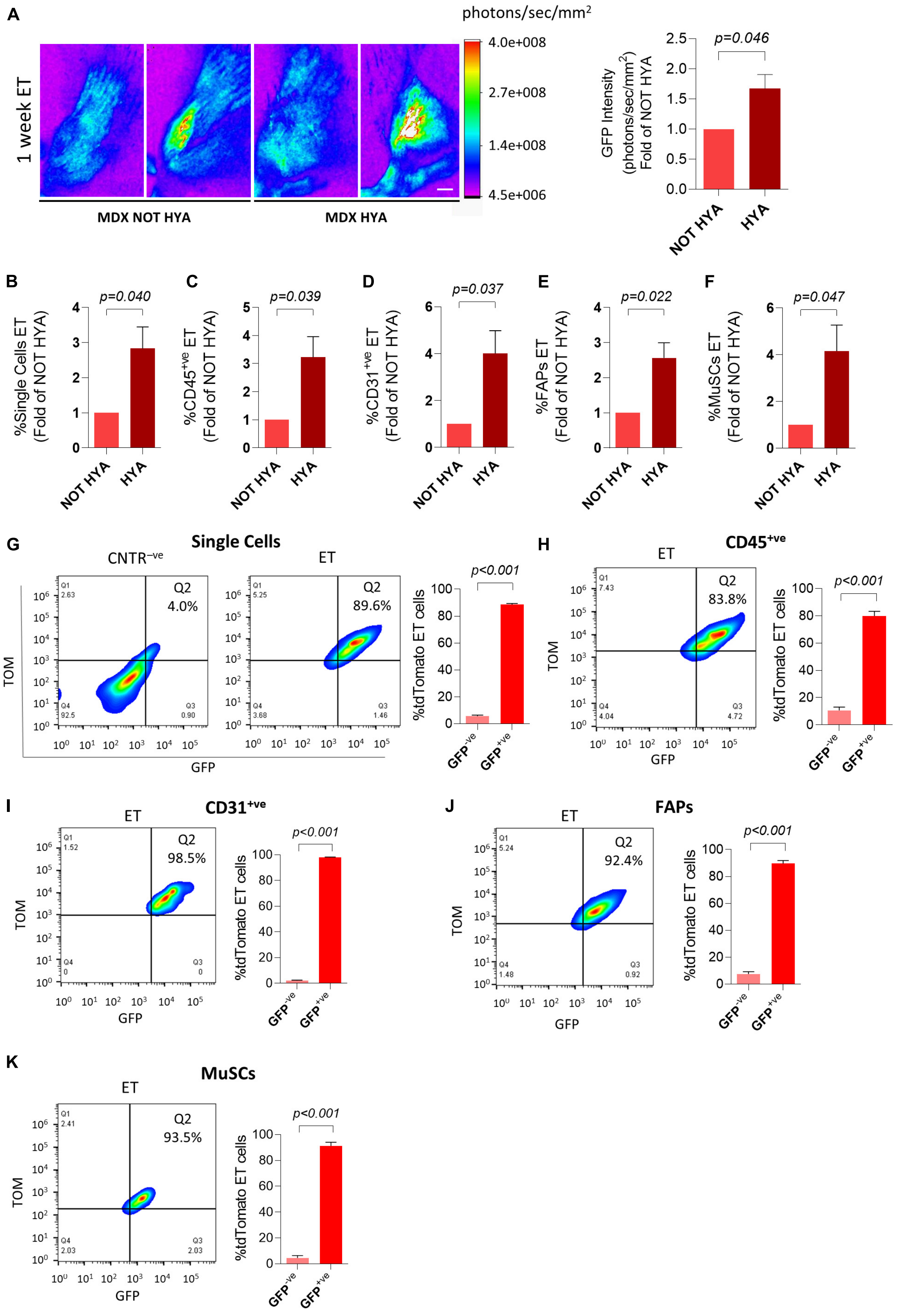

FIGURE 4 | Hyaluronidase pre-conditioning increases the efficiency of electroporation of mononucleated cells in dystrophic muscles. **(A)** Representative Bruker *In Vivo* Xtreme I images (left) and GFP intensity measurement (photons/sec/mm^2) (right) of *TA* muscles from ∼6 months-old *mdx*^{4Cv} (MDX) mice injected with hyaluronidase (HYA) or not injected (NOT HYA). 2 h after hyaluronidase injection *TA* muscles were injected with PBS (CNTR^{-ve}) or GFP plasmid (ET) and

(Continued)

FIGURE 4 | electroporated. Scale bar: 2.5 mm. White color in the figure indicates photons/sec/mm^2 > 4.0e+008. Muscles were analyzed 1 week after electroporation. $N = 3$. Refer also to **Supplementary Figure 4A** for GFP intensity measurement of the corresponding dissected muscles. **(B–F)** Quantification of electroporated (ET) single cells **(B)**, CD45^{+ve} cells **(C)**, CD31^{+ve} cells **(D)**, FAPs **(E)** and MuSCs **(F)** of *TA* muscles from the same mice as in panel **(A)**. All negative control gates were set on controls (i.e., samples treated or not treated with hyaluronidase, injected 2 h later with PBS and electroporated). The percentage of ET cells in each negative control gate was < 1% for all the analyzed cell populations. **(G–K; left)** Representative FACS plot showing in Q2 TOM^{+ve}GFP^{+ve} cells in single cell **(G)**, CD45^{+ve} cell **(H)**, CD31^{+ve} cell **(I)**, FAPs **(J)**, and MuSCs **(K)** populations from *TA* of ~6 months-old *mdx*^{4Cv} (MDX) mice injected with hyaluronidase, and subsequently electroporated with GFP/tdTomato plasmid mix and identified as effectively electroporated with tdTomato plasmid (ET). CNTR^{-ve} [shown only in **(G)**] represents non-electroporated cells of *TA* treated with hyaluronidase, then injected with PBS and electroporated. The analysis was performed 1 week after electroporation. Refer also to **Supplementary Figures 4B–E** for CNTR^{-ve} FACS plots of **(H–K)**. **(G–K; right)** Quantification of the GFP^{+ve} fraction of single cells **(G)**, CD45^{+ve} cells **(H)**, CD31^{+ve} cells **(I)**, FAPs **(J)**, and MuSCs **(K)** effectively electroporated with tdTomato plasmid (ET) in *TA* of ~6 months-old *mdx*^{4Cv} (MDX) mice injected with hyaluronidase, then electroporated with GFP/tdTomato plasmid mix. The analysis was performed 1 week after electroporation. $N = 3$. FAPs: CD45^{-ve}CD31^{-ve}sca1^{+ve} cells; MuSCs: CD45^{-ve}CD31^{-ve}sca1^{-ve}vcam^{+ve} cells.

similar expression of *collagen1a1*. A not statistically significant trend toward rising levels of *collagen 1a 1* expression was observed in MuSCs from old muscles (**Figure 6I**). Altogether, these results demonstrate the feasibility of targeting muscle mononucleated cells through electro-enhanced plasmid transfer to investigate the cellular and molecular events characterizing diseased muscle tissues.

DISCUSSION

The data presented here highlight previously unappreciated features of the *in vivo* electroporation technique, focusing on the mononucleated cells. By taking advantage of a widely used set of surface markers, we unambiguously identified MuSCs, FAPs, endothelial cells, and hematopoietic lineage cells in electroporated murine muscles and comparatively quantified their efficiencies of electroporation. Transgene expression from transferred plasmid DNA was effectively induced in all these cell populations. These results are in keeping with previous observations reporting effective plasmid uptake by Vimentin^{+ve}, Desmin^{+ve}, or MyoD^{+ve} "bona fide" MuSCs in electroporated muscles (Grønevik et al., 2003; Peng et al., 2005; Ratanamart et al., 2010). To our knowledge, this is the first study conclusively demonstrating that electroporation can effectively target both endothelial cells and FAPs. A previous report indicates the existence of rare electroporated Thy1^{+ve} muscle interstitial cells, but due to the expression of this marker in various cell types, it was not possible to unambiguously establish their nature (Grønevik et al., 2003). Past studies investigated the plasmid transfer in hematopoietic lineage cells with conflicting results. Differences in the electroporation protocols, the spe cific markers used to identify the cells, and the sensitivity of the techniques employed to evaluate plasmid uptake and transgene expression may contribute to these discrepancies. Some studies reported undetectable levels of transgene expression by lymphocytes and macrophages/monocytes upon electro-enhanced plasmid transfer (Dupuis et al., 2000; Grønevik et al., 2003; Ratanamart et al., 2010). Nevertheless, one of these studies demonstrated that mononucleated cells expressing the myeloid marker CD11b are capable of efficiently uptaking electroporated plasmid DNA, possibly resulting from phagocytosis events (Dupuis et al., 2000). Intriguingly, intramuscular DNA injection reportedly induces transgenic protein expression in cells isolated from the proximal draining lymph nodes and mainly consisting in macrophages (Chattergoon et al., 1998). Our analysis indicating that CD45^{+ve} cells from electroporated muscles, particularly the F4/80^{+ve} macrophage subset, are capable of transgene expression is in line with this latter study. It is unknown if this is the result of the direct uptake of plasmids or depends on the high phagocytic activity of these cells.

We then extended our analysis of the electroporated mononucleated cells to dystrophic muscle. We were able to easily identify electroporated MuSCs, but we also noticed a clear reduction in the efficiency of electroporation. This reduction might explain why, despite effective electroporation in the mature fibers, only rare plasmid uptake was reported in dystrophic MuSCs in a previous study (Wong et al., 2005). In apparent contrast with this latter study, our observations highlight previously unappreciated parallelism between plasmid uptake by MuSCs and muscle fibers, being both significantly reduced after electroporation in dystrophic muscle compared to age-matched controls. A reduction in muscle fibers' electroporation efficiency in *mdx* mice finds confirmation in a previous report (Molnar et al., 2004), which is inconsistent with others reporting comparable levels between *mdx* and *wild type* mice (Gollins et al., 2003). Importantly, we report compelling evidence indicating that hematopoietic cells, endothelial cells and FAPs from dystrophic mice are also less susceptible to electro-enhanced plasmid transfer, similar to their MuSCs and fiber counterparts.

Dystrophic muscle is characterized by chronic cycles of degeneration and regeneration and pronounced deposition of fibrotic tissue, all features that might potentially impact electroporation efficiency. Fibrosis might represent a physical barrier for intramuscular diffusion but is likely not the major cause of ineffective plasmid uptake that we observed in *mdx* mice. Indeed, our data indicate that electroporation efficiency is not decreasing in 2 years-old muscles, which are also characterized by fibrosis. The idea of little influence of fibrosis finds further confirmation in the observation that electroporation efficacy is not affected by the increased amount of collagen present in *mdx*^{4Cv} muscles at 21 weeks of age compared to the situation in 7 weeks-old mice (Gollins et al., 2003). MuSCs, FAPs, hematopoietic and endothelial cells are all undergoing a dramatic expansion in dystrophic tissues as part of the ongoing regenerative response (Wosczyna and Rando, 2018). The possibility that proliferating cells might be less effective in uptaking plasmids than their quiescent counterpart might explain why efficiencies are higher in all cell populations

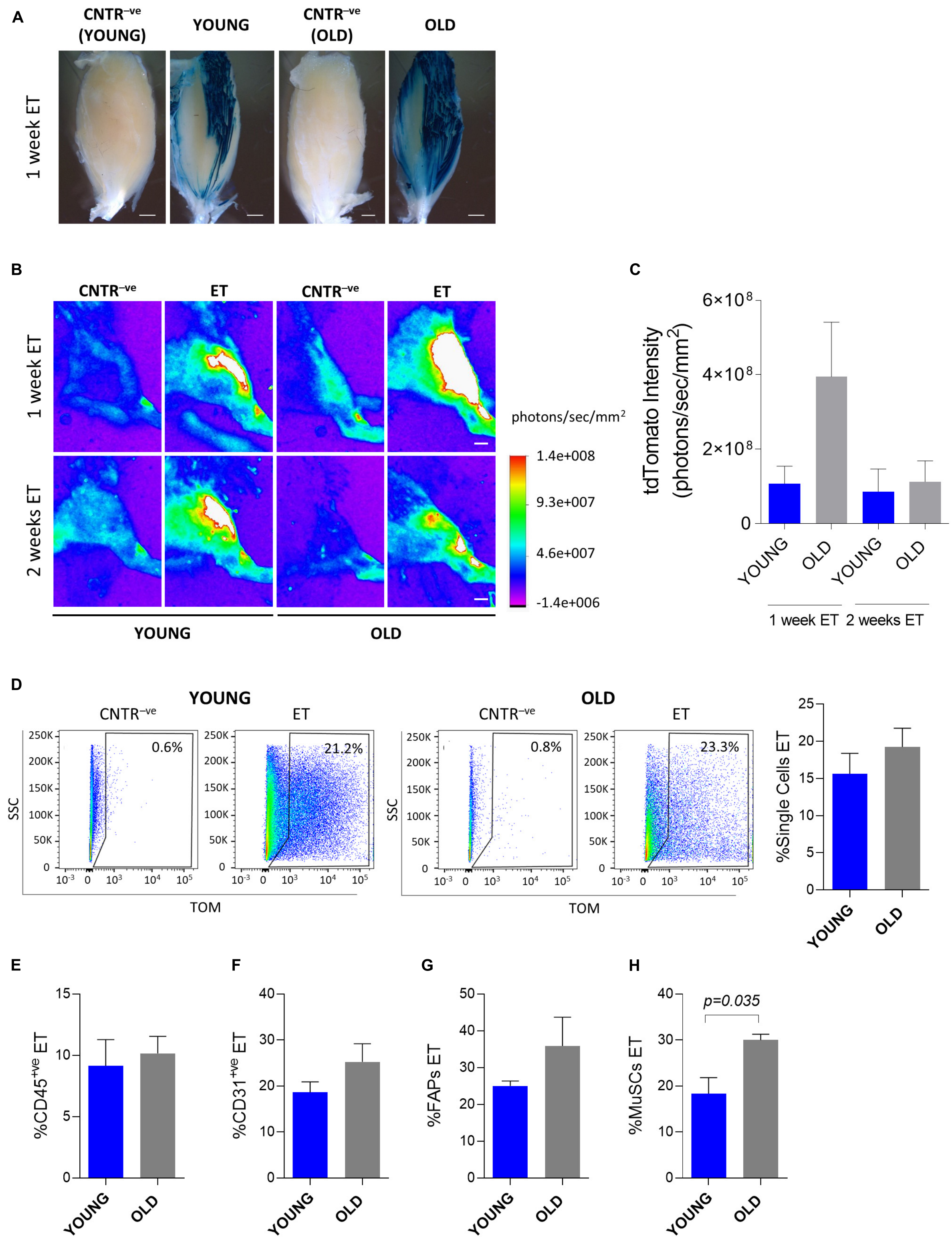

FIGURE 5 | *In vivo* electroporation of old muscles. **(A)** Whole-mount X-gal staining of *TA* from ~2 months-old *C57BL/6J* (YOUNG), and ~24 months-old *C57BL/6J* (OLD) mice. PBS (CNTR^{-ve}) or β-gal plasmid (YOUNG, OLD) were injected in muscles prior electroporation. Muscles were collected 1 week after electroporation. Scale bar: 0.85 mm. **(B)** Representative Bruker *In Vivo* Xtreme I images of tdTomato intensity (photons/sec/mm^2) of *TA* from muscles of ~2 months-old (YOUNG) and ~24 months-old (OLD) *C57BL/6J* mice injected with PBS (CNTR^{-ve}) or with tdTomato plasmid (ET) and electroporated. Scale bar: 2.5 mm. White color in the figure indicates photons/sec/mm^2 > 1.4e+008. The analysis was performed 1 and 2 weeks after electroporation. **(C)** tdTomato intensity measurement (photons/sec/mm^2) of *TA* of ~2 months-old (YOUNG) and ~24 months-old (OLD) *C57BL/6J* mice injected with tdTomato plasmid and electroporated. The analysis

(Continued)

FIGURE 5 | was performed 1 and 2 weeks after electroporation. *N* = 6 (YOUNG ET 1 week, OLD ET 1 week), *N* = 3 (YOUNG ET 2 weeks, OLD ET 2 weeks). The intensity of tdTomato of the corresponding CNTR^{-ve} samples (i.e., mice injected with PBS and electroporated) was subtracted from each sample. **(D)** Representative FACS plot (left) and quantification (right) of electroporated (ET) single cells from *TA* of ~2 months-old (YOUNG) and ~24 months-old (OLD) *C57BL/6J* mice injected with tdTomato plasmid and electroporated. The analysis was performed 2 weeks after electroporation. *N* = 3. **(E–H)** Quantification of electroporated (ET) CD45^{+ve} cells **(E)**, CD31^{+ve} cells **(F)**, FAPs **(G)** and MuSCs **(H)** from *TA* of the same mice as in panel **(D)**. All CNTR^{-ve} gates were set on control samples (i.e., sample injected with PBS and electroporated). The percentage of ET cells in each CNTR^{-ve} gate was < 1% for all the analyzed cell populations. FAPs: CD45^{-ve}CD31^{-ve}sca1^{+ve} cells; MuSCs: CD45^{-ve}CD31^{-ve}sca1^{-ve}vcam^{+ve} cells.

when non-dystrophic tissues are electroporated. The mechanism underlining this aspect may reside in the observation that electro-enhanced plasmid transfer depends on the radius of curvature of the target cell (Somiari et al., 2000). Indeed, cells undergo a dramatic change in size and morphology as they transit from quiescence to proliferation during regeneration (van Velthoven and Rando, 2019). Moreover, proliferating cells are also less resistant than quiescent cells to a variety of stressors, and this might also contribute to the overall efficiency, as electroporation is inevitably associated with a mild degree of damage (Roche et al., 2011). Newly repaired fibers derive from the fusion of activated MuSCs, and a causal link between the efficacy of plasmid uptake by MuSCs and the efficacy of electroporation in regenerating fibers has been proposed in *wild type* muscles and is indirectly supported by our data in the dystrophic setting (Peng et al., 2005). Hyaluronidase remodels the extracellular matrix and protects muscle from damage (McMahon et al., 2001). By taking these aspects into account, the observation reported here that the pretreatment with hyaluronidase increases electroporation efficiency both in whole muscle and in mononucleated cells fits with the hypothesis that activated cells are less prone to uptake DNA or present a higher tendency to lose plasmids upon electroporation. This idea is also indirectly confirmed by actively growing 2-3 weeks-old *mdx* mice, which are less efficiently electroporated than their 6 weeks-old adult counterparts (Molnar et al., 2004). Furthermore, previous reports demonstrate that the administration of damaging agents a few days before electroporation, which promotes fibers degeneration and subsequent proliferative expansion of mononucleated cells, also reduces whole muscle electroporation efficiencies (Gollins et al., 2003; Wong et al., 2005). Here we have not only extended this observation to various mononucleated cells, corroborating the parallelism between fibers and mononucleated cells electroporation, but we also have noticed poor incorporation of plasmids in mononucleated cells when the damaging agent was administered after the electroporation procedure (see above). This latter observation suggests that proliferating cells might dilute out electroporated non-integrating plasmids to result in fewer positive cells as the population expands after transfection. Therefore, although concomitant factors such as fibrosis may also play a role, the proliferative state of the mononucleated cells appears crucial to define the outcome of the electro-enhanced plasmid transfer.

Electroporation is a cost-effective procedure that might represent a valuable alternative to viral vectors, which may be troublesome to handle on the laboratory scale. Our observation that various subpopulations of mononucleated cells involved in skeletal muscle repair are amenable for electro-enhanced plasmid transfer is opening new investigative scenarios extending beyond replacement gene transfer and systemic production of therapeutic proteins that are classically accomplished through muscle fiber electroporation. Overexpression or silencing of genes potentially involved in modulating the lineage progression of MuSCs, hematopoietic cells, endothelial cells, and FAPs may represent a powerful tool to investigate the fundamental mechanisms controlling regeneration and get insight into cellular and molecular events, which are getting defective during aging and muscle diseases. The incomplete efficiency of electroporation, particularly for the dystrophic and injured muscles, might represent a limitation to this approach that may be at least in part overcome by introducing reporter genes in the electroporated plasmids to identify the fraction of effectively targeted cells in the tissue. Another limitation is that electroporation is not readily applicable to non-limb muscles, such as the diaphragm, which is diffusely used to model disease progression in DMD animal models (Stedman et al., 1991).

Electro-enhanced plasmid transfer to mononucleated cells is also rendering possible to investigate *in vivo* and in a cell-specific way the function of regulatory DNA sequences involved in the transcriptional control of specific genes without the need to turn to the generation of engineered mouse models. This possibility is highlighted by the study we are reporting here, in which a portion of 2.3 kb of the *collagen1a1* promoter was shown to recapitulate endogenous *collagen1a1* transcription in dystrophic mononuclear cells. *In vivo* electro-enhanced plasmid delivery is also attractive in gene editing experiments. The episomal nature of electroporated plasmids favors a transient "hit-and-run" approach that minimizes off-targets and undesired immune responses (Mashel et al., 2020).

We also report the possibility to effectively co-transfer multiple plasmids in the same cells by electroporation. As we show here, this feature can be exploited for normalization purposes but is potentially useful in other experimental settings. For instance, multiple gene transfer may permit the simultaneous modulation of concurrent biochemical pathways and may be exploited in basic research and therapy (Daddi et al., 2002). Co-delivery of different expression plasmids can be practical when a single plasmid expressing all the genes of interest is not available or, if generated, would result in a large construct, which can negatively affect cellular uptake. Co-electroporation is also potentially useful in studies involving CRISPR/Cas9-mediated genetic modifications, where the definition of the optimal ratio between guide RNA and Cas9 expression is required for efficient gene editing. The use of two independent plasmids, respectively expressing the guide RNA and Cas9 might facilitate the process of optimization (Gam et al., 2019).

An increasing amount of publications highlights the primary involvement of MuSCs, and potentially also of

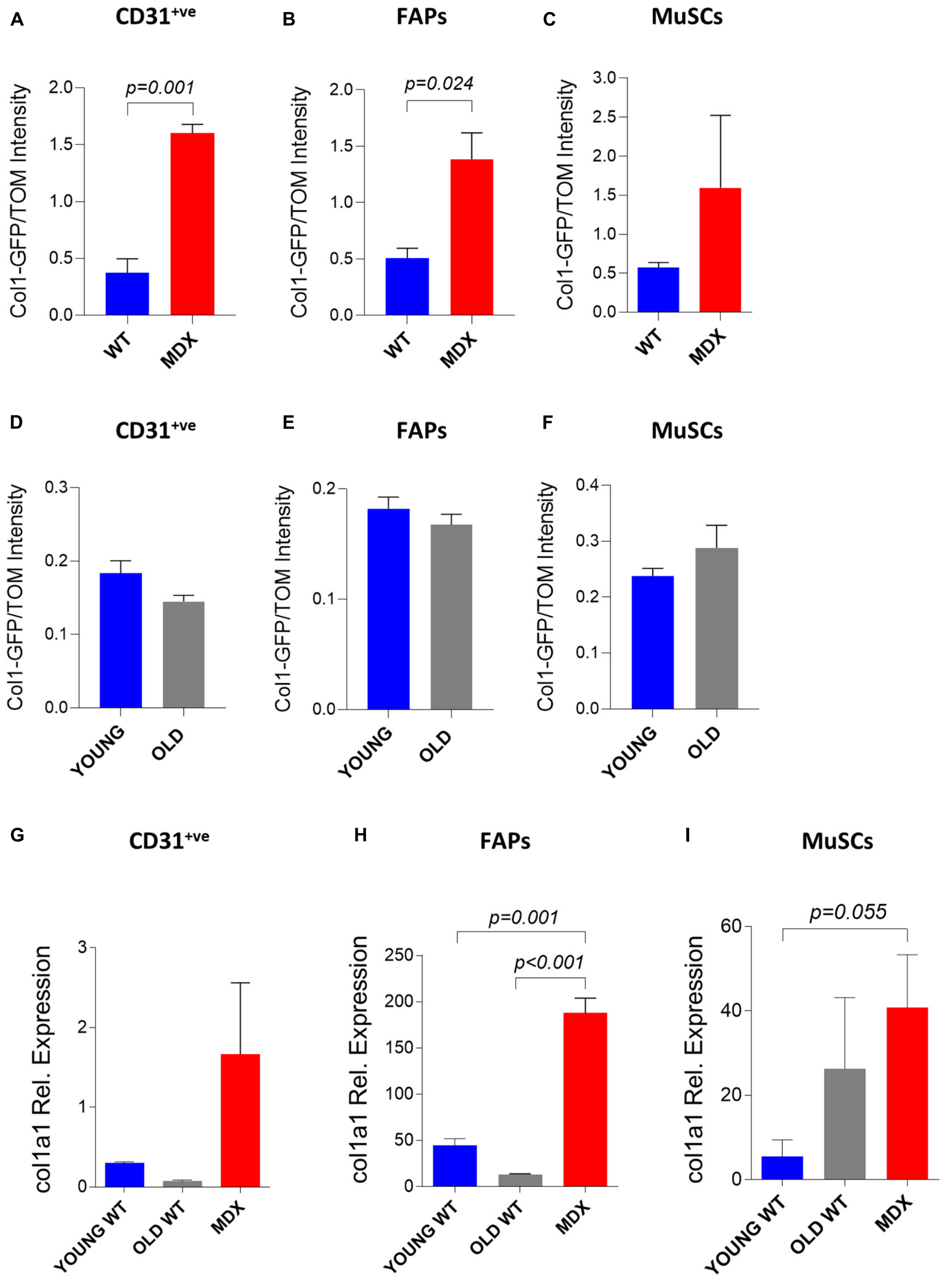

FIGURE 6 | Study of collagen 1 expression in muscle single cells through *in vivo* electroporation. **(A–C)** Col1-GFP/TOM Intensity (median) in CD31^{+ve} **(A)**, FAPs **(B)** and MuSCs **(C)** from *TA* of ~12 months-old *C57BL/6J* (WT) and *mdx^{4Cv}* (MDX) mice injected with Col1-GFP:tdTomato (Col1-GFP/TOM) mix (10:1) and electroporated. The analysis was performed 2 weeks after electroporation. *N* = 3 for all samples except MuSCs MDX (*N* = 2). **(D–F)** Col1-GFP/TOM Intensity (median) in CD31^{+ve} **(D)**, FAPs **(E)** and MuSCs **(F)** from *TA* of ~2 months-old (YOUNG) and ~24–26 months-old (OLD) *C57BL/6J* mice injected with Col1-GFP/TOM mix (10:1) and electroporated. The analysis was performed 2 weeks after electroporation. *N* = 3. **(G–I)** qPCR analysis of *collagen1a1* in CD31^{+ve} **(G)**, FAPs **(H)** and MuSCs **(I)** from ~2 months-old *C57BL/6J* (YOUNG WT), ~24 months-old (OLD WT) and ~12 months-old *mdx^{4Cv}* (MDX) hindlimb muscles. FAPs: CD45^{-ve}CD31^{-ve}sca1^{+ve} cells; MuSCs: CD45^{-ve}CD31^{-ve}sca1^{-ve}vcam^{+ve} cells.

the other muscle mononucleated cells, in the etiology of diseases previously believed to depend exclusively on muscle fibers defects (Ganassi et al., 2021). The observation that mononucleated muscle cell populations may be easily targeted *in vivo* with a versatile protocol such as electroporation offers a new weapon in the hands of researchers interested in investigating their properties and functions.

DATA AVAILABILITY STATEMENT

The raw data supporting the conclusions of this manuscript will be made available by the authors, without undue reservation, to any qualified researcher.

ETHICS STATEMENT

The animal experiments have been approved by the institutional animal use and welfare committee and the Italian Ministry of Health.

AUTHOR CONTRIBUTIONS

FF, SA, ML, and SB conducted and interpreted the experiments. FF and SB contributed to the design of the experiments and wrote the manuscript. All authors contributed to the article and approved the submitted version.

FUNDING

Work in the authors' laboratory was supported by AFM/Téléthon – France (Grant No. 23758), the Muscular Dystrophy Association – United States (Innovation Grant No. 874294), and Telethon and Provincia Autonoma di Trento – Italy (Grant No. TCP13007).

ACKNOWLEDGMENTS

We thank Sara Vencato, Isabella Pesce, Luca Tiberi, and Giorgina Scarduelli for suggestions or technical help.

SUPPLEMENTARY MATERIAL

The Supplementary Material for this article can be found online at: https://www.frontiersin.org/articles/10.3389/fphys.2022.834705/full#supplementary-material

Supplementary Figure 1 | Gating strategy used to isolate single cell populations. **(A)** Representative gating and sorting strategy used to FACS isolate CD45^{+ve}, CD31^{+ve}, FAPs (CD45^{-ve}CD31^{-ve}sca1^{+ve}) and MuSCs (CD45^{-ve}CD31^{-ve}sca1^{-ve}vcam^{+ve}) population from *C57BL/6J* and *mdx^{4Cv}* hindlimb muscles.

Supplementary Figure 2 | *In vivo* electroporation of whole muscles and single cells. **(A)** Reflectance images of untreated *gastrocnemius* (CNTR^{-ve}) and electroporated *TA* (ET) shown in **Figure 1A**. Scale bar: 2.5 mm. **(B)** Representative Bruker *In Vivo* Xtreme I images (left) and GFP intensity measurement (photons/sec/mm^2) (right) of *TA* muscles from ∼14 months-old *C57BL/6J* mice injected with GFP plasmid and electroporated (ET) or not treated (CNTR^{-ve}). Scale bar: 2.5 mm. White color in the figure indicates photons/sec/mm^2 $>$ 3.7e+008. The analysis was performed 1.5 day after electroporation. **(C–G)** Representative FACS plot (left) and quantification (right) of electroporated (ET, GFP^{+ve}) single cells **(C)**, CD45^{+ve} cells **(D)**, CD31^{+ve} cells **(E)**, FAPs **(F)** and MuSCs **(G)** from *TA* of ∼14 months-old *C57BL/6J* mice injected with PBS (CNTR^{-ve}) or with GFP-expressing plasmid (ET) and electroporated. The analysis was performed 1.5 day after electroporation. *N* = 3 (ET), *N* = 1 (CNTR^{-ve}). FAPs: CD45^{-ve}CD31^{-ve}sca1^{+ve} cells; MuSCs: CD45^{-ve}CD31^{-ve}sca1^{-ve}vcam^{+ve} cells. **(H)** Representative Bruker *In Vivo* Xtreme I images (left) and GFP intensity measurement (photons/sec/mm^2) (right) of *TA* muscles from ∼13 to 14 months-old *C57BL/6J* mice injected with β-gal (CNTR^{-ve}) or GFP plasmid (ET) and electroporated. Scale bar: 2.5 mm. White color in the figure indicates photons/sec/mm^2 $>$ 1.5e+008. The analysis was repeated 1, 2, 4, and 6 weeks (w) after electroporation. *N* = 4 (CNTR^{-ve} 1w, ET 4w), *N* = 5 (ET 1w), *N* = 1 (CNTR^{-ve} 2w, ET 2w, ET 6w).

Supplementary Figure 3 | Histological analysis of electroporated muscles. **(A)** Immunofluorescence images of *TA* from additional ∼8 months-old *C57BL/6J* mice injected with GFP plasmid, electroporated and processed as described in **Figure 1B**. Muscles were stained with anti-GFP (green), anti-F4/80 (orange) antibodies, and Hoechst (blue). BF: Bright Field. Scale bar: 10 μm. Note the presence of both electroporated (GFP^{+ve}) F4/80^{+ve} cells (red asterisks) and F4/80^{-ve} mononucleated muscle cells (red arrows). White asterisks and arrows are, respectively, marking examples of non-electroporated (GFP^{-ve}) F4/80^{+ve} and F4/80^{-ve} mononucleated muscle cells. **(B–D)** CNTR^{-ve} FACS plot referred to **Figures 1I–K** showing CD45^{+ve}CD31^{+ve} cells **(I)**, FAPs **(J)**, and MuSCs **(K)** of *TA* of ∼4 months-old *C57BL/6J* mice injected with PBS and electroporated.

Supplementary Figure 4 | Hyluronidase treatement in dystrophic muscles. **(A)** Representative Bruker *In Vivo* Xtreme I images (left) and GFP intensity measurement (photons/sec/mm^2) (right) of dissected *TA* from ∼6 months-old *mdx^{4Cv}* (MDX) mice injected with hyaluronidase (HYA) or not injected (NOT HYA). 2 h after hyaluronidase injection *TA* muscles were injected with PBS (CNTR^{-ve}) or GFP plasmid (ET) and electroporated. Scale bar: 2.5 mm. White color in the figure (left, top panel) indicates photons/sec/mm^2 $>$ 1.6e+010. Corresponding reflectance images are shown in the bottom panel. Muscles were analyzed 1 week after electroporation. *N* = 3. **(B–E)** CNTR^{-ve} FACS plots referred to **Figures 4H–K** showing CD45^{+ve} cells **(B)**, CD31^{+ve} cells **(C)**, FAPs **(D)**, and MuSCs **(E)** of *TA* of ∼6 months-old *mdx^{4Cv}* mice *C57BL/6J* mice injected with hyaluronidase, then injected with PBS and electroporated.

REFERENCES

Alexakis, C., Partridge, T., and Bou-Gharios, G. (2007). Implication of the satellite cell in dystrophic muscle fibrosis: a self-perpetuating mechanism of collagen overproduction. *Am. J. Physiol. Cell Physiol.* 293, C661–C669. doi: 10.1152/ajpcell.00061.2007

Baghdadi, M., and Tajbakhsh, S. (2018). Regulation and phylogeny of skeletal muscle regeneration. *Dev. Biol.* 433, 200–209. doi: 10.1016/J.YDBIO.2017.07.026

Bengtsson, N. E., Seto, J. T., Hall, J. K., Chamberlain, J. S., and Odom, G. L. (2016). Progress and prospects of gene therapy clinical trials for the muscular dystrophies. *Hum. Mol. Genet.* 25, R9–R17. doi: 10.1093/hmg/ddv420

Biressi, S., Miyabara, E. H., Gopinath, S. D., Carlig, P. M. M., and Rando, T. A. (2014). A Wnt-TGFβ2 axis induces a fibrogenic program in muscle stem cells from dystrophic mice. *Sci. Transl. Med.* 6:267ra176. doi: 10.1126/scitranslmed.3008411

Biressi, S., Molinaro, M., and Cossu, G. (2007). Cellular heterogeneity during vertebrate skeletal muscle development. *Dev. Biol.* 308, 281–293. doi: 10.1016/j.ydbio.2007.06.006

Blau, H. M., Webster, C., and Pavlath, G. K. (1983). Defective myoblasts identified in Duchenne muscular dystrophy. *Proc. Natl. Acad. Sci. U.S.A.* 80, 4856–4860. doi: 10.1073/pnas.80.15.4856

Bloquel, C., Fabre, E., Bureau, M. F., and Scherman, D. (2004). Plasmid DNA electrotransfer for intracellular and secreted proteins expression: New methodological developments and applications *J. Gene Med.* 6, S11–23. doi: 10.1002/JGM.508

Brack, A. S., Conboy, M. J., Roy, S., Lee, M., Kuo, C. J., Keller, C., et al. (2007). Increased Wnt signaling during aging alters muscle stem cell fate and increases fibrosis. *Science* 317, 807–810. doi: 10.1126/science.1144090

Braun, S. (2008). Muscular Gene Transfer Using Nonviral Vectors. *Curr. Gene Ther.* 8, 391–405. doi: 10.2174/156652308786070998

Bryson-Richardson, R. J., and Currie, P. D. (2008). The genetics of vertebrate myogenesis. *Nat. Rev. Genet.* 9, 632–646. doi: 10.1038/nrg2369

Burzyn, D., Kuswanto, W., Kolodin, D., Shadrach, J. L., Cerletti, M., Jang, Y., et al. (2013). A special population of regulatory T cells potentiates muscle repair. *Cell* 155, 1282–95. doi: 10.1016/j.cell.2013.10.054

Chamberlain, J. R., and Chamberlain, J. S. (2017). Progress toward Gene Therapy for Duchenne Muscular Dystrophy. *Mol. Ther.* 25, 1125–1131. doi: 10.1016/j.ymthe.2017.02.019

Chattergoon, M. A., Robinson, T. M., Boyer, J. D., and Weiner, D. B. (1998). Specific Immune Induction Following DNA-Based Immunization Through *In Vivo* Transfection and Activation of Macrophages/Antigen-Presenting Cells. *J. Immunol.* 160, 5707–5718.

Ciciliot, S., and Schiaffino, S. (2010). Regeneration of mammalian skeletal muscle Basic mechanisms and clinical implications. *Curr. Pharm. Des.* 16, 906–914. doi: 10.2174/138161210790883453

Comai, G., and Tajbakhsh, S. (2014). Molecular and Cellular Regulation of Skeletal Myogenesis. *Curr. Top. Dev. Biol.* 110, 1–73. doi: 10.1016/B978-0-12-405943-6.00001-4

Daddi, N., Suda, T., D'Ovidio, F., Kanaan, S., Tagawa, T., Grapperhaus, K., et al. (2002). Recipient intramuscular cotransfection of naked plasmid transforming growth factor beta1 and interleukin 10 ameliorates lung graft ischemia-reperfusion injury. *J. Thorac. Cardiovasc. Surg.* 124, 259–269. doi: 10.1067/MTC.2002.122295

Delaporte, C., Dautreaux, B., Rouche, A., and Fardeau, M. (1990). Changes in surface morphology and basal lamina of cultured muscle cells from Duchenne muscular dystrophy patients. *J. Neurol. Sci.* 95, 77–88. doi: 10.1016/0022-510x(90)90118-7

Delaporte, C., Dehaupas, M., and Fardeau, M. (1984). Comparison between the growth pattern of cell cultures from normal and Duchenne dystrophy muscle. *J. Neurol. Sci.* 64, 149–160. doi: 10.1016/0022-510x(84)90033-9

Dumont, N. A., Wang, Y. X., von Maltzahn, J., Pasut, A., Bentzinger, C. F., Brun, C. E., et al. (2015). Dystrophin expression in muscle stem cells regulates their polarity and asymmetric division. *Nat. Med.* 21, 1455–1463. doi: 10.1038/nm.3990

Dupuis, M., Denis-Mize, K., Woo, C., Goldbeck, C., Selby, M., Chen, M., et al. (2000). Distribution of DNA vaccines determines their immunogenicity after intramuscular injection in mice. *J. Immunol.* 165, 2850–2858. doi: 10.4049/JIMMUNOL.165.5.2850

Furling, D., Coiffier, L., Mouly, V., Barbet, J. P., St Guily, J. L., Taneja, K., et al. (2001). Defective satellite cells in congenital myotonic dystrophy. *Hum. Mol. Genet.* 10, 2079–2087. doi: 10.1093/hmg/10.19.2079

Gam, J. J., DiAndreth, B., Jones, R. D., Huh, J., and Weiss, R. (2019). A "poly-transfection" method for rapid, one-pot characterization and optimization of genetic systems. *Nucleic Acids Res.* 47:e106. doi: 10.1093/NAR/GKZ623

Ganassi, M., Muntoni, F., and Zammit, P. S. (2021). Defining and Identifying Satellite Cell-opathies within Muscular Dystrophies and Myopathies. *Exp. Cell Res.* 411:112906. doi: 10.1016/J.YEXCR.2021.112906

Gargioli, C., Coletta, M., De Grandis, F., Cannata, S. M., and Cossu, G. (2008). PlGF-MMP-9-expressing cells restore microcirculation and efficacy of cell therapy in aged dystrophic muscle. *Nat. Med.* 14, 973–978. doi: 10.1038/nm.1852

Gollins, H., McMahon, J., Wells, K. E., and Wells, D. J. (2003). High-efficiency plasmid gene transfer into dystrophic muscle. *Gene Ther.* 10, 504–512. doi: 10.1038/sj.gt.3301927

Grønevik, E., Tollefsen, S., Sikkeland, L., Haug, T., Tjelle, T., and Mathiesen, I. (2003). DNA transfection of mononuclear cells in muscle tissue. *J. Gene Med.* 5, 909–917. doi: 10.1002/JGM.416

Heredia, J. E., Mukundan, L., Chen, F. M., Mueller, A. A., Deo, R. C., Locksley, R. M., et al. (2013). Type 2 innate signals stimulate fibro/adipogenic progenitors to facilitate muscle regeneration. *Cell* 153, 376–388. doi: 10.1016/j.cell.2013.02.053

Hollinger, K., and Chamberlain, J. S. (2015). Viral vector-mediated gene therapies. *Curr. Opin. Neurol.* 28, 522–527. doi: 10.1097/WCO.0000000000000241

Ionasescu, V., and Ionasescu, R. (1982). Increased collagen synthesis by Duchenne myogenic clones. *J. Neurol. Sci.* 54, 79–87. doi: 10.1016/0022-510x(82)90220-9

Jasmin, G., Tautu, C., Vanasse, M., Brochu, P., and Simoneau, R. (1984). Impaired muscle differentiation in explant cultures of Duchenne muscular dystrophy. *Lab. Invest.* 50, 197–207.

Joe, A. W. B., Yi, L., Natarajan, A., Le Grand, F., So, L., Wang, J., et al. (2010). Muscle injury activates resident fibro/adipogenic progenitors that facilitate myogenesis. *Nat. Cell Biol.* 12, 153–163. doi: 10.1038/ncb2015

Jonuschies, J., Antoniou, M., Waddington, S., Boldrin, L., Muntoni, F., Thrasher, A., et al. (2014). The Human Desmin Promoter Drives Robust Gene Expression for Skeletal Muscle Stem Cell-Mediated Gene Therapy. *Curr. Gene Ther.* 14, 276–288. doi: 10.2174/1566523214666140612154521

Kalajzic, I., Kalajzic, Z., Kaliterna, M., Gronowicz, G., Clark, S. H., Lichtler, A. C., et al. (2002). Use of type I collagen green fluorescent protein transgenes to identify subpopulations of cells at different stages of the osteoblast lineage. *J. Bone Miner. Res.* 17, 15–25. doi: 10.1359/JBMR.2002.17.1.15

Kimura, E., Li, S., Gregorevic, P., Fall, B. M., and Chamberlain, J. S. (2010). Dystrophin delivery to muscles of mdx mice using lentiviral vectors leads to myogenic progenitor targeting and stable gene expression. *Mol. Ther.* 18, 206–213. doi: 10.1038/mt.2009.253

Kobinger, G. P., Louboutin, J. P., Barton, E. R., Sweeney, H. L., and Wilson, J. M. (2003). Correction of the Dystrophic Phenotype by *In Vivo* Targeting of Muscle Progenitor Cells. *Hum. Gene Ther.* 14, 1441–1449. doi: 10.1089/104303403769211655

Kostallari, E., Baba-Amer, Y., Alonso-Martin, S., Ngoh, P., Relaix, F., Lafuste, P., et al. (2015). Pericytes in the myovascular niche promote post-natal myofiber growth and satellite cell quiescence. *Development* 142, 1242–1253. doi: 10.1242/DEV.115386

Kuang, S., and Rudnicki, M. A. (2008). The emerging biology of satellite cells and their therapeutic potential. *Trends Mol. Med.* 14, 82–91. doi: 10.1016/j.molmed.2007.12.004

Latroche, C., Weiss-Gayet, M., Muller, L., Gitiaux, C., Leblanc, P., Liot, S., et al. (2017). Coupling between Myogenesis and Angiogenesis during Skeletal Muscle Regeneration Is Stimulated by Restorative Macrophages. *Stem Cell Rep.* 9, 2018–2033. doi: 10.1016/j.stemcr.2017.10.027

Lemos, D. R., Babaeijandaghi, F., Low, M., Chang, C.-K., Lee, S. T., Fiore, D., et al. (2015). Nilotinib reduces muscle fibrosis in chronic muscle injury by promoting TNF-mediated apoptosis of fibro/adipogenic progenitors. *Nat. Med.* 21, 786–794. doi: 10.1038/nm.3869

Liu, L., Cheung, T. H., Charville, G. W., and Rando, T. A. (2015). Isolation of skeletal muscle stem cells by fluorescence-activated cell sorting. *Nat. Protoc.* 10, 1612–1624. doi: 10.1038/nprot.2015.110

Liu, X., Liu, Y., Zhao, L., Zeng, Z., Xiao, W., and Chen, P. (2017). Macrophage depletion impairs skeletal muscle regeneration: The roles of regulatory factors for muscle regeneration. *Cell Biol. Int.* 41, 228–238. doi: 10.1002/CBIN.10705

Magarò, M. S., Bertacchini, J., Florio, F., Zavatti, M., Potì, F., Cavani, F., et al. (2021). Identification of Sclerostin as a Putative New Myokine Involved in the Muscle-to-Bone Crosstalk. *Biomedicines* 9:71. doi: 10.3390/biomedicines9010071

Mashel, T. V., Tarakanchikova, Y. V., Muslimov, A. R., Zyuzin, M. V., Timin, A. S., Lepik, K. V., et al. (2020). Overcoming the delivery problem for therapeutic genome editing: Current status and perspective of non-viral methods. *Biomaterials* 258:120282. doi: 10.1016/j.biomaterials.2020.120282

McKee, T. J., Perlman, G., Morris, M., and Komarova, S. V. (2019). Extracellular matrix composition of connective tissues: a systematic review and meta-analysis. *Sci. Rep.* 9, 1–15. doi: 10.1038/s41598-019-46896-0

McMahon, J. M., Signori, E., Wells, K. E., Fazio, V. M., and Wells, D. J. (2001). Optimisation of electrotransfer of plasmid into skeletal muscle by pretreatment with hyaluronidase - Increased expression with reduced muscle damage. *Gene Ther.* 8, 1264–1270. doi: 10.1038/SJ.GT.3301522

Melone, M. A., Peluso, G., Petillo, O., Galderisi, U., and Cotrufo, R. (1999). Defective growth *in vitro* of Duchenne Muscular Dystrophy myoblasts: the molecular and biochemical basis. *J. Cell. Biochem.* 76, 118–132. doi: 10.1002/(sici)1097-4644(20000101)76:1<118::aid-jcb12>3.3.co;2-6

Molnar, M. J., Gilbert, R., Lu, Y., Liu, A.-B. B., Guo, A., Larochelle, N., et al. (2004). Factors Influencing the Efficacy, Longevity, and Safety of electroporation-Assisted Plasmid-based Gene. *Transfer into Mouse Muscles.* 10, 447–55. doi: 10.1016/j.ymthe.2004.06.642

Morgan, J., and Cohen, L. (1974). Letter: Crystalline perinuclear inclusions in myoblasts from human dystrophic muscle. *N. Engl. J. Med.* 290:863. doi: 10.1056/NEJM197404112901525

Mozzetta, C., Consalvi, S., Saccone, V., Tierney, M., Diamantini, A., Mitchell, K. J., et al. (2013). Fibroadipogenic progenitors mediate the ability of HDAC inhibitors to promote regeneration in dystrophic muscles of young, but not old Mdx mice. *EMBO Mol. Med.* 5, 626–639. doi: 10.1002/emmm.201202096

Mueller, A. A., van Velthoven, C. T., Fukumoto, K. D., Cheung, T. H., and Rando, T. A. (2016). Intronic polyadenylation of PDGFRα in resident stem cells attenuates muscle fibrosis. *Nature* 540, 276–279. doi: 10.1038/nature20160

Muñoz-Cánoves, P., Neves, J., and Sousa-Victor, P. (2020). Understanding muscle regenerative decline with aging: new approaches to bring back youthfulness to aged stem cells. *FEBS J.* 287, 406–416. doi: 10.1111/febs.15182

Pastoret, C., and Sebille, A. (1995). mdx mice show progressive weakness and muscle deterioration with age. *J. Neurol. Sci.* 129, 97–105. doi: 10.1016/0022-510x(94)00276-t

Peng, B., Zhao, Y., Lu, H., Pang, W., and Xu, Y. (2005). *In vivo* plasmid DNA electroporation resulted in transfection of satellite cells and lasting transgene expression in regenerated muscle fibers. *Biochem. Biophys. Res. Commun.* 338, 1490–1498. doi: 10.1016/j.bbrc.2005.10.111

Pessina, P., Kharraz, Y., Jardí, M., Fukada, S., Serrano, A. L., Perdiguero, E., et al. (2015). Fibrogenic Cell Plasticity Blunts Tissue Regeneration and Aggravates Muscular Dystrophy. *Stem Cell Rep.* 4, 1046–1060. doi: 10.1016/j.stemcr.2015.04.007

Rando, T. A., and Jones, D. L. (2021). Regeneration, Rejuvenation, and Replacement: Turning Back the Clock on Tissue Aging. *Cold Spring Harb. Perspect. Biol.* 13:a040907.* doi: 10.1101/cshperspect.a040907

Ratanamart, J., Huggins, C. G., and Shaw, J. A. M. (2010). Transgene expression in mononuclear muscle cells not infiltrating inflammatory cells following intramuscular plasmid gene electrotransfer. *J. Gene Med.* 12, 377–384. doi: 10.1002/JGM.1448

Rhoads, R. P., Flann, K. L., Cardinal, T. R., Rathbone, C. R., Liu, X., and Allen, R. E. (2013). Satellite cells isolated from aged or dystrophic muscle exhibit a reduced capacity to promote angiogenesis *in vitro*. *Biochem. Biophys. Res. Commun.* 440, 399–404. doi: 10.1016/j.bbrc.2013.09.085

Roche, J. A., Ford-Speelman, D. L., Ru, L. W., Densmore, A. L., Roche, R., Reed, P. W., et al. (2011). Physiological and histological changes in skeletal muscle following *in vivo* gene transfer by electroporation. *Am. J. Physiol. Cell Physiol.* 301, C1239–50.* doi: 10.1152/ajpcell.00431.2010

Sandri, M., Bortoloso, E., Nori, A., and Volpe, P. (2003). Electrotransfer in differentiated myotubes: a novel, efficient procedure for functional gene transfer. *Exp. Cell Res.* 286, 87–95. doi: 10.1016/S0014-4827(03)00097-1

Scharner, J., and Zammit, P. S. (2011). The muscle satellite cell at 50: the formative years. *Skelet. Muscle* 1:28. doi: 10.1186/2044-5040-1-28

Schneider, A. F. E., and Aartsma-Rus, A. (2021). Developments in reading frame restoring therapy approaches for Duchenne muscular dystrophy. *Expert Opin. Biol. Ther.* 21, 343–359. doi: 10.1080/14712598.2021.1832462

Serrano, A. L., and Munoz-Canoves, P. (2010). Regulation and dysregulation of fibrosis in skeletal muscle. *Exp.Cell Res.* 316, 3050–3058. doi: 10.1016/j.yexcr.2010.05.035

Shen, W., Li, Y., Zhu, J., Schwendener, R., and Huard, J. (2008). Interaction between macrophages, TGF-beta1, and the COX-2 pathway during the inflammatory phase of skeletal muscle healing after injury. *J. Cell. Physiol.* 214, 405–412. doi: 10.1002/JCP.21212

Sokołowska, E., and Błachnio-Zabielska, A. U. (2019). A Critical Review of Electroporation as a Plasmid Delivery System in Mouse Skeletal Muscle. *Int. J. Mol. Sci.* 20:2776. doi: 10.3390/IJMS20112776

Somiari, S., Glasspool-Malone, J., Drabick, J. J., Gilbert, R. A., Heller, R., Jaroszeski, M. J., et al. (2000). Theory and *in vivo* application of electroporative gene delivery. *Mol. Ther.* 2, 178–187. doi: 10.1006/MTHE.2000.0124

Stedman, H. H., Sweeney, H. L., Shrager, J. B., Maguire, H. C., Panettieri, R. A., Petrof, B., et al. (1991). The mdx mouse diaphragm reproduces the degenerative changes of Duchenne muscular dystrophy. *Nature* 352, 536–539. doi: 10.1038/352536a0

Uezumi, A., Fukada, S., Yamamoto, N., Takeda, S., and Tsuchida, K. (2010). Mesenchymal progenitors distinct from satellite cells contribute to ectopic fat cell formation in skeletal muscle. *Nat. Cell Biol.* 12, 143–152. doi: 10.1038/ncb2014

Uezumi, A., Ito, T., Morikawa, D., Shimizu, N., Yoneda, T., Segawa, M., et al. (2011). Fibrosis and adipogenesis originate from a common mesenchymal progenitor in skeletal muscle. *J. Cell Sci.* 124, 3654–3664. doi: 10.1242/jcs.086629

van Putten, M., Lloyd, E. M., de Greef, J. C., Raz, V., Willmann, R., Grounds, M. D., et al. (2020). Mouse models for muscular dystrophies: an overview. *Dis. Model. Mech.* 13:dmm043562.

van Velthoven, C. T. J., and Rando, T. A. (2019). Stem Cell Quiescence: Dynamism Restraint, and Cellular Idling. *Cell Stem Cell* 24, 213–225. doi: 10.1016/j.stem.2019.01.001

Verma, M., Asakura, Y., Murakonda, B. S. R., Pengo, T., Latroche, C., Chazaud, B., et al. (2018). Muscle Satellite Cell Cross-Talk with a Vascular Niche Maintains Quiescence *via* VEGF and Notch Signaling. *Cell Stem Cell* 23, 530–543.e. doi: 10.1016/j.stem.2018.09.007

Villalta, S. A., Nguyen, H. X., Deng, B., Gotoh, T., Tidball, J. G., and Tidbal, J. G. (2009). Shifts in macrophage phenotypes and macrophage competition for arginine metabolism affect the severity of muscle pathology in muscular dystrophy. *Hum. Mol. Genet.* 18, 482–496. doi: 10.1093/HMG/DDN376

Wang, X., Zhao, W., Ransohoff, R. M., and Zhou, L. (2016). Identification and Function of Fibrocytes in Skeletal Muscle Injury Repair and Muscular Dystrophy. *J. Immunol.* 197, 4750–4761. doi: 10.4049/jimmunol.1601308

Wang, Y., Wehling-Henricks, M., Samengo, G., and Tidball, J. G. (2015). Increases of M2a macrophages and fibrosis in aging muscle are influenced by bone marrow aging and negatively regulated by muscle-derived nitric oxide. *Aging Cell* 14, 678–688. doi: 10.1111/acel.12350

Wong, S. H. A., Lowes, K. N., Quigley, A. F., Marotta, R., Kita, M., Byrne, E., et al. (2005). DNA electroporation *in vivo* targets mature fibers in dystrophic mdx muscle. *Neuromuscul. Disord.* 15, 630–41. doi: 10.1016/j.nmd.2005.04.008

Wosczyna, M. N., Konishi, C. T., Perez Carbajal, E. E., Wang, T. T., Walsh, R. A., Gan, Q., et al. (2019). Mesenchymal Stromal Cells Are Required for Regeneration and Homeostatic Maintenance of Skeletal Muscle. *Cell Rep.* 27, 2029–2035.e. doi: 10.1016/J.CELREP.2019.04.074

Wosczyna, M. N., and Rando, T. A. (2018). A Muscle Stem Cell Support Group: Coordinated Cellular Responses in Muscle Regeneration. *Dev. Cell* 46, 135–143. doi: 10.1016/j.devcel.2018.06.018

Conflict of Interest: The authors declare that the research was conducted in the absence of any commercial or financial relationships that could be construed as a potential conflict of interest.

frontiers | Frontiers in Physiology

REVIEW
published: 27 April 2022
doi: 10.3389/fphys.2022.837611

What Can We Learn from Single Sarcomere and Myofibril Preparations?

Walter Herzog *

Faculty of Kinesiology, The University of Calgary, Calgary, AB, Canada

Sarcomeres are the smallest functional contractile unit of muscle, and myofibrils are striated muscle organelles that are comprised of sarcomeres that are strictly aligned in series. Furthermore, passive forces in sarcomeres and myofibrils are almost exclusively produced by the structural protein titin, and all contractile, regulatory, and structural proteins are in their natural configuration. For these mechanical and structural reasons single sarcomere and myofibril preparations are arguably the most powerful to answer questions on the mechanisms of striated muscle contraction. We developed and optimized single myofibril research over the past 20 years and were the first to mechanically isolate and test single sarcomeres. The results from this research led to the uncovering of the crucial role of titin in muscle contraction, first molecular explanations for the origins of the passive and the residual force enhancement properties of skeletal and cardiac muscles, the discovery of sarcomere length stability on the descending limb of the force-length relationship, and culminating in the formulation of the three-filament theory of muscle contraction that, aside from actin and myosin, proposes a crucial role of titin in active force production. Aside from all the advantages and possibilities that single sarcomere and myofibril preparations offer, there are also disadvantages. These include the fragility of the preparation, the time-consuming training to master these preparations, the limited spatial resolution for length and force measurements, and the unavailability of commercial systems for single sarcomere/myofibril research. Ignoring the mechanics that govern serially linked systems, not considering the spatial resolution and associated accuracies of myofibril systems, and neglecting the fragility of myofibril preparations, has led to erroneous interpretations of results and misleading conclusions. Here, we will attempt to describe the methods and possible applications of single sarcomere/myofibril research and discuss the advantages and disadvantages by focusing on specific applications. It is hoped that this discussion may contribute to identifying the enormous potential of single sarcomere/myofibril research in discovering the secrets of muscle contraction.

Keywords: titin, actin, myosin, mechanics of contraction, three-filament theory, residual force enhancement, passive force enhancement, serial sarcomeres

Edited by:
Peter T. Wright,
University of Roehampton London,
United Kingdom

Reviewed by:
Anthony Hessel,
University of Münster, Germany
Rene Vandenboom,
Brock University, Canada
Tom Burghardt,
Mayo Clinic, United States

****Correspondence:***
Walter Herzog
wherzog@ucalgary.ca

Specialty section:
This article was submitted to
Striated Muscle Physiology,
a section of the journal
Frontiers in Physiology

Received: *16 December 2021*
Accepted: *06 April 2022*
Published: *27 April 2022*

Citation:
Herzog W (2022) What Can We Learn
from Single Sarcomere and Myofibril
Preparations?
Front. Physiol. 13:837611.
doi: 10.3389/fphys.2022.837611

INTRODUCTION

Muscle physiology is an exciting field that has been studied for thousands of years. Aristotle remarked on the muscular build of Olympic athletes more than 2000 years ago, contemplating their chances of winning, and Milo of Croton, a famous wrestler in ancient Greece, introduced increasing resistance training by lifting a young calf every day and as it grew heavier, requiring increasing strength to complete the task. In the late 15th and early 16th century, Leonardo da Vinci was famous for his immaculate drawings of the human body and its musculature, and in the 17th century, Giovanni Alfonso Borelli calculated the muscular forces required to perform working tasks.

However, muscle physiology as we know it today was formed by some of the greatest physiologists of the 20th century, Nobel Prize winners Otto Meyerhof, AV Hill, and AF Huxley. Their work contributed to our understanding of the muscle energetics, the force-length and force-velocity properties, and the molecular mechanisms underlying muscle contraction. Of particular interest to this treatise is the way we think about muscle contraction. In 1954, Hugh Huxley and Andrew Huxley (Huxley and Hanson, 1954; Huxley and Niedergerke, 1954) arrived independently at the idea that muscle contraction is caused by the sliding of two sets of filaments (actin and myosin) relative to each other, rather than the shortening of the myosin filament, as had been assumed prior to the 1950s. In 1957, Andrew Huxley then proposed a mechanism by which "side-pieces" (now called cross-bridges) from the myosin filament attach cyclically to the actin filament, pulling the actin past the myosin filaments with the energy provided by hydrolyzation of adenosine triphosphate (ATP) (Huxley, 1957). This theory, commonly known as the "cross-bridge theory", is the way muscle contraction appears in textbooks of muscle physiology and is taught in courses of muscle mechanics to this day. Of course, some of the details of the 1957 theory have been revised, but the basic principles of two filaments sliding against each other, powered by cross-bridges and the energy derived from ATP, has remained untouched. For excellent, and highly personal accounts of the discovery of the cross-bridge theory, the associated technical developments, and the discovery of titin, please be referred to Maruyama (1995), Huxley (2004), and Dos Remedios and Gilmour (2017).

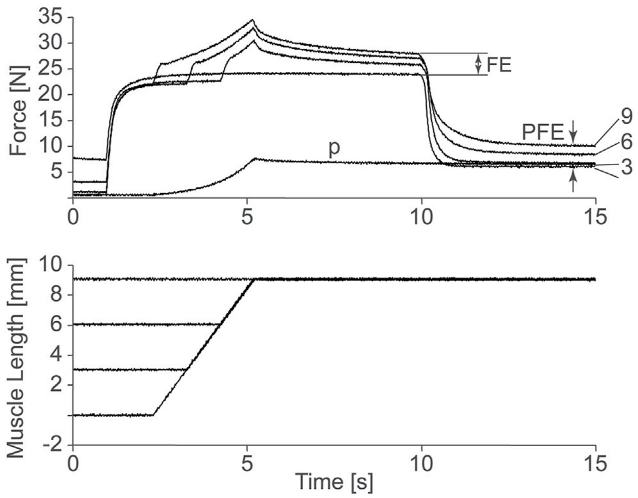

FIGURE 1 | Force as a function of time of a cat soleus muscle stretched 3, 6, and 9 mm, or about 3, 6, and 9% of its total muscle tendon until length. Observe the increase in steady-state isometric force following the active stretches compared to the corresponding purely isometric reference contraction at the final length. This so-called residual force enhancement (FE) increases with increasing stretch magnitude. Also note the increase in passive force following deactivation of the actively stretched muscle compared to the passive force obtained in the passively (P) stretched muscle. This so-called passive force enhancement (PFE) also increases with increasing active stretch magnitudes. Herzog and Leonard, 2002, permission pending.

At this point, it is important to note that the cross-bridge theory has been used successfully to predict muscle force, stiffness, and energetics for shortening (concentric) and constant length (isometric) muscle contractions but has failed to predict these mechanical parameters with equal success for lengthening (eccentric) muscle action (Huxley, 1957). Huxley (1957) was aware of the shortcomings of his initial theory, and remarked greatly on it, and proposed solutions for how the cross-bridge theory may remain untouched and still predict the mechanics of actively lengthening muscles (e.g., Huxley, 1980). In his beautiful book "Reflections on Muscle", Huxley remarked that "special features" may have evolved in muscle to account for the mechanics of eccentric muscle action, and that possibly the development of sarcomere length non-uniformities during active muscle lengthening might be responsible for the unexplained properties observed in lengthening muscle (Huxley, 1980). Among the many unexplained properties of lengthening muscle, two stand out: 1) the long-known increase in steady-state force following active muscle stretching, now referred to as "residual force enhancement" (Abbott and Aubert, 1952; Edman et al., 1982), and 2) the more recent discovery of an increase in passive force during and following active muscle stretching, discovered by us in 2002 in experiments on cat soleus muscle, and now referred to as "passive force enhancement" (Herzog and Leonard, 2002). Passive force enhancement is the increase in (passive) force after a muscle has been actively stretched and then deactivated (**Figure 1**). It is most prominent and best observed in muscle preparations that are stretched to lengths where passive force occurs naturally. Passive force enhancement is long-lasting (minutes), increases with increasing active stretch amplitude, and is seen across all structural levels, including single sarcomeres, and thus is speculated to be associated with titin.

The discovery that the passive force, force not created by the contractile filaments actin and myosin, is increased in active compared to passive muscle, changed the way many scientists thought about muscle contraction and brought up two fundamental questions: 1) what passive element(s) in muscle causes this increase in passive force when a muscle is activated and stretched, and 2) what are the molecular mechanisms underlying this increase in passive force? These two questions, we felt, could not be answered using traditional methodologies, but required the complete control of individual sarcomeres. Research on a higher structural level than the sarcomere, single fibres for example, are deemed not useful in this

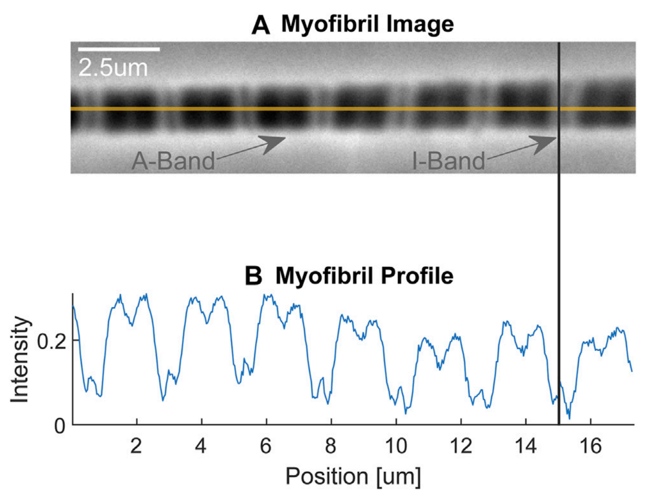

FIGURE 2 | (A) Single myofibril with dark-light striation pattern. The dark areas represent the A-bands containing the thick (myosin) filaments, while the light areas represent the I-bands containing the thin (actin) filaments. The faint dark line in the approximate centre of the I-bands is the Z-line delineating the end of the sarcomeres (indicated also with the vertical line connecting figures **(A,B)**. The myofibril is attached on its left-hand end to a rigid glass pipette, which in turn is attached to a piezo-tube motor that allows for nano-metre step size control (not shown) and is attached on its right-hand end to a silicon nitride nano-lever for force measurements (not shown). **(B)** Light intensity pattern of the myofibril shown in **(A)**. The dark, A-bands are given high intensity values, while the light, I-bands, are given small intensity values. Republished with permission of Royal Society, from Dynamics of individual sarcomeres during and after stretch in activated single myofibrils. Rassier DE, Herzog W, Pollack GH. Proc. R Soc Lond Volume 270, *p*. 1735–1740. 2003; permission conveyed through Copyright Clearance Center Inc.

context, as the crucial variables of individual sarcomere forces and individual sarcomere lengths, cannot be determined uniquely, as there is no possibility to measure or theoretically determine sarcomere forces in this highly mechanically redundant system, and a technique to measure the thousands of individual sarcomere lengths simultaneously in a single muscle fibre does not exist. Research on a lower structural level, for example using isolated cross-bridges and actin filaments, as introduced in laser trapping experiments by Finer et al. (1994), were also deemed less meaningful than myofibril preparations, as the intricate structural integrity of the sarcomere, that we believe plays a crucial role in the molecular details of muscle contraction, is lost.

For these reasons, we started to develop techniques to work with single myofibril and single, mechanically isolated sarcomere preparations. The topic of this special issue is on methods used in striated muscle mechanics and physiology, and here, we would like to describe the methods for single sarcomere and myofibril preparations. However, the technical details of these preparations can be obtained in any of the many manuscripts we (and others) have published on the topic, and thus, they will just be described briefly. More importantly, when working with single myofibrils and sarcomeres, information can be obtained that cannot be gathered from other muscle preparations. We will focus on these advantages of myofibrils over other structural preparations but will also point out the limitations of working with myofibrils and the errors that have been made by not recognizing and acknowledging these limitations.

METHODS

Single Myofibril Preparation for Mechanical Testing

Typically, we work with rabbit psoas myofibrils, but myofibrils from other muscles can be prepared in a similar manner. We isolate strips of rabbit psoas muscle from euthanized animals using forceps and tie them to wooden sticks to preserve the *in-situ* sarcomere length and prevent shrinking. These strips are then placed in a rigor-glycerol solution with protease inhibitors (Complete, Roche Diagnostics, Montreal, QB, Canada) and are then stored at −20°C for about 12 ± 2 days. On the day of experimentation, the muscle strips are placed in a +4°C rigor solution, homogenized, and placed in the experimental chamber that is typically held at room temperature of 20°C.

The mechanical testing is done by attaching the isolated myofibrils to a force transducer at one end and a glass pipette attached to a motor at the other end (**Figure 2**). Attachment to the force levers is either done by wrapping the myofibril around the force lever, or by gluing the myofibril to the force lever. Attachment to the rigid glass pipette is done by attaching a small amount of glue to the end of the pipette and then piercing the pipette into the z-line region of the end sarcomere of a myofibril. Experiments are performed on the stage of an inverted light microscope. We typically use a ×100 oil immersion objective (NA 1.3) and have the possibility to add a ×2.5 Optovar configuration for a total magnification of ×250. Depending on the question, we use myofibrils containing one (single sarcomere preparation) and up to about 20 sarcomeres. Individual sarcomere lengths are measured continuously using a linear photo diode array camera. Frequently, we define sarcomere lengths from the centroid of the A-band of one sarcomere to the centroid of the A-band of the adjacent sarcomere, but in a good preparation, where the Z-lines can be identified clearly, we measure sarcomere lengths in the traditional way from centroid to centroid of adjacent Z-lines. We use a glass pipette attached to a custom-built piezo-tube motor to perform any desired length change of a myofibril for mechanical testing. Passive and active forces in the myofibrils are measured using custom-built nanofabricated silicon nitride cantilevers with stiffness ranging from 20–200 pN/nm depending on the forces expected in active or passive experiments at different sarcomere lengths, and for shortening, isometric and lengthening contractions, all of which affect the force capacity of the myofibril. Knowing the stiffness of the nano-levers, force can be calculated by the displacement of the lever from its resting position. Typically, forces are normalized relative to the cross-sectional area for comparison between myofibrils of different size.

The great advantage of a single myofibril preparation is that all sarcomeres are strictly arranged in series. This in series alignment ensures that each sarcomere and half-sarcomere transmits the same force and that this force can be measured at the end of the myofibril (neglecting any inertial effects and mass movements, which can safely be done in myofibril preparations). More details on the properties of in series mechanical systems, how they behave, and how they can be represented mathematically, may be obtained in Epstein et al. (2006). Since a single myofibril also allows for the determination of each sarcomere and half-sarcomere length, the instantaneous force, sarcomere length, and sarcomere rate of change in length (speed of contraction) are known at any instant in time, allowing for a complete description of the mechanics of all sarcomeres. However, the concept of a system of elements that are mechanically "in series" must be treated properly, otherwise it may lead to incorrect interpretations of results and misleading conclusions, as has happened in some recent works (Mendoza and Rassier, 2020).

Single Sarcomere Isolation for Mechanical Testing

For mechanical isolation and testing of a single sarcomere, a short myofibril consisting of 5–10 sarcomeres is attached at both ends as described above using micro-manipulators that allow for movements in the sub-nano-metre range. Once attached in this manner, the sarcomere closest to the force lever is isolated by using a third micromanipulator with a stiff glass pipette and attaching it to the Z-line of that sarcomere that is away from the force lever. This third micromanipulator is then attached to the piezo-tube motor that is used for imposing length changes to the sarcomere (Leonard et al., 2010). It is a powerful but technically difficult preparation to set up properly and obtain meaningful results (Herzog et al., 2016; Schmidt et al., 2021).

One of the great advantages of the single sarcomere preparation is that the complex interaction of parallel and serially arranged sarcomeres, as they occur in single fibre and single myofibril preparations respectively, is eliminated. Therefore, the mechanical properties of this basic contractile unit of muscle can be measured without interference caused by sarcomere length non-uniformities, force transmission across the Z-lines, uneven activation of sarcomeres in a myofibril, single fibre or muscle preparation, and without passive force contributions by structural proteins and the collagen matrix network except for the forces produced by the molecular spring titin (Bartoo et al., 1997) (Linke et al., 1994) (Colomo et al., 1997) (Linke, 2018).

APPLICATIONS

There are dozens of applications that have shed light into the mechanisms of muscle contraction in general, and the role of titin specifically, using single myofibril and single sarcomere preparations. Here, we would like to briefly mention three such applications that have changed the way we think about muscle contraction today as compared to just a decade ago:

1) The discovery of titin as a spring of variable stiffness.
2) The discovery of residual force enhancement in a single sarcomere.
3) The discovery of activation-dependent unfolding of titin segments.

Titin as a Spring of Variable Stiffness

With the discovery of the passive force enhancement property in skeletal muscle, we proposed that titin might cause passive—and at least some of the residual—force enhancement in skeletal muscle (Herzog and Leonard, 2002). This proposal was supported in elegant experiments by Labeit et al. (2003), who studied recombinant PEVK segments of titin containing two highly conserved elements. Using single molecule experiments they showed that calcium-induced conformational changes altered the stiffness in these conserved PEVK fragments. Further experiments by Labeit et al. (2003) using skinned single fibers from the mouse soleus showed that titin-based force was dependent on activation. Experiments on myofibril preparations arrived at the same conclusion when single myofibrils from rabbit psoas were stretched in baths containing different concentrations of calcium. The advantage of the single myofibril over the single fibre preparation was that titin-based forces could be directly quantified by inhibiting cross-bridge based forces either chemically (Leonard and Herzog, 2010) or by selective deletion of regulatory proteins (Joumaa et al., 2008) and knowing that titin was the only structural element in sarcomeres contributing to the passive force (Bartoo et al., 1997). Further experiments on recombinant immunoglobulin domains of cardiac titin also revealed that calcium binds to these segments in a dose-dependent manner, that calcium binding is reversed when calcium is removed, and that unfolding the immunoglobulin domains in the presence of calcium requires about 20% more force than the corresponding unfolding forces in the absence of calcium (**Figure 3**) (Duvall et al., 2013). The conclusion from these studies was that titin is a calcium dependent molecular spring; that is, the stiffness of titin changes depending on the active state of a muscle.

Residual Force Enhancement in a Single Sarcomere

For approximately the past 70 years, it has been believed that sarcomere lengths and sarcomere forces are unstable once sarcomeres reach lengths greater than their optimal lengths (Hill, 1953); that is, when sarcomeres operate on the descending limb of the force-length relationship where actin-myosin filament overlap decreases with increasing length, thereby reducing the number of possible cross-bridge attachments between actin and myosin, thus decreasing the steady-state, isometric force. This notion of instability led to the idea that muscles stretched on the descending limb of the force-length relationship exhibit residual force enhancement because of the development of sarcomere length non-uniformities. A basic premise of this theory is that purely isometric contractions are associated with essentially uniform sarcomere lengths even on the descending limb of the force-length relationship, while stretching an active muscle on the descending limb causes rapid elongation of "weak" sarcomeres, causing great non-uniformities in

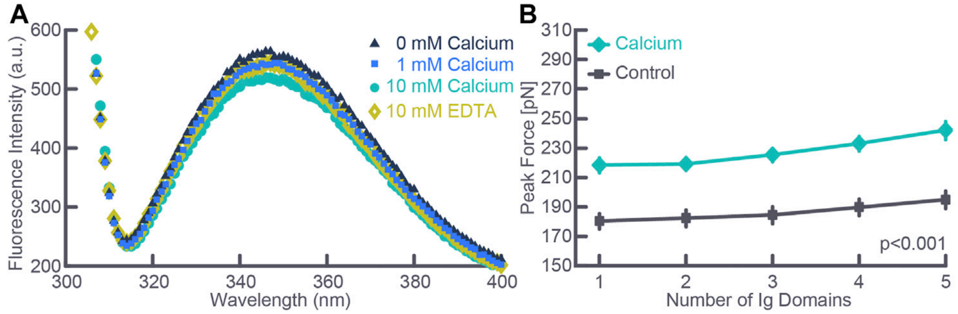

FIGURE 3 | (A) Fluorescence intensity measured using spectroscopy as a function of calcium concentration for an exemplar test. Note the depression of the peak intensity fluorescence with increasing calcium concentration and the reversal of the peak fluorescence intensity when removing free calcium using EDTA. **(B)** Force required to cause unfolding of five immunoglobulin domains in the absence (Control) and the presence (Calcium) of physiologically relevant calcium concentration. Note that the force required for immunoglobulin unfolding increased by about 20% in the presence of calcium. Note also, the slight increase in force required with each unfolding event despite identical immunoglobulin domains which is explained by the stochastic nature of the unfolding events. The total number of observations for each data point was greater than 300 in all cases, and data points where the standard deviation bars cannot be seen indicates that the standard deviations were smaller than the size of the data point. Republished with permission of American Physiological Society, from Passive force enhancement in striated muscle. Herzog W. Journal of Applied Physiology 126 (6): 1782–1789. 2019; permission conveyed through Copyright Clearance Center Inc.

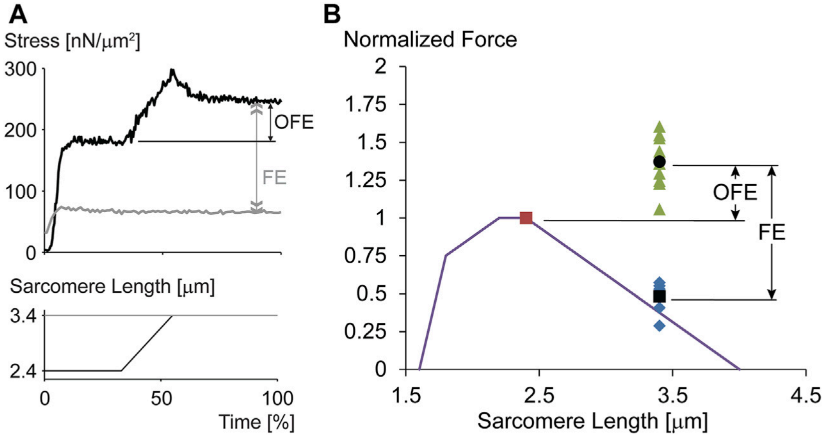

FIGURE 4 | (A) Force-time and sarcomere length-time trace for an exemplar experiment performed on a single, mechanically isolated sarcomere. The isometric reference contraction at a sarcomere length of 3.4 μm is shown in gray, and the corresponding force enhancement test (stretch from a sarcomere length of 2.4–3.4 μm) is shown in black. Note that the initial isometric contraction for the force enhancement test (black trace) was performed at optimal sarcomere length for the rabbit psoas sarcomere used here. Observe the dramatic force enhancement, FE (greater than 200% in this example), and the substantial force above the maximal isometric force at optimal length (OFE). **(B)** Theoretical sarcomere force-length relationship for rabbit skeletal muscle and isometric reference force obtained at optimal sarcomere length (red dot, normalized to 1.0), the corresponding isometric reference forces obtained at a sarcomere length of 3.4 μm, and the corresponding isometric, steady state forces obtained after stretching single sarcomeres from 2.4 to 3.4 μm while activated. The average force enhancement (FE; average values are indicated by the black dots) was 185% and the average enhanced forces exceeded the isometric optimal reference forces (OFE) by 38%. In summary, single mechanically isolated sarcomeres show great residual force enhancement and exceeded the isometric references forces at optimal sarcomere length in all cases when stretched from optimal (2.4 μm) to the final (3.4 μm) sarcomere length. Republished with permission of American Physiological Society, from Residual force enhancement following eccentric contractions: a new mechanism involving titin. Herzog W., Schappacher Tilp G, DuVall M, Leonard TR, Herzog J. Physiology 31: 300–312. 2016; permission conveyed through Copyright Clearance Center Inc.

sarcomere length that then give rise to the residual force enhancement (e.g., Morgan, 1994). This theory has support to this day, including from experiments using single myofibrils (e.g., Rassier and Pavlov, 2012), even though it has been shown unequivocally that vertebrate muscles are inherently and naturally comprised of sarcomeres of highly non-uniform lengths even in the passive state and during isometric contractions (Huxley and Peachey, 1961; Llewellyn et al., 2008; Johnston et al., 2016; Moo et al., 2016).

The sarcomere length non-uniformity theory can be used to make detailed and testable hypotheses about the properties of residual force enhancement. The most prominent of these hypotheses are that residual force enhancement cannot occur on the ascending limb of the force-length relationship (as there is no sarcomere length instability on that part of the relationship), residual force enhancement cannot exceed the plateau forces of the isometric force-length relationship (as the enhanced forces are limited to what the active sarcomeres can produce at optimal actin-myosin filament overlap), and residual force enhancement is associated with sarcomere length non-uniformities that are greater than the essentially uniform sarcomere lengths assumed for isometric contractions. All these predictions of the sarcomere length non-uniformity theory have been rejected in multiple experiments (e.g., Rassier et al., 2003; Peterson et al., 2004; Rassier, 2012; Johnston et al., 2019). Nevertheless, the ultimate proof that residual force enhancement does not depend on the development of non-uniformities in sarcomere lengths but is an inherent property of muscle, did not exist until residual force enhancement was shown to occur in single, mechanically isolated sarcomeres. For this reason, we developed the single sarcomere preparation that allowed mechanical experiments and the determination of residual force enhancement in this basic contractile unit of muscle. Not only was it shown that residual force enhancement existed in each of the single sarcomeres tested (**Figure 4**), but the force enhancement following a stretch from 2.4 to 3.4 μm averaged an impressive 185% and the average enhanced force exceeded the maximal isometric force at the plateau of the force-length relationship by 38% (Leonard et al., 2010). Since force enhancement needs to exist in both half-sarcomeres, the argument that a non-uniformity in the two half-sarcomeres could explain the results is not valid. These experiments demonstrated that the residual force enhancement property is contained within a sarcomere and does not require the development of non-uniform sarcomeres. However, it does not exclude the possibility that sarcomere length non-uniformities might contribute to the residual force enhancement on top of the force enhancement obtained due to the sarcomere internal mechanics. In fact, in some experiments using single myofibrils and sarcomeres it was concluded that residual force enhancement has a "component associated with half-sarcomere dynamics, which significantly increases the level of force enhancement after stretch." (e.g., Rassier and Pavlov, 2012). However, these results (Figure 8A in Rassier and Pavlov, 2012) must be considered with caution as the half-sarcomere length non-uniformities measured were given in ~0.4 nm increments with a maximal value of 12 nm. Such accuracy cannot be achieved with the light microscopy used in that study and comprises random noise. For sub-nm accuracy of contractile specimens, approaches such as low angle x-ray diffraction are required (Ma and Irving, 2019). Sarcomere and half-sarcomere length changes with light microscopy need to exceed about 100 nm for reliable detection (Schmidt et al., 2021).

In summary, experiments on single, mechanically isolated sarcomeres demonstrate that residual force enhancement is a property inherent to a single sarcomere. Non-uniformity of sarcomeres or half-sarcomeres has not been demonstrated to contribute directly to residual force enhancement.

Activation-Dependent Unfolding of Titin Segments

Titin is the third most abundant protein in skeletal muscle. It extends from the M-band across the half sarcomere and inserts into the Z-line bound to actin (**Figure 5**). Titin acts like a molecular spring in the I-band region and its segments unfold sequentially when a muscle/sarcomere is stretched, and then refold upon muscle/sarcomere shortening (Linke et al., 1999; Granzier and Labeit, 2002; Labeit et al., 2003). Titin steadies the myosin filament in the centre of the sarcomere, provides passive force, and is implicated in force signaling (Horowits et al., 1986; Horowits and Podolsky, 1987; Horowits, 1992; Bartoo et al., 1997; Herzog, 2018; Schappacher-Tilp, 2018). In 2002, when discovering that passive forces were greater in actively compared to passively stretched muscles, we proposed that I-band titin is an activatable spring that can change its stiffness, and thus its force contribution when a muscle is stretched. Even though the idea that titin is an adjustable spring had been formulated before (e.g., Helmes et al., 1999; Freiburg et al., 2000; Granzier and Labeit, 2002), these ideas were typically in the context of long-term adaptations, expressions of different isoforms, and changes caused by post-translational modifications. Our suggestion was that titin could adjust its spring stiffness "instantaneously" by changing its inherent spring length when a muscle was activated and produced actin-myosin-based active force. Two possibilities were suggested for the change in titin stiffness: 1) calcium binding to specialized segments of titin, thereby increasing the force required for unfolding of these segments, and 2) titin shortening its free spring length by attaching its proximal segment to actin (e.g., Leonard and Herzog, 2010). The proximal segment was proposed since titin is known to be permanently bound to actin at its proximal end, approximately 80–100 nm from inserting into the Z-line (Trombitas and Granzier, 1997).

In order to determine the elastic properties of titin in passive and active muscle, Horowits et al. (1989) used titin antibody labeling to measure the extension of proximal and distal titin segments in skinned rabbit psoas fibers using immunoelectron microscopy. They concluded that titin remained rigidly attached to the myosin filament and that the I-band elastic properties of titin were unaffected by activation. However, following antibodies in whole fibre preparations is difficult due to the large number of labels and the distortions of parallel aligned myofibrils within a fibre. Using titin specific antibodies in rabbit psoas myofibrils, we observed distinct differences in the unfolding characteristics of titin segments in actively and passively stretched myofibrils. In passively stretched myofibrils, titin elongated according to its known elastic properties in its entire I-band length (**Figure 6**). In actively stretched myofibrils, the proximal segments stopped elongating after a small stretch, suggesting that the proximal segment had become infinitely stiff. The interpretation of this observation was that titin binds to actin in actively stretched muscle, thereby losing its ability to elongate its proximal region, shortening its free spring element, thereby increasing its stiffness and force upon stretch (Duvall et al., 2017; Herzog, 2018). Although these experiments, and associated interpretations, need further independent confirmation, they suggest that titin elasticity changes when a muscle is activated. The molecular details of this change in titin elasticity remain speculation, and even though we have tentatively proposed that it occurs through binding of titin to actin, this suggestion needs direct verification in live sarcomere or myofibril preparations, rather than fixed

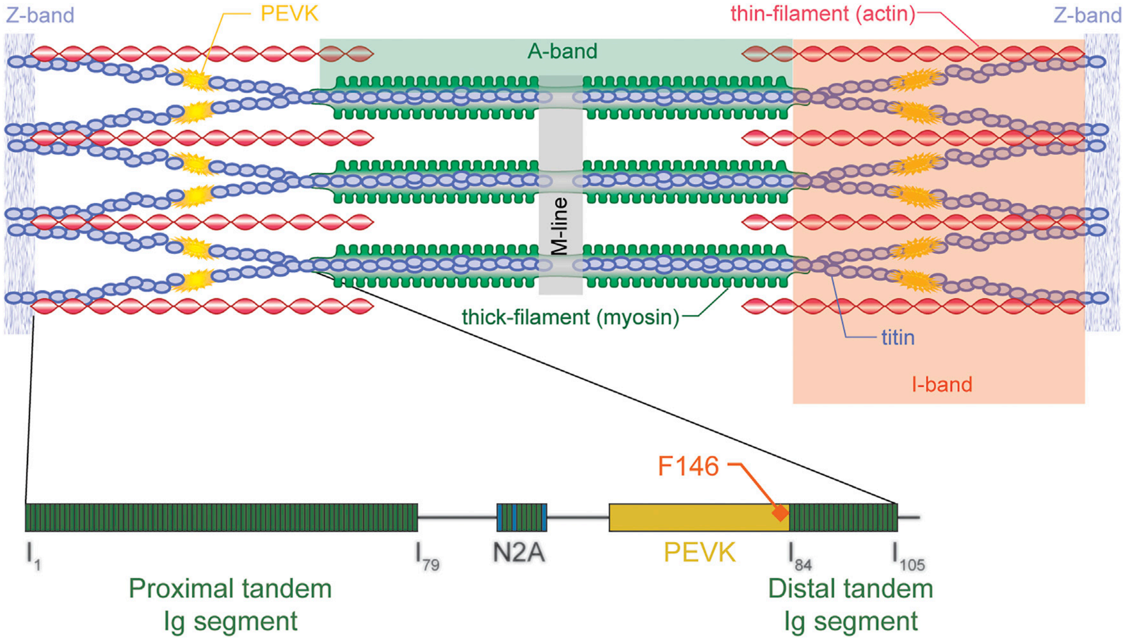

FIGURE 5 | Schematic illustration of a sarcomere (top) with actin, myosin, and titin (and titin's molecular structure - bottom) indicated. Titin inserts into the M-line in the middle of the sarcomere and the Z-line at the end of the sarcomere, thus spanning the entire half-sarcomere. Titin is "rigidly" bound to the myosin filament in the A-band region but runs freely across most of the I-band region, except at the very proximal end where it merges with actin just prior to inserting into the Z-line. In the I-band region, titin elongates, thus producing passive force when a sarcomere is stretched. For physiologically relevant elongations of skeletal muscles, titin's immunoglobulin become aligned and the PEVK segment elongates. Only towards the end of physiologically relevant elongations, or when the muscle is active (rather than passive) is it thought that immunoglobulin (Ig) domains unfold. Shown is also the F146 antibody (for further details see text below) which attaches to the distal end of the PEVK domain of titin. Republished with permission of John Wiley & Sons, Inc., from Structure-function relations of the giant elastic protein titin in striated and smooth muscle cells. Granzier H, Labeit S. Muscle & Nerve Volume 36, *p.* 740–755. 2007; permission conveyed through Copyright Clearance Center Inc.

preparations or motility assays, as we believe that the arrangement of contractile, structural, and regulatory proteins that exists in sarcomeres is of crucial importance to the function and interactions of these proteins during muscle contraction.

Advantages and Limitations of Myofibril Preparations for Studying Muscle Mechanics and Physiology

A great advantage of single myofibrils over any other muscle preparation is that myofibrils are comprised of sarcomeres that are strictly arranged in series. An in-series arrangement of sarcomeres means that each sarcomere and half-sarcomere must have the same internal force at each instant in time, independent of its material properties and regardless of its history of loading. The advantage of such an arrangement is that the force in each sarcomere can be measured with a force transducer at the end of the myofibril. Together with the relative ease of sarcomere length measurements in myofibrils, the entire mechanics of a sarcomere (force, length, and rate of change in length, that is its velocity of shortening or stretching) is known at any instant in time.

Another advantage of the myofibril preparation is that passive force arises essentially exclusively from the structural protein titin (Bartoo et al., 1997; Herzog et al., 2012). Therefore, the mechanical properties of a single, passive myofibril represent well the mechanical properties of the assembly of titin filaments in sarcomeres (Kellermayer et al., 1997). Furthermore, it is trivial in single myofibrils to manipulate cross-bridge binding, the amount of functional titin filaments, control the level of activation of each sarcomere, and manipulate the length and rate of change in length of sarcomeres accurately, thus presenting a plethora of possibilities for studying the role of titin under a variety of precisely known and precisely controllable contractile, mechanical, and activation conditions. We have used single myofibril and mechanically isolated sarcomere preparations to identify the changing force and stiffness properties of titin as a function of activation (calcium concentration), cross-bridge-associated force production, and contractile conditions, which allowed for the proposal of the three-filament (actin, myosin, and titin) theory of muscle contraction and force production (Leonard and Herzog, 2010; Herzog et al., 2015; Schappacher-Tilp et al., 2015; Herzog, 2018).

However, like any scientific approach, the myofibril preparation also has disadvantages. Primary among them the fact that there is no commercial system for myofibril and single sarcomere testing. Also, myofibril preparations are fragile, and it typically takes months of training before one can expect reliable results. Furthermore, it takes great patience to obtain and set up myofibrils for multiple activation cycles, and experiments not accounting for the force loss

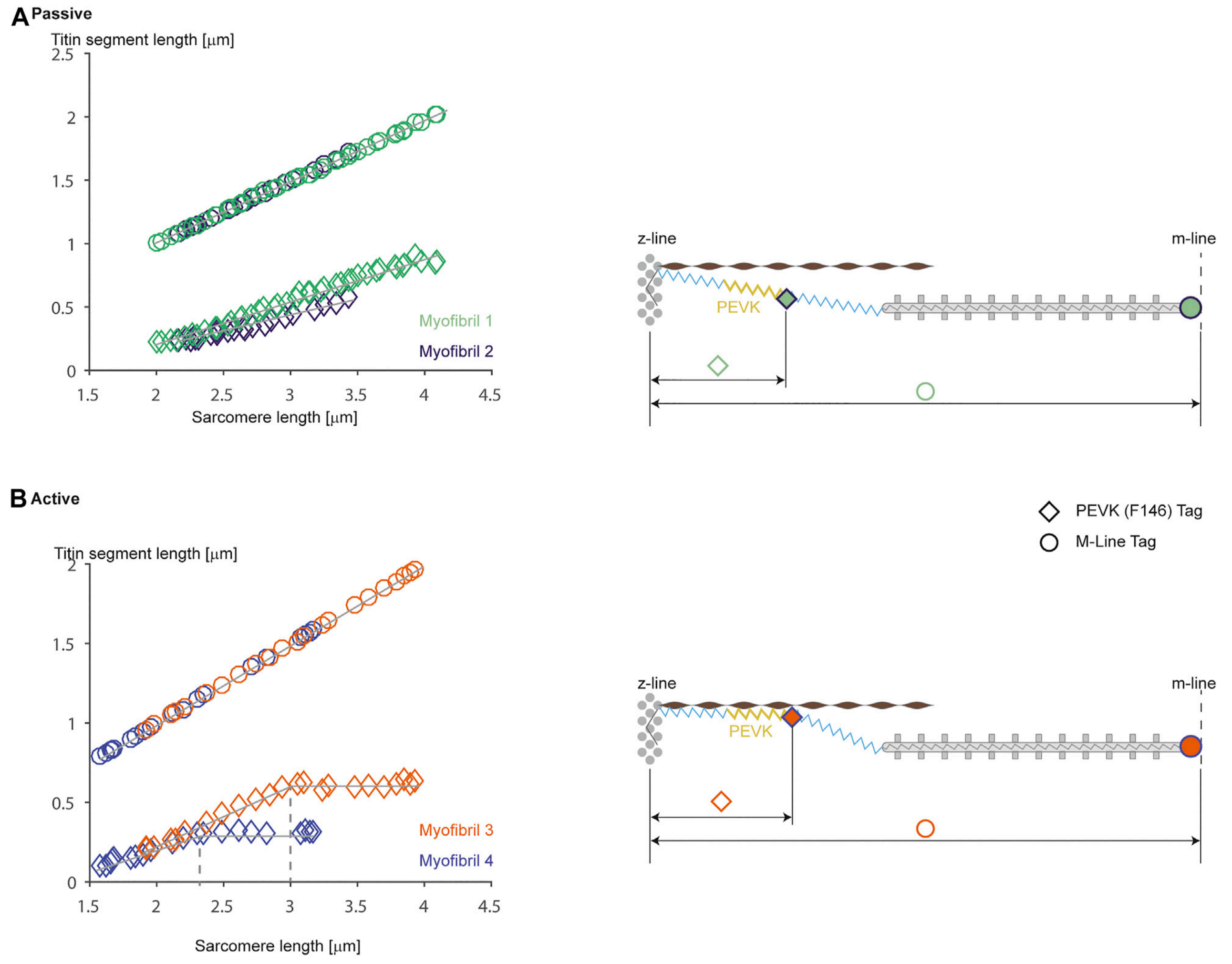

FIGURE 6 | Passive **(A)** and active **(B)** stretching of proximal titin segments labeled using an antibody [F146 that binds to the PEVK region (diamond symbols)] region that allows for measurements of proximal and distal titin segment elongations during passive and active stretching of single rabbit psoas sarcomeres. Figures on the left show elongation of the half-sarcomere [top traces (circular symbols) using an M-line label] and elongations of the proximal titin segment (bottom traces: from the Z-line to the F146 label) for two representative sarcomeres from two different myofibrils. Note in **(A)** (passive stretching) that the two proximal titin segments elongate continuously with half-sarcomere elongations, reaching final lengths of approximately 0.95 μm (at a sarcomere length of 4.0 μm) and about 0.6 μm (at a sarcomere length of about 3.5 μm). In contrast, when the myofibrils are stretched while activated, the proximal segments elongate similarly to the elongations observed in the passive condition, but then stop elongating and remain substantially shorter than in the passive case (i.e., with a length of about 0.6 and 0.35 μm, respectively). The panels on the right illustrate schematically what we believe might be happening. In the passive stretch **(A)**, the proximal and distal titin segments elongate in accordance with their stiffness properties. In the active stretch **(B)**, titin is thought to attach to actin at some point during the stretch, thereby shortening titin's free spring length, increasing its stiffness, eliminating elongation of the proximal titin segment, and increasing titin-based force. Republished with permission of American Physiological Society, from Residual force enhancement following eccentric contractions: a new mechanism involving titin. Herzog W., Schappacher Tilp G, DuVall M, Leonard TR, Herzog J. Physiology 31: 300–312. 2016; permission conveyed through Copyright Clearance Center Inc.

caused by repeat myofibril activation have led to erroneous conclusions (e.g., Cornachione et al., 2016), for example, in the proposed role of titin in cardiac muscle (Herzog, 2016). Other limitations of myofibril systems include that forces are often measured using relatively compliant nano-levers, thus there is some shortening of myofibrils and sarcomeres when force increases. For example, for our active force measurements in myofibrils, we use a nano-lever with a stiffness of 200 pN/nm. For a maximal isometric contraction of a myofibril at optimal sarcomere length, forces reach values of about 150 nN, thus the lever will bend by an amount of about 750 nm, causing the myofibril to shorten by the same amount. For an average myofibril comprised of 10 serially aligned sarcomeres at optimal length (10 × 2.4 μm for the rabbit psoas muscle), the total length before activation would be about 24 μm or 24,000 nm. A shortening of 750 nm due to lever compliance therefore constitutes a shortening of about 3% of the myofibril and thus the average sarcomere length. Or in other words, a sarcomere of 2.400 μm before activation would shorten to about 2.325 μm, a difference that would be hard to detect reliably with light microscopy. In order to minimize shortening during force production and maintain a good resolution for force measurements, we (and others) developed systems based on the principle of atomic force microscopy with negligible bending of the force lever (stiffness of 2–4 nN/nm) upon myofibril activation (e.g., Telley et al., 2006; Duvall et al., 2017).

Another limitation of the myofibril system is the accuracy with which absolute forces can be determined. Absolute force depends on the stiffness of the nano-force levers, the fixation technique (with or without glue, where on the lever the myofibril is attached), and the optical resolution of light microscopy. However, even though absolute forces might not be as accurate as one might wish, relative changes in force can be identified easily. For example, in experiments aimed at comparing force levels between an isometric reference contraction and a force enhanced state, forces are normalized to the isometric reference contraction, and force enhancement is provided as a percent change from the reference force. Therefore, any systematic error, for example, an error in nano-lever stiffness, would not affect this result. However, if one is interested in accurate absolute forces of a myofibril, factors that may affect the stiffness of the nano-levers used for force measurements, would need to be carefully accounted for.

When testing single myofibrils, sarcomere lengths are obtained using light microscopy which limits the spatial resolution to about 200 nm. For typical experiments, this resolution limit is not a problem. However, when trying to identify potential step-wise shortening of sarcomeres in the nano-metre range (e.g., Pollack et al., 1977; Pollack, 1986) or relate sub-nano-metre non-uniformities in half-sarcomere lengths to residual force enhancement properties (e.g., Rassier, 2012; Rassier and Pavlov, 2012), methods other than light microscopy need to be used. Optical resolution providing sub-nm accuracy are possible using electron microscopy or low angle x-ray diffraction (Ma and Irving, 2019). However, electron microscopy requires fixed specimens and cannot be performed on live muscles/myofibrils that are contracting and changing length, and while x-ray diffraction can be used with live and contracting muscle preparations, optimal diffraction patterns require specimens that are greater than single myofibrils/sarcomeres. Careful analysis of the capability of sarcomere length measurements in myofibril preparations using light microscopy suggests that a feasible accuracy may be in the 100 nm range, under extremely favourable conditions, changes of 50 nm might be detectable (Schmidt et al., 2021).

CONCLUSION

Single myofibril and single sarcomere preparations offer great advantages to study the molecular mechanisms of muscle contraction with the sarcomeric proteins in their natural configuration. We believe that the proper protein configuration is of utmost importance when trying to determine the molecular details of muscle contraction, and differences in the structural arrangement of the contractile, regulatory and structural proteins might explain differences in observations made with myofibril, single molecule (e.g., Finer et al., 1994), or motility assay preparations (e.g., Riveline et al., 1998). Single myofibrils also have the advantage of serially arranged sarcomeres and the possibility to measure force, length, and rate of change in length for each sarcomere. However, myofibril experiments are technically difficult, require intensive and time-consuming training, and myofibrils are fragile, thus usually only allowing for a handful of experiments per specimen. Furthermore, the limits of accuracy in sarcomere lengths and force measurements, as well as the mechanics of serially linked mechanical systems must be kept in mind when interpreting results and formulating conclusions.

AUTHOR CONTRIBUTIONS

WH is responsible for all parts of this work.

FUNDING

This study was partly supported by, NSERC of Canada RPGIN-2020-03920 Canada Research Chair Programme 950-200955 The Killam Foundation 10001203, The Canada Research Chair Programme, and the Killam Foundation.

ACKNOWLEDGMENTS

I would like to acknowledge the technical expertise of Tim Leonard who designed and built all of our single sarcomere and myofibril testing stations and performed many of the crucial experiments cited here, and Azim Jinha for writing the corresponding data collection and analysis software.

REFERENCES

Abbott, B. C., and Aubert, X. M. (1952). The Force Exerted by Active Striated Muscle during and after Change of Length. *J.Physiol.* 117, 77–86. doi:10.1113/jphysiol.1952.sp004755

Bartoo, M. L., Linke, W. A., and Pollack, G. H. (1997). Basis of Passive Tension and Stiffness in Isolated Rabbit Myofibrils. *Am. J. Physiology-Cell Physiol.* 273, C266–C276. doi:10.1152/ajpcell.1997.273.1.c266

Colomo, F., Piroddi, N., Poggesi, C., te Kronnie, G., and Tesi, C. (1997). Active and Passive Forces of Isolated Myofibrils from Cardiac and Fast Skeletal Muscle of the Frog. *J. Physiol.* 500 (Pt 2) (Pt 2), 535–548. doi:10.1113/jphysiol.1997.sp022039

Cornachione, A. S., Leite, F., Bagni, M. A., and Rassier, D. E. (2016). The Increase in Non-cross-bridge Forces after Stretch of Activated Striated Muscle Is Related to Titin Isoforms. *Am. J. Physiology-Cell Physiol.* 310, C19–C26. doi:10.1152/ajpcell.00156.2015

Dos Remedios, C., and Gilmour, D. (2017). An Historical Perspective of the Discovery of Titin Filaments. *Biophys. Rev.* 9, 179–188. doi:10.1007/s12551-017-0269-3

Duvall, M. M., Jinha, A., Schappacher-Tilp, G., Leonard, T. R., and Herzog, W. (2017). Differences in Titin Segmental Elongation between Passive and

Active Stretch in Skeletal Muscle. *J. Exp. Biol.* 220, 4418–4425. doi:10.1242/jeb.160762

Duvall, M. M., Gifford, J. L., Amrein, M., and Herzog, W. (2013). Altered Mechanical Properties of Titin Immunoglobulin Domain 27 in the Presence of Calcium. *Eur. Biophys. J.* 42, 301–307. doi:10.1007/s00249-012-0875-8

Edman, K. A., Elzinga, G., and Noble, M. I. (1982). Residual Force Enhancement after Stretch of Contracting Frog Single Muscle Fibers. *J.Gen.Physiol.* 80, 769–784. doi:10.1085/jgp.80.5.769

Epstein, M., Wong, M., and Herzog, W. (2006). Should Tendon and Aponeurosis Be Considered in Series? *J. Biomech.* 39, 2020–2025. doi:10.1016/j.jbiomech.2005.06.011

Finer, J. T., Simmons, R. M., and Spudich, J. A. (1994). Single Myosin Molecule Mechanics: Piconewton Forces and Nanometre Steps. *Nature* 368, 113–119. doi:10.1038/368113a0

Freiburg, A., Trombitas, K., Hell, W., Cazorla, O., Fougerousse, F., Centner, T., et al. (2000). Series of Exon-Skipping Events in the Elastic spring Region of Titin as the Structural Basis for Myofibrillar Elastic Diversity. *Circ. Res.* 86, 1114–1121. doi:10.1161/01.res.86.11.1114

Granzier, H., and Labeit, S. (2002). Cardiac Titin: an Adjustable Multi-functional spring. *J. Physiol.* 541, 335–342. doi:10.1113/jphysiol.2001.014381

Helmes, M., Trombita´s, K., Centner, T., Kellermayer, M., Labeit, S., Linke, W. A., et al. (1999). Mechanically Driven Contour-Length Adjustment in Rat Cardiac Titin's Unique N2B Sequence. *Circ. Res.* 84, 1339–1352. doi:10.1161/01.res.84.11.1339

Herzog, J. A., Leonard, T. R., Jinha, A., and Herzog, W. (2012). Are Titin Properties Reflected in Single Myofibrils? *J. Biomech.* 45, 1893–1899. doi:10.1016/j.jbiomech.2012.05.021

Herzog, W. (2018). The Multiple Roles of Titin in Muscle Contraction and Force Production. *Biophys. Rev.* 10, 1187–1199. doi:10.1007/s12551-017-0395-y

Herzog, W., and Leonard, T. R. (2002). Force Enhancement Following Stretching of Skeletal Muscle. *J.Exp.Biol.* 205, 1275–1283. doi:10.1242/jeb.205.9.1275

Herzog, W. (2016). Letter to the editor: Comments on Cornachione et al. (2016): "The increase in non-cross-bridge forces after stretch of activated striated muscle is related to titin isoforms"The increase in non-cross-bridge forces after stretch of activated striated muscle is related to titin isoforms. *Am. J. Physiology-Cell Physiol.* 311, C158–C159. doi:10.1152/ajpcell.00373.2015

Herzog, W., Powers, K., Johnston, K., and Duvall, M. (2015). A New Paradigm for Muscle Contraction. *Front. Physiol.* 6, 174–185. doi:10.3389/fphys.2015.00174

Herzog, W., Schappacher, G., Duvall, M., Leonard, T. R., and Herzog, J. A. (2016). Residual Force Enhancement Following Eccentric Contractions: a New Mechanism Involving Titin. *Physiology* 31, 300–312. doi:10.1152/physiol.00049.2014

Hill, A. V. (1953). The Mechanics of Active Muscle. *Proc. R.Soc.Lond.* 141, 104–117.

Horowits, R., Kempner, E. S., Bisher, M. E., and Podolsky, R. J. (1986). A Physiological Role for Titin and Nebulin in Skeletal Muscle. *Nature* 323, 160–164. doi:10.1038/323160a0

Horowits, R., Maruyama, K., and Podolsky, R. J. (1989). Elastic Behavior of Connectin Filaments during Thick Filament Movement in Activated Skeletal Muscle. *J.Cell Biol.* 109, 2169–2176. doi:10.1083/jcb.109.5.2169

Horowits, R. (1992). Passive Force Generation and Titin Isoforms in Mammalian Skeletal Muscle. *Biophysical J.* 61, 392–398. doi:10.1016/s0006-3495(92)81845-3

Horowits, R., and Podolsky, R. J. (1987). The Positional Stability of Thick Filaments in Activated Skeletal Muscle Depends on Sarcomere Length: Evidence for the Role of Titin Filaments. *J.Cell Biol.* 105, 2217–2223. doi:10.1083/jcb.105.5.2217

Huxley, A. F. (1957). Muscle Structure and Theories of Contraction. *Prog. Biophys. Biophysical Chem.* 7, 255–318. doi:10.1016/s0096-4174(18)30128-8

Huxley, A. F., and Niedergerke, R. (1954). Structural Changes in Muscle during Contraction: Interference Microscopy of Living Muscle Fibres. *Nature* 173, 971–973. doi:10.1038/173971a0

Huxley, A. F., and Peachey, L. D. (1961). The Maximum Length for Contraction in Vertebrate Striated Muscle. *J.Physiol.* 156, 150–165. doi:10.1113/jphysiol.1961.sp006665

Huxley, A. F. (1980). *Reflections on Muscle*. Liverpool: Liverpool University Press.

Huxley, H. E. (2004). Fifty Years of Muscle and the Sliding Filament Hypothesis. *Eur. J. Biochem.* 271, 1403–1415. doi:10.1111/j.1432-1033.2004.04044.x

Huxley, H., and Hanson, J. (1954). Changes in the Cross-Striations of Muscle during Contraction and Stretch and Their Structural Interpretation. *Nature* 173, 973–976. doi:10.1038/173973a0

Johnston, K., Jinha, A., and Herzog, W. (2016). The Role of Sarcomere Length Non-uniformities in Residual Force Enhancement of Skeletal Muscle Myofibrils. *R. Soc. Open Sci.* 3, 150657. doi:10.1098/rsos.150657

Johnston, K., Moo, E. K., Jinha, A., and Herzog, W. (2019). On Sarcomere Length Stability during Isometric and post-active-stretch Isometric Contractions. *J.Exp.Biol.* 222, 209924. doi:10.1242/jeb.209924

Joumaa, V., Rassier, D. E., Leonard, T. R., and Herzog, W. (2008). The Origin of Passive Force Enhancement in Skeletal Muscle. *Am. J. Physiology-Cell Physiol.* 294, C74–C78. doi:10.1152/ajpcell.00218.2007

Kellermayer, M. S. Z., Smith, S. B., Granzier, H. L., and Bustamante, C. (1997). Folding-unfolding Transitions in Single Titin Molecules Characterized with Laser Tweezers. *Science* 276, 1112–1116. doi:10.1126/science.276.5315.1112

Labeit, D., Watanabe, K., Witt, C., Fujita, H., Wu, Y., Lahmers, S., et al. (2003). Calcium-dependent Molecular spring Elements in the Giant Protein Titin. *Proc. Natl. Acad. Sci. U.S.A.* 100, 13716–13721. doi:10.1073/pnas.2235652100

Leonard, T. R., Duvall, M., and Herzog, W. (2010). Force Enhancement Following Stretch in a Single Sarcomere. *Am. J. Physiology-Cell Physiol.* 299 (6), C1398–C1401. doi:10.1152/ajpcell.00222.2010

Leonard, T. R., and Herzog, W. (2010). Regulation of Muscle Force in the Absence of Actin-Myosin-Based Cross-Bridge Interaction. *Am. J. Physiology-Cell Physiol.* 299, C14–C20. doi:10.1152/ajpcell.00049.2010

Linke, W. A., Popov, V. I., and Pollack, G. H. (1994). Passive and Active Tension in Single Cardiac Myofibrils. *Biophysical J.* 67, 782–792. doi:10.1016/s0006-3495(94)80538-7

Linke, W. A., Rudy, D. E., Centner, T., Gautel, M., Witt, C., Labeit, S., et al. (1999). I-band Titin in Cardiac Muscle Is a Three-Element Molecular spring and Is Critical for Maintaining Thin Filament Structure. *J.Cell Biol.* 146, 631–644. doi:10.1083/jcb.146.3.631

Linke, W. A. (2018). Titin Gene and Protein Functions in Passive and Active Muscle. *Annu. Rev. Physiol.* 80, 389–411. doi:10.1146/annurev-physiol-021317-121234

Llewellyn, M. E., Barretto, R. P. J., Delp, S. L., and Schnitzer, M. J. (2008). Minimally Invasive High-Speed Imaging of Sarcomere Contractile Dynamics in Mice and Humans. *Nature* 454, 784–788. doi:10.1038/nature07104

Ma, W., and Irving, T. C. (2019). X-ray Diffraction of Intact Murine Skeletal Muscle as a Tool for Studying the Structural Basis of Muscle Disease. *JoVE (Journal of Visualized Experiments)* 149, e59559. doi:10.3791/59559

Maruyama, K. (1995). Birth of the Sliding Filament Concept in Muscle Contraction. *J. Biochem.* 117, 1–6. doi:10.1093/oxfordjournals.jbchem.a124692

Mendoza, A. C., and Rassier, D. E. (2020). Extraction of Thick Filaments in Individual Sarcomeres Affects Force Production by Single Myofibrils. *Biophysical J.* 118, 1921–1929. doi:10.1016/j.bpj.2020.03.007

Moo, E. K., Fortuna, R., Sibole, S. C., Abusara, Z., and Herzog, W. (2016). *In Vivo* sarcomere Lengths and Sarcomere Elongations Are Not Uniform across an Intact Muscle. *Front. Physiol.* 7, 187–189. doi:10.3389/fphys.2016.00187

Morgan, D. (1994). An Explanation for Residual Increased Tension in Striated Muscle after Stretch during Contraction. *Exp. Physiol.* 79, 831–838. doi:10.1113/expphysiol.1994.sp003811

Peterson, D. R., Rassier, D. E., and Herzog, W. (2004). Force Enhancement in Single Skeletal Muscle Fibres on the Ascending Limb of the Force-Length Relationship. *J.Exp.Biol.* 207, 2787–2791. doi:10.1242/jeb.01095

Pollack, G. H., Iwazumi, T., Ter Keurs, H. E. D. J., and Shibata, E. F. (1977). Sarcomere Shortening in Striated Muscle Occurs in Stepwise Fashion. *Nature* 268, 757–759. doi:10.1038/268757a0

Pollack, G. H. (1986). Quantal Mechanisms in Cardiac Contraction. *Circ. Res.* 59, 1–8. doi:10.1161/01.res.59.1.1

Rassier, D. E., Herzog, W., Wakeling, J., and Syme, D. A. (2003). Stretch-induced, Steady-State Force Enhancement in Single Skeletal Muscle Fibers Exceeds the Isometric Force at Optimum Fiber Length. *J. Biomech.* 36, 1309–1316. doi:10.1016/s0021-9290(03)00155-6

Rassier, D. E., and Pavlov, I. (2012). Force Produced by Isolated Sarcomeres and Half-Sarcomeres after an Imposed Stretch. *Am. J. Physiology-Cell Physiol.* 302, C240–C248. doi:10.1152/ajpcell.00208.2011

Rassier, D. E. (2012). Residual Force Enhancement in Skeletal Muscles: One Sarcomere after the Other. *J. Muscle Res. Cel Motil* 33, 155–165. doi:10.1007/s10974-012-9308-7

Riveline, D., Ott, A., Jülicher, F., Winkelmann, D. A., Cardoso, O., Lacapère, J.-J., et al. (1998). Acting on Actin: the Electric Motility Assay. *Eur. Biophys. J.* 27, 403–408. doi:10.1007/s002490050147

Schappacher-Tilp, G., Leonard, T., Desch, G., and Herzog, W. (2015). A Novel Three-Filament Model of Force Generation in Eccentric Contraction of Skeletal Muscles. *PLoS ONE* 10, e0117634. doi:10.1371/journal.pone.0117634

Schappacher-Tilp, G. (2018). Titin-mediated Thick Filament Activation Stabilizes Myofibrils on the Descending Limb of Their Force-Length Relationship. *J. Sport Health Sci.* 7, 326–332. doi:10.1016/j.jshs.2018.05.002

Schmidt, J., Jinha, A., and Herzog, W. (2021). Sarcomere Length Measurement Reliability in Single Myofibrils. *J. Biomech.* 126, 110628. doi:10.1016/j.jbiomech.2021.110628

Telley, I. A., Denoth, J., Stüssi, E., Pfitzer, G., and Stehle, R. (2006). Half-sarcomere Dynamics in Myofibrils during Activation and Relaxation Studied by Tracking Fluorescent Markers. *Biophysical J.* 90, 514–530. doi:10.1529/biophysj.105.070334

Trombitas, K., and Granzier, H. (1997). Actin Removal from Cardiac Myocytes Shows that Near Z Line Titin Attaches to Actin while under Tension. *Am. J. Physiology-Cell Physiol.* 273, C662–C670. doi:10.1152/ajpcell.1997.273.2.c662

Conflict of Interest: The author declares that the research was conducted in the absence of any commercial or financial relationships that could be construed as a potential conflict of interest.

Frontiers
Avenue du Tribunal-Fédéral 34
1005 Lausanne | Switzerland

Visit us: www.frontiersin.org
Contact us: frontiersin.org/about/contact